مجلة صرمان للعلوم والتقنية

ISSN: P 2790-5721 | E 2790-5713

المجلد 3

العدد 1

السنة 2021

تصدر عن

كلية صرمان للعلوم والتقنية

sjst.scst.edu.ly

sjst@scst.edu.ly

SJST Surman Journal for Science and Technology | ISSN: E 2790-5721 P 2790-5713
Vol3, No.1, Dec_2021 , pp. 001 ~ 027

Techniques Study for Apply Control on Nonlinear Systems and the Concept of the Sliding Mode Control (SMC)

[1]Imad Omar Shebani Etomi, [2]Adel Ali Ramadan Gamati, [3]Ltfei Abdalsmd, [4]Nezar G. Arabi Ayad

[1,2]Department of Electrical Engineering, Surman College for Science and Technology, Surman, Libya.
[3]Department of Computer Science, Faculty of Art and Science-Musallata, El-Mergib University, Libya.
[4]Electrical and Electronic Engineering Department, Faculty of Engineering, Zawia University, Libya
[1]Imad.etomi@gmail.com
[2]adel1972uk@yahoo.com.uk
[3]Lutfi.abd1977@gmail.com
[4]neezo.1978@gmail.com

الملخص:

المبادئ الأساسية لهذه الورقة هو دراسة بعض التقنيات المستخدمة لتطبيق التحكم على الأنظمة غير الخطية .و يتم تطبيق هذه الطرق على ثلاثة أمثلة غير خطية مختلفة من أجل التحقق من أداء هذه التقنيات. وكذلك تهدف هذه الورقة إلى فهم مفهوم التحكم في وضع الانزلاق وهناك ثلاث مشاكل يجب حلها لهذه الورقة وهي أولاً التحكم في وضع الانزلاق ، الإحماء و الثاني في وضع الانزلاق لمعادلة فان دير بول (VDP) ، والثالث تحكم (MIMO) للذراع المستوي ثنائي الوصلة.

Abstract:

The basic principles of this paper are some techniques that used to apply control on nonlinear systems. These methods were applied to three different nonlinear examples in order to check the performance of these techniques. Moreover, this paper is to understand the concept of the sliding mode control and there are three problems that we should solve for this paper first Sliding Mode Control Warm-Up, second Sliding Mode control for the van der pol Equation (VDP), and third MIMO control of two-link Planar Arm.

Keywords: Sliding mode control (SMC) . Van der pol Equation (VDP) . Multiple input, multiple output (MIMO)

1. Introduction:

The Nonlinear control is the part of control theory which deals with systems that are nonlinear, time-variant, or both. Moreover, the control theory is an interdisciplinary branch of engineering and mathematics that is concerned with the behavior of dynamical systems with inputs, and how to modify the output by changes in the input using feedback, feed forward, or signal filtering. Also, the system to be controlled is called the "plant" , and one way to make the output of a system follow a desired reference signal is to compare the output of the plant to the desired output, and provide feedback to the plant to modify the output to bring it closer to the desired output. Therefore, in this paper to clarification the concept of the sliding mode control for the Sliding Mode control Warm-Up, the Sliding Mode control for the van der pol Equation (VDP), and the MIMO control of a Two-link Planar Arm

2. Sliding Mode Control Warm-Up

In control systems the sliding mode control Warm Up (SMC) is a nonlinear control method that alters the dynamics of a nonlinear system by applying a discontinuous control signal (or more rigorously, a set-valued control signal) that forces the system to "slide" along a cross-section of the system's normal behavior. And, the system differential equation and controller design and the system differential equation as follows:-

$$\dot{x}_1 = x_2 + ax_1 sinx_1 \qquad \& \qquad \dot{x}_2 = bx_1x_2 + u$$

Where x_1 is the first variable and x_2 is the second variable and u is input, and $sinx_1$ is slip angle for first variable. Also, a and b are unknown constants but we know that $0 \le |a| \le 2$ *and* $1 \le |b| \le 3$ .In this experiment we will apply feedback linearization approach to check the system convergence to zero; and the second approach sliding mode control will be applied as well.

$$\overline{f}(x) = \begin{bmatrix} x_2 + ax_1 sinx_1 \\ bx_1x_2 \end{bmatrix} \quad ; \quad \overline{g}(x) = \begin{bmatrix} 0 \\ 1 \end{bmatrix}$$

In this part, we will deal with the system's parameters a, b as unknown parameters $\hat{a}$ and $\hat{b}$. Also, nominal values will be plugged in for them to come up with a diffeomorphism and a controller such that the system converges to zero. For the last two, the system parameters will be changed to another nominal values to check if the controller still effective with system

of not. Now to apply feedback linearization, we need to find a diffeomorphism such that the system will be on chain of integral form.

We need to find $\mathbf{z = T(x)}$ **statisfying**:

$$\frac{\partial T_1}{\partial x}\overline{g} = 0 \quad , \quad \frac{\partial T_2}{\partial x}\overline{g} \neq 0 \quad and \quad T_2 = \frac{\partial T_1}{\partial x}\overline{f}$$

We can write all conditions:

$$(\mathbf{1}) \quad \frac{\partial T_1}{\partial x}\overline{g} = 0 \Longrightarrow \begin{bmatrix}\frac{\partial T_1}{\partial x_1} & \frac{\partial T_1}{\partial x_2}\end{bmatrix}\begin{bmatrix}0\\1\end{bmatrix} = 0 \implies \frac{\partial T_1}{\partial x_2} = 0 \implies T_1 = T_1(x_1)$$

$$(\mathbf{2}) \quad \frac{\partial T_2}{\partial x}\overline{g} \neq 0 \Longrightarrow \begin{bmatrix}\frac{\partial T_2}{\partial x_1} & \frac{\partial T_2}{\partial x_2}\end{bmatrix}\begin{bmatrix}0\\1\end{bmatrix} \neq 0 \implies \frac{\partial T_2}{\partial x_2} \neq 0 \implies T_2 = T_2(x_1, x_2)$$

$$(\mathbf{3}) \quad T_2 = \frac{\partial T_1}{\partial x}\overline{f} = \begin{bmatrix}\frac{\partial T_1}{\partial x_1} & \frac{\partial T_1}{\partial x_2}\end{bmatrix}\begin{bmatrix}x_2 + ax_1 sinx_1\\ bx_1x_2\end{bmatrix} = \frac{\partial T_1}{\partial x_1}(x_2 + ax_1 sinx_1)$$

Let's choose that $T_1 = x_1 \Longrightarrow \frac{\partial T_1}{\partial x_2}\overline{g} = 0 \implies Satisfies\ condition$ [1]

$$T_2 = \frac{\partial T_1}{\partial x}\overline{f} = \begin{bmatrix}\frac{\partial T_1}{\partial x_1} & \frac{\partial T_1}{\partial x_2}\end{bmatrix}\begin{bmatrix}x_2 + ax_1 sinx_1\\ bx_1x_2\end{bmatrix} = \frac{\partial T_1}{\partial x_1}(x_2 + ax_1 sinx_1)$$

$\frac{\partial T_1}{\partial x_1} = 1 \implies T_2 = (x_2 + ax_1 sinx_1) \Longrightarrow Satisfies\ condition$ [2] *and* [3]

So, now we need to satisfy the second condition.

$$\frac{\partial T_2}{\partial x}\bar{g} = \begin{bmatrix}\frac{\partial T_2}{\partial x_1} & \frac{\partial T_2}{\partial x_2}\end{bmatrix}\begin{bmatrix}0\\1\end{bmatrix} = [ax_1\cos(x_1) + a\sin(x_1) \quad 1]\begin{bmatrix}0\\1\end{bmatrix} = 1 \neq 0$$

Then, we conclude that the system is state feedback linearizable.

To get the controller of the system, first, we have to get the diffeomorphism $\boldsymbol{z = T(x)}$ as follows:

$$z = T(x) = \begin{bmatrix}x_1\\ x_2 + ax_1 sinx_1\end{bmatrix} \implies \begin{matrix}z_1 = x_1\\ z_2 = x_2 + ax_1 sinx_1\end{matrix}$$

Here, we need to find $\mathbf{x = T^{-1}(z)}$

$x_1 = z_1$

$z_2 = x_2 + ax_1 sinx_1 \implies z_2 = x_2 + az_1 sinz_1 \implies x_2 = z_2 - az_1 sinz_1$

Then $x = T^{-1}(z)$ will be $\implies \begin{bmatrix}x_1\\x_2\end{bmatrix} = T^{-1}(z) = \begin{bmatrix}z_1\\ z_2 - az_1 sin\ z_1\end{bmatrix}$

To design SFL controller that regulates z $\Longrightarrow 0$

$$\dot{z}_1 = \frac{\partial z_1}{\partial x_1} * \dot{x}_1 + \frac{\partial z_1}{\partial x_2} * \dot{x}_2$$

$$\dot{z}_1 = 1 * \dot{x}_1 + 0 * \dot{x}_2$$

$$\dot{z}_1 = x_2 + ax_1 \sin(x_1)$$

$$\dot{z}_1 = z_2 - az_1 \sin(z_1) + az_1 \sin(z_1)$$

$$\dot{z}_1 = z_2$$

$$\dot{z}_2 = \frac{\partial z_2}{\partial x_1} * \dot{x}_1 + \frac{\partial z_2}{\partial x_2} * \dot{x}_2$$

$$\dot{z}_2 = [ax_1 \cos(x_1) + a \sin(x_1)] * [x_2 + ax_1 \sin(x_1)] + 1 * (bx_1x_2 + u)$$

$$\dot{z}_2 = [ax_1x_2 \cos(x_1) + a^2x_1^2 \cos(x_1) * \sin(x_1) + ax_2 \sin(x_1) + a^2x_1 \sin(x_1) * \sin(x_1)] + bx_1x_2 + u$$

$$\dot{z}_2 = az_1[z_2 - az_1 \sin(z_1)] \cos(z_1) + a^2z_1^2 \cos(z_1) * \sin(z_1) +$$

$$a\,[z_2 - z_1 \sin(z_1)] \sin(z_1) + a^2\, z_1 \sin^2(z_1) + bz_1[z_2 - az_1 \sin(z_1)] + u$$

$$\dot{z}_2 = az_1z_2 \cos(z_1) - a^2z_1^2 \sin(z_1) * \cos(z_1) + a^2z_1^2 \cos(z_1) * \sin(z_1) + az_2 \sin(z_1) - a^2z_1 \sin^2(z_1) + a^2z_1 \sin^2(z_1) + bz_1z_2 - abz_1^2 \sin(z_1) + u$$

$$\dot{z}_2 = az_1z_2 \cos(z_1) + az_2 \sin(z_1) + bz_1z_2 - abz_1^2 \sin(z_1) + u$$

Then the system will be:

$$\dot{z}_1 = z_2$$
$$\dot{z}_2 = f(x) + g(x)u$$

From $\dot{z}_2$, we can get $f(x)$, $g(x)$, $f(z)$, and $g(z)$.

$$f(x) = ax_1x_2 \cos(x_1) + a^2x_1^2 \cos(x_1) * \sin(x_1) + ax_2 \sin(x_1) + a^2x_1 \sin(x_1) * \sin(x_1) + bx_1x_2$$

$$g(x) = 1$$

Now, in *x*- coordinates, we let the controller be

$$u = \frac{1}{g(x)}[-f(x) + v]$$

$$u = -[ax_1x_2\cos(x_1) + a^2x_1^2\cos(x_1) * \sin(x_1) + ax_2\sin(x_1) + a^2x_1\sin(x_1) * \sin(x_1) + bx_1x_2] + v$$

$$u = \frac{1}{g(z)}[-f(z) + v]$$

$$f(z) = az_1z_2\cos(z_1) + az_2\sin(z_1) + bz_1z_2 - abz_1^2\sin(z_1)$$

$$g(z) = 1$$

$$u = -[az_1z_2\cos(z_1) + az_2\sin(z_1) + bz_1z_2 - abz_1^2\sin(z_1)] + v$$

For Simulation and results:

$$u = \frac{1}{g(z)}[-f(z) + v] \quad \Longrightarrow \quad v = -(k_1z_1 + k_2z_2)$$

$\mathbf{k_1}$ & $\mathbf{k_2}$ have to selected to make the location for system poles in the left hand side

thus the system is state feed back linearizable, where $a = 1$, $b = 1.5$, and $v = -k_1z_1 - k_2z_2$ then the control law u that state-feedback linearizes the system will be:

$$u = [-z_1z_2\cos(z_1) - z_2\sin(z_1) - 1.5\,z_1z_2 + 1.5\,z_1^2\sin(z_1) - k_1z_1 - k_2z_2]$$

Substituting u in $\dot{z}_2$, we get; $\dot{z}_2 = -k_1\,z_1 - k_2\,z_2$

Where $\boldsymbol{k_1}$ and $\boldsymbol{k_2}$ are positive and should be chosen to place the system poles the LHP.

Then the state–space for the system will be:

$$\begin{bmatrix}\dot{z}_1\\ \dot{z}_2\end{bmatrix} = \begin{bmatrix}0 & 1\\ -k_1 & -k_2\end{bmatrix}\begin{bmatrix}z_1\\ z_2\end{bmatrix}$$

By simulating the above controller with MATLAB at $a = \hat{a} = 1$ *and* $b = \hat{b} = 1.5$. when we simulate the controller by $a = \hat{a} = 1$ and $b = \hat{b} = 1.5$ or by nominal values of *a* and *b* that we used for feedback linearizing controller we

will get the response shown in Figure (1). By using the MATLAB statement [k = place (A, B, P)] to make the system stable, we can find the values of $\boldsymbol{k_1}$ and $\boldsymbol{k_2}$.

where $A = \begin{bmatrix} 0 & 1 \\ 0 & 0 \end{bmatrix}$, $B = \begin{bmatrix} 0 \\ 1 \end{bmatrix}$, and $P = [-1 \quad -2]$

So, P is the desired eigenvalues. Then, the values will be; $\boldsymbol{k_1 = 2}$ and $\boldsymbol{k_2 = 3}$. So, the obtained state–space will be:

$$\begin{bmatrix} \dot{z}_1 \\ \dot{z}_2 \end{bmatrix} = \begin{bmatrix} 0 & 1 \\ -2 & -3 \end{bmatrix} \begin{bmatrix} z_1 \\ z_2 \end{bmatrix}$$

Here, from the above system we can make that the system becomes linear.

In the simulation part, we simulate the controller u by regulating the states to zero.

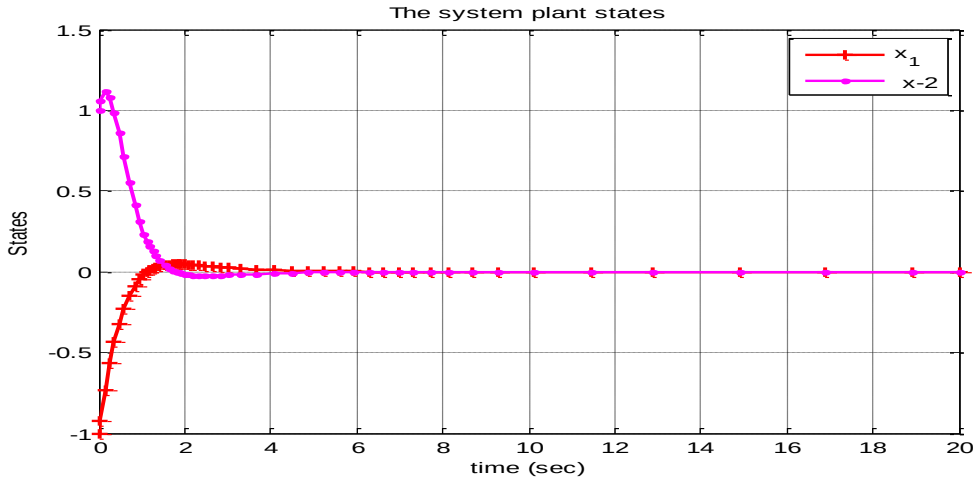

Figure (1) The feedback linearization controller regulates the system states to zero

Here, we can to see clear that both states x_1 and x_2 go to zero and suppose that $\hat{a} \neq a$ and $\hat{b} \neq b$, and that the values of a and b are $a = -1$ and $b = 2$. Using Matlab, plot the phase portrait of the open-loop system (1), and identify the regions where the system exhibits different behaviors. In this part, it was supposed that $a \neq \hat{a}$ *and* $b \neq \hat{b}$ and by setting a=-1 and b=2 in using MATLAB we will plot the phase portrait of the open-loop system (1), and the regions where the system exhibits different behaviors, also we let $u = 0$ of the open-loop system. By simulating the system, we get the phase portrait of the open-loop system using different initial conditions. The Figure (2) and (3) show the results of the simulation for the states of the plant and the phase portrait plot.

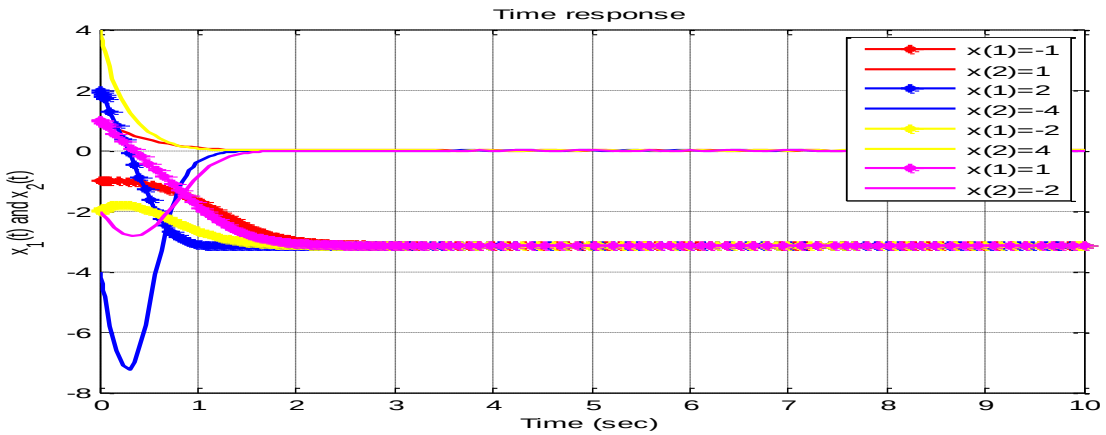

Figure (2): The states vector x of the plant vs time.

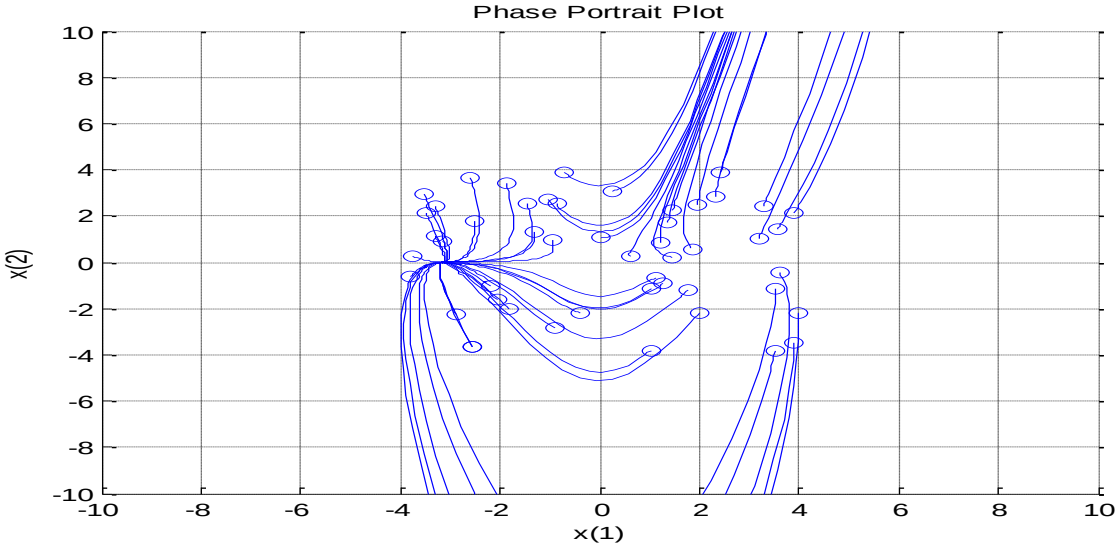

Figure (3): The phase portrait of the system.

For Simulation and results:

The states vector x of the plant vs time sis shown in Figure (2), and the phase portrait of the system is shown in Figure (3).

From Figure (2), we can see that the state x_1 goes to almost -3, and the state x_2 goes to zero. Also, all trajectories in Figure (3) go to almost the points (-3.5, 0) and infinite.

Moreover, we will Explain why it is not possible anymore to use your controller from (a) when $\hat{a} \neq a$ and $\hat{b} \neq b$ and guarantee convergence to zero. In particular pay attention to the diffeomorphism and the controller itself. Verify by setting $a = -1$ and $b = 2$ in your simulation

with the same u and diffeomorphism you got in (a). Hint: be sure to use $\hat{a} = 1$ and $\hat{b} = 1.5$ to do your coordinate transformation and to compute your controller, since you assume not to know the real values for control design purposes! At the same time, use the real a =-1 and b = 2 values in your simulation. From part (a), the controller in z-coordinates is:

$$u = \frac{1}{g(z)}[-f(z) + v]$$

$$f(z) = az_1z_2\cos(z_1) + az_2\sin(z_1) + bz_1z_2 - abz_1^2\sin(z_1)$$

$$g(z) = 1$$

$$u = -[az_1z_2\cos(z_1) + az_2\sin(z_1) + bz_1z_2 - abz_1^2\sin(z_1)] + v$$

In this section, we let a, b and v are the same values that we have found in Part (a). Therefore, we put $a = -1$ and $b = 2$ in the simulation part.

$$u = [z_1z_2\cos(z_1) + z_2\sin(z_1) - 2z_1z_2 - 2\,z_1^2\sin(z_1) - 2z_1 - 3z_2]$$

For Simulation and results:

Figure (4) shows the states vector $[x_1 \quad x_2]$ with respect of time. Also, From Figure (4) we can verify that t it is not possible any more to use the controller from (a) to get the states converged to zero. By choosing $a = -1$ and $b = 2$ which the value of a is out of controller limit, the system becomes impossible to use and make the states regulate to zero.

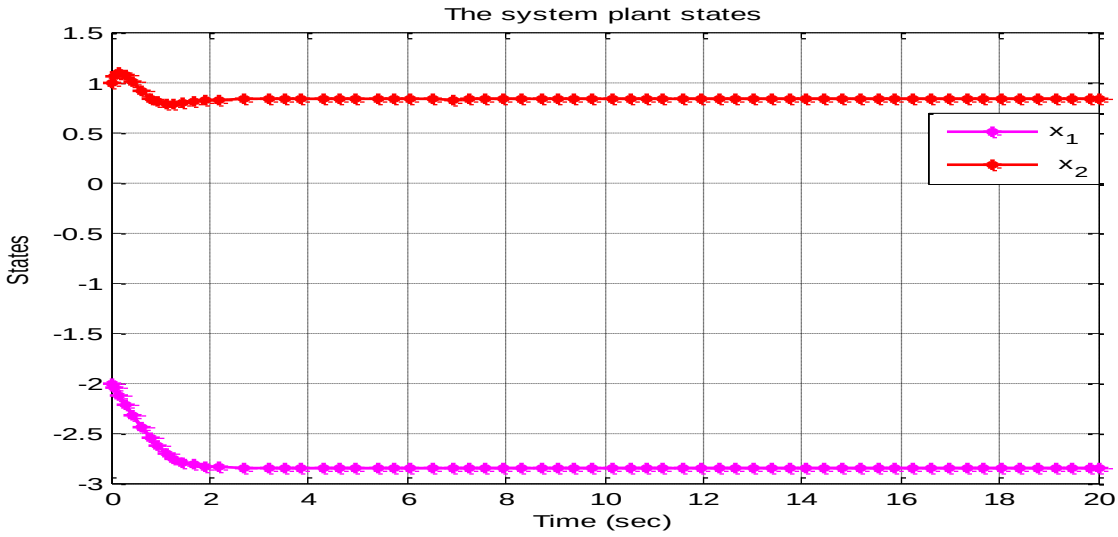

Figure (4): The states vector *x* of the system

Instead of feedback linearization and we will now implement a sliding mode controller. The approach is to figure out what x_2 should be if we considered it as an input to the $\dot{x}_1$ equation so that x_1 is driven to zero. Design a linear manifold of the form $\boldsymbol{s = cx_1 + x_2}$ that does the job by considering what happens when $s = 0$. Next, analyze the dynamics of s and determine a sliding mode controller that drives s to zero (and consequently to zero).

$\dot{x}_1 = x_2 + ax_1 sinx_1$

$\dot{x}_2 = bx_1x_2 + u$

The system is considered as:

$\dot{x} = \bar{f}(x) + \bar{g}(x)u$

Where $\bar{f}(x) = \begin{bmatrix} x_2 + ax_1 \sin(x_1) \\ bx_1x_2 \end{bmatrix}$ and $\bar{g}(x) = \begin{bmatrix} 0 \\ 1 \end{bmatrix}$.

The sliding mode controller which is $\boldsymbol{s = cx_1 + x_2}$, where $\boldsymbol{c}$ is a positive number.

Let's check the sliding mode by forcing the following:

$s = cx_1 + x_2 = 0$

$x_2 = -cx_1$

$v(x) = \frac{1}{2}x_1^2 \quad p.d \quad \Longrightarrow \quad \dot{x}_1 = x_2 + ax_1 sinx_1$

The derivative of it will be:

$\dot{v}(x) = x_1 * \dot{x}_1$

$\dot{v}(x) = x_1 * [\, x_2 + ax_1 \sin(x_1)]$

$\dot{v}(x) = x_1\, x_2 + ax_1^2 \sin(x_1)$

$\dot{v}(x) = x_1\, (-cx_1) + ax_1^2 \sin(x_1)$

$\dot{v}(x) = -cx_1^2 + ax_1^2 \sin(x_1)$

As we know that where $0 \leq a \leq 2$, and $\sin(x_1)$ is between the values $+1$ *and* -1. Then,

$\dot{v}(x) \leq -cx_1^2 + |a|x_1^2$

where $c > 2$, so we let $= 4$, and we will get:

$\dot{v}(x) \leq -4x_1^2 + |a|x_1^2$

Here, we will use Lyapunov's first method by assuming the following:

$v(s) = \frac{1}{2}s^2$

Also, the derivative of it will be:

$\dot{v}(s) = s * \dot{s}$

$\dot{v}(s) = s * (c[\, x_2 + ax_1 \sin(x_1)] + bx_1x_2 + u)$

$\dot{v}(s) = s\, c[\, x_2 + ax_1 \sin(x_1)] + s\, (bx_1x_2) + s\, u$

$\dot{v}(s) \leq s\, c[\, x_2 + ax_1 \sin(x_1)] + s\, (bx_1x_2) + s(1)u$

For $\dot{\boldsymbol{s}}$, we cancel the known term on the right-hand side, we can do

$u = -4x_2 + v$

Then, dynamics $\dot{\boldsymbol{s}}$ will be:

$\dot{s} = 4x_2 + 4ax_1 \sin(x_1) + bx_1x_2 - 4x_2 + v$

$\dot{s} = 4ax_1 \sin(x_1) + bx_1x_2 + v$

Now, we let the part

$|4ax_1 \sin(x_1) + bx_1x_2| \leq 4\rho|x_1| + \sigma|x_1||x_2|$

Where $a \leq \rho$ and $b \leq \sigma$, and let's pick $\rho = 1\ and\ \sigma = 2$. then,

$|4ax_1 \sin(x_1) + bx_1x_2| \leq \beta(x) = 4|x_1| + 2|x_1||x_2|$

Now, $\beta(x)$ will to be:

$\beta(x) = 4|x_1| + 2|x_1||x_2| + k$

where $k > 0$, so let's make it $k = 1$. Then, v will be:

$v = -\beta(x) * \text{sgn}(s)]$

$v = -[4|x_1| + 2|x_1||x_2| + 1] * \text{sgn}(s)]$

Suppose that v in the controller, we will get that

$$u = -4x_2 + v$$

$$u = -4x_2 - [4|x_1| + 2|x_1||x_2| + 1] * \text{sgn}(s)$$

We conclude that $(s = 0)$ is GUAS, and it can be proved that $s(t) \Longrightarrow 0$ in finite time.

Simulate the sliding mode design and the 'sign' function in Matlab, ode45 will take a very long time to run. Instead, it is suggested that we used the approximation $sgn(y) \approx sat(\frac{y}{\epsilon})$

Here, we will simulate the sliding mode design by $\text{sgn}(y) \approx sat(y/\varepsilon)$ function in MATLAB

Where $\boldsymbol{sat(y)} = \begin{cases} \mathbf{1} & \mathbf{if} \quad \boldsymbol{y \geq 1} \\ \boldsymbol{y} & \mathbf{if} \quad \boldsymbol{-1 < y < 1} \\ \mathbf{-1} & \mathbf{if} \quad \boldsymbol{y \leq -1} \end{cases}$, as tune ε to understand the trade-off involved

We use saturation function and let $\epsilon = 0.01$. The sliding mode controller using saturation function is:

$$u = -4x_2 - [4|x_1| + 2|x_1||x_2| + 1] * \text{sat}(s)$$

The simulation results will be shown in Figure (5) and (6) for the states of the plant and the phase portrait plot.

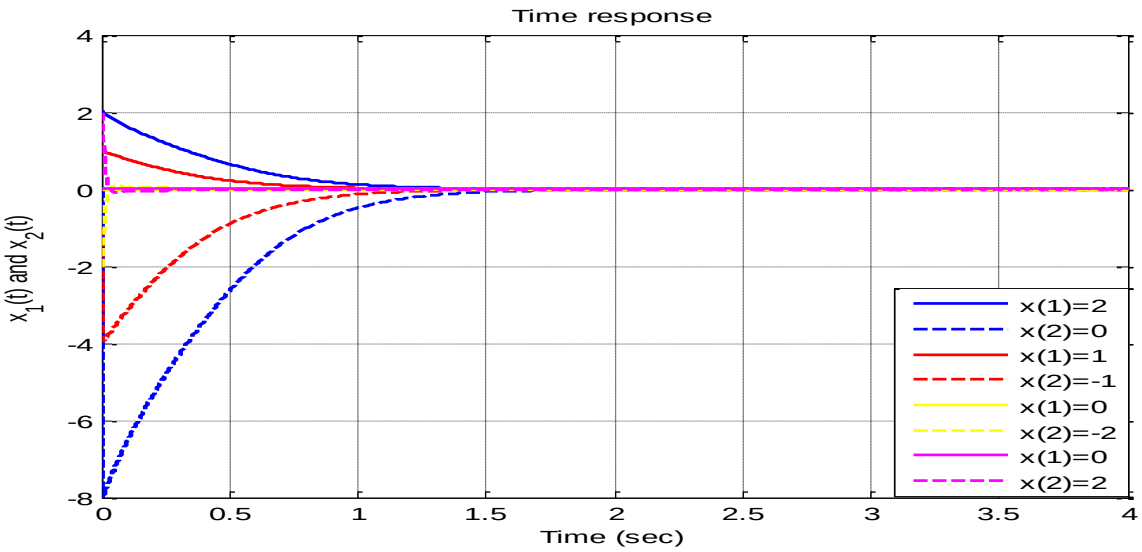

Figure (5): The states vector x of the plan

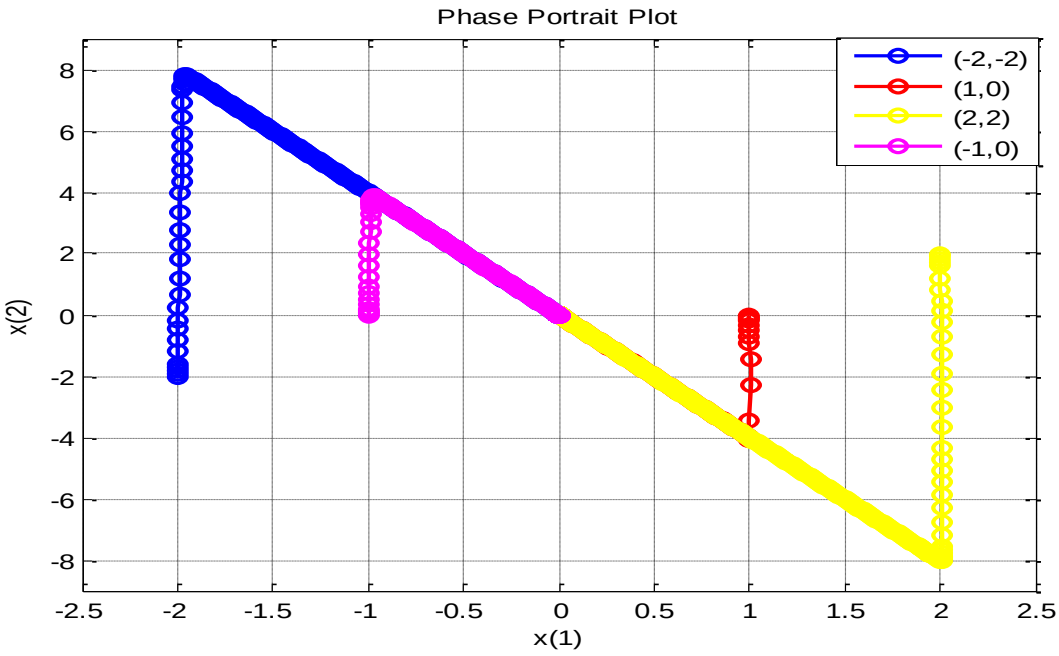

Figure (6): The phase portrait of the plant.

By using MATLAB we have found Figure (5) and (6) show the designed controller of the system regulates all states to zero.

3. Sliding Mode Control for the van der Pol Equation.

Sliding mode control is an area of increasing interest in control engineering , and this method is proved to be robust against disturbances and discrepancies between the physical plant and its mathematical model. However, it has mainly been applied to linear systems and its application to nonlinear systems is based on utilizing linear sliding surfaces and the controlled van der Pol system is given by:

$\dot{x_1} = x_2$

$\dot{x_2} = -\omega^2 x_1 + \varepsilon\omega(1-\mu^2 x_1^2)x_2 u$

Where ω , ε and μ are positive constants and u is the control input.

We will pick some values for ω , ε and μ and verify via simulation that for $u = 1$ and the van der Pol system exhibits a stable limit cycle outside the surface $x_1^2 + x_2^2/\omega^2 = 1/\mu^2$ and that $u =$

There exists an unstable limit cycle outside the same surface, and we can find that limit cycle or oscillation is one of the most important phenomena that occur in dynamical systems and the system oscillates when it has a nontrivial periodic solution

$x(t+T)=x(t), \forall t \geq 0$ For some $T > \mathbf{0}$. Also, for $\boldsymbol{u = 1}$ this is the standard van der Pol oscillator which is known to have a stable limit cycle. And, the fact that the limit cycle is outside a circle of radius by $\mathbf{1/\mu}$ in the plane $\mathbf{(x_1 , x_2/\omega)}$ can be shown by transforming the Equation into polar coordinates.

The surface $x_1^2 + x_2^2/\omega^2 = 1/\mu^2$ is re-written as:

$$\frac{x_2^2}{\omega^2} + x_1^2 = \frac{1}{\mu^2}$$

We let the values $\omega = 1,\ \epsilon = 1\ ,$ and $\mu = 1.$

$$x_2^2 + x_1^2 = 1$$

when $u = 1$, the system will be:

$$\dot{x}_1 = x_2$$
$$\dot{x}_2 = -x_1 + (1 - x_1^2)x_2$$

Here we will shows the phase portrait plot when $u = 1$ in Figures (7)

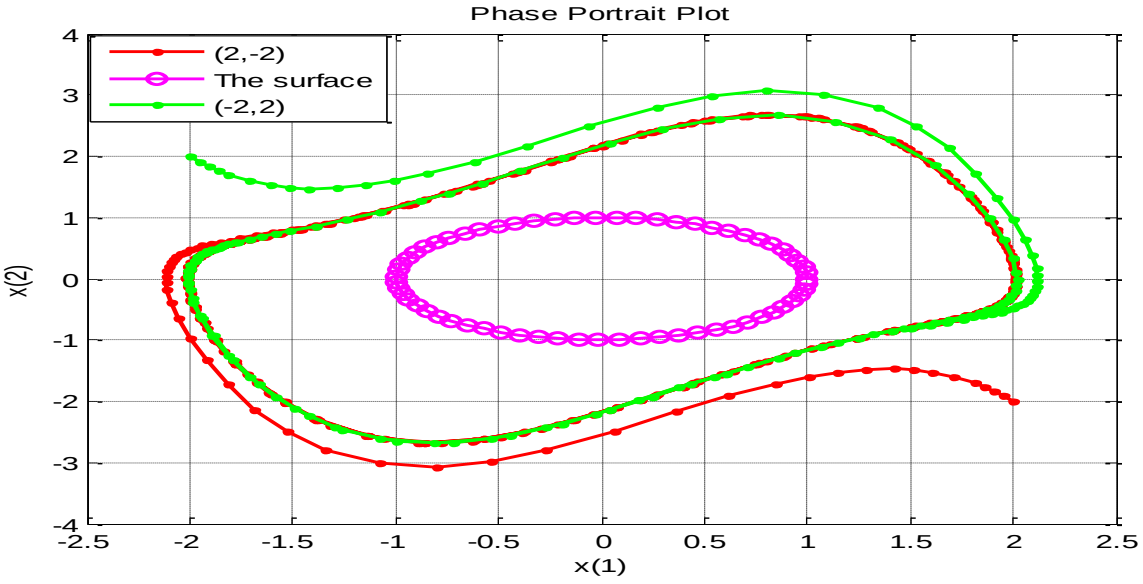

Figure (7): The phase portrait of the plant when $u = 1$

From Figure (7), the conclusion is that this limit cycle is stable outside the surface $\boldsymbol{x_1^2 + x_2^2/\omega^2 = 1/\mu^2}$. Since that, all trajectories on this limit cycle must go to the outside. Therefore, the stable limit must be outside the circle.

When the control input $u = -1$, the system will be:

$$\dot{x}_1 = x_2$$
$$\dot{x}_2 = -x_1 - (1 - x_1^2)x_2$$

The simulation result of the phase portrait plot when $u = -1$ is shown in Figure (8).

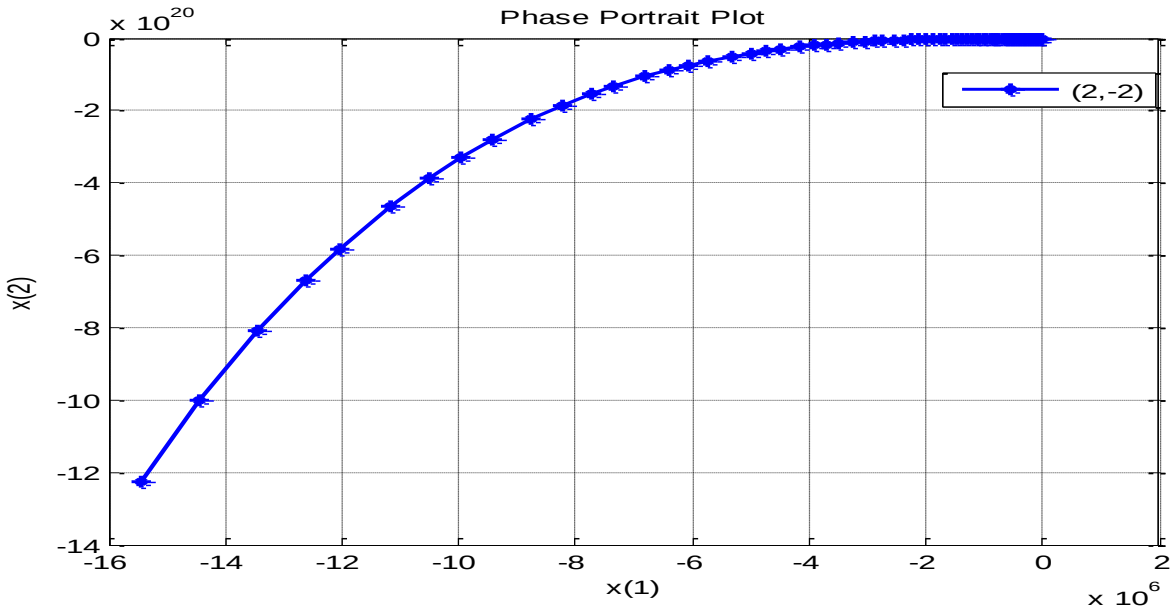

Figure (8): The phase portrait of the plant when $u = -1$

From Figure (8), we can conclude that the existence of the unstable limit cycle by reversing time and scaling the states, so it is unstable limit cycle outside the surface $\boldsymbol{x_1^2 + x_2^2/\omega^2 = 1/\mu^2}$.

Now we will define the sliding manifold $\boldsymbol{s = x_1^2 + x_2^2/\omega^2 - r^2}$, where $\boldsymbol{r < 1/\mu}$ and we will show that if restrict the motion of the system to the surface $\boldsymbol{s = 0}$, and that's we force $\boldsymbol{s(t) \equiv 0}$

Then the resulting behavior is that of the linear harmonic oscillator

$\boldsymbol{\dot{x}_1 = x_2}$ and $\boldsymbol{\dot{x}_2 = -\omega^2 x_1}$ which exhibits a sinusoidal oscillation of frequency $\boldsymbol{\omega}$ and amplitude $\boldsymbol{r}$.

We can write dynamics of the manifold:

$\dot{x_1} = x_2$

$\dot{x_2} = -\omega^2 x_1 + \varepsilon\omega(1-\mu^2 x_1^2)x_2 u$

$s = x_1^2 + \frac{x_2^2}{\omega^2} - r^2 \implies \dot{s} = 2x_1\dot{x}_1 + 2\, {x_2\, \dot{x}_2}/{\omega^2} - r^2$

We let $r = 0.6$, and the sliding manifold is:

$$s = x_1^2 + \frac{x_2^2}{\omega^2} - r^2 \qquad \Longrightarrow \qquad s = x_1^2 + x_2^2 - (0.5)^2 = 0$$

Hence, we can found the dynamics of the sliding manifold:

$$\dot{s} = \frac{\partial s}{\partial x}$$

$$\dot{s} = 2x_1\dot{x}_1 + 2x_2\dot{x}_2$$

$$\dot{s} = 2x_1x_2 + 2x_2(-x_1 + (1 - x_1^2)x_2\, u)$$

$$\dot{s} = 2x_1x_2 - 2x_1x_2 + 2(1 - x_1^2)x_2^2\, u$$

$$\dot{s} = 2(1 - x_1^2)x_2^2\, u$$

$\dot{s}(t) \equiv 0 \Longrightarrow s(t) \equiv 0 \Longrightarrow u(t) \equiv 0$ Then the resulting behavior the linear harmonic oscillator from the original Equation for system when the input zero $u(t) \equiv 0$ we can get the state equation reduces to a harmonic oscillator:

$\dot{x_1} = x_2$ and $\dot{x_2} = -\omega^2 x_1 + \varepsilon\omega(1-\mu^2 x_1^2)x_2 u \implies \dot{x_2} = -\omega^2 x_1$

In this part we will designing a sliding mode controller that driver or leads all trajectories whose initial is within the region $\{x \in R^2 : |x_1| \; 1/\mu\}$ to the manifold $s = 0$ and then has the states slide on the manifold towards the origin. Also, we will simulate the controller and verify that it's able to regulate the state to zero.

$$V(s) = \frac{1}{2}s^2$$

$$\dot{V}(s) = s\dot{s} = s\, 2(1 - x_1^2)x_2^2\, u$$

When we make $s \neq 0$, we have to let the control input is $u = -\text{sgn}(s)$. So, it will be:

$s\dot{s} = 2(1 - x_1^2)x_2^2 * s * \text{sgn}(s)$

$s\dot{s} = 2(1 - x_1^2)x_2^2 * |s|$

The simulation results with different initial conditions will be:

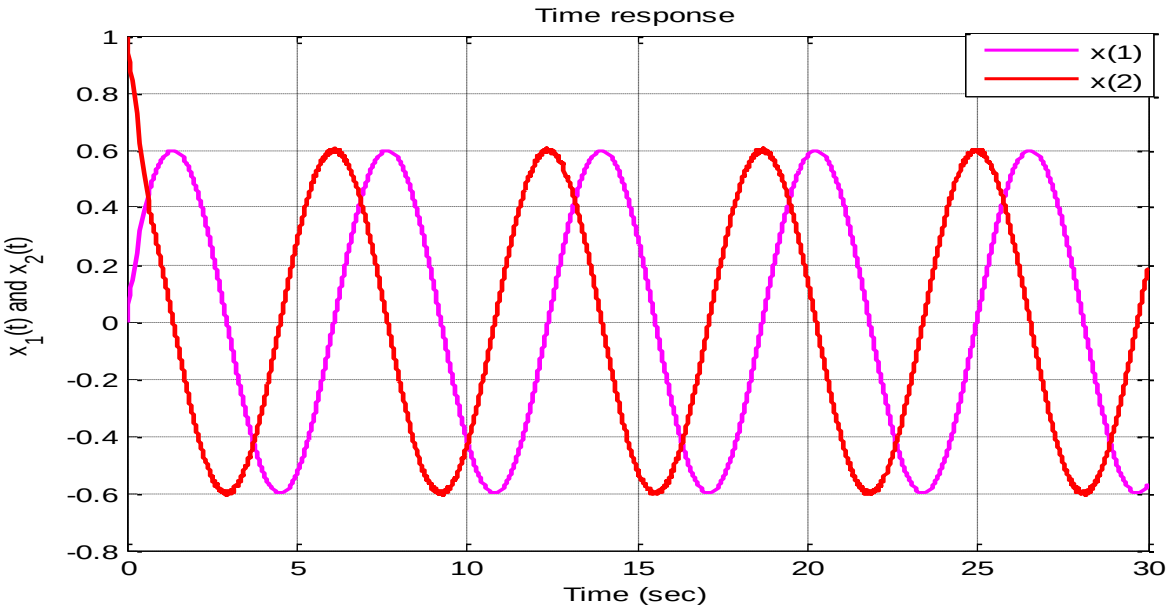

Figure (9): The states vector x of the plant.

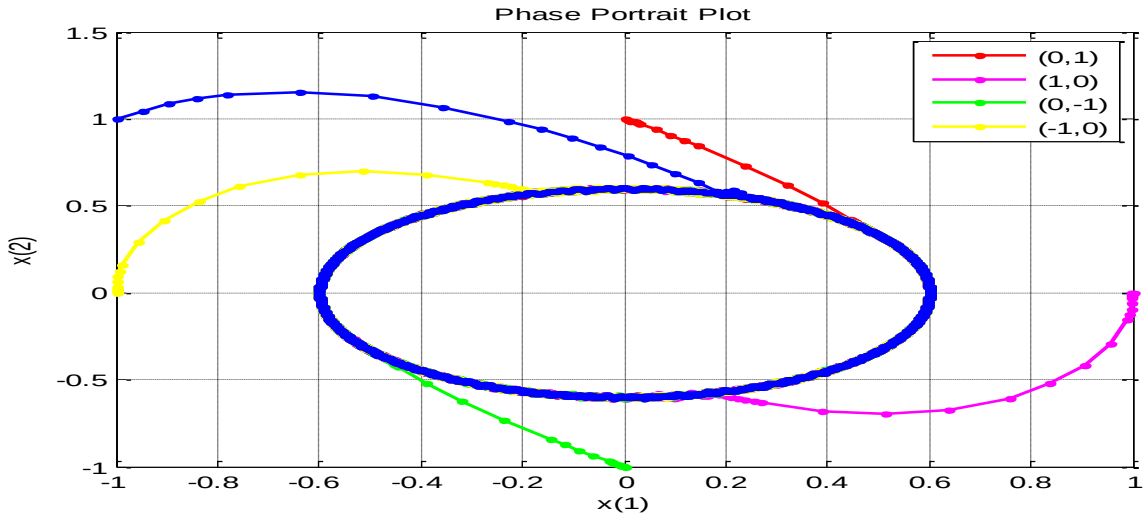

Figure (10): The phase portrait of the plant.

From the Figures (9) and (10), we can show that when $x_2 = 0$, there will be no trajectory shown. Also, we conclude that all trajectories in Figure (10) reach the sliding manifold $\boldsymbol{s = x_1^2 + \frac{x_2^2}{\omega^2} - r^2}$.

4. MIMO Control of a Two-Link Planar Arm.

The Multiple input, multiple output (MIMO) systems describe processes with more than one input and more than one output which require multiple control loops and Single variable input or single variable Output (SISO) control schemes are just one type of control scheme that engineers in industry use to control their process. In this part, we will consist of two links and the first one mounted on a rigid base by means of a frictionless hinge and the second mounted at the end of link one. The joint axes z_0 and z_1 and we establish the base frame $x_0 y_0 z_0$ as the work space frame, which means the arm moves within the $x-y$ plane. The inputs to the system are always the torques τ_1 and τ_2 applied at the joints.

Two - link planar manipulator.

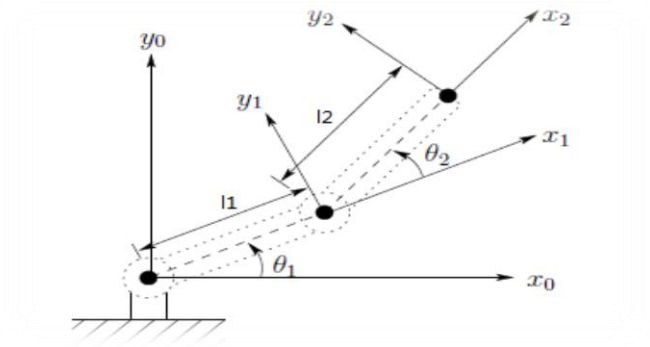

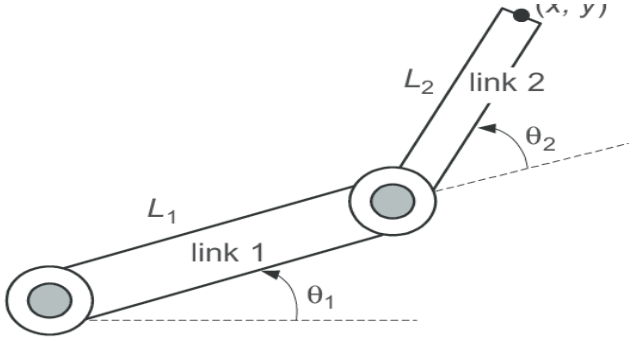

A dynamic model of this system can be derived using Lagrangian equations and is given by

$$\begin{bmatrix} \boldsymbol{H_{11}} & \boldsymbol{H_{12}} \\ \boldsymbol{H_{21}} & \boldsymbol{H_{22}} \end{bmatrix} \begin{bmatrix} \ddot{\boldsymbol{\theta}}_1 \\ \ddot{\boldsymbol{\theta}}_2 \end{bmatrix} + \begin{bmatrix} -\boldsymbol{h}\dot{\boldsymbol{\theta}}_2 & -\boldsymbol{h}\boldsymbol{\theta}_1 - \dot{\boldsymbol{h}}\dot{\boldsymbol{\theta}}_2 \\ \boldsymbol{h}\dot{\boldsymbol{\theta}}_1 & \boldsymbol{0} \end{bmatrix} \begin{bmatrix} \dot{\boldsymbol{\theta}}_1 \\ \dot{\boldsymbol{\theta}}_2 \end{bmatrix} + \begin{bmatrix} \boldsymbol{g_1} \\ \boldsymbol{g_2} \end{bmatrix} = \begin{bmatrix} \boldsymbol{\tau_1} \\ \boldsymbol{\tau_2} \end{bmatrix} \quad \text{where}$$

$$H_{11} = I_1 + I_2 + m_1 l_{c1}^{\ 2} + m_2[l^2_{\ 1} + l^2_{\ c2} + 2l_1 l_{c2}\cos(\theta_2)],$$

$$H_{22} = I_2 + m_2 l_{c2}^{\ 2},$$

$H_{12} = H_{21} = I_2 + m_2[l_{c2}{}^2 + l_1 l_{c2}\cos(\theta_2)]$,

$h = m_2 l_1 l_{c2}\sin(\theta_2)$,

$g_1 = m_1 l_{c1} g\cos(\theta_1) + m_2 g[l^2{}_{c2}\cos(\theta_1+\theta_2) + l_1\cos(\theta_1)]$,

$g_2 = m_2 l_{c2} g\cos(\theta_1+\theta_2)$

In this part, we use the following parameter values $m_1 = 1.0kg$, mass of link one $m_2 = 1.0kg$, mass of link two $l_1 = 1.0m$ length of link one $l_2 = 1.0m$, length of link two $l_{c1} = 0.5m$, distance from the joint of link one to its center of gravity $l_{c2g} = 0.5m$, distance from the joint of link two to its center of gravity $I_1 = 0.2kgm^2$ lengthwise centroid inertia of link one $I_2 = 0.2kgm^2$, lengthwise centroidal inertia of link two and $g = 9.804m/s^2$, acceleration of gravity.

we will do joint space MIMO control of the arm, where the inputs are the two torques and the outputs are the joint angles θ_1 and θ_2 . Write a MIMO state space representation of the system dynamics. Then design the MIMO state feedback controllers ($\boldsymbol{\tau_1}$ ***and*** $\boldsymbol{\tau_2}$) for this system that regulate all the states to zero, and simulate the closed loop system for the initial conditions $\boldsymbol{\theta_1(0)} = \frac{\pi}{2}$, $\dot{\theta}_1(0) = 0$, $\boldsymbol{\theta_2(0)} = -\frac{\pi}{2}$, $\dot{\theta}_2(0) = 0$,we will to plot the controllers and all the states versus time, and provide an interpretation of the plot.

$$\begin{bmatrix} \boldsymbol{H_{11}} & \boldsymbol{H_{12}} \\ \boldsymbol{H_{21}} & \boldsymbol{H_{22}} \end{bmatrix}\begin{bmatrix} \ddot{\boldsymbol{\theta}}_1 \\ \ddot{\boldsymbol{\theta}}_2 \end{bmatrix} + \begin{bmatrix} -\boldsymbol{h}\dot{\boldsymbol{\theta}}_2 & -\boldsymbol{h}\boldsymbol{\theta}_1 - \dot{\boldsymbol{h}}\dot{\boldsymbol{\theta}}_2 \\ \boldsymbol{h}\dot{\boldsymbol{\theta}}_1 & \boldsymbol{0} \end{bmatrix}\begin{bmatrix} \dot{\boldsymbol{\theta}}_1 \\ \dot{\boldsymbol{\theta}}_2 \end{bmatrix} + \begin{bmatrix} \boldsymbol{g_1} \\ \boldsymbol{g_2} \end{bmatrix} = \begin{bmatrix} \boldsymbol{\tau_1} \\ \boldsymbol{\tau_2} \end{bmatrix}$$ where

$H_{11} = I_1 + I_2 + m_1 l_{c1}{}^2 + m_2[l^2{}_1 + l^2{}_{c2} + 2l_1 l_{c2}\cos(\theta_2)]$,

$H_{22} = I_2 + m_2 l_{c2}{}^2$,

$H_{12} = H_{21} = I_2 + m_2[l_{c2}{}^2 + l_1 l_{c2}\cos(\theta_2)]$,

$h = m_2 l_1 l_{c2}\sin(\theta_2)$,

$g_1 = m_1 l_{c1} g\cos(\theta_1) + m_2 g[l^2{}_{c2}\cos(\theta_1+\theta_2) + l_1\cos(\theta_1)]$,

$g_2 = m_2 l_{c2} g\cos(\theta_1+\theta_2)$

$H_{11}\ddot{\theta} + H_{12}\ddot{\theta}_2 - h\dot{\theta}_2\dot{\theta}_1 - h\dot{\theta}_1\dot{\theta}_2 - h\dot{\theta}_2^2 + g_1 = \tau_1$

$$H_{21}\ddot{\theta} + H_{22}\ddot{\theta_2} + h\dot{\theta_1^2} + g_2 = \tau_2$$

$$\ddot{\theta_1} = -\frac{H_{12}}{H_{11}}\ddot{\theta_2} + \frac{h}{H_{11}}\dot{\theta_2}\dot{\theta_1} + \frac{h}{H_{11}}\dot{\theta_1}\dot{\theta_2} + \frac{h}{H_{11}}\dot{\theta_2^2} - \frac{g_1}{H_{11}} + \frac{\tau_1}{H_{11}}$$

$$\ddot{\theta_2} = -\frac{H_{21}}{H_{22}}\ddot{\theta_1} - \frac{h}{H_{22}}\dot{\theta_1^2} - \frac{g}{H_{22}} + \frac{\tau_2}{H_{22}}$$

$$\ddot{\theta_1} = -\frac{H_{21}}{H_{22}}\left[-\frac{H_{21}}{H_{22}}\ddot{\theta_1} - \frac{h}{H_{22}}\dot{\theta_1^2} - \frac{g_2}{H_{22}} + \frac{\tau_2}{H_{22}}\right] + \frac{h}{H_{11}}\dot{\theta_2}\dot{\theta_1} + \frac{h}{H_{11}}\dot{\theta_1}\dot{\theta_2} + \frac{h}{H_{11}}\dot{\theta_2^2} - \frac{g_1}{H_{11}} + \frac{\tau_1}{H_{11}}$$

We will define that:

$$M = \begin{bmatrix} H_{11} & H_{12} \\ H_{21} & H_{22} \end{bmatrix}^{-1} \begin{bmatrix} -h\dot{\theta}_2 & -h\dot{\theta}_1 - h\dot{\theta}_2 \\ h\dot{\theta}_1 & 0 \end{bmatrix}$$

$$G = \begin{bmatrix} H_{11} & H_{12} \\ H_{21} & H_{22} \end{bmatrix}^{-1} \begin{bmatrix} g1 \\ g2 \end{bmatrix}$$

$$Hinv = \begin{bmatrix} H_{11} & H_{12} \\ H_{21} & H_{22} \end{bmatrix}^{-1}$$

And define that:

$$q_1 = \theta_1$$
$$q_2 = \theta_2$$
$$q_3 = \dot{\theta}_1$$
$$q_4 = \dot{\theta}_2$$

Then the state space representation of the system will be:

$$\begin{bmatrix} \dot{q}_1 \\ \dot{q}_2 \\ \dot{q}_3 \\ \dot{q}_4 \end{bmatrix} = \begin{bmatrix} 0 & 0 & 1 & 0 \\ 0 & 0 & 0 & 1 \\ 0 & 0 & M(1,1) & M(1,2) \\ 0 & 0 & M(2,1) & M(2,2) \end{bmatrix} \begin{bmatrix} q_1 \\ q_2 \\ q_3 \\ q_4 \end{bmatrix} + \begin{bmatrix} 0 \\ 0 \\ G(1,1) \\ G(2,1) \end{bmatrix} + \begin{bmatrix} 0 & 0 \\ 0 & 0 \\ Hinv(1,1) & Hinv(1,2) \\ Hinv(2,1) & Hinv(2,2) \end{bmatrix} \begin{bmatrix} \tau_1 \\ \tau_2 \end{bmatrix}$$

Then we can start to design our control torque input. Note that we have to control q1 and q2 independently, so that we have decoupled the 2 inputs.

Than we will define that:

$$\begin{bmatrix} \tau_1 \\ \tau_2 \end{bmatrix} = \tau = Hu = H \begin{bmatrix} u_1 \\ u_2 \end{bmatrix}$$ where, $Hinv*H=I$

And let that:

$$u_1 = -M(1,1)q_3 - M(1,2)q_4 - G(1,1) - \mathrm{k}_{11}\, q_1 - k_{12}q_3$$
$$u_2 = -M(2,1)q_3 - M(2,2)q_4 - G(2,1) - \mathrm{k}_{21}\, q_2 - k_{22}q_4$$

Where, H_{11}=H_{12}=H_{22}=H_{22} =1

$$\ddot{\theta}_1 = \frac{H_{12}^2\ddot{\theta}_1}{H_{11}H_{22}} + \frac{hH_{12}}{H_{22}H_{11}}\dot{\theta}_1^2 + \frac{g_2H_{12}}{H_{11}H_{12}} - \frac{\tau_2H_{12}}{H_{11}H_{12}} + \frac{h}{H_{11}}\dot{\theta}_2\dot{\theta}_1 + \frac{h}{H_{11}}\dot{\theta}_1\dot{\theta}_2 + \frac{h}{H_{11}} + \frac{h}{H_{11}}\dot{\theta}_2^2 - \frac{g_1}{H_{11}} + \frac{\tau_1}{H_{11}}$$

$$\ddot{\theta}_1 = \frac{H_{11}H_{22}}{H_{11}H_{22}-H_{12}^2}\left[\frac{hH_{12}}{H_{22}H_{11}}\dot{\theta}_1^2 + \frac{g_2H_{12}}{H_{11}H_{22}} - \frac{H_{12}}{H_{11}H_{22}}\tau_2 + 2\frac{h}{H_{11}}\dot{\theta}_2\dot{\theta}_1 + + \frac{h}{H_{11}}\dot{\theta}_2^2 - \frac{g_1}{H_{11}} + \frac{\tau_1}{H_{11}}\right]$$

$$\ddot{\theta}_1 = \frac{1}{H_{11}H_{22}-H_{12}^2}\left[h\dot{\theta}_1^2H_{12} + g_2H_{12} - H_{12}\tau_2 + 2h\dot{\theta}_1\dot{\theta}_2H_{12} + h\dot{\theta}_2^2H_{12} - g_1H_{12} + H_{12}\tau_1\right]$$

$$\ddot{\theta}_1 = \frac{H_{12}}{H_{11}H_{22}-H_{12}^2}\left(h\dot{\theta}_1^2 + h\dot{\theta}_2^2 - g_1 + g_2 + 2h\dot{\theta}_1\dot{\theta}_2 + \tau_1 - \tau_2\right)$$

$$\ddot{\theta}_2 = -\frac{H_{21}}{H_{22}}\left[\frac{H_{12}}{H_{11}H_{22}-H_{12}^2}\left(h\dot{\theta}_1^2 + h\dot{\theta}_2^2 - g_1 + g_2 + 2h\dot{\theta}_1\dot{\theta}_2 + \tau_1 - \tau_2\right)\right] - \frac{h}{H_{22}}\dot{\theta}_1^2 - \frac{g_2}{H_{22}} + \frac{\tau_2}{H_{22}}$$

$$\ddot{\theta}_2 = -\frac{H_{12}^2}{H_{22}\left[H_{11}H_{22}-H_{12}^2\right]}\left[h\dot{\theta}_1^2 + h\dot{\theta}_2^2 - g_1 + g_2 + 2h\dot{\theta}_1\dot{\theta}_2 + \tau_1 - \tau_2\right] - \frac{h}{H_{22}}\dot{\theta}_1^2 - \frac{g_2}{H_{22}} + \frac{\tau_2}{H_{22}} \quad \dot{\theta}_1 = \theta_1$$

$$\ddot{\theta}_1 = \frac{H_{11}H_{22}}{H_{11}H_{22}-H_{12}^2}\left[h\dot{\theta}_1^2 + h\dot{\theta}_2^2 - g_1 + g_2 + 2h\dot{\theta}_1\dot{\theta}_2 + \tau_1 - \tau_2\right]$$

$$\dot{\theta}_2 = \theta_2$$

$$\ddot{\theta}_2 = -\frac{H_{12}^2}{\left[H_{11}H_{22}-H_{12}^2\right]}\left[\frac{h\dot{\theta}_1^2}{H_{22}} + \frac{h\dot{\theta}_2^2}{H_{22}} - \frac{g_1}{H_{22}} + \frac{g_2}{H_{22}} + \frac{2h\dot{\theta}_1\dot{\theta}_2}{H_{22}} + \frac{\tau_1}{H_{22}} - \frac{\tau_2}{H_{22}}\right] - \frac{h}{H_{22}}\dot{\theta}_1^2 - \frac{g_2}{H_{22}} + \frac{\tau_2}{H_{22}}$$

$$x_1 = \theta_1 \quad , \quad x_2 = \dot{\theta}_1 \quad , \quad x_3 = \theta_2 \quad , \quad x_4 = \dot{\theta}_2$$

$$\dot{x}_1 = x_2$$

$$x_2 = \frac{H_{12}}{H_{11}H_{22}-H_{12}^2}\left[hx_2^2 + hx_4^2 - g_1 + g_2 + 2hx_2x_4 + \tau_1 - \tau_2\right]$$

$$\dot{x}_3 = x_4$$

$$\dot{x}_4 = -\frac{H_{12}^2}{\left[H_{11}H_{22}-H_{12}^2\right]}\left[\frac{hx_2^2}{H_{22}} + \frac{hx_4^2}{H_{22}} - \frac{g_1}{H_{22}} + \frac{g_2}{H_{22}} + \frac{2hx_2x_4}{H_{22}} + \frac{\tau_1}{H_{22}} - \frac{\tau_2}{H_{22}}\right] - \frac{h}{H_{22}}x_2^2 - \frac{g_2}{H_{22}} + \frac{\tau_2}{H_{22}}$$

$$g_1 = \theta_1 \quad , \quad \dot{g}_1 = \dot{\theta}_1$$

$$\ddot{g}_1 = \ddot{\theta}_1 = \frac{H_{12}}{H_{11}H_{22}-H_{12}^2}\left(h\dot{\theta}_1^2 + h\dot{\theta}_2^2 - g_1 + g_2 + 2h\dot{\theta}_1\dot{\theta}_2 + \frac{H_{12}}{H_{11}H_{22}-H_{12}^2}\tau_1 - \frac{H_{12}}{H_{11}H_{22}-H_{12}^2}\tau_2\right)$$

$$g_2 = \theta_2 \qquad \text{and} \qquad \dot{g}_2 = \dot{\theta}_2$$

$$\ddot{g}_2 = \ddot{\theta}_2 = -\frac{H_{12}^2}{H_{11}H_{22}-H_{12}^2}\left[\frac{h\dot{\theta}_1^2}{H_{22}} + \frac{h\dot{\theta}_1^2}{H_{22}} - \frac{g_1}{H_{22}} + \frac{g_2}{H_{22}} + \frac{2h\theta_1\dot{\theta}_2}{H_{22}}\right]\frac{h}{H_{22}}\dot{\theta}_1^2 - \frac{g_2}{H_{22}} + \frac{1}{H_{22}}\left[-\frac{H_{12}^2}{H_{11}H_{22}-H_{12}^2} + 1\right]\tau_1 + \left[\frac{H_{12}^2}{H_{22}[H_{11}H_{22}-H_{12}^2]}\right]\tau_2$$

$$F_1(x) = \frac{H_{12}}{H_{11}H_{22}-H_{12}^2}\left(h\dot{\theta}_1^2 + h\dot{\theta}_2^2 - g_1 + g_2 + 2h\dot{\theta}_1\dot{\theta}_2\right)$$

$$F_2(x) = -\frac{H_{12}^2}{H_{11}H_{22}-H_{12}^2}\left[\frac{h\dot{\theta}_1^2}{H_{22}} + \frac{h\dot{\theta}_1^2}{H_{22}} - \frac{g_1}{H_{22}} + \frac{g_2}{H_{22}} + \frac{2h\theta_1\dot{\theta}_2}{H_{22}}\right]\frac{h}{H_{22}}\dot{\theta}_1^2 - \frac{g_2}{H_{22}}$$

$$g_1(x) = \left[\frac{H_{12}}{H_{11}H_{22}-H_{12}^2}\tau_1\right] \quad , \quad g_2(x) = \left[-\frac{H_{12}}{H_{11}H_{22}-H_{12}^2}\tau_2\right]$$

$$g_3(x) = \left[\left(\frac{1}{H_{22}} - \frac{H_{12}}{H_{11}H_{22}-H_{12}^2} + 1\right)\tau_1\right] \quad , \quad g_4(x) = \left[\frac{H_{12}^2}{H_{22}[H_{11}H_{22}-H_{12}^2]}\tau_2\right]$$

$$\ddot{g}_1 = \begin{bmatrix} f_1(x) \\ f_2(x) \end{bmatrix} + \begin{bmatrix} g_1(x) & g_2(x) \\ g_3(x) & g_4(x) \end{bmatrix}\begin{bmatrix} \tau_1 \\ \tau_2 \end{bmatrix} \quad \rightarrow \quad \begin{bmatrix} \tau_1 \\ \tau_2 \end{bmatrix} = \begin{bmatrix} g_1(x) & g_2(x) \\ g_3(x) & g_4(x) \end{bmatrix} - \left(\begin{bmatrix} f_1(x) \\ f_2(x) \end{bmatrix} + v\right)$$

$$v_1 = -k_1 g_1 - k_2 \dot{g}_1 = 2x_1 - 3x_2$$

$$v2 = -k_1 g_2 - k_2 \dot{g}_2 = 24x_3 - 10x_4$$

$$u_1 = -\frac{g_2}{g_1}\left[\frac{1}{g_1 g_4 - g_2 g_3}(g_3 f_1 - g_3 v_1 - g_1 f_2 + g_1 - \frac{f_1}{g_1} + \frac{v_1}{g_1}\right]$$

$$u_1 = \left[\frac{1}{g_1 g_4 - g_3 g_2}(g_3 f_1 - g_3 v_1 - g_1 f_1 + g_1 v_2\right]$$

$$\begin{bmatrix} \ddot{\theta}_1 \\ \ddot{\theta}_2 \end{bmatrix} = \frac{1}{H_{11}H_{22}-H^2}\begin{bmatrix} H_{22} & -H_{21} \\ H_{21} & H_{11} \end{bmatrix}\begin{bmatrix} 2h\dot{\theta}_1\dot{\theta}_2 + h\dot{\theta}_2^2 - g_1 + \tau_1 \\ -h\dot{\theta}_1^2 - g_2 + \tau_2 \end{bmatrix}$$

$$\begin{bmatrix} \ddot{\theta}_1 \\ \ddot{\theta}_2 \end{bmatrix} = \frac{1}{H_{11}H_{22}-H^2}\begin{bmatrix} H_{22}\left(2h\dot{\theta}_1\dot{\theta}_2 + h\dot{\theta}_2^2 - g_1 + \tau_1\right) - H_{21}(-h\dot{\theta}_1^2 - g_2 + \tau_2) \\ \left(-H_{21}\left(2h\dot{\theta}_1\dot{\theta}_2 + h\dot{\theta}_2^2 - g_1 + \tau_1\right) + H_{11}\left(h\dot{\theta}_1^2 - g_2 + \tau_2\right)\right) \end{bmatrix}$$

$$\ddot{\theta}_1 = \frac{H_{22}}{H_{11}H_{22}-H^2}\left(2h\dot{\theta}_1\dot{\theta}_2 + h\dot{\theta}_2^2 - g_1 + \tau_1\right) - \frac{H_{11}}{H_{11}H_{22}-H^2}\left(-h\dot{\theta}_1^2 - g_2 + \tau_2\right)$$

$$\dot{x}_2 = \frac{H_{22}}{H_{11}H_{22}-H^2}\left(2hx_2x_4 + hx_4^2 - g_1 + u_1\right) - \frac{H_{21}}{H_{11}H_{22}-H^2}\left(-hx_2^2 - g_2 + u_2\right)$$

$$\ddot{\theta}_2 = \frac{-H_{21}}{H_{11}H_{22}-H^2}\left(2h\dot{\theta}_1\dot{\theta}_2 + h\dot{\theta}_2^2 - g_1 + \tau_1\right) - \frac{H_{11}}{H_{11}H_{22}-H^2}\left(-h\dot{\theta}_1^2 - g_2 + \tau_2\right)$$

$$\dot{x}_4 = \frac{-H_{21}}{H_{11}H_{22}-H^2}\left(2hx_2x_4 + hx_4^2 - g_1 + u_1\right) - \frac{H_{21}}{H_{11}H_{22}-H^2}\left(-hx_2^2 - g_2 + u_2\right)$$

$$y_1 = x_1 \qquad \Rrightarrow \qquad y_2 = x_2$$

$$H_{11}H_{22} - H^2 = 0.405 - 1.1125\cos\theta_2 - 0.25\cos\theta_2^2$$

$$H_{11}H_{22} - H^2 = 0.405 - 1.1125\cos x_3 - 0.25\cos x_1^2$$

$$x_1 = \theta_1 \quad , \quad x_2 = \dot{\theta}_1 \quad , \quad x_3 = \theta_2 \quad , \; x_4 = \dot{\theta}_2$$

$$\dot{y}_1 = \dot{x}_1 = x_2 \qquad \Rightarrow \quad \ddot{y}_1 = \dot{x}_2$$

$$\dot{y}_2 = \dot{x}_3 = x_4 \qquad \Rightarrow \quad \ddot{y}_2 = \dot{x}_4$$

$$\begin{bmatrix}\ddot{y}_1\\ \ddot{y}_2\end{bmatrix} = \begin{bmatrix}\dfrac{H_{22}}{H_{11}H_{22}-H^2}(2hx_2x_4 + hx_4^2 - g_1) - \dfrac{H_{21}}{H_{11}H_{22}-H^2}(-hx_2^2 - g_2)\\ \dfrac{-H_{21}}{H_{11}H_{22}-H^2}(2hx_2x_4 + hx_4^2 - g_1) + \dfrac{H_{11}}{H_{11}H_{22}-H^2}(-hx_2^2 - g_2)\end{bmatrix} +$$

$$\begin{bmatrix}\frac{H_{22}}{H_{11}H_{22}-H^2} & -\frac{H_{21}}{H_{11}H_{22}-H^2}\\ -\frac{H_{21}}{H_{11}H_{22}-H^2} & \frac{H_{11}}{H_{11}H_{22}-H^2}\end{bmatrix}\begin{bmatrix}u_1\\ u_2\end{bmatrix}$$

$$\begin{bmatrix}u_1\\ u_2\end{bmatrix} = \begin{bmatrix}\frac{1}{H_{11}H_{22}-H^2}(2hH_{22}x_2x_4 + H_{22}hx_4^2 - H_{22}g_1 + H_{21}hx_2^2 + H_{21}g_2)\\ \frac{1}{H_{11}H_{22}-H^2}(-2hH_{22}x_2x_4 - H_{22}hx_4^2 + H_{22}g_1 + H_{21}hx_2^2 + H_{21}g_2)\end{bmatrix} -$$

$$\begin{bmatrix}K_{11} & K_{12} & 0 & 0\\ 0 & 0 & K_{23} & K_{24}\end{bmatrix}\begin{bmatrix}y_1\\ \dot{y}_1\\ y_2\\ \dot{y}_2\end{bmatrix}$$

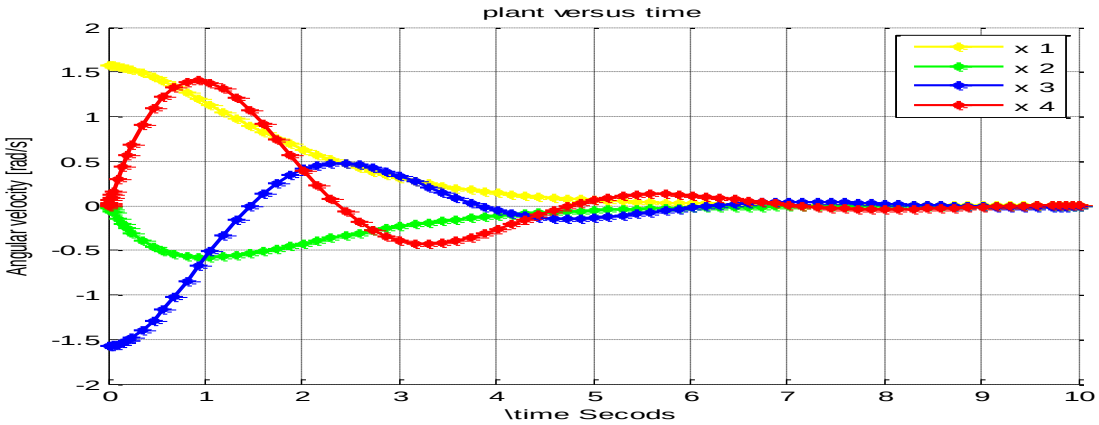

Figure (11): Angular velocity [rad/s]

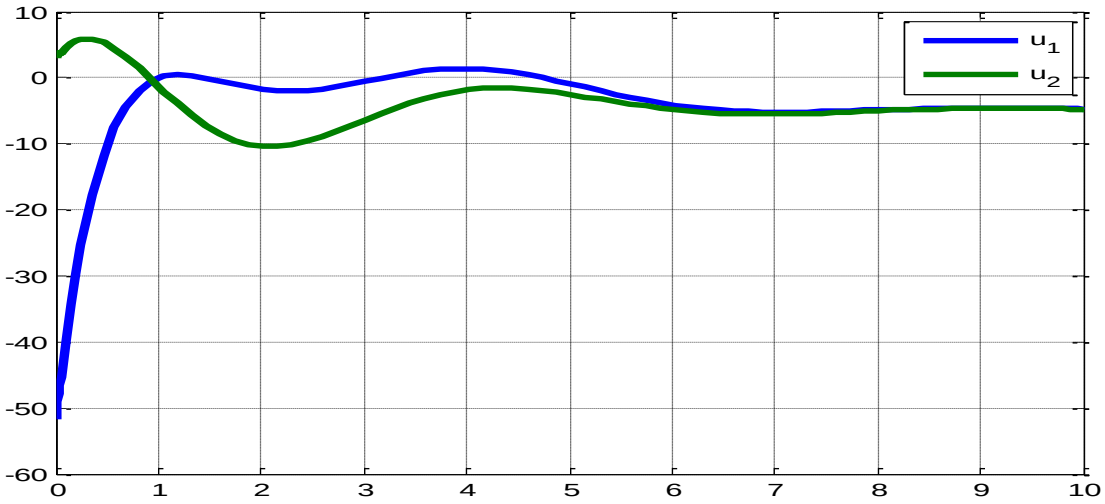

Figure (12): input u_1 and u_2

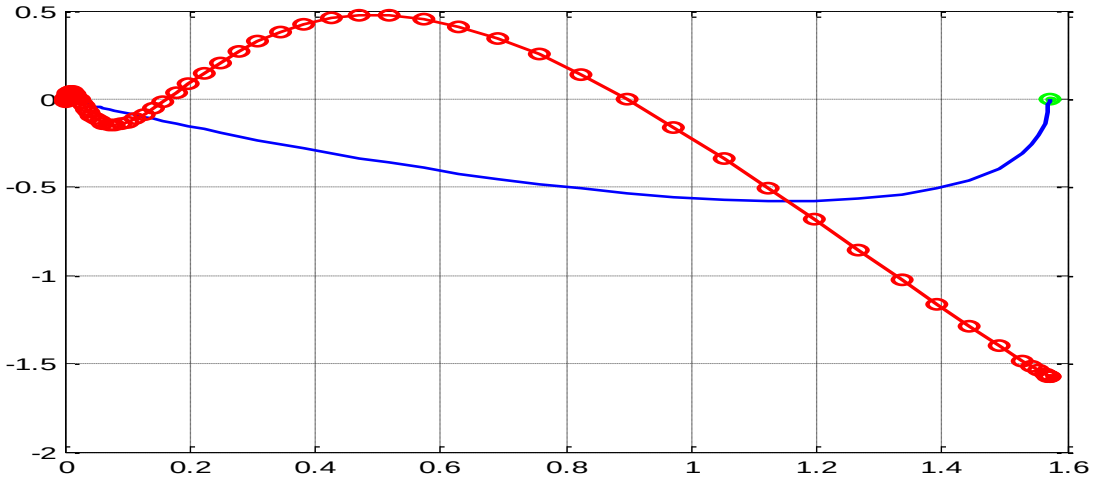

Figure (13): Plot x (1,1), x(1,2) and y1(1), y2(1)

Now we want to control the end-effector of the arm to generate a path in $x-y$ plan. The output s are the position coordinates x and y (z is always zero) of the end-effector. Let

Be a smooth and invertible mapping between the joint vector $\theta=[\theta_1,\theta_2]^T \in Q$ and the workspace variables. The space Q is a suitably chosen rage of angles for θ_1 and θ_2, then $X=[X_0,Y_0]^T$ is the position of the end-effector on the (x_0-y_0) plane. In other words $X=f(\theta)$, so that the position of the end-effector can be computed from the two joint angles, and mapping f is known as the

arm's forward kinematics, and it can lead us directly into so-called work space control, which means that we will perform instead of joint space control. Also, the exists a relationship between the vector of linear velocities of the end-effector $\dot{\boldsymbol{X}}$ and the vector of velocities of joint variables $\dot{\boldsymbol{\theta}}$ given by $\dot{\boldsymbol{X}} = \boldsymbol{J}\dot{\boldsymbol{\theta}}$ where $\boldsymbol{J}$ is as the Jacobian matrix, and the forward kinematic function , and we will using trigonometry to show that the Jacobian is given by:

$$J = \begin{bmatrix} -l_1 \sin(\theta_1) - l_2 \sin(\theta_1 + \theta_2) & -l_2 \sin(\theta_1 + \theta_2) \\ l_1 \cos(\theta_1) + l_2 \cos(\theta_1 + \theta_2) & l_2 \cos(\theta_1 + \theta_2) \end{bmatrix}$$

Then, the derive the new MIMO state space representation of the system dynamics, where the state vector is X instead of Θ. We will design the MIMO state feedback controllers ($\hat{\tau}_1$ and $\hat{\tau}_2$)

$$\begin{cases} \boldsymbol{x = \sqrt{2}\ (m)} \\ \boldsymbol{y = sin\left(\frac{\pi t}{30}\right)\ (m)} \end{cases}$$

And we should verify design with simulation for initial conditions$\boldsymbol{\theta_1 = (0)}$, $\boldsymbol{\dot{\theta}_1 = (0)}$, $\boldsymbol{\dot{\theta}_2 = 0.2}$, $\boldsymbol{\dot{\theta}_2 = (0)}$. We will plot the control signals and all the states versus time, and demonstrate an animation of the arm's motion.

Here, we want to control the end-effector of the arm to generate a path in $x - y$ plan. The output s are the position coordinates x and y (z is always zero) of the end-effector.

$$\boldsymbol{x = l_1 \cos\theta_1 + l_2 \cos(\theta_1 + \theta_2)}$$

$$\boldsymbol{y = l_1 \sin\theta_1 + l_2 \sin(\theta_1 + \theta_2)}$$

Let's the position equation to find the velocity:

$$\boldsymbol{\dot{x} = l_1 \dot{\theta}_1 \sin\theta_1 - l_2(\dot{\theta}_1 + \dot{\theta}_2)\sin(\theta_1 + \theta_2)}$$

$$\boldsymbol{\dot{y} = l_1 \dot{\theta}_1 \cos\theta_1 - l_2(\dot{\theta}_1 + \dot{\theta}_2)\cos(\theta_1 + \theta_2)}$$

$$\begin{bmatrix} \dot{x} \\ \dot{y} \end{bmatrix} = \begin{bmatrix} l_1 \sin\theta_1 - l_2 \sin\ (\theta_1 + \theta_2) & -l_2(\theta_1 + \theta_2) \\ l_1 \cos\theta_1 - l_2 \cos\ (\theta_1 + \theta_2) & l_2(\theta_1 + \theta_2) \end{bmatrix} \begin{bmatrix} \dot{\theta}_1 \\ \dot{\theta}_2 \end{bmatrix}$$

$$X = \dot{J}\Theta \quad \Rrightarrow \quad \Theta = \gamma^{-1}X$$

$$y_1 = l_1 \cos x_1 + l_2 \cos(x_1 + x_3)$$

$$\ddot{y}_1 = -l_1 \dot{x}_1 \sin x_1 - l_2\,(\dot{x}_1 + \dot{x}_3)\sin(x_1 + x_3) \Rrightarrow -l_1 x_2 \sin x_1 - l_2(x_2 + x_4)\sin(x_1 + x_3)$$

$$\ddot{y}_1 = -l_1 x_2 \sin x_1 - l_2 x_2 sin(x_1 + x_3) - l_2 x_4 \sin(x_1 + x_3)$$

$$\ddot{y} = \quad -l_1(x_2\dot{x}_1\cos x_1 + \dot{x}_2\sin x_1) - l_2[x_2(\dot{x}_1+\dot{x}_3)cos(x_1+x_3) + \dot{x}_2 sin(x_1+x_3)] - l_2[x_4(\dot{x}_1+\dot{x}_3)\cos(x_1+x_3) + \dot{x}_4\sin(x_1+x_3)]$$

$$\ddot{y} = \quad -l_1x_2^2(\cos x_1 - l_1\dot{x}_2\sin x_1) - l_2x_2^2\cos(x_1+x_3) - l_2x_2x_4\cos(x_1+x_3) - l_2\dot{x}_2\sin(x_1+x_3) - l_2\,x_2x_4\cos(x_1+x_3) - l_2x_2^4\cos(x_1+x_3) - l_2\dot{x}_4\sin(x_1+x_3)$$

$$\ddot{y} = -l_1x_2^2\cos x_1 - \dot{x}_2[-l_1\sin x_1 - l_2\sin(x_{1+}x_3)] \quad - l_2x_2^4\cos(x_1+x_3) - l_2\dot{x}_4\sin(x_1+x_3) - 2l_2x_2x_4\cos(x_1+x_3) - l_2x_4^2\cos(x_1+x_3) - l_2x_4^2\sin(x_1+x_3)$$

$$\ddot{y}_1 = -l_1\sin x_1\left[\frac{H_{22}}{H_{11}H_{22}-H^2}(2hx_2x_4 + hx_4^2 - g_1 + u_1)\right] - \frac{H_{21}}{H_{11}H_{22}-H^2}(-hx_2^2 - g_2 + u_2) - l_2\sin(x_1+x_3)\left[\frac{H_{22}}{H_{11}H_{22}-H^2}(2hx_2x_4 + hx_4^2 - g_1 + u_1)\right] - \frac{H_{21}}{H_{11}H_{22}-H^2}(-hx_2^2 - g_2 + u_2) - l_2\sin(x_1+x_3)\left[-\frac{H_{21}}{H_{11}H_{22}-H^2}(2hx_2x_4 + hx_4^2 - g_1 + u_1)\right] + \frac{H_{11}}{H_{11}H_{22}-H^2}(-hx_2^2 - g_2 + u_2) - -l_1x_2^2\cos x_1 - -l_1x_2^2\cos(x_1+x_3) - 2l_2x_2x_4\cos(x_1+x_3)$$

$$\left[\frac{-l_1\sin x_1H_{22}}{H_{11}H_{22}-H^2} - \frac{-l_2\sin(x_1+x_3)H_{22}}{H_{11}H_{22}-H^2} + \frac{l_2\sin(x_1+x_3)H_{22}}{H_{11}H_{22}-H^2}\right]u_1 \quad \Rightarrow \quad \textit{The first equation} \quad \Rightarrow \quad \ddot{\boldsymbol{y}}_{\boldsymbol{1}}$$

$$\left[\frac{l_1\sin x_1H_{21}}{H_{11}H_{22}-H^2} + \frac{l_2\sin(x_1+x_3)H_{21}}{H_{11}H_{22}-H^2} - \frac{l_2\sin(x_1+x_3)H_{11}}{H_{11}H_{22}-H^2}\right]u_2 \quad \Rightarrow \quad \textit{The second equation} \quad \Rightarrow \quad \ddot{\boldsymbol{y}}_{\boldsymbol{1}}$$

$$y = l_1\sin x_1 + l_2\sin(x_1+x_3)$$

$$\dot{y} = l_1\dot{x}_1\cos x_1 + l_2\,(\dot{x}_1+\dot{x}_3)\cos(x_1+x_3)$$

$$\dot{y} = l_1\,x_2\cos x_1 + l_2x_2\cos(x_{1+}x_3) + l_2\,x_4\cos(x_{1+}x_3)$$

$$\dot{y} = l_1[-x_2\dot{x}_1\sin x_1 + \dot{x}_2\cos x_1] + l_2[-x_2\sin(x_1+x_3)(\dot{x}_1+\dot{x}_3) + \dot{x}_2\cos(x_1+x_3)] + l_2[-x_4\sin(x_1+x_3)(\dot{x}_1+\dot{x}_3) + \dot{x}_4\cos(x_1+x_3)]$$

$$\dot{y} = l_1\,[-x_2^2\sin x_1 + \dot{x}_2\cos x_1] + l_2[-x_2\sin(x_1+x_3)(x_2+x_4) + \dot{x}_2\cos(x_1+x_3)] + l_2[-x_4\sin(x_1+x_3)(x_2+x_4) + \dot{x}_4\cos(x_1+x_3)]$$

$$\dot{y} = -l_1\,x_2^2\sin x_1 + l_1\dot{x}_2\cos x_1 - l_2\sin(x_1+x_3)(x_2+x_4) + l_2\dot{x}_2\cos(x_1+x_3) - l_2x_4\sin(x_1+x_3)(x_2+x_4) + l_2\dot{x}_4\cos(x_1+x_3)$$

$$\dot{y} = \dot{x}_2[l_1\cos(x_1) + l_2\cos(x_1+x_3) + l_2\dot{x}_4\cos(x_1+x_3)]$$

$$\ddot{y}_2 = -l_1\,x_2^2\sin x_1 + l_1\dot{x}_2\cos x_1 - l_2\sin(x_1+x_3)(x_2+x_4) + l_2\dot{x}_2\cos(x_1+x_3) - l_2x_4\sin(x_1+x_3)(x_2+x_4) + l_2\dot{x}_4\cos(x_1+x_3)$$

$$\ddot{y}_2 = -l_1\, x_2^2 \sin x_1 + l_1 \dot{x}_2 \cos x_1 - l_2\, x_2^2 \sin(x_1 + x_3) - l_2 x_4 \sin(x_1 + x_3) + l_2 \dot{x}_2 \cos(x_1 + x_3) - l_2 x_4 \sin(x_1 + x_3) - l_2\, x_4^2 \sin(x_1 + x_3) + l_2 \dot{x}_4 \cos(x_1 + x_3)$$

$$\ddot{y}_2 = -l_1\, x_2^2 \sin x_1 + l_1 \dot{x}_2 \cos x_1 \left[\frac{H_{22}}{H_{11}H_{22}-H^2}(2hx_2x_4 + hx_4^2 - g_1 + u_1) - \frac{H_{21}}{H_{11}H_{22}-H^2}(-hx_2^2 - g_2 + u_2)\right] - l_2\, x_2^2 \sin(x_1 + x_3) - l_2 x_4 \sin(x_1 + x_3) + l_2 \cos(x_1 + x_3)\left[\frac{H_{22}}{H_{11}H_{22}-H^2}(2hx_2x_4 + hx_4^2 - g_1 + u_1) - \frac{H_{21}}{H_{11}H_{22}-H^2}(-hx_2^2 - g_2 + u_2)\right] - l_2\, x_2x_4 \sin(x_1 + x_3) - l_2\, x_2^2 \sin(x_1 + x_3) + l_2 \cos(x_1 + x_3)\left[-\frac{H_{21}}{H_{11}H_{22}-H^2}(-hx_2^2 - g_2 + u_2) + \frac{H_{11}}{H_{11}H_{22}-H^2}(-hx_2^2 - g_2 + u_2)\right]$$

$$\left[\frac{l_1 \cos x_1 H_{22}}{H_{11}H_{22}-H^2} + \frac{l_2 \cos(x_1+x_3)H_{22}}{H_{11}H_{22}-H^2} - \frac{l_2 \sin(x_1+x_3)H_{21}}{H_{11}H_{22}-H^2}\right]u_1 \quad \Rightarrow \quad \textit{The first equation} \quad \Rightarrow \quad \ddot{y}_2$$

$$\left[-\frac{l_1 \cos x_1 H_{21}}{H_{11}H_{22}-H^2} - \frac{l_2 \cos(x_1+x_3)H_{21}}{H_{11}H_{22}-H^2} + \frac{l_2 \cos(x_1+x_3)H_{11}}{H_{11}H_{22}-H^2}\right]u_2 \quad \Rightarrow \quad \textit{The second equation} \Rightarrow \quad \ddot{y}_2$$

5. Conclusions:

According to the results we got from this paper we found that the feedback linearization technique controls the system only within the certain constrains. Also, we have found the sliding manifold and we restrict the motion of the system to the surface $s = 0$. And, we have simulated the controller to regulate the state to zero.in third part, which means MIMO control of a Two-Link Planar Arm. In the analysis, nonlinear closed-loop system is assumed to have been designed and it is necessary to determine the characteristic of the system's behavior. In the design it is given a nonlinear plant to be controlled and some specifications of closed-loop system meets the desired characteristics. When a linear controller is used to control robot motion, it neglects the inherent nonlinear forces associated with the motion of the robot links. The
Controller's accuracy thus quickly degrades as the speed of motion increases, because many of the dynamic forces, such as Coriolis, centripetal forces, vary as square of the speed. However, in control systems there are much nonlinearity whose discontinuous nature does not allow linear approximation (friction, saturation, dead-zone, hysteresis and backlash).

References:

[1] linear Notes 2013, ECE 547 Non-linear system Control, Prof. Raúl Ordóñe.

[2] Non-linear system Third edition, Hassan K. Khali, Department of Electrical and computer Engineering, Michigan state university, 2002, 1996 by prentice Hall Inc, upper saddle river, NJ 07458.

[3] Dombre, E.; Khalil, W. (2007): Robot Manipulators (Modeling, Performance, Analysis and Control of Robot Manipulators). ISTE Ltd, USA.Khalil, H. (2002): Nonlinear Systems. Printice.

[4] Receanu, D. (2012): Nonlinear control in the servomechanisms for positioning of an industrial robot. Buletinul I.P.Ia¸si, Tomul LVII(LXI), Fasc.2, 2012,Sec¸tia Construc¸tii de Ma¸sini.

[5] Spong, M. W.; Hutchinson, S.; Vidyasagar, M. (2006): Robot Modeling and Control, John Wiley&Sons,Inc.,New York

SJST Surman Journal for Science and Technology | ISSN: E 2790-5721 P 2790-5713
Vol3, No.1, Dec_2021 , pp. 028 ~ 036

Isothermal Transformation Temperatures and Its Effect in Hardiness of Pearlite Eutectic Steels R350HT Rails

[1]Nizar Ramadan, [2]Khaled ali Osman

[1]Department of Mechanical Engineering, Surman College for Science and Technology, Surman, Libya.

[2]Department of Manufacture Engineering, Higher Institute of Science and Technology, Zawia, Libya.

[1]nizar.r@scst.edu.ly

[2]khaledaliosman@yahoo.com

الملخص

يتميز الفولاذ المقاوم للصدأ بعدد من الخواص الميكانيكية المرغوبة ، وبالتالي تمت دراسته على أنه بنية مجهرية مرشحة للسكك الحديدية المقواة برأس R350HT وفقًا لمعيار EN-13674. يدرس هذا العمل دور درجة حرارة التحويل لصف السكك الحديدية R350HT وتأثيرها على صلابة السكك الحديدية. تم الحصول على بنية الدقيقة المرغوبة تحت درجات حرارة تحويل مختلفة. يتوافق تباين صلابة البرليت التي يتم الحصول عليها في ظل ظروف TTT مع التغيرات في تركيبها الداخيلي ودرجة حرارة التحول

Abstract

Fine pearlitic eutectic steel have a number of desirable mechanical properties and have thus been studied as candidate microstructure for R350HT head hardened rail according to EN-13674 standard. This work examines the role of transformation temperature of R350HT rail grade and their effect on rail hardiness. The fine pearlite structure has been obtained under different isothermal transformation temperatures. The variation of pearlite hardiness that obtained under TTT conditions conform to the changes in its structure and transformation temperature.

Keywords: *TTT, Pearlitic, R350HT rails, isothermal temperatures, Hardiness.*

1- Introduction

Time transform occur when steel holding at any constant austenitic temperature lower than the minimum, where austenite is stable. Isothermal transformation can be represented by recorded the austenite transformed plotting percentage against corresponding elapsed time at constant temperature. Hardness, toughness and strength from the most important mechanical properties, which related to cooling rate as well as interlamellar spacing. From other hand, inter lamellar spacing controlled by the heat treatment variable [1]. Because of their remarkable effect on functional and structural properties the Studies on the microstructures of alloys continues to be conclusive. Pearlitic steel, from the alloys that have lamellar structures, which are in practical use and have been studied extensively [1, 2]. As principles of the controlled cooling and heat treatment of steels and their alloys, TTT curves (Time Temperature Transformation or isothermal transformation) [3]. The TTT curves idea is description of phase transformation and analyze quantitatively the transformation process of steels and the relationship between the microstructure and the resulted mechanical

properties [3, 4]. The pearlite mechanical properties and microstructure can be tailored out of difference of the interlamellar spacing during processing which is immediately connected to strength [5].

Displacement and charge sensing indentation technology enables the determination of mechanical properties at penetration depths as low as 20 nm, avoiding the influence of the substrate on measurements. The ability to test at very small scales makes this technology one of the tools of choice for characterizing the mechanical properties of thin films, coatings, second-stage particles, and magnetic hard drive recording media [6].

A well-defined bleed geometry is required to obtain well-defined bleed prints. It is difficult to achieve a perfect tip shape. Berkowitz is a three-sided pyramid, which provides a sharp point, compared to the Vickers indenter, which is a quadrangular pyramid and has a slight offset (0.5 - μm). This is the main reason for using the Berkovich three-sided notch in depth sensing machines. However, any sharp point notch has a limitation, but it is exceptionally difficult to measure. Experimental procedures were developed to correct the edge shape of the Vickers and Berkovich indentations.

In this study, the investigated of rails R350HT hardness with different cooling rate and isothermal temperature during the isothermal transformation. Which measured by experiments, with focused on the relationship models and obtained by data regression. All TTT cooling condition done by used in dilatometer tester DIL805 sample, which is austenitised in a specially designed furnace and then controlled cooled.

1.1 Objectives

The study aimed to investigation in relationship between cooling rate and hardiness of pearlitic eutectic steels in R350HT head hardened rails. With applying different isothermal transformation temperatures. In addition, finding out the following:

- Sensitivity of hardiness to transformation temperatures
- The relationship between cooling rate and hardiness.

2- Materials and Equipment.

As the principal requirements involved, the steels used for wheels and rails have a majority pearlitic microstructure involving hard cementite lamellae that ensures high resistance to wear. Material properties of rails requiring verification are set out in European standard EN 13674-1 [7]. Due to EN 13674-1 exclusively covers pearlitic steels for rails, those being R220, R260, R320Cr and R350HT, whose carbon content lies between 0.6 and 0.8 % [8]. In addition, the main chemical composition of R350HT tested samples showing in table (1):

Table 1: showing the chemical composition of R350HT rails.

The chemical composition					
R350HT	C	Si	Mn	P	S
	0.65~0.77	0.15~0.35	1.10~1.5	<0.04	<0.04

Figure 1, R350HT head hardened Rail profile. Where the specific descriptions are: Cross-sectional area: 76,70 cm^2, Mass per meter : 60,21 kg/m, Moment of inertia x-x axis : 3038,3 cm^4, Section modulus - Head : 333,6 cm^3, Section modulus - Base : 375,5 cm^3, Moment of inertia y-y axis : 512,3 cm^4, Section modulus y-y axis : 68,3 cm^3 and Indicative dimensions : A = 20,456 mm, B = 52,053 mm.

R350HT rail samples as shown in figure 2, with 4 mm in width, 2 mm in thickness and 10 mm length to dial with dilatometer DIL805 taken from the head of rail.

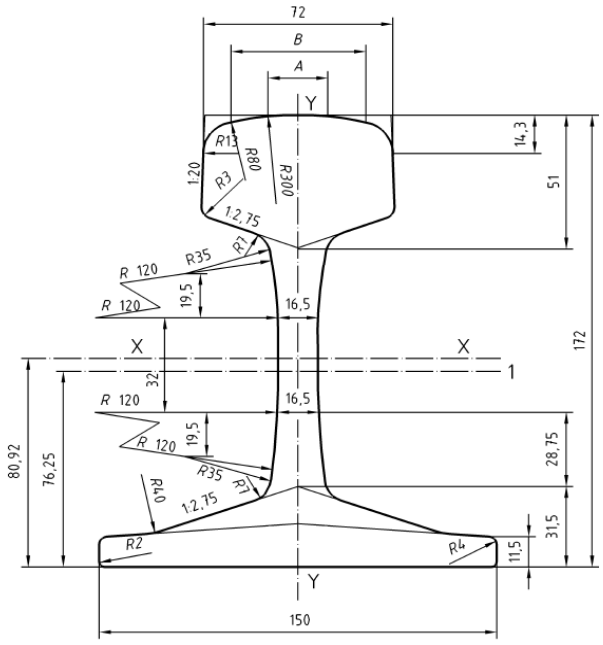

Figure 1: R350HT Rail profile [8].

Figure 2: showing samples dimensions

By dilatometer DIL805 a solid or hollow samples is inductively heated as shown in figure 3 under air and the system can be vacuum or inert gas to a specific temperature and is then continuously cooled with different (linear or exponential) rates. The phase transitions occurring in both continuous cooling process or in the time temperature transformation and it can be seen in the change of length.

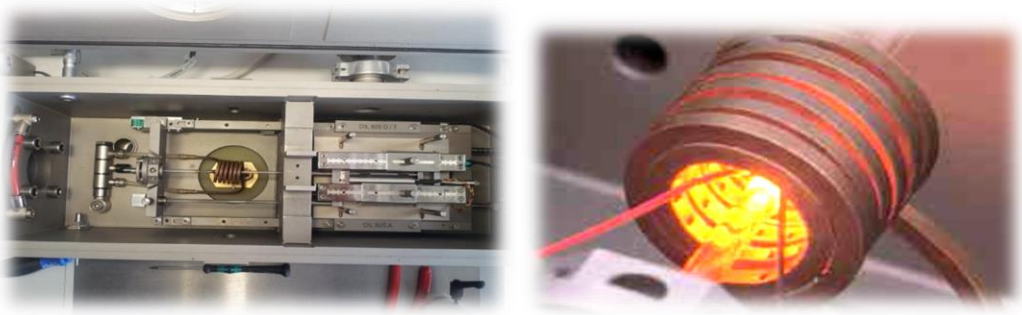

Figure 3: Dilatometer equipment

Dilatometer indicates phase transformation by monitoring slope change. Figure 4, gives more details by drawing dilation vs temperature where the dilation at different temperatures at different cooling rate. By behavior of sample shrink or expand the dilation due to thermal specific volume change because of changing in temperature. Generally, slope in dilation curve do not changed while amount of phase or the relative amount of phases in a phase mixture does not change during cooling or heating as well.

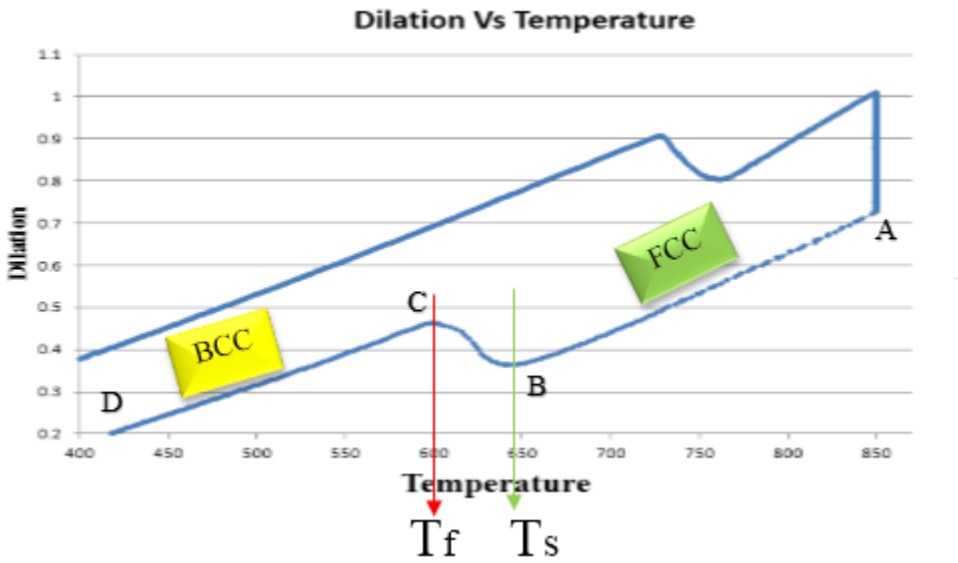

Figure 4: showing dilation vs temperature and transformation temperature.

Dilation from A to B is due to specific volume change of high temperature phase austenite. However, at Ts slope of the curve changes, the transformation starts at Ts from austenite to pearlite. One more time, slope of the curve from C to D is constant but is different from the slope of the curve from A to B. where there is no phase transformation between the temperatures from C to D. The curve from point B to C is variable with temperature that signal the change in relative amount of phase because of cooling.

Moreover, the phase density controls the sample expansion, some part of dilation compensates by thermal change due to cooling. So the dilation curve takes complex shape, firstly slope reduces and reaches to a minimum value and then rise to the characteristic value of the phase mixture at point C. as showing in figure 4, the mechanism of phase transformations start at point B at temperature Ts and the end of transformation at point C with temperature Tf. The nature of transformation has been determined in laboratory by metallography when austenite fully transforms to pearlite, the final pearlite phase transformation is immediately proportional to the relative change in length and this is the key. The ability of materials to resist deformation and destruction is the main idea of hardiness. Also hardiness can be known as the ability of materials to resist elastic deformation and plastic deformation as well [9, 10]. In addition, the major properties of the hardness are resist plastic deformation of a material, where the penetration is the main key of measured it. Moreover, according to EN 13674-1, Berinall vs Vickers hardness testing are measurement techniques [8]. The test measurement technique is applying constant load on the rail surface to printing an impression with an indenter of known geometry, then subsequently analyzing the load vs. displacement data [11]. Figure 5, showing surface printing with an indenter in Vickers hardness testing. Then apply those data in Vickers formula to obtain hardiness. Where, F is load in kgf. And d is Arithmetic mean of the two diagonals, d_1 and d_2 in mm.

$$HV = \frac{2F\sin\frac{136°}{2}}{d^2}$$

Approximately $$HV = 1.854\frac{F}{d^2}$$

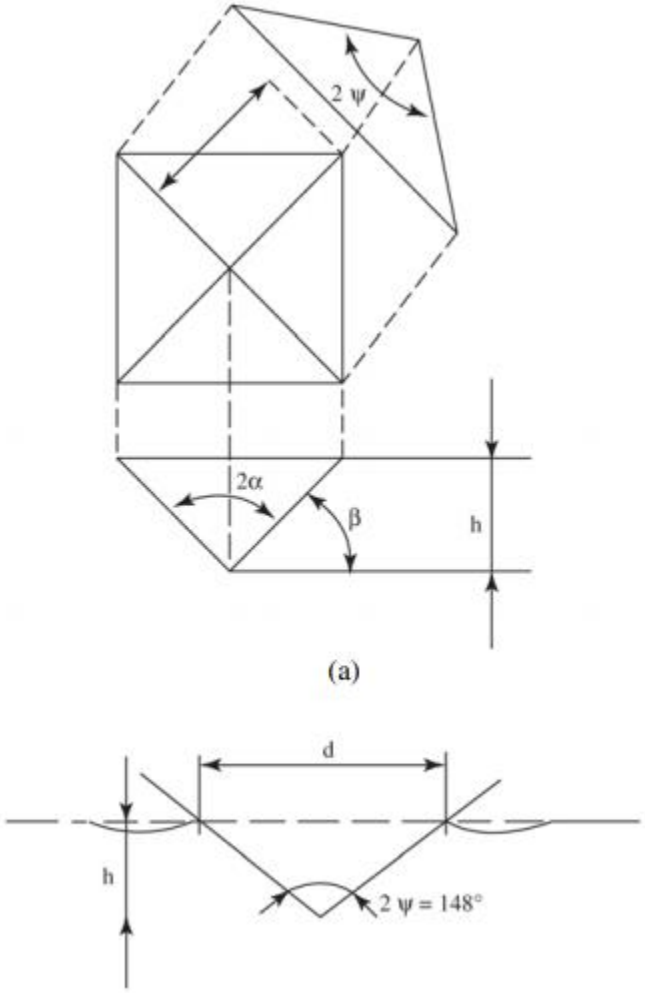

Figure 5: Showing surface printing with an indenter in Vickers hardness testing [11].

3- Extramarital methods

Measuring some physical properties during cooling are the main key to determine the TTT, which normally the specific volume. However, the plurality of the work has been done by measured specific volume change (dilatometric method). Usually, this method is complete by metallography and hardness measurement. In this case, dilatometer test done in vacuum. Cooling data recorded as temperature vs time as shown in figure 5, as same as cooling data the dilation is recorded against temperature, where Figure 4 shown in details and phase transformation indicates by slope change. the TTT diagram mechanism are after cooling to a transformation temperature then keep the temperature constant until the austenite transformation finished, the required transformation product (in our case pearlite) and then cool to the room temperature.

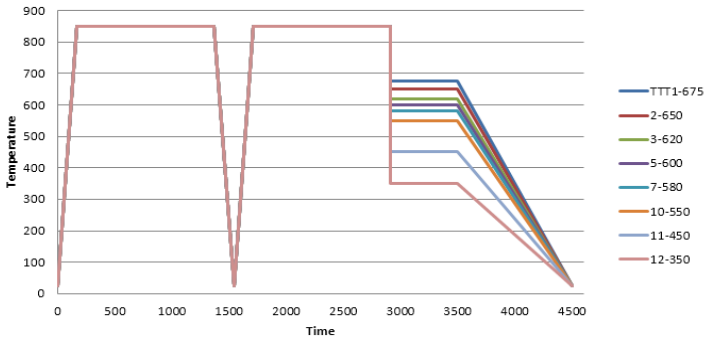

Figure 6: shown TTT curve with 20 minute holding time and different transformation temperature.

4- Results and discussion

4.1 Hardiness

The isothermal transformation of austenite to R350HT head hardened rails has been studied, with different isothermal temperature and then morphologies examination and finally hardiness test recorded against different transformation temperature as showing in table 3. Where isothermal temperature started from 350 C° that recorded 494 Hv0.2 until 675 C° with 186 Hv0.2. The relationship between transformation temperature and hardiness has been recorded and explain graphically in figure 8.

Table 3: showing different transformation temperature and hardiness.

No:	I T	Hv0.2
1	675	186
2	650	207
3	620	225
4	610	260
5	600	293
6	590	301
7	580	308
8	570	337

9	560	345
10	550	349
13	500	339
11	450	378
12	350	494

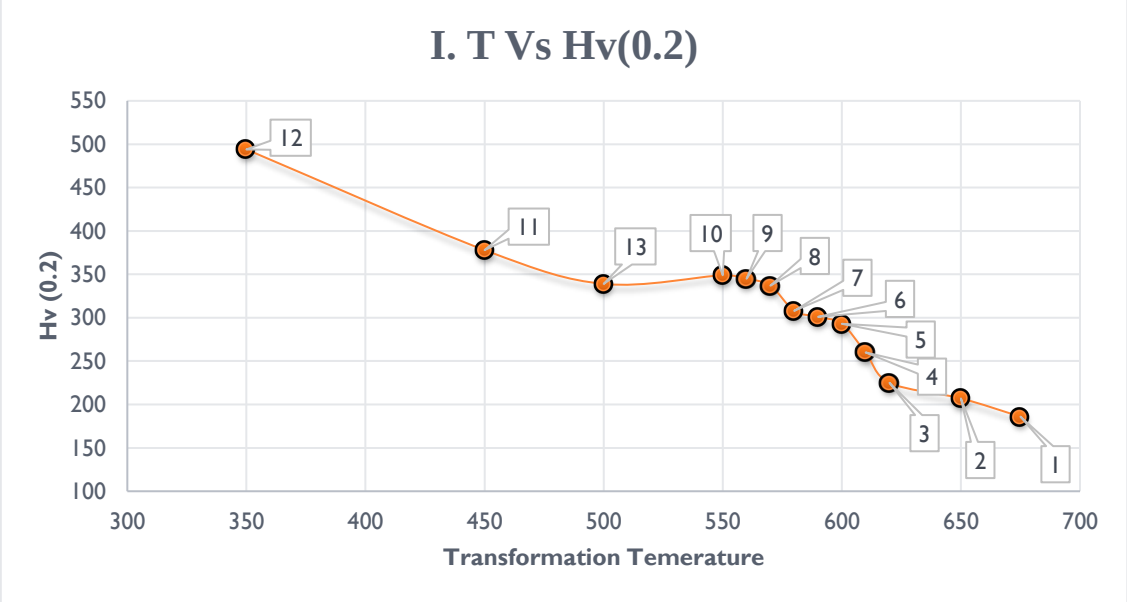

Figure 7: showing transformation temperature Vs hardiness of R350HT rails.

5- Conclusion

In the isothermal transformation temperatures, TTT process with different isothermal temperatures the hardness were measure and the relationship model between the cooling rate and hardiness was obtained to R350HT head hardened rail duo to EN-13674 slandered. Where, experimental results showing sensitivity and relationship that connected hardiness and isothermal temperatures of pearlitic eutectic steel, which can be listed as:

- Lanier positive relationship connected between interlamellar spacing and isothermal temperature, the best isothermal temperatures produced clear fine pearlitic are between (625, 600 and 575 C°/s).

- Study results display inverse relationship connected hardiness to transformation temperatures, where with the increase of isothermal temperature the hardiness decreases, where best transformation group that in between (550 to 575 C°).

6- References

1. Vander Voort, G., The Interlamellar Spacing of Pearlite. Practical Metallography, 2015. 52(8): p. 419-436.
2. Ikeda, T., V.A. Ravi, and G.J. Snyder, Evaluation of true interlamellar spacing from microstructural observations. Journal of Materials Research, 2008. 23(09): p. 2538-2544.
3. Jin-Qiao, X., L. Ya-Zheng, and Z. Shu-Mei, Calculation models of interlamellar spacing of pearlite in high-speed 82B rod. Journal of Iron and Steel Research, International, 2008. 15(4): p. 57-60.
4. Cai, Z., et al., Process simulation and microstructure analysis of low carbon Si-Mn quenched and partitioned steel. Journal of iron and steel research, international, 2008. 15(4): p. 82-85.
5. Gladman, T. and F. Pickering, The effect of grain size on the mechanical properties of ferrous materials. Yield, flow and fracture of polycrystals, 1982: p. 141-198.
6. Elwazri, A., P. Wanjara, and S. Yue, Measurement of pearlite interlamellar spacing in hypereutectoid steels. Materials characterization, 2005. 54(4): p. 473-478.
7. Mädler, K., et al. Rail Materials-Alternatives and Limits. in Proceedings of the 8th World Congress on Railway Research (WCRR), May. 2008.
8. EN, B., 13674-1 (2011).“. Railway applications-Track-Railpart. 1.
9. Ghorbal, G.B., et al., Comparison of conventional Knoop and Vickers hardness of ceramic materials. Journal of the European Ceramic Society, 2017. 37(6): p. 2531-2535.
10. Westbrook, J.H., The science of hardness testing and its research applications. 1973.
11. Franco Jr, A.R., et al., The use of a Vickers indenter in depth sensing indentation for measuring elastic modulus and Vickers hardness. Materials Research, 2004. 7(3): p. 483-491.

SJST Surman Journal for Science and Technology | ISSN: E 2790-5721 P 2790-5713
Vol.3, No.1, Dec 2021, pp. 037 ~ 046

The Influence of the Quality of Libyan Banks' Services on Achieving Customer Satisfaction

[1]Nizar Ramadan, [2]Sohaila G Khalifa, [3]Aisha Abdllh Marzoug khalifa, [4]Houria Alhadi Moftah

[1]Department of Mechanical Engineering, Surman College for Science and Technology, Surman, Libya
[1,2,3]Department of Administrative and Financial Sciences, Surman College for Science and Technology, Surman, Libya
[1]nizar.r@scst.edu.ly
[2]Abofrok.alfy@gmail.com
[3]aisha.am.khalifa@scst.edu.ly
[4]hour.elfaagi@gmail.com

الملخص

الهدف الرئيسي من هذه الدراسة هو توفير إطار نظري يحدد ويعرف المفاهيم المختلفة المتعلقة بجودة الخدمات المصرفية من حيث المؤشرات والنماذج ، بالإضافة إلى معالجة قياس رضا العملاء لمعرفة مدى وعيهم بجودة الخدمات التي تقدمها المؤسسات المصرفية الليبية من أجل إيجاد طرق لتحسين جودة الخدمات. تنعكس مشكلة هذه الدراسة في واقع المنافسة التي تواجهها البنوك العامة في ليبيا، وحاجتها إلى اتخاذ مجموعة من الإجراءات لغرض قياس وتحسين جودة الخدمات المقدمة. تعتمد الدراسة على استخدام المنهج الوصفي التحليلي وهو الأنسب لتحقيق أهداف هذه الدراسة من الواقع الحقيقي لمشكلة البحث. تمت معالجة البيانات وتحليلها إحصائياً بواسطة برنامجي Microsoft Excel و SPSS لاختبار الفرضيات والوصول إلى النتائج التي تحقق أهداف الدراسة. أشارت النتائج إلى وجود وعي بأن جودة الخدمات المصرفية لها تأثير كبير في تحقيق رضا العملاء.

الكلمات الأساسية: الجودة ؛ الخدمات البنكية؛ العميل؛ الإشباع؛ والوعي.

Abstract

The main objective of this study is to provide a theoretical framework that defines the various concepts related to the quality of banking services in terms of indicators and models, in addition to addressing the measurement of customer satisfaction to know the extent of customers' awareness of the services provided by Libyan banking institutions in order to find ways to improve the quality of services. The problem of this study is reflected in the reality of competition faced by public banks in Libya, and their need to take a set of measures for the purpose of measuring and improving the quality of the services provide. The study depends on the use of the descriptive analytical method, which is the most appropriate to achieve the objectives of this study from the real reality of the research problem. The data was subsequently processed and analyzed statistically by Microsoft Excel and SPSS software to test the hypotheses and reach results that achieve the objectives of the study. The results indicated that there is an awareness that the quality of banking services has a significant impact on achieving customer satisfaction.

Key words: The quality; Banking Services; Customer; Satisfaction; and awareness.

An introduction

The world is heading towards globalization in all its forms, especially financial ones, as the financial services industry plays an important and distinctive role in the economies and markets of different countries. This requires banks to understand and measure the quality of banking services provided as well as to study the expectations and perceptions of customers for the quality of services (Brumbaugh 1992, Chaoprasert 2003, Drigă and Isac 2014).

In light of the major competitive conflicts that the World is witnessing today and in the context of economic globalization that led to the transfer of competition from local markets to global markets, service institutions are facing a set of challenges that fall within the new economic climate. Its services towards its customers in order to achieve their satisfaction. This is considered as one of the main entrances to achieving success and development in its competitive capabilities while gaining a distinguished market position and increasing the profitability of the institution (Jeanneau 2007, Iranzadeh and Chakherlouy 2012, Belás, Chochol'áková et al. 2015).

The increasing interest in the quality of electronic banking services, whether for the bank or the customer, is considered an effective tool for improving and knowing the level of services provided and expected from customers. The quality of electronic service has effects on customers' attitudes, satisfaction and behavioral intentions. Accordingly, customers' evaluation of quality enables practitioners to allocating the organization's resources to ensure the performance of services that bring them satisfaction. The evaluation of the quality of services and their improvement and development on a permanent basis depends mainly on collecting information about the services provided to the customers of the institution, by adopting effective strategies in marketing its services with the application of modern methods aimed at meeting the needs and expectations of customers and satisfying their desires (Husnain and Akhtar 2016, Moenardy, Arifin et al. 2016).

Not a day goes by without a bank/client relationship taking place but today the customer has a better place than in the past. In today's world, it can be accepted that intense competition in terms of quantity and quality makes it very difficult for a company to differentiate itself from its competitors (Ha, Minh et al. 2015, Vu and Huan 2016).

For this reason, the organization must pay close attention to the client, and establish commercial agencies as a link between it and its clients. In addition to accessing that direct relationship, its characterized by transparency and security, when this is achieved, the institution has achieved customer satisfaction. Excellent business processes leading to product or service quality that can be viewed as the direct factors influencing customer satisfaction and loyalty (Brady, Cronin et al. 2002, Chi Cui, Lewis et al. 2003).

Considering that the quality and satisfaction of the customer represent the real concern of all service institutions that wish to achieve the appropriate marketing position and seek stability and continuity in the scope of their work, it was worth addressing by asking some questions, including (Is there any effect on the quality of the banking service for the public sector in achieving satisfaction for its customers?). Through this question, it must first know the answer to some sub-questions, including:

- What do we mean by quality of service?
- How does the customer evaluate the quality of services provided by public banks?
- What are the criteria that customers use in evaluating the quality of service?
- How can a public banking institution keep pace with the performance and quality of its services with the expectations of its customers?

The study aims to know the impact of the quality of services provided by banks to their customers, in order to develop the quality of their services and work to satisfy their customers. This study aims to define concepts related to service quality, methods of measuring, improving and evaluation models, in addition to identifying on customer satisfaction and ways to measure it. Getting to know customers' evaluation of the level of quality of services provided. Reaching some results and suggestions that could contribute to developing the quality of banking services.

The importance of this study lies in expressing the level of quality of services provided by Libyan public banks to their customers and their compatibility with their desires and needs in order to gain their satisfaction. As well as, trying to show the relationship between three effective variables: quality as a strategy taken by the institution, customer satisfaction as a result, and measurement as a means to assess the degree of satisfaction or dissatisfaction.

The problem of this study is reflected in the reality of competition faced by public banks in Libya, and their need to take a set of measures for the purpose of measuring and improving the quality of the services provide. Using their dimensions to identify the sites of shortcomings and address them to enjoy the satisfaction and confidence of customers. In additional to increase their market share and achieve competitive advantages. In fact, public banks are vital institutions with a direct impact on the national economy and development. Especially, with the increased satisfaction of customers with the contemporary electronic lifestyle, and that many citizens do not want to deal with private banks.

Study Hypotheses

Based on the questions raised, the following hypotheses were developed:

H_{01}: There is awareness that a quality of the banking services highly influences in achieving the customer's satisfaction.

H_{02}: There is positive impact of services quality on the bank performance.

Study Model

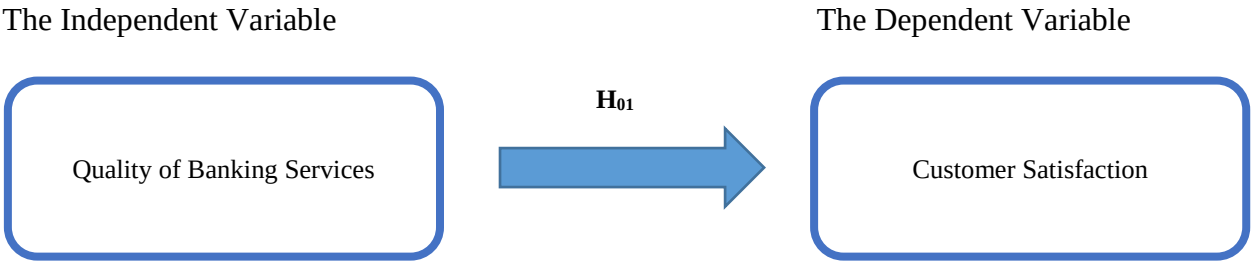

Figure 1: The study model.

Study Methodology

The study depends on the use of the descriptive analytical method, which is the most appropriate to achieve the objectives of this study from the real reality of the research problem. The questionnaire was used as a source for collecting data and information about the study variables that was distributed to the study sample. The data was subsequently processed and analyzed statistically by Microsoft Excel and SPSS software to test the hypotheses and reach results that achieve the objectives of the study.

- **Evaluation**

The customers feeling and satisfaction of Libyan banks was reflected by includes four questions. Evaluate the actual performance of their services provided to their customers to determine their satisfaction with these services. Where, the measurement degree of responses to the questionnaire was measured by a five-point scale, ranging from (strongly disagree to strongly agree), as shown in table:

Table 1: The five-point approval scale

Approval scale	No. of point
Strongly Agree	5
Agree	4
Neutral	3
Disagree	2
Disagree strongly	1

- **sample selection**

This study focused on a customer sample from the Libyan Banks. The questionnaire was randomly implemented and distributed personally. 250 questionnaires are distributed, while 210 questionnaires were applied to the bank's clients.

- **Data Analysis Tools**

The questionnaire was designed to respond to research variables, answer research questions, and measure instrument stability that focusing on Cronbach's alpha test was performed and stability coefficients were determined. To determine the degree of customer agreement with the services provided the Microsoft Excel and SPSS programs were used to analyze the data and the results were tested using the mean and standard deviation, in additional to T-test and ANOVA to test hypotheses. The Cronbach's alpha coefficient was calculated for the stability of the study instrument and the questionnaire was constructed was taken as an indicator of its logical honesty, as well as the honesty that is reflected in the judges' opinions. The number of elements tested and their dimensions affected the alpha value (Cortina 1993, Tavakol and Dennick 2011). In general, there are various references to accepted alpha values, which range from 0.70 to 0.95 (Nunnally 1975, Bland and Altman 1997). An alpha value (KMO value) of 0.932 is sufficient, that is, more than 0.7. Indeed, all factors with eigenvalues greater than 0.5 were retained.

RESULTS DISCUSSION AND ANALYSIS

- **Demography**

The demographic characteristics of study sample participating in the field study, the first part of the questionnaire treated some data for the study sample by SPSS software, such as gender, age, educational level and frequency of use of the bank. More details in follows table:

Table 2: Study samples demography features

Variables		Categories	Repetition	%
Gender	1	Male	145	69%
	2	Female	65	31%
Age	1	18 to 25	71	31%
	2	26 to 40	80	40%
	3	41 and above	59	29%
Educational level	1	Intermediate / Secondary	58	20%
	2	undergraduate	120	59%
	3	Postgraduates	32	21%
Using the bank	1	Daily	37	19%
	2	Weekly	24	15%
	3	Monthly	72	30%
	4	Other	77	36%

- **Service Quality and Customer Satisfaction**

The Libyan Banks costumer was divided by their questionnaire's answers include strongly agree, agree, natural, disagree and strongly disagree. The question of whether the Libyan Banks has modern looking equipment. The opinions of bank's customers ware believe that Libyan Bank has modern looking equipment with standard deviation about

1.02 and mean 3.56, which main that concentration and non-dispersion. on other question, Libyan Bank have physical features are visually appealing, the highest answers are positive side with standard deviation 0.85 and mean 3.54, which means that concentration and non-dispersion in answers, and the Normality test significant value becomes nearly (0.0). The question is whether the Libyan Bank reception desk employees are neat appearing. the banks costumer believe that Bank has good looking.

Study samples of Libyan Bank answers the question of When the Bank promises to do something in certain time, it does so. The opinions believe that Bank work with time function with standard deviation 1.10 and mean 3.54, which mean showed concentration and non-dispersion as well as in Normality test significant value becomes nearly zero. More details in Figures that shows normality test distribution in answers. The questionnaires responsiveness of answers of the research samples of Bank was divided into five groups, strongly agree, agree, natural, disagree and strongly disagree. The question whether The Libyan Bank of Commerce and Development's employees tell you exactly when services will be performed. The opinions of bank's customers believe that the bank's employees tell you exactly when services will be performed. In other question, whether The Bank's employees never too busy to respond to your request. After using SPSS software, the answers regarding the analysis become the highest percentage become as natural, which means that the costumers are not sure if the bank's employees never too busy to respond to their request.

- **Hypothesis Tests**

H_{01}. There is awareness that a quality of the banking services highly influences in achieving the customer's satisfaction.

- If value of statistically significant differences is ($\alpha < 0.05$), the H_{01} hypothesis will be accepted.

The hypothesis H_{01} of research, considering that there is awareness that a quality of the banking services highly influences in achieving the customer's satisfaction.

- If value of statistically significant differences is ($\alpha > 0.05$), the H_{11} Alternative hypothesis will be accepted.

The H_{11} Alternative hypothesis there is no awareness that a quality of the banking services highly influences in achieving the customer's satisfaction.

The research current data that analyzed by standard deviation, mean and T-Test in SPSS software was supported the H01 hypothesis, which influence become real as of human resources practices like Tangible elements, Reliability, Responsiveness, Safety, Empathy and Overall evaluation in bank services and its relationship of all those with bank performance. The value of the significance level is 0.000, which is less than 0.05, which means accepting the H_{01} hypothesis that exists the awareness that a quality of the banking services highly influences in achieving the satisfaction of their customers.

Table 4: The H_{01} hypothesis SPSS details (One sample T-Test).

Hypothesis	N	Mean	Standard deviation	Standard error mean	df	One samples T-test significance (2-tailed)
H_1	210	3.77	0.887	0.065	209	0.000

H_{02}. There is positive impact of services quality on the bank performance.

- If value of statistically significant differences is ($\alpha < 0.05$), the H_{02} hypothesis will be accepted.

H_{02} hypothesis: There is positive impact of services quality on the bank performance.

- If value of statistically significant differences is ($\alpha > 0.05$), the H_{12} Alternative hypothesis will be accepted.

H_{12} Alternative Hypothesis: There is no positive impact of services quality on the bank performance.

Current research data analyzed by standard deviation, mean, normality test, and T-test using SPSS software presented hypothesis H_{02}. Where the value of the significance value is 0.000, that is less than value of 0.05 this means that there is an impact of the human resources department in the institutions, more details in table.

Table 3: The H_{02} hypothesis SPSS details (One sample T-Test).

Hypothesis	N	Mean	Standard deviation	Standard error mean	df	One samples T-test significance (2-tailed)
H_1	210	3.38	1.090	0.078	209	0.000

Conclusions

The study aims to know the impact of the quality of services provided by banks to their customers, in order to develop the quality of their services and work to satisfy their customers. The ability of banks to gain the satisfaction of their customers by providing high quality services that meet their expectations. It is the main reason for the success of banking institutions in distinguishing their competitiveness and providing high quality services. The research questions and hypotheses, by identifying different concepts related to theoretical and practical aspects, reached some conclusions, including that the concept of service quality focuses on maintaining and satisfying customers by providing the service to meet or exceed their expectations. Quality is a competitive advantage, it is used as a strategy among customer satisfaction strategies and it has a positive impact of the quality of services on banking performance.

The results indicated that there is an awareness that the quality of banking services has a significant impact on achieving customer satisfaction. Also, there is a difference in the responses of the research samples about the positive impact of the quality of services on the performance of banks due to educational qualification. There is no difference in the responses of the research samples about the positive impact of the quality of services on the performance of the bank due to the frequency of using the bank.

References

Belás, J., A. Chochol'áková and L. Gabcová (2015). "Satisfaction and loyalty of banking customers: a gender approach." Economics & Sociology **8**(1): 176.
Bland, J. M. and D. G. Altman (1997). "Statistics notes: Cronbach's alpha." Bmj **314**(7080): 572.
Brady, M. K., J. J. Cronin and R. R. Brand (2002). "Performance-only measurement of service quality: a replication and extension." Journal of business research **55**(1): 17-31.
Brumbaugh, R. D. (1992). The future of American banking, ME Sharpe.

Chaoprasert, C. (2003). "Literature Review of service Quality Improvement in the Retail banking Industry." Journal of business Administration **26**: 79-88.
Chi Cui, C., B. R. Lewis and W. Park (2003). "Service quality measurement in the banking sector in South Korea." International Journal of Bank Marketing **21**(4): 191-201.
Cortina, J. M. (1993). "What is coefficient alpha? An examination of theory and applications." Journal of applied psychology **78**(1): 98.
Drigă, I. and C. Isac (2014). "E-banking services-features, challenges and benefits." Annals of the University of Petroşani, Economics **14**(1): 41-50.
Ha, N. T., N. H. Minh, P. C. Anh and Y. Matsui (2015). "The relationship between service quality and customer loyalty in specialty supermarket-Empirical evidence in Vietnam."
Husnain, M. and W. Akhtar (2016). "Relationship marketing and customer loyalty: evidence from banking sector in Pakistan." Global Journal of Management And Business Research.
Iranzadeh, S. and F. Chakherlouy (2012). Service Quality Dimensions in the Banking Industry and It's Effect on Customer Satisfaction (Case Study). Quality Management and Practices, InTech.
Jeanneau, S. (2007). "Banking systems: characteristics and structural changes." BIS Papers **33**: 3-16.
Moenardy, K. K., S. Arifin and S. Kumadji (2016). "The effect of service quality and relationship marketing to customer value, customer satisfaction, switching cost, and customer retention: a case study on the customers of bank NTT at East Nusa Tenggara Province." International journal of management and administrative sciences **3**(4): 48-63.
Nunnally, J. C. (1975). "Psychometric theory—25 years ago and now." Educational Researcher **4**(10): 7-21.
Tavakol, M. and R. Dennick (2011). "Making sense of Cronbach's alpha." International journal of medical education **2**: 53.
Vu, M. V. and H. H. Huan (2016). "The relationship between service quality, customer satisfaction and customer loyalty: An investigation in Vietnamese retail banking sector." Journal of Competitiveness **8**(2).

SJST Surman Journal for Science and Technology | ISSN: E 2790-5721 P 2790-5713
Vol3, No.1, Dec_2021 , pp. 047 ~ 058

Optimization of Cutting Parameters for Surfaces Roughness of Medium Carbon Steel C-45 in CNC Turning Machining by Using Taguchi Method

[1]Salem. A. Sultan, [2]Samir S. Abubaker, [3]Abdarazag A. [4]Hassan, Salah Iddin A. S. Issa
Mechanical Engineering and Energy Department, College of Engineering Technology-Janzour, Tripoli – Libya.
salemsultan901@gmail.com
Samirabub@gmail.com
abdoz_ali@yahoo.com
Salaheadi-72@yahoo.com

1- الملخص.

الهدف من هذه الدراسة هو الحصول على افضل متغيرات الة الخراطة الرقمية (CNC) و التي تعطى انعم نهاية لقطع مصنوعة من الصلب المتوسط الكربوني باستخدام عدة قطع كربيديه لديها مقاومة عالية لتأكل و الاحتكاك في وجود سوائل التبريد, وذلك لان نعومة السطح النهائية هي من أهم الخصائص المطلوبة للمنتج النهائي.

اعتمادا على دراسات أجريت حديثا فى العالم وجد ان عملية الخراطة الصلدة لها اكثر فائدة مقارنة بعملية التجليخ, نذكر منها نقص التكلفة في الوقت المستهلك في خراطة الاجزاء, فى هذه الدراسة, تأثير خشونة السطح على مقاومة الاحتكاك للخراطة الصلدة النهأية للمعدن المتوسط الكربون عمليا وتحليليا وكذلك البنية المجهرية تم التحقق منها. وللحصول على أفضل نهاية سطح تم استخدام تصميم تاقوتشي (Taguchi method) لأفضل خراطة عملية معتمدا على تصميم المضروب الكلى لتحديد ثلاثة متغيرات مختلفة و مستويات باستخدام المصفوفات الثمانية, و تسع تجارب تم اجرائهاعمليا. تم اختيار ثلاث متغيرات وهى (معدل التغذية، سرعة القطع، عمق القطع) كانت مهمة, تم اختبار متغيرات القطع على النحو التالي: معدل التغذية (0.075, 0.10, 0.125 مم/لفة) سرعة القطع (166.24, 180.70, 197.32 ملم/دقيقة) عمق القطع (2.0, 2.5, 3.0مم) هذه المتغيرات اختيرت كما هو مطلوب من شركة ساندفك لتصنيع العدة(SANDVIC Tool Manufacturing Company).

عمليات الخراطة العملية التي انجزت تم قياس خشونة السطح للقطع التي دُرست باستخدام (MINITAB Statistical Software) و ذلك لحساب مؤشر (S/N) وكذلك تحليل التباين (ANOVA)، حيث تم الحصول على أفضل مستويات لأفضل متغيرات قطع و مدى تأثيرها على خشونة السطح , وكذلك متغيرات تجربة خشونة السطح كانت بمعدل تغذية (0.075 مم/لفة) وسرعة القطع (180.70ملم/دقيقة) وبعمق قطع (3.0 مم) و هذه تم الحصول عليها فى التجربة رقم خمسة (5). لتأكيد التجربة والحصول على المستوى الامثل لعملية التغيرات و التى اجريت لتحديد تأثير كفاءة طريقة تاقوشى كأداة لقياس خشونة السطح.

Abstract.

The objective of this study is to optimize the Computer Numerical Control machine (CNC) turning parameters that gives the fine surface finish for the parts that made of medium carbon steel C45 using carbide cutting tool (coated insert cemented carbide) which have high resistance of deflection, wear and fraction on CNC turning operation with coolant. The surface finish quality is one of the most specified requirements in the machining process.

To obtain the optimal surface finish, the Taguchi method used for optimization of the turning experiments based on a full factorial design, to determine three different parameters and levels

by using orthogonal arrays, 9 experiments were obtained. Choice of three parameters (feed rate, cutting speed and depth of cut) were important, the cutting parameters were selected as follow: Feed rate (0.075, 0.100, 0.125mm), cutting speed (166.24, 180.70, 197.32 mm/min), depth of cut (0.5, 0.75, 1.0 mm) these parameters were chosen according to SANDVIC Tool Manufacturing Company. The series of turning experiments were performed to measure the surface roughness.

The MINITAB Statistical Software was used to calculate the signal-to-noise ratio (S/N), and analysis of the variance (ANOVA), the best optimal levels and the effect of the process parameters on surface roughness were obtained.

The parameters for experiment surface roughness were the feed (0.075mm/rev), cutting speed (180.70 mm/min), depth of cut (3.0mm) and that conducted in experiment number five (5).

A conformation of experiment to obtained optimal levels of process parameters was carried out in order to demonstrate the effectiveness and efficiency of the employed Taguchi method as a tool to measure surface roughness.

Key words: - Computer Numerical Control machine (CNC), Taguchi method, SANDVIC Tools, MINITAB Statistical Software.

Introduction:

The surface quality of the machined parts is one of the most specified customer requirements. Hard machining technique allows manufacturers to simplify their processes and still achieve the desired surface finish quality [1].

The quality of the surface plays a very important role in the performance of the turning as a good quality turned surface significantly improves fatigue strength, corrosion resistance, or creep life[2]. Surface roughness also affects several functional attributes of parts, such as contact causing surface friction, wearing, and light reflection, load bearing capacity, coating or resisting fatigue. Therefore, the desired finish surface is usually specified and the appropriate processes are selected to reach the required quality [3].

The surface roughness is a measure of the irregularities on the surface of a component resulting from machining operations. It is denoted by Ra namely, average roughness. Ra is theoretically derived as the arithmetic average value of departure of the profile from the mean line along a sampling length[4]. On the other hand, surface roughness depends on process parameters and machining irregularities, such as cutting speed, the rate of feed, the depth of cut, material properties, nose radius of tool and cutting fluid. A small change in any of the above factors can have a significant effect on the surface produced [4,5].

3.0 Experimental Procedure.

Equipment required, workpiece material, cutting tool type carbide with radius of (1.6mm), CNC lath machine, MINITAB software for analyzing the data and surface roughness device.

3.1 Instruments and equipment used for the research.

The material investigated in this study was a medium carbon, steel C45 (AISI 1045) steel, supplied in the form of Ø 10 mm rolled rods of a nominal composition listed in Table 1.

Table 1. (chemical composition AISI 1045)[5]

Element	C	Si	Mn	Ni	P	S	Cr	Mo
Composition %	0,43-0.5	Max 0.4	0.5-0.8	Max 0.6	0.045	0.045	Max 0.4	Max 0.1

Figure 1. Work pieces Medium carbon steel (AISI 104).

3.2. CNC Machine.

In this work, External turning tests were performed. All of the turning tests were performed under cooling conditions on Computer Numerical Control lathe machine (CNC). Type Samsung PLA25 CNC lath which is shown in (figure 2a) and carbide cutting tool (coated insert cemented carbide) (b). The CNC lathe having a maximum spindle speed of 3500 rpm and a maximum power of 20 KW.

Figure 2a: Lath machine (CNC).

Figure 2 (b): Shows the carbide cutting tool (coated insert cemented carbide).

3.3 Surface Roughness Measurement.

The Surtronic 25 has a uniquely engineered stylus lift mechanism which allows a vertical adjustment of 50mm and rotation of the pick-up to different measuring positions, including right angle or inverted measurements. These adjustments to the height and position of the gauge allow areas and features of a part to be easily measured without additional complex fixtures. This feature saves the operator a huge amount of set up time and allows total flexibility.

Figure 3: Roughness test device (Surtronic 25).

3.4 Taguchi's design.

The method which presented in this study is an experimental design process called the Taguchi design method, (figure 4) illustrate the Procedure and steps of Taguchi Parameter design [4].

1-Select the Quality characteristic
2-Select noise factors and control factors
3- Select Orthogonal Array
4-Conduct the experiments
5-Analyze results: determine optimum factor-level combination
6-Predict optimum performance
7- Confirm Experimental Design

Figure 4: Procedure and steps of Taguchi Parameter design [5]

The employing design of experiments (DOE), described by Dr Taguchi, is one of the most important statistical technique of Total quality management (TQM) for designing high quality systems at reduced cost. Taguchi methods provide an efficient and systematic way to optimize designs for performance, quality, and cost. Fundamentally, traditional experimental design procedures are too complicated and not easy to use. A large number of experimental works have to be carried out when the number of the process parameters increases. To solve this problem, the Taguchi method has used a special design of orthogonal arrays to study the entire parameter space with only a small number of experiments [6]. Taguchi methods has been widely utilized in engineering analysis and consists of a plan of experiments with the objective of acquiring data in a controlled way and in order to obtain information about the behavior of a given process. The greatest advantage of this method is to save the effort in conducting experiments. Therefore, it reduces the experimental time as well as the cost by finding out significant factors fast [7].

Taguchi's parameter design offers a simple, systematic approach and can reduce number experiment to optimize design for performance, quality and cost. Taguchi method offers the quality of product is measured by quality characteristics such as: nominal is the best, smaller is better and larger is better. Optimization with Taguchi method in turning using conceptual S/N ratio approach and Analysis of variance ANOVA can be concluded that Taguchi's robust design method is suitable to analyze the metal cutting problem. Conceptual signal-to-noise S/N ratio and ANOVA approaches for data analysis draw similar conclusion.

3.5 Analysis Software.

MINITAB statistical software is used in this study for selecting the types of design to be used for running the experiments, to display all possible combination of controllable factors and analyzing data representing main and interaction relationship between them. This software provides a wide range of basic and advanced data analysis capabilities [8]

4.Results and Discussion.

Considering that the literature suggested that feed rate has a much higher effect on surface roughness and material removal rate than the other two parameters [9]. The feed rate, cutting speed and depth of cut were then given three levels as shown in the table (2). These ranges would be expected to produce a good finishing surface on the parts.

Table 2. Variable factor levels of medium carbon steel (1045).

Factor	Level 1	Level 2	Level 3
Feed rate (mm/rev)	**0.075**	**0.100**	**0.125**
Cutting speed (rpm	**166.24**	**180.70**	**197.32**
Depth of cut (mm	**2**	**2.5**	**3.0**

4.1. Select of orthogonal Array.

One of Taguchi method steps is selecting the proper orthogonal array (OA) according to the number of controllable factors (cutting parameters). Since three factors were selected to study in this research, three levels for each factor were considered. Therefore, L9 Taguchi method has used special design of orthogonal arrays L9 (3^3) to study the entire parameter with only a small number of experiments for surface roughness and material removal rate table (3).

Table 3. L9 (3^3) Taguchi orthogonal array.

Experiment number	Feed rate A	Cutting speed B	Depth of cut C
1	1	1	1
2	1	2	2
3	1	3	3
4	2	1	2
5	2	2	3
6	2	3	1
7	3	1	3
8	3	2	1
9	3	3	2

4.2 Conducting the Experiments.

The experiments, sorted in table (4), is randomly run by the CNC turning machine and Three measured surface roughness data values were collected, S/N signal-to-noise ratio of each experimental run were calculated in table 4. The signal-to-noise ratio is often written as S/N or represented by the Greek letter (η). In the Taguchi method, the term (signal) represented the desirable value (mean) for the output characteristic and the term (noise) represented the undesirable value Standard deviation (S.D) for output characteristic because of some other factors which called (noise factors). Noise factors are those factors that are not controllable, and whose influences are not known.

Table 4: Experimental design of medium carbon steel (1045)

Experiment number	Feed rate A (mm/rev)	Cutting speed B (rpm)	Depth of cut C (mm)	Ra1	Ra2	Ra3
1	0.075	166.24	2.0	1.90	1.96	2.06
2	0.075	180.70	2.5	0.96	0.92	0.95
3	0.075	197.32	3.0	3.50	3.59	3.38
4	0.100	166.24	2.5	1.68	1.66	1.66
5	0.100	180.70	3.0	0.50	0.46	0.54
6	0.100	197.32	2.0	0.60	0.72	0.68
7	0.125	166.24	3.0	0.78	0.72	0.74
8	0.125	180.70	2.0	0.94	1.20	0.96
9	0.125	197.32	2.5	0.96	0.96	1.00

Deflection and vibration, which may be occur on cutting tool and work piece material because of cutting force during machining. The effect of uncontrollable noise factors is not the subject of this study. Therefore, the S/N ratio is the ratio of the mean to the (S.D). Taguchi uses the S/N ratio to measure the quality characteristic deviating from the desired value. The S/N ratios seek out the strong effects and ascertain the best levels. The most desired situation is reached when the signal is strong and the impact of the noise is weak. There are several S/N ratios available depending on type of characteristic, lower is better (LB), nominal is better (NB), or higher is better (HB) [6,.7]. The smaller is better quality characteristic can be explained as:

$$S/N = -10 \, Log \, MSD \tag{1}$$

Where:

MSD = the mean square deviation.

The mean square deviation for smaller-the –better characteristic is:

$$MSD = \frac{y_1^{\,2} + \ldots + y_n^{\,2}}{n} \tag{2}$$

Where n = number of measurements in trial/row, in this case, n=3 and yi is the measured value in a run/row. We can then rewrite the S/N equation as:

$$S/N = -10 \log \left| \frac{y_1^{\,2} + \ldots + y_n^{\,2}}{n} \right| \tag{13}$$

Table 5. Experimental Results for Surface Roughness

Experiment number	Response value			S/N value	Mean
	Ra1(µm)	Ra2 (µm)	Ra3(µm)		
1	1.90	1.96	2.06	-5.9089	1.97333
2	0.96	0.92	0.95	0.5053	0.94333
3	3.50	3.59	3.38	-10.8591	3.49000
4	1.68	1.66	1.66	-4.4022	1.66000
5	0.50	0.46	0.54	6.0021	0.50000
6	0.60	0.72	0.68	3.4976	0.66667
7	0.78	0.72	0.74	2.5326	0.74667
8	0.94	1.20	0.96	-0.3412	1.03333
9	0.96	0.96	1.00	0.2331	1.0100

Table 6. Experimental Results for Surface Roughness

Level	Feed rate	Cutting speed	Depth of cut
1	-5.4209	-2.5928	-0.9175
2	1.6992	2.0554	-1.2212
3	0.8082	-2.3761	-0.7748
Delta	7.1201	4.6482	0.4464
Rank	1	2	3

Table 7. Response Table for Signal to Noise Ratio value of Surface Roughness.

Level	Feed rate	Cutting speed	Depth of cut
1	2.1356	1.4600	1.2244
2	0.9422	0.8256	1.1922
3	0.9178	1.7100	1.5789
Delta	1.2178	0.8844	0.3867
Rank	1	2	3

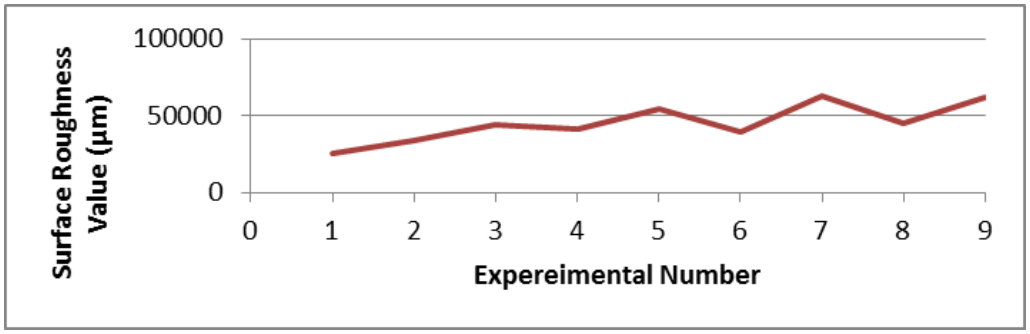

Figure 5. Experimental Result of Surface Roughness Value.

Table (7) shows that the best surface roughness value was at machining the sample NO (5) under the cutting parameters (feed rate = 0.100 mm/rev, cutting speed = 180.70 m/min and depth of cut = 3.0 mm). All these data can be represented graphically as in figure (6).

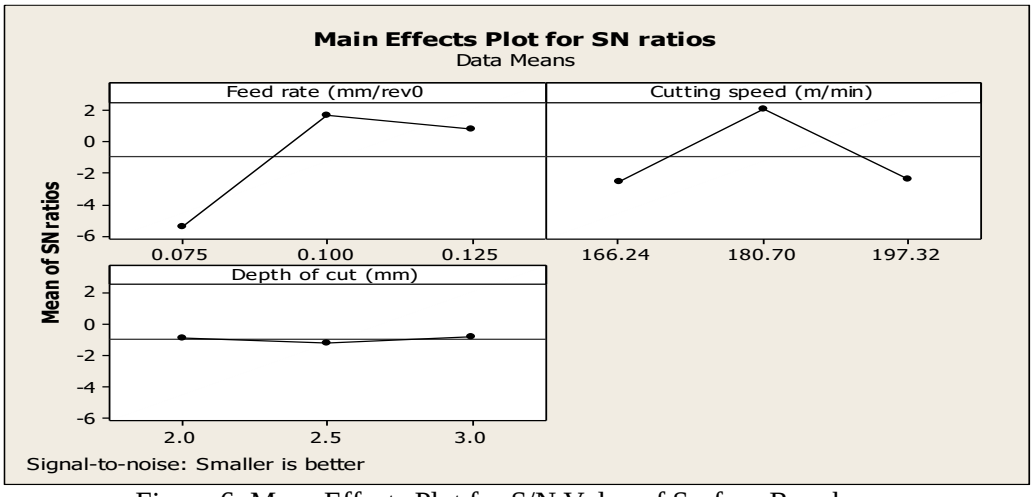

Figure 6: Mean Effects Plot for S/N Value of Surface Roughness

4.3 The response surface for surface roughness.

Response surface are usually drawn to further appreciate the effect of cutting condition in the tool performance in terms of surface roughness. Since the depth of cut is always specified by the stock allowance, only feed rate and cutting speed are usually selectable in most finish hard turning cases. The response surface is generated by changing cutting speed and feed rate within the interested range.

This response surface in figures (9,10) is shows that from the 3D graph the small value for the surface roughness are the better as mentioned in Taguchi methodology that the small value is the better. It can be seen that cutting speed impacts the surface roughness performance more significantly than feed rate does. Such response surface can help designers and engineers to choose optimal cutting conditions in machining hardened materials.

Table 8. Response Table for the value of Surface Roughness.

Experiment number	surface roughness Ra	Cutting condition
1	+261.96891	Feed Rate
2	+0.18787	Cutting Speed
3	+5.68112	Depth of Cut
4	-1.00832	Cutting Speed
5	-42.56580	Depth of Cut
6	+0.034946	Feed Rate
7	-275.32842	Feed Rate
8	-2.69229004	Cutting Speed
9	-4.95625	Depth of Cut

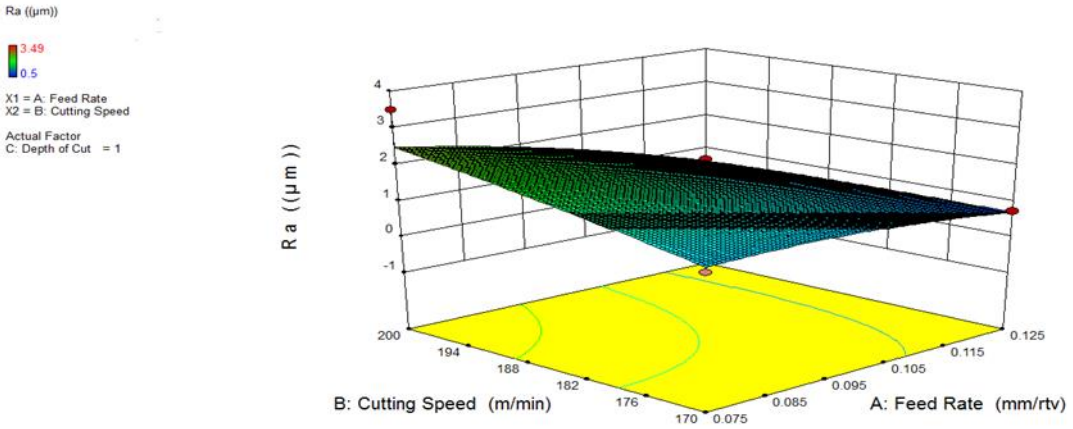

Figure 9. The relationship between surface roughness and both cutting speed and feed rate.

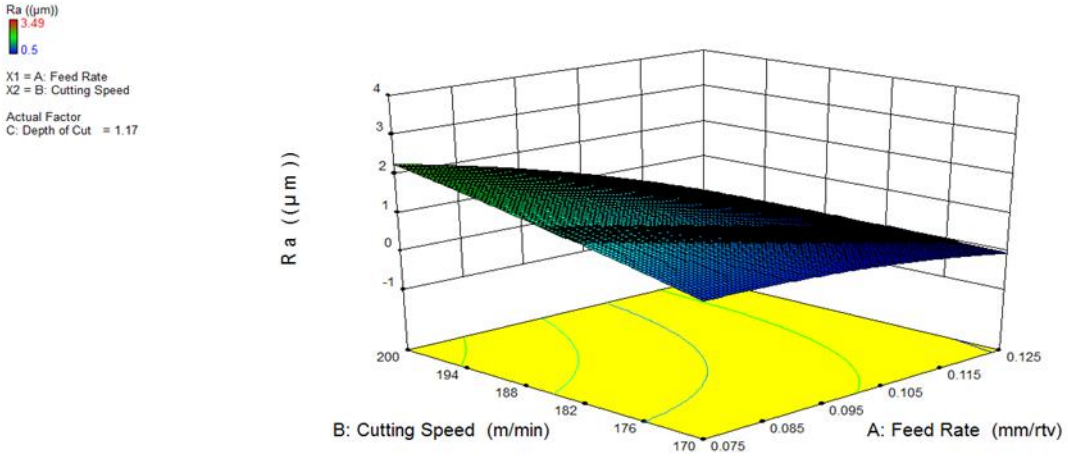

Figure 10. The relationship between surface roughness and both cutting speed and feed rate.

4.4. Surface Roughness.

The optimum cutting parameters are feed rate 0.100 mm/rev, cutting speed 180.70 m/min and depth of cut 3.0 mm. Three samples were machined under the optimal parameters that optimized in the study for the purpose of confirmation experimental.

Table (9) shows the results of the conformation experimental. Compared with the predicted value, the mean surface roughness of the two conformation experimental samples (0.503 µm), which was very close to the predicted value of surface roughness (0.5000 µm). There for, the conformation run indicated that the selection of the optimal levels for all the parameters produced the best surface roughness

Table 9. Results of Conformation Experiments for Surface Roughness.

Sample Number	Mean of Ra (µm)
1	0.485
2	0.521
Mean	0.503

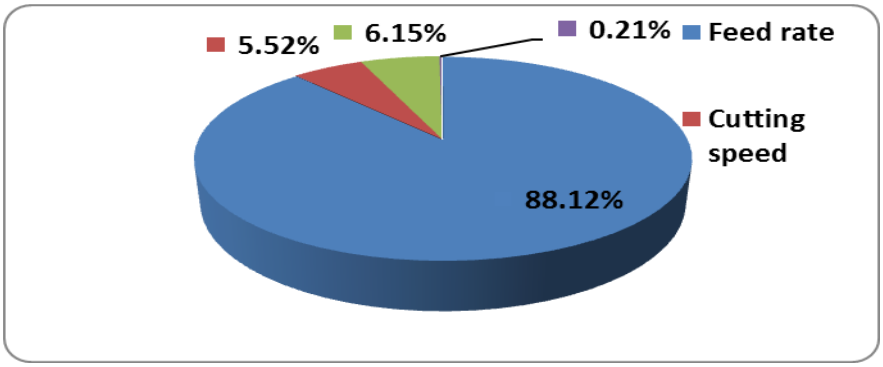

Figure 11. percent of control parameters on surface roughness of medium carbon steel (C45).

The ANOVA analysis results can be seen in figures (11), shows the influence of each factor on the performance of the turning process. According to ANOVA analysis of surface roughness of medium carbon steel (C45), the feed rate influences the performance by 88.12%, the depth of cut by 6.15% and cutting speed by 5.52%, and according to ANOVA analysis of material removal rate of medium carbon steel (C45), the feed rate by 84.32%, the cutting speed by 9.30% and depth of cut by 5.87%.

5. Conclusion.

In the study the Taguchi orthogonal array is employed to optimize the machining parameters, with respect to surface roughness and material removal rate which produce by CNC turning machine when machining medium carbon steel. Taguchi method used to study the effect of three factors, such as feed rate, cutting speed and depth of cut under the same conditions.

1- Case one surface roughness

The optimum parameters for best surface roughness are obtained at feed rate 0.100 mm/rev, cutting speed 180.70 m/min and depth of cut 3.0 mm. It has been observed that the feed rate has the got the most significant influence on the surface roughness. A confirmation experiments were carried out to obtain the optimal conditions. The minimum surface roughness is calculated as 0.500 µm which is close to 0.503 µm that obtained in confirmation experiments.

2-Case three the proposed methodology

The proposed methodology can help improve the state of the art of the cutting condition optimization in machine turning. Eventually it will help machine turning to be a viable technology. This modelling approach can also be further extended to appreciate the tool performance of other machining processes.

6. References.

1. LAWRENCE E. DOYLE manufacturing processes and materials for engineers, University of Illinois, 1985, P508-510.
2. A Jayant, V Kumar, 2008. " Prediction of Surface Roughness in CNC Turning Operation using Taguchi Design of Experiments".Volume88, IE(I)Journal–PR.
3. B. Sidda Reddy, J. Suresh Kumar, K. Vijaya Kumar Reddy, 2009." Prediction of Surface Roughness in Turning Using Adaptive Neuro-Fuzzy Inference System". Volume 3, No 4 Jordan Journal of Mechanical and Industrial Engineering.
4. S. Thamizhmanii, S. Saparudin, S. Hasan, 2007." Analyses of surface roughness by turning process using Taguchi method". Volume 20, Journal of Achievements in Materials and Manufacturing Engineering, issues 1-2.
5. Gusri, A.I., Che Hassan, C.H., Jaharah, A.G., Yanuar,B, Yasir, A, Nagi,A. 2008 ." Application of Taguchi method in optimizing turning parameters of Titanium alloy". Engineering Mathematics Group.

6. Lindman H, Analysis of variance in experimental design, (Springer-Verlag, New York, 1992).
7. N. Nalbant, H. Gokkaya, G. Sur, Application of Taguchi method in the optimization of cutting parameters for surface roughness in turning, Materials and Design, date received 21.07.2006 and date accepted 06.01.2006.
8. RANJIT K. ROY, "design of experimental using the Taguchi approach". Volume 01/50118-BLIN steps to product and process [pp 172-206]-16.
9. Peace, Glen Stuart. Taguchi methods-A hands-on Approach to Quality Engineering.

SJST Surman Journal for Science and Technology | ISSN: E 2790-5721 P 2790-5713
Vol3, No.1, Dec_2021 , pp. 059 ~ 071

Optimization Process Parameters of Submerged Arc Welding Using Factorial Design Approach

[1]Al-sonosi Abohusina, [2]Mohamed Aljadi, [3]Khaled Marwan, [4]Ali Elhatmi

[1]Education ministry, Zliten, Libya.

[2,3,4]Advanced occupational center of welding, Tripoli, Libya.

[1]elsanose4@gmail.com

[2]maljadi251@gmail.com

[3]khaledgewa@gmail.com

[4]ali_banor@yahoo.com

Abstract:

This research study is investigating the weldability of the low carbon steel through studying the effects of the welding process parameters [welding current (I), arc voltage (U), welding speed (S)] on the weld joints' quality on the weld bead geometry [bead width (W), bead height (H), bead penetration (P)]. The crosses were welded using submerged arc welding. This study is based on the assumption that the optimum parameters of the welding process that lead to the optimum geometry of weld bead, must achieve high-quality welds, which can result in better weld bead geometry, mechanical, and metallurgical properties. Where an experimental part is based on the level factorial design of three process parameters. Then, the weld bead characteristics were measured for each sample. A series of experimental data was used to construct the mathematical models to predict the weld bead geometry characteristics for any given welding conditions. The mathematical modelling was developed using the multiple regression method by applying the multiple linear regression equation. The values of coefficients of the linear equation for the weld bead characteristics were calculated by regression method using package for social science SPSS software

Keywords: SAM, Weld Bead Geometry, Regression Analysis, Factorial Design, SPSS.

1. Introduction.

Submerged Arc Welding (SAW) is a high-quality welding process with a very high deposition rate. It is commonly used to join thick sections in the flat position. SAW is usually operated either as fully mechanized or automatically processed. However, it can be used semi automatically as well. During SAW process, the operator cannot observe the weld pool and not directly interfere with the welding process. As the automation in the SAW process increases, the direct effect of the operator decreases and the precise setting of parameters becomes much more important than manual welding processes. Figure (1) shows a schematic of the sample, wire, and flux during submerged arc welding.

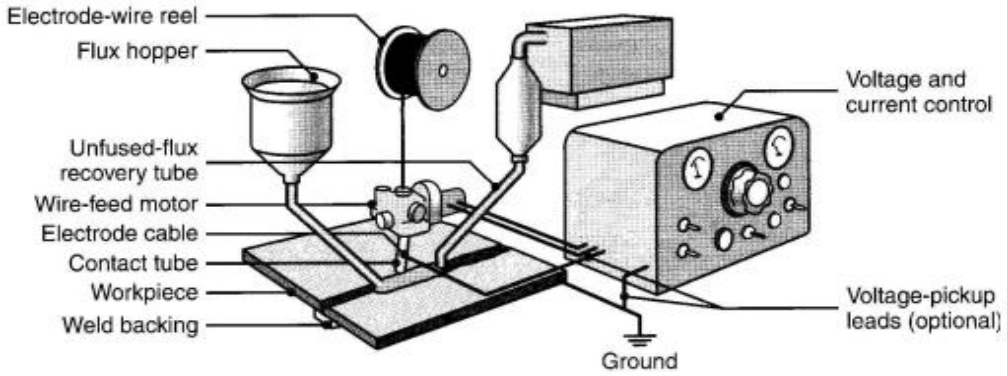

Figure 1. a schematic of the sample, wire, and flux during submerged arc welding

The experimental part is based on three-level factorial design process parameters and analysis of various process control variables and important weld bead parameters in SAW. In order to investigate the effect of input parameters on output parameters that determine the weld bead geometry, a series of experimental data was used to construct the mathematical models to predict the weld bead geometry characteristics for any given welding conditions. The mathematical modeling was developed using the multiple regression method by applying the multiple linear regression equation. The value of coefficients of the linear equations for the weld characteristics were calculated by a regression method using the package for social science SPSS software. Murugan et al. [1] studied the relationships between the submerged arc welding process parameters and the weld bead geometry of pipes. They reported that wire feed rate has a significant positive effect, but welding speed has an appreciable negative effect on penetration, whereas arc voltage has a less significant negative effect on penetration and reinforcement, which indicate that weld bead geometry is influenced by these process parameters. Serdar et al. [2] carried out a study on the sensitivity analysis of submerged arc welding process parameters; they reported that the current is the most important parameter in determining the penetration. Gunaragj et al. [3] in their study on heat-affected zone characteristics in submerged arc welding of structural steel pipes, they developed mathematical models to predict the heat-affected zone characteristics in submerged arc welding and concluded that heat input and wire feed rate have a considerable positive effect on almost all heat affected zone dimensions. Welding speed has a negative on all heat affected zone dimensions, whereas different HAZ layers increase with the increase in arc voltage. In addition to all these studies and investigations, there is still more work needed for the optimization of process variables for various alloys**.** S. kumanan et al. [4] experiments are conducted in the semi-automatic arc welding machine and S/N ratio are computed to determine the optimum parameters, the percentage contribution of each factorial is validated by multi regression analysis and ANOVA is conducted by using the SPSS software and the mathematical model is built to predict the weld bead geometry for given input parameters over output. Yang et al. [5] applied the curvilinear regression equation for modeling the submerged arc welding process, they found that curvilinear equations are very helpful in providing useful information. It is estimated that metal loss through vaporization was 4% for electrode positive polarity and 8% for electrode negative polarity.

2. Experimental Work:

The experimental part of this work is concerned with study the effect of input parameters on output parameters. The input parameters selected are welding current, arc voltage, and welding speed. The bead geometry characteristics (bead width, bead height, and bead penetration) were measured and used as output parameters as shown in figure (2).

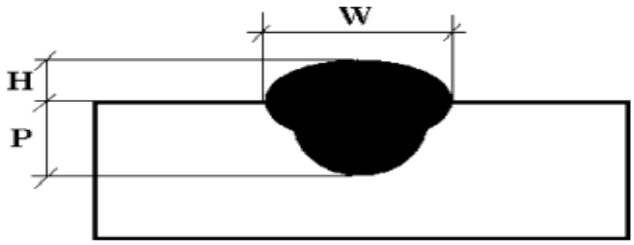

Figure 2. The weld bead geometry characteristic.

The as-received material used is a plate of low carbon steel (mild) steel, bead-on-plate type welds were deposited on samples that were cut from the as-received material in a rectangular with dimensions of 200*200*10 mm. The work piece used for the experiment is shown in Figure (3). Where three levels factorial design of three process parameters including interactions effects of the three parameters was used. This work involved performing a number of 27 welds to obtain the necessary data to construct the mathematical models. Table (1) shows three levels factorial design of three process parameters, while welding conditions according to factorial design were presented in table (2). The measured values of the weld bead characteristics were presented in table (3a and table 3 b and 3 c).

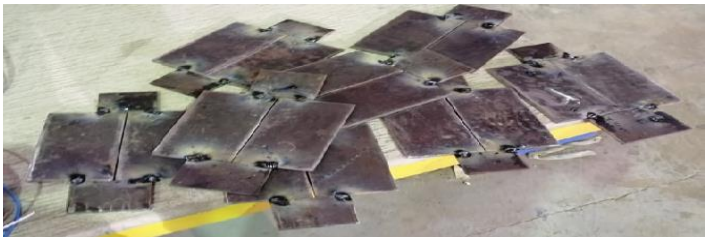

Figure 3. A workpieces used for the experiments

After performance of welding process, cross sections of the welds were cut and metallographic samples were prepared using standard methods such as grinding, polishing, and etching is shown in Figure (2), then the weld bead geometry characteristics were measured by measuring instrument for measuring the micro-dimensions up to micrometer of type Nikon V12 Tool Room Microscopy is shown in Figure (4).

Figure 4. Nikon V12 Tool Room Microscopy

Table 1. Three levels factorial design of three process parameters.

Exp No.	Process Parameters			Exp No.	Process Parameters			Exp No.	Process Parameters		
	A	B	C		A	B	C		A	B	C
1	1	1	1	10	2	1	1	19	3	1	1
2	1	1	2	11	2	1	2	20	3	1	2
3	1	1	3	12	2	1	3	21	3	1	3
4	1	2	1	13	2	2	1	22	3	2	1
5	1	2	2	14	2	2	2	23	3	2	2
6	1	2	3	15	2	2	3	24	3	2	3
7	1	3	1	16	2	3	1	25	3	3	1
8	1	3	2	17	2	3	2	26	3	3	2
9	1	3	3	18	2	3	3	27	3	3	3

Table 2. Welding conditions according to factorial design.

Exp No.	Current I(A)	Voltage U(V)	Speed S(mm/min)	Exp No.	Current I(A)	Voltage U(V)	Speed S (mm/min)
1	350	26	400	15	450	27	600
2	350	26	500	16	450	28	400
3	350	26	600	17	450	28	500
4	350	27	400	18	450	28	600
5	350	27	500	19	550	26	400
6	350	27	600	20	550	26	500
7	350	28	400	21	550	26	600
8	350	28	500	22	550	27	400
9	350	28	600	23	550	27	500
10	450	26	400	24	550	27	600
11	450	26	500	25	550	28	400
12	450	26	600	26	550	28	500
13	450	27	400	27	550	28	600
14	450	27	500				

Table 3a. bead width (W): welding conditions and measured values according to factorial design.

Exp No.	Current I(A)	Voltage U(V)	Speed S(mm/min)	Bead width (W_1) (mm)	Bead width (W_2) (mm)	Bead width (W^-) (mm)
1	350	26	400	15.430	15.570	15.500
2	350	26	500	14.125	14.095	14.110
3	350	26	600	11.175	11.125	11.150
4	350	27	400	16.650	16.658	16.654
5	350	27	500	15.340	15.280	15.310
6	350	27	600	12.355	12.375	12.365
7	350	28	400	17.835	17.815	17.825
8	350	28	500	15.745	15.775	15.760
9	350	28	600	13.250	13.180	13.215
10	450	26	400	21.340	21.320	21.330
11	450	26	500	18.935	18.975	18.955
12	450	26	600	15.380	15.360	15.370
13	450	27	400	22.845	22.855	22.850
14	450	27	500	19.350	19.650	19.500
15	450	27	600	15.580	15.620	15.600
16	450	28	400	22.870	22.910	22.890
17	450	28	500	18.835	18.855	18.845
18	450	28	600	16.525	16.565	16.545
19	550	26	400	23.460	23.480	23.470
20	550	26	500	20.625	20.655	20.640
21	550	26	600	18.080	18.040	18.060
22	550	27	400	25.040	24.960	25.000
23	550	27	500	21.250	21.350	21.300
24	550	27	600	18.725	18.715	18.700
25	550	28	400	27.240	27.280	27.260
26	550	28	500	23.700	23.740	23.720
27	550	28	600	19.450	19.550	19.500

[Bead width (W); W_1, W_2 the measured values, and W^- the mean of the measured value = $(W_1+W_2)/2$]

Table 3b. bead height (H); welding conditions and measured values according to factorial design.

Exp No.	Current I(A)	Voltage U(V)	Speed S(mm/min)	Bead height (H_1) (mm)	height width (H_2) (mm)	height width (H^-) (mm)
1	350	26	400	3.805	3.795	3.800
2	350	26	500	3.745	3.775	3.760
3	350	26	600	3.335	3.365	3.350
4	350	27	400	3.640	3.660	3.650
5	350	27	500	3.140	3.360	3.250
6	350	27	600	2.735	2.665	2.700
7	350	28	400	3.085	3.115	3.100
8	350	28	500	2.595	2.655	2.625
9	350	28	600	2.100	2.220	2.160
10	450	26	400	3.730	3.770	3.750
11	450	26	500	3.250	3.300	3.275
12	450	26	600	2.795	2.825	2.810
13	450	27	400	3.230	3.300	3.265
14	450	27	500	2.715	2.795	2.755
15	450	27	600	2.350	2.280	2.315
16	450	28	400	2.620	2.560	2.590
17	450	28	500	2.295	2.275	2.285
18	450	28	600	1.740	1.790	1.765
19	550	26	400	3.300	3.240	3.270

20	550	26	500	2.900	2.820	2.860
21	550	26	600	2.400	2.560	2.480
22	550	27	400	2.700	2.780	2.740
23	550	27	500	2.425	2.375	2.400
24	550	27	600	1.950	1.750	1.850
25	550	28	400	2.625	2.595	2.610
26	550	28	500	1.845	1.755	1.800
27	550	28	600	1.420	1.380	1.400

[Bead height (H); H_1, H_2 the measured values, and H^- the mean of the measured value = $(H_1+H_2)/2$]

Table 3c. bead penetration (P): welding conditions and measured values according to factorial design.

Exp No.	Current I(A)	Voltage U(V)	Speed S(mm/min)	Bead penetration(P_1) (mm)	Bead penetration (P_2) (mm)	Bead penetration (P^-) (mm)
1	350	26	400	4.820	4.860	4.840
2	350	26	500	5.050	5.150	5.100
3	350	26	600	5.275	5.325	5.300
4	350	27	400	4.690	4.730	4.710
5	350	27	500	5.130	5.170	5.150
6	350	27	600	5.175	5.055	5.115
7	350	28	400	4.400	4.360	4.380
8	350	28	500	4.800	4.850	4.825
9	350	28	600	5.000	5.030	5.015
10	450	26	400	5.295	5.315	5.305
11	450	26	500	5.220	5.210	5.215
12	450	26	600	5.550	5.510	5.530
13	450	27	400	5.160	5.200	5.180
14	450	27	500	5.405	5.385	5.395
15	450	27	600	5.625	5.675	5.650
16	450	28	400	4.940	5.060	5.000
17	450	28	500	5.285	5.305	5.295
18	450	28	600	5.405	5.445	5.425
19	550	26	400	6.000	5.920	5.960
20	550	26	500	6.435	6.465	6.450
21	550	26	600	6.200	6.160	6.180
22	550	27	400	5.820	5.900	5.860
23	550	27	500	6.015	5.985	6.000
24	550	27	600	6.225	6.275	6.250
25	550	28	400	5.800	5.740	5.770
26	550	28	500	5.640	5.800	5.720
27	550	28	600	6.100	6.000	6.050

[Bead penetration (P); P_1, P_2 the measured values, and P^- the mean of the measured value = $(P_1+P_2)/2$]

3. MATHEMATICAL MODELING:

3.1 Analysis of multiple linear regression:

Mathematical modeling of the SAW process may be constructed using multiple curvilinear regression analysis. In this regard, first, a mathematical form simulating the relation between weld bead characteristics (bead width, bead height, and penetration) and process parameters (welding current, welding voltage, welding speed) should be selected. The regression coefficients are calculated based on this selected form by correlating the

experimental data series. The general equation of the multiple linear regressions takes the following form:

$$Y=a+b_1X_1+b_2X_2+b_3X_3+\ldots. +b_kX_k +e \quad (1)$$

Where:

Y is the dependent variable, which is to be predicted. X_1, X2, X3…X_K are the k known variables on which the predictions are to be made. a, b_1, b_2, b_3,…., b_k are the regression coefficients.

e is the error.

The equation (1) can be written in the following form:

$$Y=a+b_1I+b_2U+b_3S+e \quad (2)$$

Y= (W=bead width, H=bead height, P=bead penetration, all in mm) I= welding current (A), U=arc voltage (V), S=welding speed (mm/min) (a, b_1, b_2, b_3) are the regression coefficients.

e is the error.

3.1.1 The regression coefficients:

The coefficients values of the linear equations were calculated by the regression method using the commercial statistical program SPSS software (statistical package for social science). After the calculation of the regression coefficients, these coefficients were evaluated for their significance at 95% confidence level by T-test.

Table 4 a. calculated regression coefficients for bead width (W)

Weld bead characteristic	Regression coefficients	a	b_1	b_2	b_3
		-8.811	0.037	0.943	-0.029
Bead width	T-test	-1.644	18.971	4.897	-15.080
	Significant	0.114	0.000	0.000	0.000

Table 4 b. calculated regression coefficients for bead height (H)

Weld bead characteristic	Regression coefficients	a	b_1	b_2	b_3
		20.247	-0.004	-0.501	-0.004
Bead height	T-test	28.623	-15.272	-19.721	-17.370
	Significant	0.000	0.000	0.000	0.000

Table 4 c. calculated regression coefficients for bead penetration (P)

Weld bead characteristic	Regression coefficients	a	b_1	b_2	b_3
		5.606	0.005	-0.133	0.002
Bead penetration	T-test	5.781	16.638	-3.828	5.598
	Significant	0.000	0.000	0.001	0.000

Substituting these regression coefficients into equation (2), three mathematical models for submerged arc welding can be obtained for weld bead characteristics. These models were expressed by equations (3), (4), and (5).

$$W=-8.811+ (0.037*I) + (0.943*U)-(0.029*S) \quad (3)$$

$$H=20.247-(0.004*I)-(0.501*U)-(0.004*S) \quad (4)$$

$$P=5.606+ (0.005*I)-(0.133*U) + (0.002*S) \quad (5)$$

The correlation coefficients, which were used in this study to evaluate the total significant of the mathematical models, are R, R^2, and adjusted-R^2.

R is the simple correlation coeficient.it measures the relation power between two variables or more. R^2 is the determination coefficient. It is used to measure the explanatory power of the developed models for the simple linear regression case (one independent variable with one dependent variable). It is defined as the ratio of the sum of squares of the regression and the total sum of squares. It can take on any value between 0 and 1 with a value closer to 1 Adjusted-R^2 is the correlation coefficient. It is to report the total explanatory power of the multiple linear regression models (because it considers the number of the independent variables). In general, it is best indicator of the fit quality. It also can take on any value less than or equal to 1, with a value closer to 1 indicating a better fit. The values of the coefficients R, R^2, and adjusted-R^2 for the bead characteristics are calculated by regression method using SPSS software. The results were presented in tables (5a), (5b), and (5 c). indicates a better fit.

Table 5 a. correlation coefficients for bead width (W) model.

Model	R	R^2	Adjusted- R^2	Std. Error of the Estimate
Bead width	0.982	0.964	0.959	0.817052

Table 5 b. correlation coefficients for bead height (H) model.

Model	R	R^2	Adjusted- R^2	Std. Error of the Estimate
Bead height	0.988	0.976	0.973	0.107807

Table 5 c. correlation coefficients for bead penetration (P) model.

Model	R	R^2	Adjusted- R^2	Std. Error of the Estimate
Bead penetration	0.982	0.964	0.959	0.817052

3.2 accuracy of the models:

To determine the residual value in each experiment, the developed mathematical models were used to predict the weld bead characteristics values [bead width (W), bead high (H), bead penetration (P)] for 27 experiments according to factorial design of experiments, then these values were compared with the measured and the residual values were calculated to determine the error percentage in each experiment. The error percentage can be calculated by the following equation:

% Error = [(measured value-predicted value)/predicted value]*100
Or % Error = [(residual/predicted value)*100] (6)
Tables (6 a), (6 b), and (6 c) present the measured, predicted, residual values, and the error percentage in each experiment.

Table 6 a. bead width (W); measured, predicted values, residual, and error percentage according to factorial design.

Exp No.	Bead width W^{-}(mm)	Bead width $W^{\wedge}$ (mm)	Re	Error (%)	Exp No.	Bead width W^{-}(mm)	Bead width $W^{\wedge}$ (mm)	Re	Error (%)
1	15.500	17.057	-1.557	-9.12	15	15.600	15.900	-0.300	-1.88
2	14.110	14.157	-0.047	-0.33	16	22.890	22.643	0.247	1.09
3	11.150	11.257	-0.107	-0.95	17	18.845	19.743	-0.898	-4.54
4	16.654	18.000	-1.346	-7.47	18	16.545	16.843	-0.298	-1.76

5	15.310	15.100	0.210	1.39	19	23.470	24.457	-0.987	-4.03
6	12.365	12.200	0.165	1.35	20	20.640	21.557	-0.917	-4.25
7	17.825	18.943	-1.118	-5.90	21	18.060	18.657	-0.597	-3.19
8	15.760	16.043	-0.283	-1.76	22	25.000	25.400	-0.400	-1.57
9	13.215	13.143	0.072	0.54	23	21.300	22.500	-1.200	-5.33
10	21.330	20.757	0.573	2.76	24	18.700	19.600	-0.900	-4.59
11	18.955	17.857	1.098	6.14	25	27.260	26.343	0.917	3.48
12	15.370	14.957	0.413	2.76	26	23.720	23.443	0.277	1.18
13	22.850	21.700	1.150	5.29	27	19.500	20.543	-1.043	-5.07
14	19.500	18.800	0.700	3.72	Average of error percentage = -1.19				

(W^= the predicted, Residual Re=W⁻-W^)

Table 6 b. bead height (H); measured, predicted values, residual, and error percentage according to factorial design.

Exp No.	Bead height H⁻(mm)	Bead height H^ (mm)	Re	Error (%)	Exp No.	Bead height H⁻(mm)	Bead height H^ (mm)	Re	Error (%)
1	3.800	4.221	-0.421	-9.97	15	2.315	2.520	-0.205	-8.13
2	3.760	3.821	-0.061	-1.59	16	2.590	2.819	-0.229	-8.12
3	3.350	3.421	-0.071	-2.07	17	2.285	2.419	-0.134	-5.53
4	3.650	3.720	-0.070	-1.88	18	1.765	2.019	-0.254	-12.58
5	3.250	3.320	-0.070	-2.10	19	3.270	3.421	-0.151	-4.41
6	2.700	2.920	-0.220	-7.53	20	2.860	3.021	-0.161	-5.37
7	3.100	3.219	-0.119	-3.69	21	2.480	2.621	-0.141	-6.16
8	2.625	2.819	-0.194	-6.88	22	2.740	2.920	-0.180	-4.76
9	2.160	2.419	-0.259	-10.70	23	2.400	2.520	-0.120	-12.73
10	3.750	3.821	-0.071	-1.85	24	1.850	2.120	-0.270	7.89
11	3.275	3.421	-0.146	-4.26	25	2.610	2.419	0.191	-10.84
12	2.810	3.021	-0.211	-6.98	26	1.800	2.019	-0.219	-13.52
13	3.265	3.320	-0.055	-1.65	27	1.400	1.619	-0.219	-5.78
14	2.755	2.920	-0.165	-5.65	Average of error percentage = -5.78				

(H^= the predicted value, Residual Re=H⁻-H^)

Table 6 c. bead penetration (H); measured, predicted values, residual, and error percentage according to factorial design.

Exp No.	Bead penetration P⁻ (mm)	Bead penetration P^ (mm)	Re	Error (%)	Exp No.	Bead penetration P⁻ (mm)	Bead penetration P^ (mm)	Re	Error (%)
1	4.840	4.698	0.142	3.02	15	5.650	5.465	0.185	3.38
2	5.100	4.898	0.202	4.12	16	5.000	4.932	0.068	1.37
3	5.300	5.098	0.202	3.96	17	5.295	5.132	0.163	3.17
4	4.710	4.565	0.145	3.17	18	5.425	5.332	0.093	1.74
5	5.150	4.765	0.385	8.07	19	5.960	5.698	0.262	4.59
6	5.115	4.965	0.150	3.02	20	6.450	5.898	0.552	9.35
7	4.380	4.432	-0.052	-1.17	21	6.180	6.098	0.082	1.34
8	4.825	4.632	0.193	4.16	22	5.860	5.565	0.295	5.30

9	5.015	4.832	0.183	3.78	23	6.000	5.765	0.235	4.07
10	5.305	5.198	0.107	2.05	24	6.250	5.965	0.285	4.77
11	5.215	5.398	-0.183	-3.39	25	5.770	5.432	0.338	6.22
12	5.530	5.598	-0.068	-1.21	26	5.720	5.632	0.088	1.56
13	5.180	5.065	0.115	2.27	27	6.050	5.832	0.218	3.73
14	5.395	5.265	0.130	2.46	Average of error percentage = 3.14				

(P^= the predicted value, Residual Re=P⁻- P^)

4. Results and Discussion

In the first stage of this study (weld-on-plate), the application of the factorial design of experiments was used performing 27 welds. Tables (3a), (3b) and (3c) present the welding conditions and the measured values of the weld bead characteristics for 27 welds. Tables (4a), (4b) and (4c) present the values of the regression coefficients and their statistical significance for independent variables and that all the independent variables have significant effects on the multiple regression models according to T-test at a significant level of sig (pe)0.05; namely, welding current (I), arc voltage, and welding speed on the dependent variables; namely, bead width, bead height, and bead penetration using SPSS software. It is observed from table (5a) that the value of adjusted-R^2=0.959 for the bead width, this means that the independent variables, welding current, arc voltage, and welding speed could explain≈96% from the occurred changes in the bead width, and the rest ≈4% is referred to other factors, while the value of adjusted-R^2=0.973 for the bead height model as shown in table (5b), it indicates that the independent variables could explain ≈97% from the occurred changes in the bead height, and the rest =3% is referred to other factors. For the bead penetration model, the value of adjusted-R^2=0.917 as shown in table (5c), indicates that the independent variables could explain ≈92% from the occurred changes in the bead penetration, and the rest≈8% is referred to other factors. The presented results in table (6a) indicate that the average =1.19%. This means that the accuracy of the developed mathematical model =98.81% for the bead width. For the bead height, table (6b), the absolute value of the error percentage average=5.78%, this means that the accuracy of the developed mathematical model=94.22%. For the bead penetration, table (6c), the average of the error percentage=3.14, which means that the accuracy of the developed mathematical model=96.86%. It is clear from figures (5a), (5b) and (5c) that there is good accordance between the measured and the predicted values for the three characteristics of the weld bead, which supports the validity of the developed mathematical models.

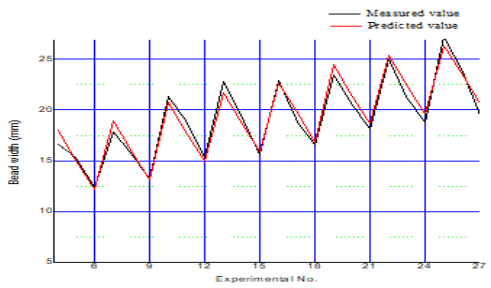

Figure 5a. the diagram representative of the measured and predicted values for bead width (W)

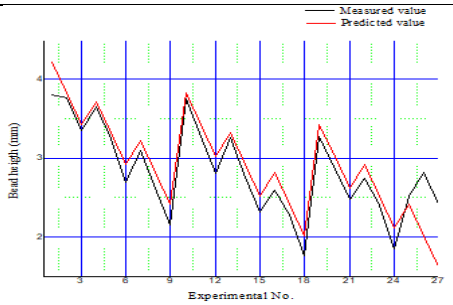

Figure 5b. the diagram representative of the measured and predicted values for bead height (H)

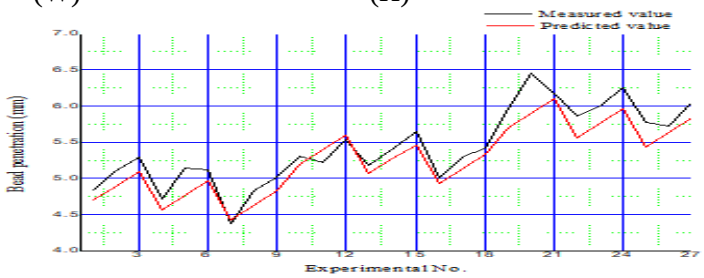

Figure 5 c. The diagram representative of the measured and predicted values for bead penetration **(P)**

It is clear from figures (6a), (6b) and (6c) that most points are located near the straight line. It is an indication that the normal distribution of errors. In other words, the assumption of the normal distribution is not violated.

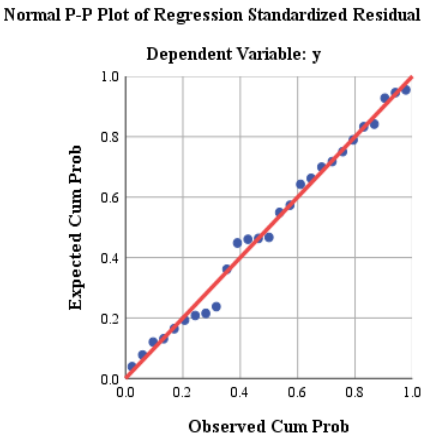

Figure 6a. Normality distributed errors for bead width (W)

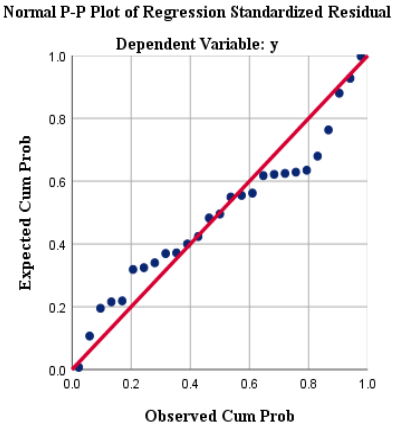

Figure 6b. Normality distributed errors for bead height (H)

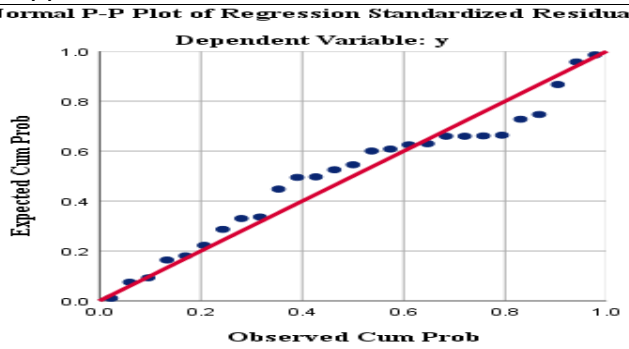

Figure 6a. Normality distributed errors for bead penetration (P).

5. Conclusions:

Based on experimental investigations and foregoing analysis, the following conclusions can be drawn:

1. The three levels factorial design was found to be an effective tool for quantifying the main and interaction effect of variables on the weld bead geometry dimensions.
2. The mathematical modeling was developed from the experimental data using the regression method applying the multiple linear regression equation using SPSS software.
3. The developed mathematical models in this study can be effectively used to predict the desired dimensions of weld bead geometry [bead width (W), bead height (H), bead penetration (P)] for any given welding conditions. These mathematical models can be used to optimize the processes and to develop an automatic control system for welding power sources.
4. The F-test indicated that the mathematical model as a whole is significant.
5. Validation of the models and comparison of the measured and predicted values for the weld bead geometry characteristics revealed that the average of the models accuracy is about 97%.
6. The output result from the effect of the process parameters on the weld bead geometry characteristics revealed that the bead width increases with the increase in the welding current and the arc voltage; and decreases with an increase in the welding speed. The bead height decreases with the increase in the welding current, arc voltage, and welding speed. The bead penetration increases with the increase in the welding current and speed; and decreases with an increase in the arc voltage.

6. References:

[1] Murugu, N. & Gunaraj, V. (2002). Prediction and Control of Weld Bead Geometry and Shape Relationships in Submerged Arc Welding of Pipes. Journal of Material Processing Technology, Vol. 168, pp.478-487.

[2] Karagolu, S. & Secgin, A. (2007). Sensitivity Analysis of Submerged Arc Welding Process Parameters. Journal of Material Processing Technology, Vol. 202, pp.500-507.

[3] Gunaraj, V. & Murugun, N. (2002). Prdiction of Heat Affected Zone Characteristics in Submerged Arc Welding of Structural Steel Pipes. Welding Journal, Vol. 5, pp. 94-98

[4] S.kumanan, j Edwin raja dhas &Gowthaman.K. (2007). Determination of Submerged Arc Welding Process Parameters Using Taguchi Method and Regression Analysis. Indian Journal of Engineering & Material Science, Vol. 14, pp. 177-183.

[5] Yang, L. J. &Bibby, M. J. &Chandel, R. S. (1993). An Analysis of Curvilinear Regression Equation for Modeling the Submerged Arc sWelding Process. . Journal of Material Processing Technology, Vol. 37, pp. 601-611.

SJST Surman Journal for Science and Technology | ISSN: E 2790-5721 P 2790-5713
Vol3, No.1, Dec_2021 , pp. 072 ~ 077

Design and Testing Neuro Networks Control System for Direct Current Machine

[1]Ali Mustafa Madi, [2]Ahmad Altaher Zuglem, [3]Jamal Abdeltayef Esghaer
[1,2,3]Department of Electrical Engineering, Surman College for Science and Technology, Surman, Libya
[1]amadi@scst.edu.ly
[2]ahmedzu@scst.edu.ly
[3]jamal-esghaer@scst.edu.ly

الملخص

تقدم الورقة طريقة تحكم ذكية تكيفية للتغلب على تأثيرات بعض العوامل غير المحددة وغير الملموسة التي يعاني منها محرك التيار المستمر. نستخدم شبكات عصبية ثلاثية الطبقات من خلال خوارزمية ((backpropagation (BP) لتحقيق تكتيكات التحكم الضبابي. نستخدم وحدة الخلايا العصبية من خلال التعلم الديناميكي لخوارزمية Hebb لتحقيق آلية التكيف. تعتمد المحاكاة على مجموعة أدوات MATLAB للشبكات العصبية مع simulink. تظهر نتائج المحاكاة أن طريقة التحكم الذكي التكيفية تمكن النظام من الحصول على أداء ديناميكي واستقرار جيد. تعمل الطريقة المقترحة على تطوير استخدام المحاكاة في مجال المحرك الكهربائي للتحكم التكيفي الذكي.

Abstract

The paper presents an adaptive intelligent control method to overcome effects of some indeterminate and undealt factors that a DC. drive is suffered. In the speed loop, we use a three-layer neural networks through a backpropagation (BP) algorithm out of line learning to realize the fuzzy-control tactics. We use unit neuron through Hebb algorithm on-line dynamic learning to realize adaptive mechanism. The simulation is based on a MATLAB neural networks toolbox with simulink. The results of the simulation show that adaptive intelligent control method enables the system to have good dynamic and stability performance. The proposed method develops the use of simulink in the field of electrical drive of adaptive intelligent control.

***Keywords**: DC motor, neural networks, and adaptive control.*

1. Introduction

The performance of a DC drive system is effected by some indeterminate and undeal factors, for example, the changes of moment of inertia, the change of amplificative multiple for controlled object and driving device, etc [1]. How does the Controller automatically change self-parameters to keep good performance of a system? One of many methods is to use adaptive intelligent control. In order to check correctness and effectiveness of the scheme, we use simulation experimentation. The senior languages BC or VC can be used for our simulation. Also, we can use MATLAB directly for simulation. The paper uses MATLAB6.0 to realize Simulation.

2. Scheme Design of Adaptive Intelligent Control

2.1 Adaptive Intelligent Control System

The construction of adaptive intelligent control for a DC drive system is shown in Fig.1.

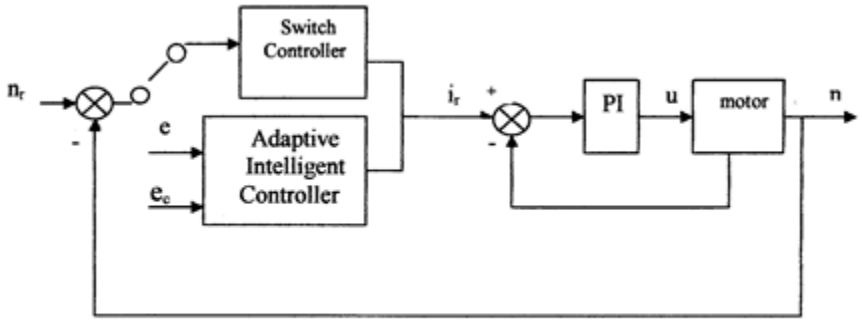

fig.1 DC drive System of adaptive intelligent control

Where, PI is the current regulator controller, the speed regulator is Combined by adaptive intelligent controller with switch controller. When the motor is in starting stage, the switch controller acts on. After the speed reaches a given value, adaptive intelligent controller acts on.

2.2 The Construction of Adaptive Intelligent Controller

The construction of adaptive intelligent controller is shown Fig.2.

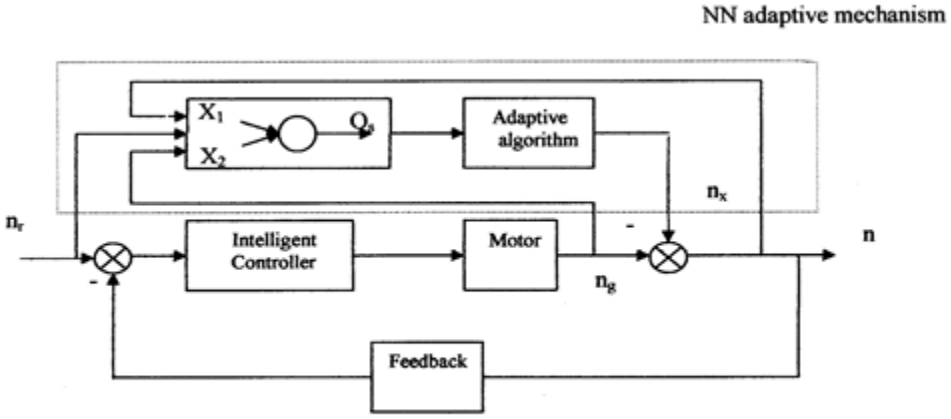

fig.2 Construction of adaptive intelligent controller

Where, intelligent controller is realized by fuzzy-neural networks controller (FNC),the adaptive mechanism consists of the neuron predictor, model-distinguish and adaptive algorithm.

2.3 Design of Adaptive Intelligent Controller

2.3.1 *intelligent controller*

Intelligent controller uses a three-layer front neural networks of 3-4-1 construction. Two inputs are the speed deviation (e) and the rate of the deviation (e_c). The output is current-giving value i_r. The neural networks determine their weight values through the BP algorithm out-line learning. The training data of neural networks are determinated by the system specifications of following performance and resist-disturbance performance through fuzzy control rules.

2.3.2 *Adaptive Mechanism*

Adaptive mechanism is the most characteristic part of all links for a DC drive system. Its main function is that the system can automatically change self-parameters and control rules to maintain high performance [2]. For example, if moment of inertia is changed in a large scope, or mathematical models of controlled object is changed, output speed keeps unchanged. This function is not able to realize if only depends on the control of front-series controller (intelligent controller). Because the summarization and inference of mankind experience, dividing language variables into group, selecting membership function of language variables, learning of neural networks, etc. Cannot avoid having large or small errors, during design and realization of intelligent controller. Therefore, control rules of intelligent controller cannot suit controlled object. After introduced neuron adaptive mechanism, as the system operates, the models-distinguish is more and more approximative controlled object. Control rules are also modified more and more suitale to controlled object. So that, the system itself is able to regulate to satisfactory working condition [3].

Since adaptive mechanism uninterruptedly distinguishes controlled object on-line during system operating, selecting the construction of neural networks is required to suit working performance on line learning and to learn fast. Therefore, the system uses the neuron dynamic learning to realize distinguishing function on line. The construction of neuron predictor and model-distinguish is shown in Fig.3.

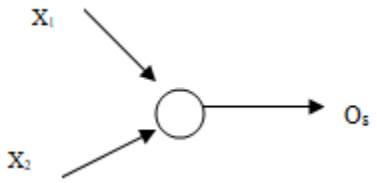

Fig.3. Neuron of adaptive mechanism

Where:

x_1, x_2: are the inputs of the neuron

O_s: is the output of the neuron.

We use linear simulative function. Its slope equals 0.1; its characteristic can be represented as:

$$\begin{aligned} &O_s=0.1(w_1x_1+w_2x_2)\\ &\text{if } \quad O_s>1 \quad \text{then } O_s=1\\ &\quad\ O_s<-1 \quad \text{then } O_s=-1 \end{aligned} \qquad (1)$$

Because the neuron of adaptive mechanism needs uninterruptedly learn on-line during system operation. The Hebb algorithm was selectd as a learning supervisory algorithm.

$$\begin{aligned} \Delta w_2 &= \eta_2(d-O_s)x_2O_s\\ \Delta w_1 &= \eta_1(d-O_s)x_1O_s\\ w_1 &= w_1+\Delta w_1\\ w_2 &= w_2+\Delta w_2 \end{aligned} \qquad (2)$$

Where: d is ideal output of the neuron i.e. teaching signal;η_1,η_2 are learning factor.

The following equations describe the learning factors:

Working process is divided into distinguishing and modifying processes. For example, during the k order distinguishing process, input sample of the neuron is the speed $n_g(k-1)$ without adaptive control and the speed n(k-1), expectance output is the speed n(k). We use [n_g (k-1), n(k-1), n(k)] as training samples and use supervisory Hebb learning algorithm to realize dynamic study. In equations (1) and (2), we use $x_1=n_g(k-1)$, $x_2=n(k-1)$, $d=n(k)$ instead. After dynamic learning, we can get modified weight values w_1 and w_2. Thus, the information of mathematic a models about controlled object are kept in these weight values.

Modifying process is divided into two stages. Thus are predictive stage and error reverse-transfer stage, (or adaptive algorithm stage). For example, in predictive stage of the k order the neuron is in positive calculating condition

$$n(k+1) = 0.1[w_1 n_g(k) + w_2 n(k)] \quad (3)$$

Where: $n_g(k)$ is output of front intelligent controller; $n(k)$ is the k-order speed output of the system.

In error-reverse transfer stage the output of adaptive mechanism is determinated according to predictive error between predictive speed $n(k+1)$ and speed giving value n_r.

$$n_x = -0.1(O_s - d)\, w_1 \quad (4)$$

Where: $O_s = n(k+1)$, it is predictive value,

$d = n_r$, it is speed giving value.

The final output of the K-order for adaptive intelligent controller is the sum of the k-order control value for front intelligent controller and the k-order output of adaptive mechanism.

$$n(k) = n_g(k) + n_x \quad (5)$$

In summary, neural networks adaptive mechanism regulates control rules according to modifying the output of front intelligent controller. Thus, the design of adaptive intelligent controller is completed well.

3. Simulation for realizing control tactics

The requirement of dynamic performance for a DC drive system is to be as high as the development of science and technology. Thus, modern control technology is widely used in the field [4]. Consequently, the paper uses adaptive intelligent control. The Simulink and neural networks toolbox based on MATLAB6.0 plat form provide better environment for building models and simulation of complex and high-performance dynamic system.

3.1 Simulation Construction Drawing

A block diagram of the system simulation construction drawing of adaptive intelligent control in simulink is shown in Fig.4.

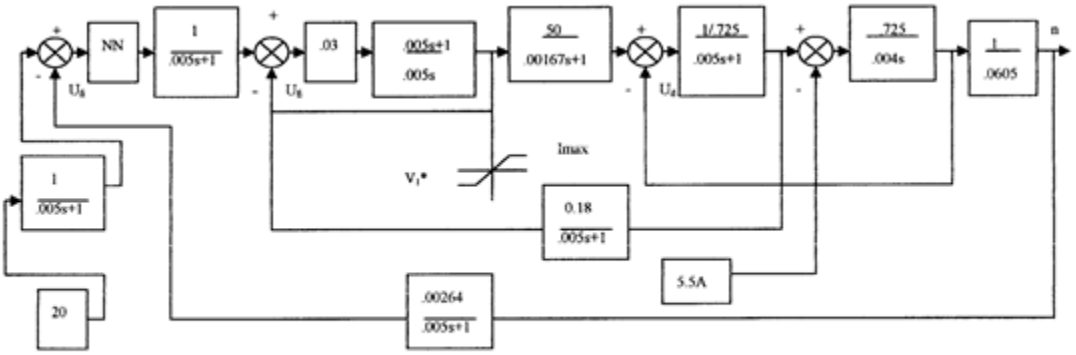

Fig.4 System simulation construction drawing

Building adaptive intelligent controller needs to design through neural networks toolbox and transfers into the model block in simulink environment [5]. First, we use net= newff function to build three-layers front Bp networks of an intelligent controller, then we sequentially need to use net. train Parma. goal to establish training objective error, to use net=init (net), net=train (net, p, t) (where p,t is input and output sample vector data) to train neural networks. After finishing training,

we use sim function and sample data to simulate trained neural networks. Finally, we use gensim function to transfer designed object of neural networks into simulink type.
In the same way, we can build the neuron of adaptive mechanism and transfer it into simulink type. Then, we take simulink types of intelligent controller and adaptive mechanism to build subsystem in simulink , as neural networks model unit in Fig.4.

3.2 Simulation Results

We carried out the simulation corresponding to general PI control and adaptive intelligent control for speed controller under the following situations: Motor parameter (as the resistance) changes from Ra to (1+10%) Ra, supply voltage changes from rated value U_N to 50% U_N, the load of the motor suddly changes from zero to rated value, speed giving value equals 3800rpm.
One Part of simulation curves are shown in Fig.5 and Fig.6

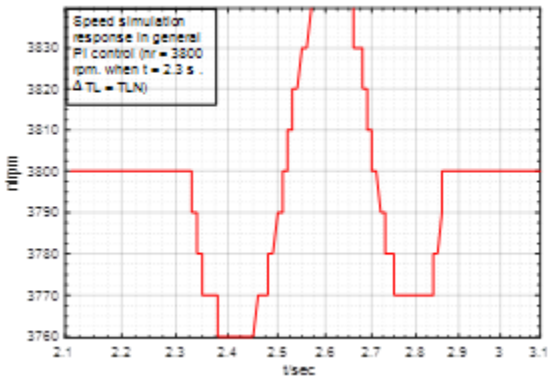

Fig.5. Speed simulation response in general PI control (n_r = 3800 rpm, when t = 2.3 s , $\Delta T_L = T_{LN}$)

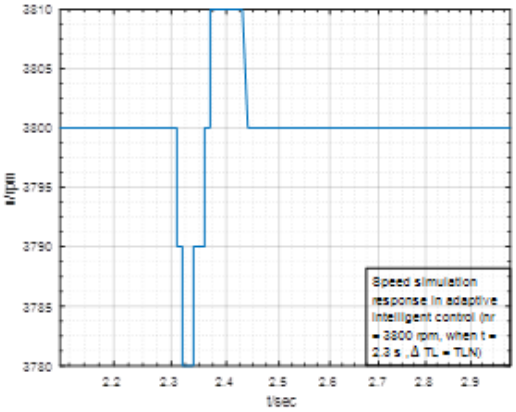

Fig.6. Speed simulation response in adaptive intelligent control (n_r = 3800 rpm, when t = 2.3 s , $\Delta T_L = T_{LN}$)

Table 1 shows a comparison between PI control and adaptive intelligent control

Table 1. Anti-interference Performance Comparison

	PI control		Adaptiv Intelligent control	
	ΔCmax(rpm)	t_f (s)	ΔCmax(rpm)	t_f (s)
ΔTL = TLN	28 rpm	0.49	9	0.19
ΔUd = ½UN	10.36 rpm	0.49	4	0.1

Where: ΔC_{max} is maximum dynamic speed drop, t_f is recovery time

The results of the simulation show that the speed of the motor can be kept in stability level when operating conditions of the motor change. After, we use adaptive intelligent control. The system has better adaptive stability.

The reason behind that is in PI control the parameters of speed regulator cannot be changed with the changes of operating condition. While, in adaptive control they can automatically change. Because neural network has this function which were trained before they are used as speed regulator. Except for this reason, attached component nx (refer to fig.2) can compensate the change of the speed deeply.

4 Conclusion

In this paper, neural networks toolbox and a simulink are combined to successfully carry out the simulation of an adaptive intelligent control method for a DC motor drive system.

The results of the experiments conducted in this research show that the adaptive intelligent control method used in a DC motor drive system has a high performance and the system keeps in a steady-state.

5 Reference

[1] Fan Zheng-qiao Ma shutong, New control method of adaptive fuzzy-neural networks for Brush less D.C. Motor, Journal of Beijing University Aeronautics and Astronautics Vo1.26 No.1, 2001,1: 34-37.

[2] Neto, João, and Gustavo Araujo de Andrade. "Design of Decision Making Unit for Neuro-fuzzy Control of Dynamic Systems." 2011 UkSim 13th International Conference on Computer Modelling and Simulation. IEEE, 2011.

[3] Sigeru Omatu, etc, Neuro-Control and its applications, Advances in industrial control, springer-Verlag London Limited 1996.

[4] Y.S. Dung, C.M. Liaw, and M . S. Ouyang, "Adaptive speed control for induction motor drives using neural networks", IEEE Trans. On Industrial Electronics, vol. 42,no.1,Feb.1995.

[5] Jamal, Ali, Altayef and jalal. Self-correct intelligent control based on Fuzzy-Neural Networks, International Science and Technology Journal, Vol.23, P: 395-406, Oct: 2020.

SJST Surman Journal for Science and Technology | ISSN: E 2790-5721 P 2790-5713
Vol3, No.1, Dec_2021 , pp. 078 ~ 093

Molecular Systematic Study Of The Genus *Fagonia* L. In Libya

[1]Wafaa K. Taia, [2]Salem A. Hassan, [3]Manaser M. Ibrahim, [4]Sanaa A. Riad, [5]Adel D. El Werfalyi
[1,3]Botany and Microbiology Department, Faculty of Science, Alexandria University, Alexandria, Egypt.
[2]Biology Department (Botany), Faculty of Science, EL Mergib University, Al-Komus, Libya.
[4]Genetics Department, faculty of Agriculture, Alexandria University, Alexandria, Egypt.
[5]Biology Department (Botany), Faculty Arts and Science, EL MergibUniversity, Musallata, Libya.

taiataxonomy86@gmail.com[1]
salemtaxonomy2@gmail.com[2]
manaser99@yahoo.com[3]
sanaaahmed53@hotmail.com[4]
adeldaw@yahoo.com[5]

ABSTRACT

Molecular analyses of ten *Fagonia* species grown widely in the Libyan Desert have been carried to investigate the taxonomic relationship between them and to evaluate the genetic distances among them. To achieve our aim RAPD technique carried out through six arbitrary primers. Comparing with ladder DNA marker, the obtained data were computerized and analyzed using SYSTAT program. The studied species are *F. arabica* L., *F. bruguieri* DC, *F. cretica* L., *F.glutinosa* Delile, *F. indica* Burm., *F. microphylla* Pomel, *F. sinaica* Boiss, *F. schweinfurthii* Hadidi, *F. tenuifolia* Steud. and *F.thebaica* Boiss. The genetic variability among the ten *Fagonia* species estimated using the DNA protein sequencing obtained from primer 1, indicates that *F. indica* and *F. glutinosa* are very closely related while *F.cretica*, *F.microphylla* and *F.arabica* related to each other and gathered together in another group. The dendrograms of the six primers via UPGMA method according to RAPD finger printing gave two clusters with homology percentage 9%. The first one has *F.microphylla* and *F.schweinfurthii* at 50% similarity index. The second cluster divided into two sub-clusters. The first one included three *Fagonia* species (*F.cretica; F.indica* and *F.glutinosa*). The second sub-cluster subdivided into two other sub-clusters. The first one contained *F.arabica* and *F.bruguieri* at 50% similarity index. The other sub-cluster gathered *F.sinaica* and *F.thebaica* and, both species in genetic relationship with *F.tenuifolia*.

Key words: DNA sequencing - *Fagonia*- Libya- Molecular analyses- Taxonomy- RAPD.

1. INTRODUCTION

Genus *Fagonia* is a member of Zygophyllaceae, subfamily Zygophiloideae which is included in the eurosid I clade (APG III, 2009). The genus comprises Thirty-five species all over the world (Plant of the World, 2018). In Libya, there are only ten species growing in different phyto-geographical regions (Abdul Ghafoor, 1977). *Fagonia* species are generally spiked under-hedge, erect herbs, some species covered by glandular hairs, branches malign, stem terete, striate and glabrous. Leaves simple or compound, 1-3 foliate; petioles from 3 - 30 mm long, profoundly striate, extremely thin; stipules 2 sets of sharp thin thistles (Farheen et al, 2015; Puri and Bhandari,

2014, Taia et al., 2015). The taxonomy of the genus is very difficult mainly due to a high degree of phenotypic plasticity and adaptations to climatic conditions (Zohary 1972; Danin 1996). Accordingly the taxonomy of the genus has been faced with many proposals. From the most important work in the taxonomy of the genus is that done by Ozenda and Quézel (1956) who grouped the North African *Fagonia* species into four natural groups, which can be considered as sections according to Melbourne System of Nomenclature (2012). This division based mainly on vegetative morphological characters, the Quezel four groups of *Fagonia* is (1) *F. kahirina-cretica*-flamandii, (2) *F. arabica-bruguieri*, (3) *F. glutinosa-latifolia*, and (4) *F. microphylla*. Also, the works done by El Hadidi (1966) and Batanouny and Batanouny (1970) add another contribution to the taxonomy of the genus. They grouped the 18 Egyptian species of *Fagonia* into three groups based on anatomical structures; they constructed an artificial key for their identification based on both morphological and anatomical characters. Taia et al. (2015, 2016, 2017 & 2021) studied the Libyan species in different aspects to clarify the relationships between them. They found that the morphological and floral characters can be of use in solving the taxonomical confussion between the species.

After all the studies done, the delimitation of species in *Fagonia* is still in need to more investigations for being notoriously difficult and confusing. This is caused by the great variation in most morphological characters within many species and between individuals of the same species grown in different habitats. The first complete modern treatment of the genus has been done by (Beier, 2005). His work was mainly concerning the geographical distribution of the African species, their center of origin and distribution. According to this revision, *Fagonia* considered a genus of 34 species, distributed mainly in warm and arid areas all over the world, except Australia, with great diversity of species in the Horn of Africa region and Baja California. Genus *Fagonia* is one of the critical genera of the Zygophyllaceae family, as mentioned. Many species are very closely allied and are linked by intermediate forms, which make a species delimitation rather difficult. Previous works on the genus based mainly on vegetative, floral and anatomical characters. Palynological investigations are few and when done it did not give important suggestion for the division of the genus, For that, this study carried to clarify the taxonomical relationship within the *Fagonia* species grown in Libyan desert by molecular analysis.

2. MATERIALS AND METHODS

Ten species belonging to genus *Fagonia* (*F.arabica*L., *F.bruguieri*DC., *F.cretica*L., *F.glutinosa*Delile., *F.indica*Burm, *F.schweinfurthii*Hadidi, *F.sinaica*L., *F. microphylla*, *F.tenuifolia*Steud., *and F.thebaica*Boiss.) were subjected in this study. These species grown mainly in sandy or gravelly habitats and tolerate with soil salinity. The specimens collected through field trips during 2014 till 2017, to different locations covering most of the habitats in Libya. The study area extends from the eastern plains (Al-Gabal Al-Akhdar) in the east to GabalNaffusah (Nalut and Ghadames) in the west to Sebha and El-Kufra in south, the name of 20 visited locations as shown in (Table1) (Map 1) during the period from 2014 till 2017. Ten individuals from each species have been collected for herbarium preparations and allocated at EL-

Mergib university herbaria. Leaves from each species were gathered, put in paper bags for the molecular analyses.

Map 1. A sataliate google earth map showing detailed sector and the distribution of the diffreent locations in the study area in Libya (■ and arrows: Locations, ●: Cities)

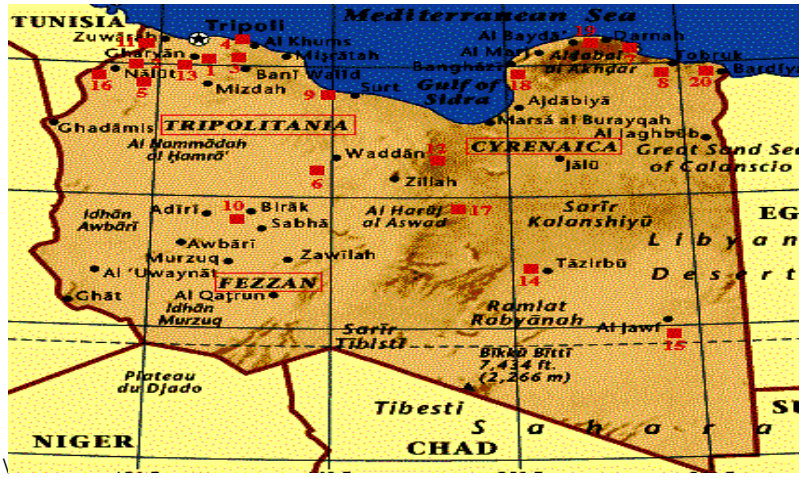

Table 1. Name of 20 locations of the collected *Fagonia* species in Libya.

No	Location	Region	No	Location	Region
1	Gharian ,Gebel Nafousa	West	11	Wadi El-Aital	west
2	Giado,GebelNafousa	West	12	Sokna	Middle
3	Mesallata	west	13	Tagrenna, Jefren	West
4	Alkhums	west	14	Tazerbo	South
5	WadiMalah, Nalut	west	15	Gebel Uwainat	South
6	Hun	Middle	16	Wazen	West
7	WadiDerna	East	17	El-Soda mountain	South
8	Tobruk	East	18	Benghazi, Teka	East
9	Weshka	Middle	19	Al-Abidaa, Shahat, Ras El-Hellal	East
10	Brak, Sebha	South	20	Musaid	East

- **Extraction of genomic DNA**

Genomic DNAs of the ten *Fagonia* species were prepared according to Omega Co. (USA.LMt.) manufacturer protocol as the following:

For each 100 mg leaf powders, 550 µL of lysis buffer solution were added; shacked gently; incubated for 30 min on ice; centrifuged at 1200 rpm for 10 min at 4°C and the supernatant was removed. The pellet was re-suspended in 1 ml of lysis buffer; centrifuged at 1200 rpm for 10 min at 4°C and the supernatant was removed. The pellet was resuspended in 0.5 ml SE-buffer and centrifuged at 1200 rpm for 10 minutes at 4°C. The supernatant was removed and the pellet was resuspended in 1 ml SE-buffer. 40 µl proteinase K (10 mg/ml) and 250 µl 20% SDS were added; shaked gently and incubated overnight at 37°C in a water bath. Then, 5 ml SE-buffer and 10 ml

phenol were added; shaked by hand for 10 min and centrifuged at 3000 rpm for 5 min at 10°C. The supernatant was transferred into a new tube; 1 ml phenol/chloroform/ isoamyl alcohol (25:24:1) was added; shaked by hand for 10 min and centrifuged at 3000 rpm for 5 min at 10°C. The supernatant was transferred again into a new tube; 1 ml chloroform/ isoamyl alcohol (24:1) was added; shake by hand for 10 min and centrifuged at 3000 rpm for 5 min at 10°C. The supernatant was transferred into a new tube; 100 µl of 3 M sodium acetate (pH 5.2) and 10 ml isopropanol were added and shaked gently until the DNA precipitated. Finally, the DNA was captured and transferred into a new tube by a glass pipette; washed with 70% ethanol; dissolved in 0.1 ml TE-buffer (10mM Tris-HCl and 1mM EDTA-pH8) overnight at 4°C on a rotating shaker and stored at the same temperature until use.

- **Random Amplifid Polymorphic DNA (RAPD) procedure**

Ready-To-Go RAPD Analysis Beads (GE Healthcare Life Sciences, 27-9502-01, with primers) was used for the Random Amplified Polymorphic DNA (RAPD) technique according to manufacturer protocol as the following:

- **RAPD -PCR amplification**

Using six arbitrary 10 mer primers Table (2), the total genomic DNAs were amplified through GeneAmpPolymerase Chain Reaction (PCR) system cycler. The PCR reaction components are shown in Table (3). The PCR program was performed in a thermal cycler programmed at 40 cycles. Each cycle consisted of denaturation at 93°C for 30 sec followed by annealing at 51°C for 30 sec and extension at 72°C for 30 sec. There was an initial delay for 15 min at 95°C at the beginning of the first cycle and 10 min delay at 72°C in the end of the last cycle as a post extension step. The product was stored at –20 or 4°C.

Table 2. Arbitrary primers used for Fagonia genomic DNAs amplifications

Number of primer	Nucleotide sequence (5′- 3′)
1	GGTGCGGGAA
2	GTTTCGCTCC
3	GTAGACCCGT
4	AAGAGCCCGT
5	AACGCGCAAC
6	CCCGTCAGCA

Table 3. Master Mix components for PCR reactions

Master Mix component	Amount	Final concentration
Sterile nuclease free water	17.8 µl	
10x Taq buffer	2.5 µl	1.0 x
4mM PCR nucleotide mix	2.5 µl	0.2 mM
Primer (5pmol /µl)	1.0 µl	5.0 pmol
Taq DNA polymerase (5u /µl)	0.2 µl	1.0 u
DNA extracted sample (50ng /µl)	1.0 µl	25.0 ng
Total	**25.0 µl**	

- **Agarose gel electrophoresis and detection of the amplified products**

5 µl of each PCR products were separated on agarose gel electrophoresis using 1.5% (w/v) agarose in 0.5x TBE buffer. Electrophoresis was performed at 80 Volt for 100 min in 0.5x TBE buffer (50 ml of 10X TBE stock solution {Tris-base (108g); Boric acid (55g) and EDTA -pH 8 (9.3g) in 1 L distilled H_2O} was added to 950 ml distilled H_2O) as running buffer. Then, the gel was stained with 0.5µg/ cm^3 (w/v) ethidium bromide solution for 30 min followed by 20 min destain in distilled water. Finally, the gel was photographed by gel documentation system and the lengthof each band was estimated usingthe DNA ladder marker.

- **Data analysis**

Gel documentation system (Geldoc-it, UVP, England) was applied for data analysis using Totallab analysis software, ww.totallab.com, (Ver.1.0.1).

3. RESULTS

Random amplified polymorphic DNA (RAPD) analysis:

In order to evaluate the genetic distances among the ten*Fagonia* species understudy, RAPD technique was employed through six arbitrary primers. Comparing with ladder DNA marker, the obtained data were computerized and analyzed.

For each primer, the numbers and lengths of the reproducible fragments varied from species to another (Figure 1 and Tables 4). The maximum number of the amplified bands (9) was recorded for *Fagonia thebaica* with primer-5. The DNA lengths of these fragments ranged from 1030.769 to 88.000bp. On the contrary, primers 1 and 2 amplified only 2 bands for *F. sinaica* (769.884 and 306.473bp) and *F. cretica* (339.142 and 149.588bp). The largest DNA fragment lengh (1033.333bp) was recorded for *F.tenuifolia* with primer-4 and the lowest one (76.000bp) was for *F.sinaica* with primer-5.

Also, the computraized RAPD data revealed that, the amplified fragments ranged from 34 for primer-3 to 62 for primer-5 with total of 268 reproducible fragments (Table 5 and Figure 2). The polymorphic bands were 107 (39.9% polymorphism). The minimum number of the polymorphic fragments (10) was indicated for primer-2 with polymorphism percentage 25.6%. In contrast, primer-5 exhibited the maximum number of polymorphic bands (41) and polymorphism (66.1%). Intermediate valus were illustrated with the other primers. The polymorphic fragments for primers-1; 3; 4 and 6 were 13; 14; 15 and 14 with 34.2; 41.1; 35.7 and 26.4% polymorphism, respectively.

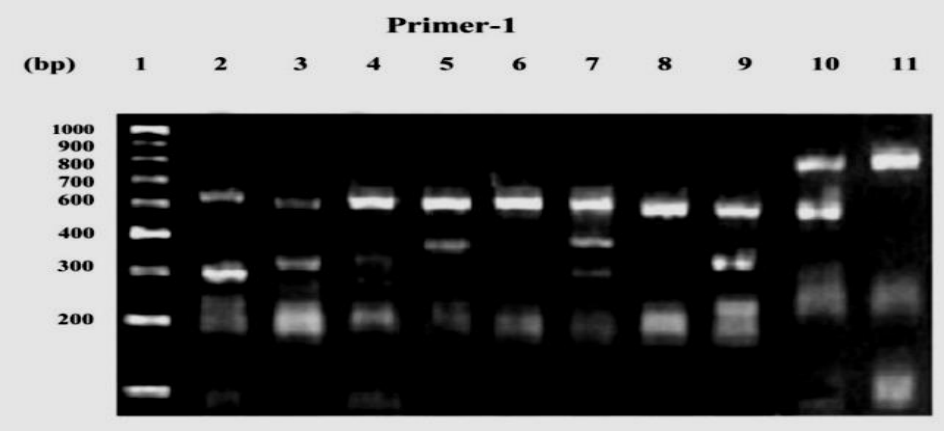
Primer-1
(bp) 1 2 3 4 5 6 7 8 9 10 11
1000
900
800
700
600
400
300
200

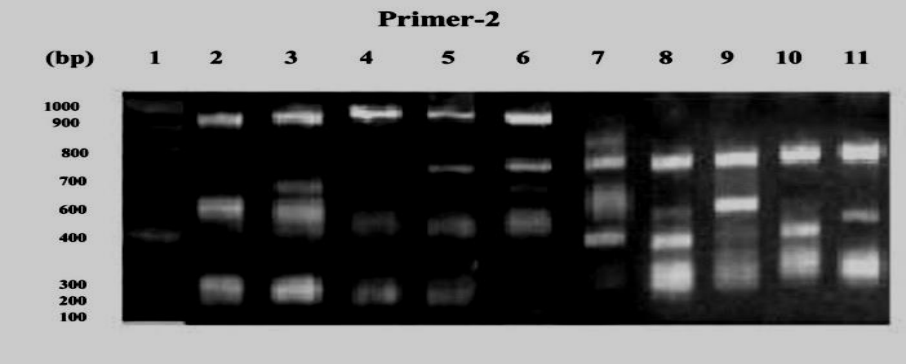
Primer-2
(bp) 1 2 3 4 5 6 7 8 9 10 11
1000
900
800
700
600
400
300
200
100

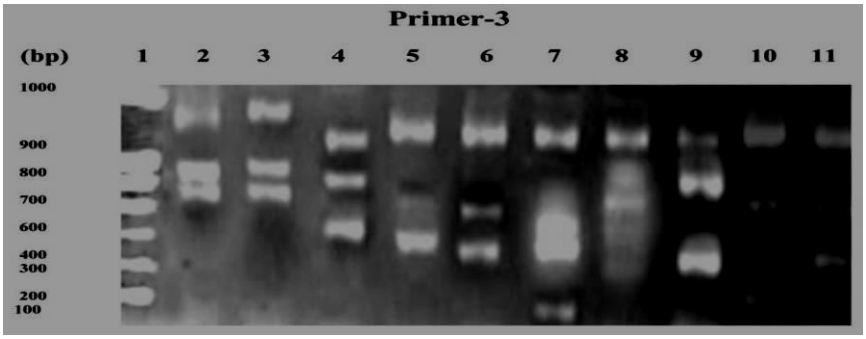
Primer-3
(bp) 1 2 3 4 5 6 7 8 9 10 11
1000
900
800
700
600
400
300
200
100

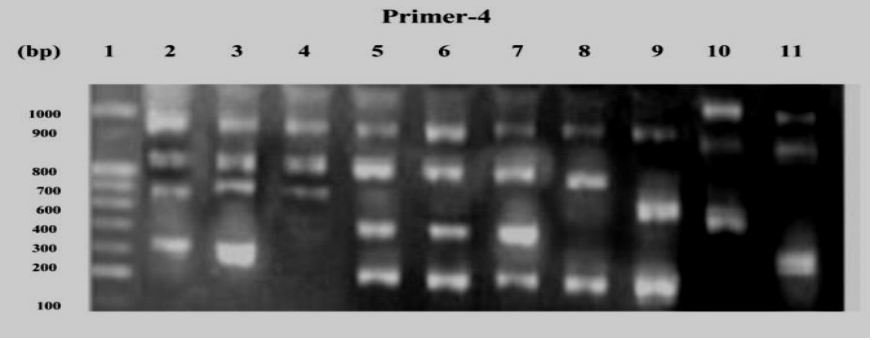
Primer-4
(bp) 1 2 3 4 5 6 7 8 9 10 11
1000
900
800
700
600
400
300
200
100

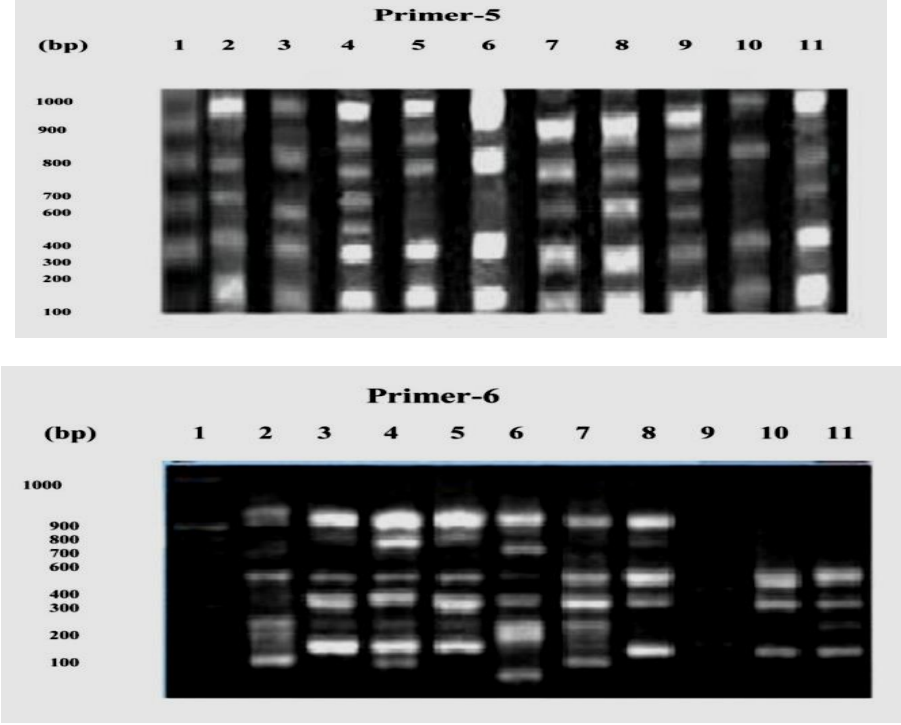

Figure1. Photographs illustrating RAPD products for ten *Fagonia* species using six randomly primers. Lane 1: ladder DNA marker with fragments lengths in base pairs (bp); Lanes 2-11: *Fagonia arabica; Fagonia bruguieri; Fagonia cretica; Fagonia indica; Fagonia glutinosa; Fagonia microphylla; Fagonia sinaica; Fagonia schweinfurthii; Fagonia tenuifolia* and *Fagonia thebaica*, respectively.

Table4. Numbers and lengths of the reproducible fragments for ten *Fagonia* species using primers 1 to 6:

Primer-1

Species	Numbers of fragments	Fragments lengths (bp)
Fagonia arabica	5	816.496 – 28.571
F. bruguieri	4	784.604 – 305.649
F. cretica	5	808.088 – 335.282
F. indica	3	800.000 – 351.282
F. glutinosa	3	816.496 – 305.649
F. microphylla	4	808.088 – 314.608
F. sinaica	2	769.884 - 306.473
F. schweinfurthii	4	769.884 – 306.473
F. tenuifolia	4	1014. 286 – 553.291
F. thebaica	4	984.944 – 100.000
Total	**38**	

Primer-2

Species	Numbers of fragments	Fragments lengths (bp)
Fagonia arabica	6	970.327 – 139.980
F. bruguieri	4	536.609 – 139.980
F. cretica	2	339.142 – 149.588
F. indica	3	632.243 – 158.937
F. glutinosa	3	632.243 – 356.681
F. microphylla	4	818.413 – 290.597
F. sinaica	5	700.000 – 206.729
F. schweinfurthii	4	700.000 -218.640
F. tenuifolia	4	736.608 – 237.373
F. thebaica	4	725.542 – 228.750
Total	**39**	

Primer-3

Species	Numbers of fragments	Fragments lengths (bp)
Fagonia arabica	3	996.316 – 749.568
F. bruguieri	3	1000.000 – 736.673
F. cretica	3	967.981 – 619.900
F. indica	4	992.344 – 577.093
F. glutinosa	3	992.344 -446.694
F. microphylla	4	987.579 – 85.714
F. sinaica	4	987.579 – 676.136
F. schweinfurthii	3	971.840 -490.312
F. tenuifolia	4	975.452 -169.118
F. thebaica	3	957.452 -469.280
Total	**34**	

Primer-4

Species	Numbers of fragments	Fragments lengths (bp)
Fagonia arabica	4	936.145 – 411.427
F. bruguieri	5	936.145 – 343.964
F. cretica	4	936.145 – 630.555
F. indica	5	913.014 – 187.799
F. glutinosa	4	894.345 – 157.593
F. microphylla	4	906.233 – 166.681
F. sinaica	3	920.292 – 166.681
F. schweinfurthii	4	889.219 – 135.170
F. tenuifolia	4	1033.333 – 483.065
F. thebaica	5	981.009 – 242.313
Tolal	**42**	

Primer-5

Species	Numbers of fragments	Fragments lengths (bp)
Fagonia arabica	5	1000.000 – 119.951
F. bruguieri	5	1007.692 – 131.926
F. cretica	8	925.996 – 100.000
F. indica	5	982.627 – 100.000
F. glutinosa	7	1030.769 – 127.934
F. microphylla	6	857.248 – 88.000
F. sinaica	7	876.967 – 76.000
F. schweinfurthii	6	880.816 – 80.000
F. tenuifolia	4	982.627 – 139.914
F. thebaica	9	1030.769 – 88.000
Total	**62**	

Primer-6

Species	Numbers of fragments	Fragments length (bp)
Fagonia arabica	8	967.797 – 153.737
F. bruguieri	5	926.442 – 214.831
F. cretica	6	933.972 -189.473
F. indica	5	909.486 – 228.385
F. glutinosa	7	944.168 – 142.721
F. microphylla	7	922.445 – 153.737
F. sinaica	5	930.282 – 204.660
F. schweinfurthii	3	707.991 – 221.857
F. tenuifolia	3	522.397 -210.979
F. thebaica	4	555.991 – 202.379
Total	**53**	

Table5. Numbers of the amplified and polymorphic fragments as well as polymorphism percentage for ten *Fagonia* species using six randomly primers.

Primer	Total number of amplified fragment	Number of polymorphic fragment	Percentage of polymorphism (%)
1	38	13	34.2
2	39	10	25.6
3	34	14	41.1
4	42	15	35.7
5	62	41	66.1
6	53	14	26.4
Total	268	107	39.9

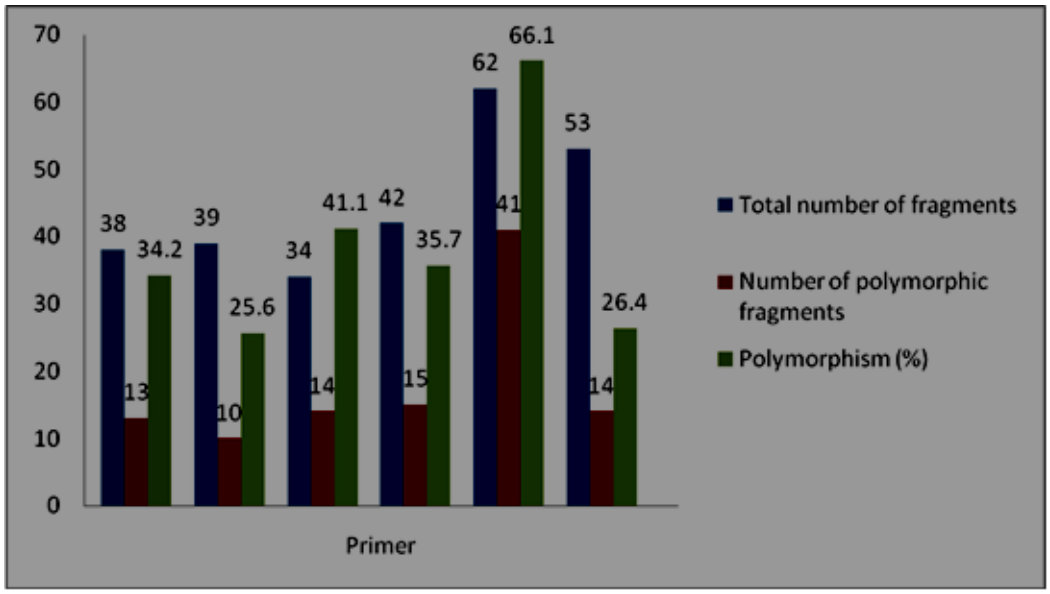

Figure2. Histogram illustrating the computerized RAPD results of ten *Fagonia* species using six arbitrary primers.

The phylogenetic relationships among *Fagonia*species baesd on RAPD data:

The genetic variability among the ten *Fagonia* species were estimated using the DNA fingerprinting data of each primer (Figure 3) and all primers (Figure 4) via UPGMA method.

The dendrogram based on primer-1 demonstrated two clusters with homogeneity < 5%. The first one contained only *F. bruguieri*. The second cluster divided into two subclusters with similarity 7%. The first subcluster grouped five species. The most related species were *F. indica* and *F. glutinosa* with homogeneity 69% and, both species had homology percentages 51; 37 and 29% with *F.cretica*, *F. microphylla* and *F. arabica*, respectively. The second subcluster consisted of four species. The similarity of *F. sinaica* and *F. schweinfurthii* was 69% as well as *F. tenuifolia* and *F. thebaica* had relative homogeneity 51%.

Two main clusters were also detected for primer-2 with homology percentage <10%. The first one included *F. microphylla; F. sinaica* and *F. schweinfurthii*. *F. sinaica* and *F. schweinfurthii* had homogeneity 67% and, both species were similar to *Fagonia microphylla* with 36%. The other cluster divided into two subclusters with homology percentage 11%. The first one included *F. arabica, F. bruguieri, F. cretica, F. indica* and *F. glutinosa*. The most related species were *F. cretica* and *F.indica* with homogeneity 81% and, both species had similarity 64 and 55% with *F.bruguieri* and *F. glutinosa*, respectively. All the four species had relative homogeneity 23% with *Fagonia arabica*. The second subcluster contained *F. tenuifolia* and *F.thebaica* with homology percentage 76%.

The dendrogram based on primer-3 exhibited two main clusters with similarity 5%. Each cluster divided into two groups forming finally four subclusters. The first subclusterhad

homogeneity 9% with the second one and included only *F. microphylla*. The second cluster grouped three species. *F. arabica* and *F.bruguieri* related to each other with homology percentage 34% and, both species similar to *F. sinaica* with 29%. The relative homogeneity betwee the third and fourth subclusters was 11%. The third subcluster consisted of *F. indica* and *F. glutinosa* with similarity 59%. The three species *F. cretica, F. schweinfurthii* and *F. thebaica* of the fourth subcluster had homology percentage 35% and, were similar to *F. tenuifolia* with 25%.

Three clusters were detected for primer-4. The first one divided into two subclusters with homogeniety 23%. The first subcluster included *F. bruguieri* and *F. cretica* with homology percentage 72% and, both species were similar to *F. arabica* with 35%. Four species were grouped in the second subcluster. *F.glutinosa* and *F. microphylla* were closly related with similarity 80% and hadhomology percentages 52 and 42% with *F. sinaica* and *F. indica*, respectively. The second cluster was related to the first one with homogeniety 20% and included only *F. schweinfurthii.* The genetic relationship between the third and the second clusters was 19% and, the third one cosisted of *F. tenuifolia* and *F. thebaica* with similarity 34%.

For primer-5, two clusters were indicated with homology percentage 5%. The first one diveded into two subclusters with similarity 9%. The first subcluster grouped *Fagonia indica* and *Fagonia sinaica* with homogeneity 34% and, both species were similar to *Fagonia cretica* with 22%. The second subcluster included *Fagonia schweinfurthii* and *Fagonia tenuifolia* with homology percentage 21%. The second cluster divided also into two subclusters with similarity 15%. *F.arabica* and *F. glutinosa* grouped in the first subcluster with homogeniety 33% and, both species were related to *F.bruguieri* with homology percentage 26%. The second subcluster consisted of *F.microphylla* and *F. thebaica* with 26% similarty.

Primer-6 exhibited two main clusters with homogeneity < 5%. The first one grouped *F.bruguieri* and *F. indica* with genetic homology 40% and, both species were similar to *F. sinaica* with 25%. The second cluster divided into two subclusters with homology percentage 5% and, the first subcluster contained only *F. schweinfurthii.* The second one subdivided into two sub-subcluster. The first one included only *F. thebaica* with similarity 26% and, five species were grouped in the second sub-subcluster. The most related species were *F. arabica* and *F. microphylla* with homology percntage 53%. *F. cretica* and *F. glutinosa* were also similar with 45%. The four species were related to *F.thebaica* with 31% similarity.

Primer-1

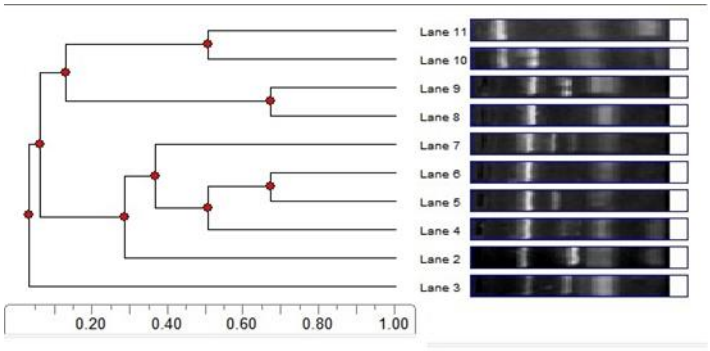

Primer-2

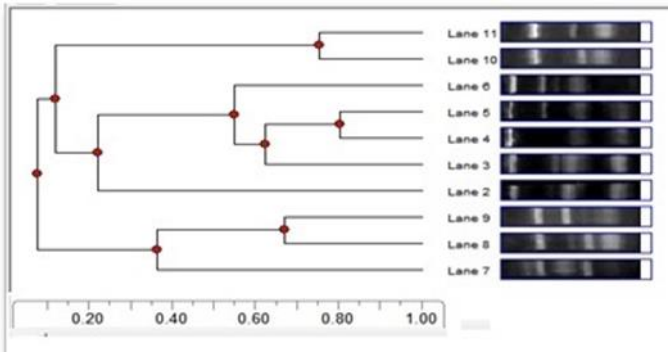

Primer-3

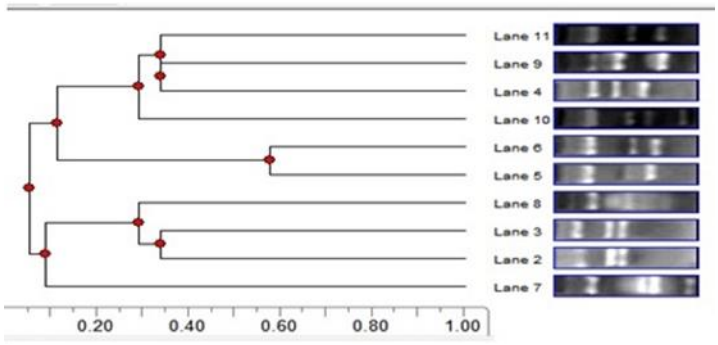

Primer-4

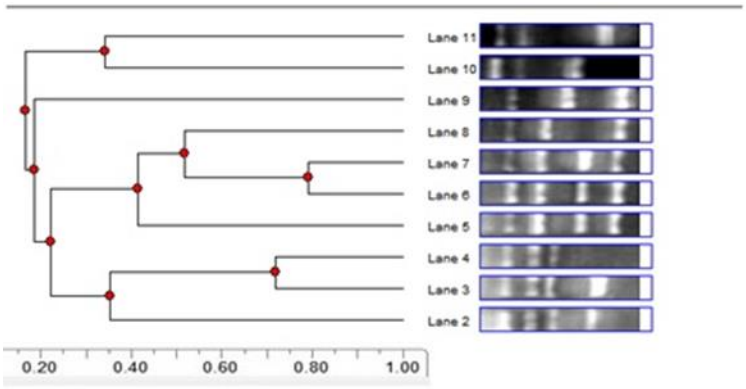

Primer-5

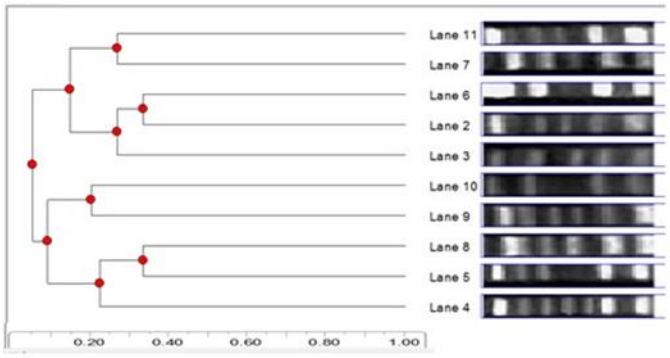

Primer-6

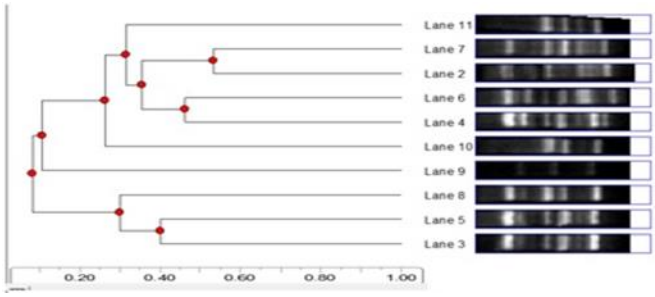

Fig.3. Dendrograms presenting the phyllogenetic relationships among the ten *Fagonia* species based on each primer data. Lanes 2-11: *Fagonia arabica; Fagonia bruguieri; Fagonia cretica; Fagonia indica; Fagonia glutinosa; Fagonia microphylla; Fagonia sinaica; Fagonia schweinfurthii; Fagonia tenuifolia and Fagonia thebaica*, respectively.

Figure (4) presents the dendrogram of all primers via UPGMA method according to RAPD fingerprinting. Two clusters with homology percentage 9% were indicated. The first one contained *F. microphylla* and *F. schweinfurthii* with similarity 50%. The second cluster divided into two subclusters. The first one included three *Fagonia* species (*F. cretica*, *F. indica* and *F. glutinosa*). The homogeniety between *Fagonia cretica* and *F. indica* was 50% and, both species related to *F. glutinosa* with 40%. The second subcluster subdivided into two sub-subclusters. The first one contained *F.arabica* and *F. bruguieri* with 50% similarity. The other sub-subcluster

grouped *F. sinaica* and *F. thebaica* with homogeniety 50% and, both species in genetic relatioship 40% with *F. tenuifolia.*

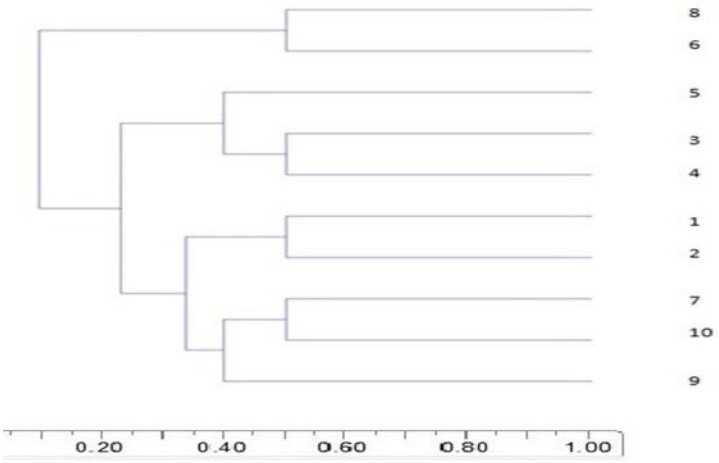

Fig. 4. Dendrogram showing the phyllogenetic relationships among the ten *Fagonia* species based on all primers data. 1-10: *F. arabica, F. bruguieri, F. cretica; F. indica, F. glutinosa, F. microphylla, F. sinaica, F. schweinfurthii, F. tenuifolia and F.thebaica*, respectively.

4. DISCUSSION

Genus *Fagonia* belongs to subfamily Zygophylloideae which is the largest subfamily of the Zygophyllaceae and consists of six genera; *Zygophyllum, Fagonia, Augea, Roepera, Tetraena* and *Melocarpum* (Beier et al., 2003, Bellstedt et al., 2008). Genus *Fagonia* considered as one of the most difficult genera in the circumscription of the species belonging to it. This genus is objected to many taxonomic investigations to clarify the most significant relations between its species. From the most important taxonomical studies are those of Quezel (1956), El-Hadidi (1966), Batanony and Batonony (1970) and Taia (2015, 2016, 2017 & 2021). The morphological, floral and anatomical investigations done by (Taia *et al*., 2015, 2016 & 2017) clarified that the vegetative characters can help in identifying some species. They clarified that the spiny stipules beside the leaf micro-morphological characters can be of help in the identification of some species. From the most noticeable character which can be important taxonomic one in grouping of the species is the presence of the knee-like structure in the style of the carpels in some species, this add new characters in the delimitation of the taxa (Taia et al., 2016). Internal structures especially the pith shape can be of use in the grouping of the species as mentioned before by Boissier (1867). El-Hadid (1966) and Taia et al. (2017) found that the internal structure variations can help in the discrimination of the species. Palynological studies on this genus are few and did not give valuable opinions about the delimitation of the species. For that, this investigation has been done as a trial to clarify the Molecular variations among the Libyan species.

Molecular analyses of the *Fagonia* species have not investigated till now and previous works dealt with the origin and distribution of some species. Accordingly, this work considered from the first

works in this concern. The data obtained from the DNA analysis using primer 1 indicated that *F. indica* and *F.glutinosa* are very closely related as well as *F.cretica*; *F.microphylla* and *F.arabica*, which came together in another group. These groupings don't coincide with the clustering of the species according to their vegetative morphological ones (Taia et al., 2015), but partly in agreement with the floral morphological characters (Taia et al., 2016). The genetic similarity between both *F.sinaica* and *F.schweinfurthii* cannot be noticed externally by their vegetative morphological characters, but the genetic similarity between *F.tenuifolia* and *F.thebaica* is obvious morphologically by both vegetative and floral characters. The same results obtained by using primer 2, as both *F.cretica* and *F.indica* are morphologically and anatomically different, while *F.bruguieri* and *F.glutinosa* partly share their floral characters.

Primer 3, grouped the studied taxa in two main groups, all of them in one homogenous group while *F.microphylla* alone in another group. This result indicates that all the *Fagonia* species are closely related and coincide with the other morphological and anatomical investigations. Primers 4 and 5 grouped the taxa into two main groups and kept both *F.sinaica* and *F.indica* as well as *F.tenuifolia* and *F.thebaica*, each two, closely related. Primer 6 bring *F.sinaica* and *F.indica* together, as the previous primers, but *F.thebaica* and *F. schweinfurthii*, each came in a separate subgroups, while *F.cretica* and *F.glutinosa* came together and both closely related to *F.thebaica*.

The dendrogram of all primers via UPGMA method according to RAPD fingerprinting gave two clusters with homology percentage 9%. The first one containing *F.microphylla* and *F.schweinfurthii* with similarity 50%. The second cluster divided into two subclusters. The first one included three *Fagonia* species (*F.cretica; F.indica* and *F.glutinosa*). The second subcluster subdivided into two sub-subclusters. The first one contained *F.arabica* and *F.bruguieri* with 50% similarity. The other sub-subcluster grouped *F.sinaica* and *F.thebaica* and, both species in genetic relationship with *F.tenuifolia*. Meanwhile the division of the studied taxa is not the same in each tool separately. This reveals that the delimitation of the *Fagonia* species is still unclear and the relation between the species is confusing as well. For better understanding the genetic relationship between the *Fagonia* species more molecular and chemical analyses needed for better taxonomic classification and genetic relations.

From this study we can conclude that the Molecular analysis done of genus *Fagonia* are of limited help in the classification of the genus, and more detailed analyses needed. Also the taxa within that genus need further breeding experiments to investigate the delimitations within its taxa.

5. REFERENCES

[1] Abdul Ghafoor, A. (1977): Zygophyllaceae. In Flora of Libya. Ed. Al-Faateh University. Department of Botany, Tripoli. 38: 55.

[2] Angiosperm Phylogeny Group III (2009): "An update of the Angiosperm Phylogeny Group classification for the orders and families of flowering plants: APG III", Botanical Journal of Linnean Society 161 (2): 105–121.

[3] Batanouny, K. and Batanouny, M. (1970): Autecology of common Egyptian Fagoniaspecies - Phyton (Austria) 14 (1 - 2): 79-92.
[4] Beier, B.A. (2005): A revision of the desert shrub Fagonia (Zygophyllaceae) – Systematic Biodiversity 3: 221-263.
[5] Bellstedt, D.U, Van Zyl, L., Marais, E.M., Bytebier, B.L.G., De Villiers, C.A., Makwarela, A.M. and Dreyer, L.L. (2008): Phylogenetic relationships, character evolution and biogeography of southern African members of genus Zygophyllum (Zygophyllaceae) based on three plastid regions. Mol. Phylogenet. Evol., 47 (2008), pp. 932-949
[6] Boissier E. (1867): Flora Orientales 1: 906-909 H. Georg, Basel-Geneve.
[7] Danin, A. (1996): Plants of Desert Dunes. Berlin Heidelberg, Springer.P. 153 – 156.
[8] El Hadidi, M. N. (1966): The genus FagoniaL. in Egypt. Candollea 21(1): 13 - 53.
[9] Fagonia Tourn. ex L. (2018): " Plants of the World Online. Royal Botanic Gardens, Kew. Retrieved 2018-01-26.
[10] Farheen, R., Siddiquit, B.S., Mahmood, I., Simjee, S.U. (2015): Triterpenoids and triterpenoid saponins from the aerial parts of F.induca Burn Phytochemistry letters, 13: 256-261
[11] Puri, D. and Bhandari, A. (2014): Fagonia: a potential medicinal desert plant. Journal of Nepal Pharmaceutical Association, 27:28-33.
[12] Taia, W.K., Ibrahim, M.; Riyad, S. and Hassan, S.A. (2015): 'Morphological Revision of the desert shrub Fagonia L. in Libya', Sci .J. Damietta Fac. Sci., 5(2), pp. 8 - 22.
[13] Taia, W.K., Ibrahim, M., Riyad, S. and Hassan, S.A. (2016): 'Floral and Fruit Studies of the desert shrub Fagonia L. species in Libya', Taeckholmia, Sp., pp. 63 - 84.
[14] Taia, W.K., Ibrahim, M., Riyad, S. and Hassan, S.A. (2017): 'Anatomical Studies of genus FagoniaL. in Libya', Egypt. Exp. Biol. (bot.), pp. 135-144.
[15] Taia, W.K., Ibrahim, M., Hassan, S.A. and Asker, A. M. (2021): Palynological study of the genus Fagonia L. (Zygophyllaceae, Zygophylloideae) in Libya. Libyan Journal of Science & Technology 13(1): 1–9.
[16] Ozenda, P. and Quézel, P. (1956): Les Zygophyllacees de l, Afrique du Nord et du Sahara. Travaux de l'Institut de RecherchesSahariennes 14: 23 - 84.
[17] Zohary, M. (1972): Flora Palaestina 2. Jerusalem, Israel Academy of Sciences and Humanities, 247- 252.

SJST Surman Journal for Science and Technology | ISSN: E 2790-5721 P 2790-5713
Vol3, No.1, Dec_2021 , pp. 094 ~ 103

An Enhanced Computer Vision By Using MLP Approach To Forensic Face Sketch Recognition System

Abdulrazag Mukhtar Atomi[1], Walid Hasen Atomi[2], Abdelrazak A. Yousef Elbunan[3] , Inas Mohammed Milad[4]

Higher Institute of Science and Technology, Messallata [1,3]
University of Alhadera for Humanity Applied Science[2] – Elmergib University[2]
Higher Institute of Science and Technology - Al-khomes[4]
[1]abdulrazag.atomi@gmail.com
[2]wal_ltt@ltt@hotmail.com
[3]Abdelrazk.elbunan1892@gmail.com
[4]inasmilad2007@gmail.com

الملخص

أصبحت تقنيات تحديد هوية المشتبه بهم واكتشافها والتعرف عليها أكثر أهمية في السنوات الأخيرة. ونتيجة لذلك ، فإن التعرف على الوجوه يكاد يكون من الشائع استخدام تقنيات القياسات الحيوية. يهتم المحققون من باحثي الرؤية الحاسوبية الجنائية والطب الشرعي بالرسوم التخطيطية للوجه التي رسمها الفنانون. ووفقًا للدراسات ، لا تزال الرسومات التخطيطية للوجه المرسومة يدويًا نادرة للغاية ، سواء من حيث الفنانين أو عدد الرسومات ، نظرًا لأن فناني الطب الشرعي يعدون رسومات الضحايا بناءً على الأوصاف التي قدمها شهود العيان بعد الحادث. تُستخدم الأقنعة أحيانًا لإخفاء ملامح الوجه القياسية مثل الأنف والعينين والشفتين ولون البشرة ، ولكن من المستحيل إخفاء ميزات الخطوط الخارجية للقياسات الحيوية للوجه. ركزت هذه الورقة على تحليل ملامح الوجه حيث يمكنها حساب نسب التشابه و التطابق بين صور القالب و الرسومات الجنائية ، تم استخدام تقنيات الرؤية الحاسوبية مثل تحويل جيب التمام المنفصل ثنائي الأبعاد (2-D DCT) والشبكة العصبية لخريطة التنظيم الذاتي (SOM) لتصميم نظام للتعرف على رسم الوجوه الشرعي.

Abstract

Technologies for suspect identification, detection, and recognition have become more critical in recent years. As a result, face recognition is an almost commonly used biometric technique. Investigators for Criminal and forensic computer vision researchers are interested in the human-recognized face sketches were drawn by artists. Hand-drawn face sketches are, according to studies, still extremely rare, both in terms of artists and number of drawings, since forensic artists prepare victim drawings based on descriptions were provided by eyewitnesses following an incident. Masks are sometimes used to conceal standard facial features such as noses, eyes, lips, and skin color, but face biometrics' outliner features are impossible to conceal. This paper concentrated on a particular face-geometrical feature that could calculate some similarity ratios between composite template photos and forensic sketches. Computer vision techniques such as Two-Dimensional Discrete Cosine Transform (2D-DCT) and the Self-Organizing Map (SOM) Neural Network are used to design a system for composite and forensic face sketch recognition.

Introduction:

Face recognition relies on still images, which can be divided into two categories: image-based and feature-based. Human-machine interfaces, automatic access control systems, and forensic investigations use face recognition to identify faces in images by comparing them to a database of stored faces [3]. It involves the design and development of a system for identifying forensic face sketches. Faces cropped from images are compressed using the 2D-DCT image compression technique. Using pixel reshaping after image compression, the neural network is prepared to accept image classes as inputs. An algorithm for training neural networks using image data is called SOM (Self-Organizing Maps). Simulink assigns unsupervised weights to inputted face sketches during

training and learning[6]. Facial recognition systems are used as the basis for this project. Simulation and program source code are executed in MATLAB and Simulink.

Related Work

Face detection matching between two facial photographs is a widely studied problem in computer vision, pattern recognition, and biometrics. Matching facial sketches to photographs and detection is the most problem with only a limited amount for published working [2]. Most study has been used viewed sketches drawn when viewing the mugshot photograph. Further, the studies that considered operational forensic sketches did not address the use of sketches[3].

Previous studies have been focused on automatic face recognition systems using composite sketches. The first used a combination of local and global features to represent sketches [5], but it required user input in the form of relevance feedback in the matching or recognition and phase detection. The authors in [7] used a small gallery in their experiments (300 facial photographs). The method proposed by Han et al. [9], used a component-based approach to match facial sketches to mugshots. While Han et al. used a large gallery and created a method that is fully automatic by machine, the composite sketches using the create while viewing the mugshot photograph (viewed forensic composite sketches) which does not reflect operational scenarios. This study was used forensic sketches from trusted URL websites (biometrics) and composite sketches were created. Furthermore, were compared the recognition accuracy of composite sketches forensic sketches using two different automated face recognition systems[8].

Problem Statement

Criminal suspect face sketch recognition has grown in popularity due to increased security demands, forensic investigation, and potential commercial and law enforcement applications. Forensic face sketch recognition is a challenging problem, and there is no feasible technique that can provide a robust solution to all situations and different applications. It is for these reasons that this study is focused on developing an efficient face sketch identification system. In addition to being used as an original face image police database, the digital mugshot is thought to be drawn by forensic artists.

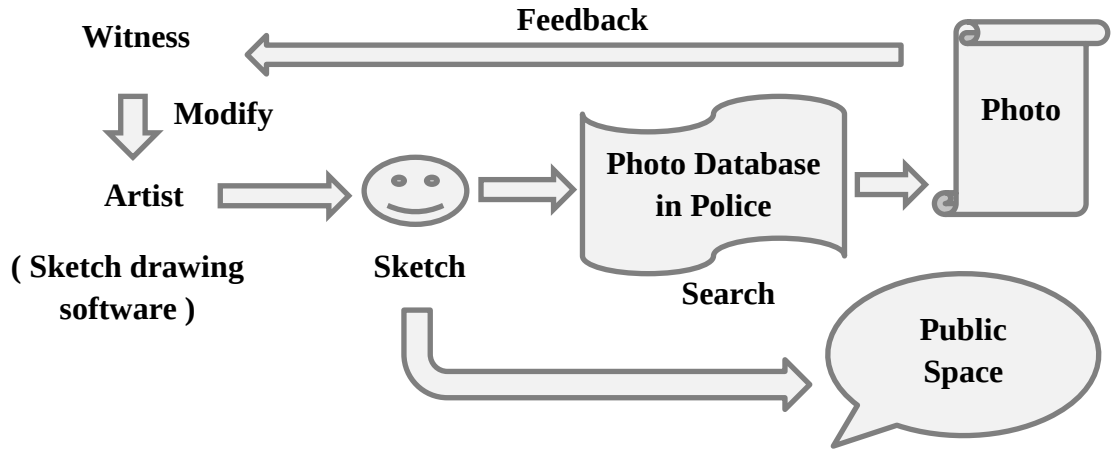

Figure 1 : Search for suspects from photo database using sketch drawing.

Methodology

This work's methodology was developed based on information gathered and processed during the study and research phases. The following technique will be used to design and implement the forensic face sketch identification system.

Step1: Data gathering of face images of subjects from database.
Step2: Pre-processing of face images, i.e., copping, grayscale conversion.
Step3: Importing face images into MATLAB.
Step4: Discrete Cosine Transform (DCT) image compression of face image classes.
Step5: Design of a Self-Organizing Map (SOM) Neural Network in MATLAB.
Step6: Input faces image classes into SOM Artificial Neural Network (ANN).
Step 7: Training the neural network and simulating it for different input face sketch images.
Step8: Testing and validation of the program and technique.

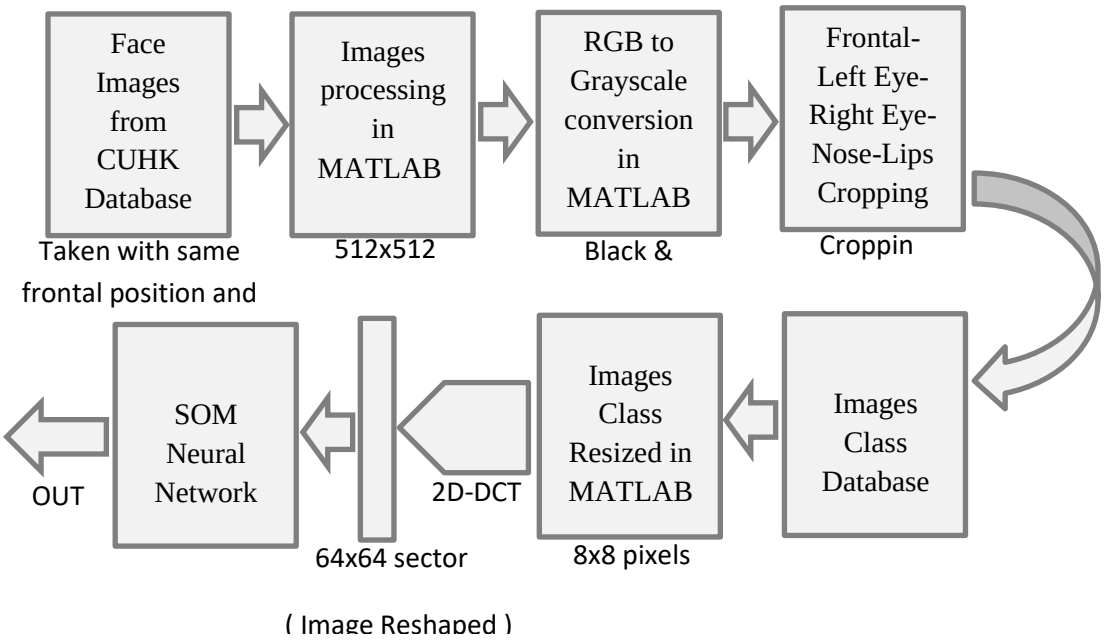

Figure 2: illustrates the flowchart proposed for designing the forensic and composite face sketch recognition system based on the methodology.

Face Detection

To locate and extract the facial region from a face sketch image background, face detection is a necessary first step in the process.

A. General Background

Humans perceive faces in their entirety, not in their features. According to this theory, features' presence and geometrical relationship are far more important than their specific details. Humans can also detect faces in a wide range of conditions, including dim lighting and from a distance[11]. Humans are believed to detect faces in images with two grey levels of 100 to 200 pixels.

Face detection, on the other hand, is a difficult task in computer vision. A face can be detected in a digital image through segmentation, extraction, and verification. A great deal of research has been done on this topic, which is why it is so essential in the computer vision field. As shown in Figure 3, all existing methods for automated face recognition rely on three steps: face detection, facial feature extraction, and expression classification.

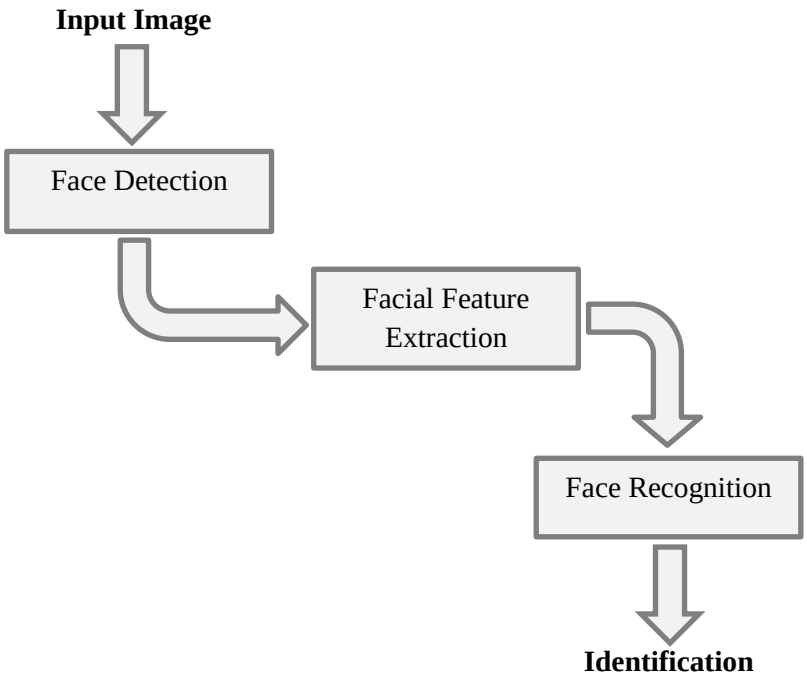

Figure 3: General Steps for Face Recognition

B. Face Sketch Recognition

Generic and discriminative approaches to sketch recognition can be distinguished. Digital images are represented by sketches, which are matched to the query sketch or vice versa. Differential methods extract and match features from a given digital image and sketch pair but do not create the corresponding digital image from sketches.

C. JPEG Image Coding Standard

Encoding and decoding were based on the Discrete Cosine Transform (DCT) when the Joint Photographic Experts Group (JPEG) created the first international standard for still image compression. As a lossy image compression format, JPEG is widely used. Codec and file format are both specified by JPEG. JPEG specifies both the codec and file format. Due to specified by Annex B, it is referred to as "JPEG Interchange Format." In terms of lossy encoding, the JPEG standard specifies three different modes: sequential, progressive, and hierarchical, and a single mode of lossless encoding[13]. When it comes to JPEG image compression, there are four basic steps.

- Block Preparation
- Discrete Cosine Transform
- Quantization
- Encoding

This transform sums up sinusoids of varying magnitudes and frequencies to represent an image. A two-dimensional discrete cosine transform (DCT) of an image can be computed using the dct2 function. Most visually important information about the image is concentrated in just some coefficients of the DCT for a typical picture. Thus, DCT has become a popular image compression method in recent years. The DCT, for example, is at the heart of the JPEG algorithm, an international standard for lossy image compression.

Simulink Description

Simulink is a dynamic systems modeling, simulation, and analysis tool that comes with MATLAB. System models can be in continuous time, sampled time, or a hybrid. Different parts of a system can be sampled or updated at different rates, making the system multi-rate. A system can be modeled using Simulink, and users can see what happens due to their questions. As well as building models from scratch, Simulink also allows for the addition of existing models[14]. A large number of engineers use Simulink to model and solve real problems in a variety of industries around the world

Neural Network Design

Self-Organizing Maps (SOMs) were selected as the technique for the face sketch identification system based on improved data management and neural network accuracy. MATLAB was used to create the training database for SOM, which consisted of many image data points divided into five classes: left eye, right eye, nose, frontal face, and lips. Next, a SOM was created using MATLAB's Newsom command. Each row of vector P was given a minimum and maximum point in the SOM network's parameters. There were a total of 64 minimum and maximum points chosen.The SOM neural network was trained for 1000 epochs when it was created. The trained images were used to simulate the SOM neural network. This was done after the SOM neural network was trained and simulated for images in the training database. Using a minimum absolute deviation, the SOM neural network is simulated for an input face image. After finding the images from the training database that match the closest, they are classified. In the forensic face sketch recognition system, the subject is classified. Simple if and else statements were used in MATLAB to classify data.

Holistic based face recognition

There were many methods that have been shown to be effective techniques for matching a facial sketch probe against a gallery of mugshots [9]. Following normalization, three filters are applied to both the probe sketch and the gallery image to compensate for the differences in modality. After a facial sketch/mugshot into many uniform patches, SIFT and multi-scale local binary pattern (MLBP) [10] features are extracted from each patched. Training for machines in the form of the sampling linear discriminant analysis (RS-LDA) [12] is used to improve the recognition accuracy.

To measure the similarity between feature vectors, the holistic method uses the cosine similarity measure.

Component based face recognition

The component based method was proposed into match composite sketches to photos using two different facial composite systems (FACES and IdentiKit). In the component based method, facial components are automatically localized by detecting landmarks with an active shape model. A local descriptor-based representation by MLBP , then utilized to capture the texture and structure at various scales in each facial component. The component based method uses linear discriminant analysis to improve recognition accuracy. Block based feature extraction is employed to spatially encode the structural information of each facial component. The most accurate components to be used during score fusion are determined empirically for each sketch modality. This representation is consistent with the process of composite sketch synthesis in facial composite systems.

Experimental Results

In total, our facial sketch dataset consists of many forensic sketches and composite sketches with corresponding mugshots and demographic information. The true mugshot age was calculated to be the average of the age range provided by the volunteer while describing the suspect. To make analysis more realistic, this extended the gallery to include more than 1000 mugshots. resulting in a gallery size of about a thousand . Demographic information of the subjects in this dataset can be found in Table 1.

Table1: Demographic information of the many subjects in the gallery set.

Males						Females				
Ethnicity	Age Range					Ethnicity	Age Range			
	>18 and <25	>26 and <35	> 35 and < 50	> 60			>18 and <25	>26 and <35	> 35 and < 50	> 60
Black	90	270	378	45		Black	8	99	62	0
Dark Skin	490	22	15	3		Dark Skin	98	44	250	2
blonde	0	125	33	77		blonde	40	150	480	0
White	1	15	0	6		White	5	25	0	9

Note that the other race/ethnicity contains all subjects not belonging to the black, hispanic, or white races/ethnicities. Filtering is not performed when encountering a probe with the other race/ethnicity. In forensic and biometrics scenarios involving facial sketch to mugshot matching, the standard procedure involves law enforcement officers looking through top-N matches (rather than only considering rank-one retrieval rates). In our experiments, N = 200. We also used the performance of a commercial-off-the-shelf face matcher, FaceVACS v8.2 [8] as a baseline. As shown in Fig. 5, FaceVACS achieves rank-200 retrieval rates of 4.1% and 6.7% for forensic and composite sketches, respectively. The holistic and component representations each have

significantly better performance compared to Face-VACS as ahown in table 2 ,for both forensic and composite sketches under both the filtered and unfiltered scenarios as expained in Fig. 4.

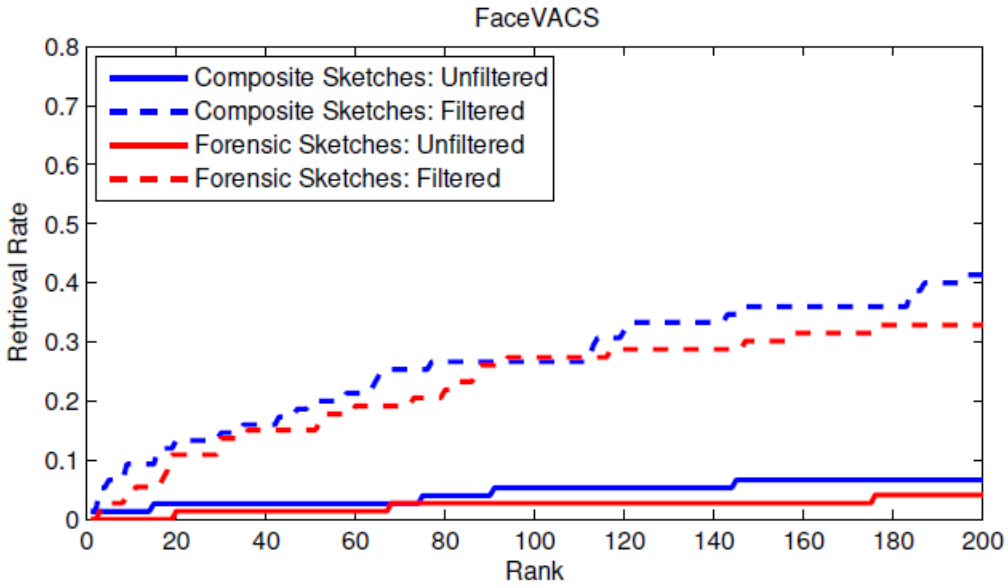

Figure 4: CMC plots for matching facial sketches to mugshots using the commercial matcher FaceVACS

The component based method improves upon the performance of the holistic method in matching forensic sketches when neither system has been trained . The retrieval rate for composite sketches is worse due to the fact that most components are inaccurate . After training , the rank-retrieval rate of the component based method is nearly identical to that of the holistic method for composite sketches and is worse than the holistic method for forensic sketches. This result is perhaps expected, since the training method employed by the holistic method (RS-LDA) is more advanced than the training method used by the component based method (LDA). Similar to the holistic method, training the component based method improves the retrieval rate of composite sketches (12.00% without training to 26.67% with training) more than that of forensic sketches (20.27% without training to 21.62% with training).

Table2: Holistic and face VACS comparison.

Comparing Face Matching			
Face Matcher	**Sketch Type**	**Accuracy**	**Execution Time (Sec)**
Holistic	**Forensic**	***89%***	***58***
	Composite	***92%***	***89***
Face VACS	**Forensic**	***81%***	***67***
	Composite	***90%***	***75***

Conclusion

To reduce DCT processing time and increase program execution time, the optimal number of DCT coefficients should be chosen for face image compression. When simulating a neural network, the size of the input image and training database images is used to determine the optimal number of input neurons. If the SOM neural network output is most accurate with the fewest image pixels, then the SOM neural network's input neurons should be as small as possible.

Summary

Facial sketches drawn by forensic artists (forensic sketches) or created using software (composite sketches) are used by law enforcement agencies to assist in identification and apprehension of suspects involved in criminal activities. Using a new dataset of forensic sketches and composite sketches available at(*http://biometrics.cse.msu.edu/pubs/databases.html*), we have performed the first comparison of the effectiveness of both modalities when used with two state-of-the-art sketchto- photo matchers. A commercial face matcher was also used as a baseline. Demographic information was further explored to filter the gallery (mugshots) to improve the matching performance. Composite sketches were found to be more effective in identifying the suspect's mugshots.

References

[1] Yang, S.; Wen, Y.; He, L.; Zhou, M.C.; Abusorrah, A. Sparse Individual Low-rank Component Representation for Face Recognition in IoT-based System. IEEE Internet Things J. 2021.

[2] Sharif, A.; Li, J.P.; Saleem, M.A.; Manogran, G.; Kadry, S.; Basit, A.; Khan, M.A. A dynamic clustering technique based on deep reinforcement learning for Internet of vehicles. J. Intell. Manuf. 2021, 32, 757–768.

[3] Khan, M.A.; Zhang, Y.-D.; Alhusseni, M.; Kadry, S.; Wang, S.-H.; Saba, T.; Iqbal, T. A Fused Heterogeneous Deep Neural Network and Robust Feature Selection Framework for Human Actions Recognition. Arab. J. Sci. Eng. 2021, 1–16.

[4] Khan, M.A.; Muhammad, K.; Sharif, M.; Akram, T.; de Albuquerque, V.H.C. Multi-Class Skin Lesion Detection and Classification via Teledermatology. IEEE J. Biomed. Heal. Inform. 2021,1.

[5] Geremek, M.; Szklanny, K. Deep Learning-Based Analysis of Face Images as a Screening Tool for Genetic Syndromes. Sensors 2021, 21, 6595.

[6] H. Bhatt, S. Bharadwaj, R. Singh, and M. Vatsa, “Memetically optimized mcwld for matching sketches with digital face images,” IEEE Trans. on Information Forensics and Security, vol. 7, pp. 1522–1535, October 2021.

[7] Kanwal, S.; Iqbal, Z.; Al-Turjman, F.; Irtaza, A.; Khan, M.A. Multiphase fault tolerance genetic algorithm for vm and task scheduling in datacenter. Inf. Process. Manag. 2021, 58, 102676.

[8] Sujitha, B.; Parvathy, V.S.; Lydia, E.L.; Rani, P.; Polkowski, Z.; Shankar, K. Optimal deep learning based image compression technique for data transmission on industrial Internet of things applications. Trans. Emerg. Telecommun. Technol. 2020, 32, e3976.

[9] Goyal, P.; Sahoo, A.K.; Sharma, T.K.; Singh, P.K. Internet of Things: Applications, security and privacy: A survey. Mater. Today Proc. 2021, 34, 752–759.

[10] Akhtar, Z.; Lee, J.W.; Khan, M.A.; Sharif, M.; Khan, S.A.; Riaz, N. Optical character recognition (OCR) using partial least square (PLS) based feature reduction: An application to artificial intelligence for biometric identification. J. Enterp. Inf. Manag. 2020.

[11] Khan, M.A.; Javed, K.; Khan, S.A.; Saba, T.; Habib, U.; Khan, J.A.; Abbasi, A.A. Human action recognition using fusion of multiview and deep features: An application to video surveillance. Multimed. Tools Appl. 2020, 1–27.

[12] T. Ojala, M. Pietik¨ainen, and T. M¨aenp¨a¨a, “Multiresolution grayscale and rotation invariant texture classification with local binary patterns,” IEEE Trans. on Pattern Analysis and Machine Intelligence, vol. 24, no. 7, pp. 971–987, 2020.

[13] X. Gao, J. Zhong, and C. Tian, “Face sketch synthesis algorithm based on e-hmm and selective ensemble,” IEEE Trans. on Circuits and Systems for Video Technology, vol. 18, pp. 487–496, April 2018.

[14] B. Klare, Z. Li, and A. Jain, “Matching forensic sketches to mug shot photos,” IEEE Trans. Pattern Analysis and Machine Intelligence, vol. 33, pp. 639–646, March 2019.

[15] Y. Zhang, C. McCullough, J. Sullins, and C. Ross, “Handdrawn face sketch recognition by humans and a pca-based algorithm for forensic applications,” IEEE Trans. SMC, Part A: Systems and Humans, vol. 40, pp. 475–485, May 2019.

[16] Galea, C., and Farrugia, R. A.2017. Forensic Face Photo Sketch Recognition Using a Deep Learning-Based Architecture. IEEE Signal Processing Letters. 24, 11(Nov 2017)1586.

[17] X. Wang and X. Tang, "Random sampling for subspace face recognition," Int. Journal of Computer Vision, vol. 70, no. 1, pp. 91–104, 2016.

[18] Mittal, P., Vatsa, M., and Singh, R.2015. Composite sketch recognition via deep network - a transfer learning approach. In the Proceedings of the IEEE Conference on Biometrics. (Phuket, Thailand 19-22 May 2015) ICB 2015 Paris.

[19] Saurav Pramanik, Debotosh Bhattacharjee, "Geometric Feature Based Face-Sketch Recognition", Proceedings of the International Conference on Pattern Recognition, Informatics and Medical Engineering, March 21-23, 2012.

[20] Amit R. Sharma, Prakash. R. Devale, "An Application to Human Face Photo and Sketch Synthesis and Recognition", May IJAET 2012.

[21] Pong C. Yuen, C.H. Man, "Human Face Image Searching System Using Sketches", IEEE Transactions on Systems, Man, And Cybernetics-Part A: Systems And Humans, Vol.37, No.4, July 2007.

SJST Surman Journal for Science and Technology | ISSN: E 2790-5721 P 2790-5713
Vol3, No.1, Dec_2021 , pp. 104 ~ 114

The Role of Topography in Reducing the Impact of Global Sea Level Rise; a Case Study on the Northwestern Coast of Libya

Ali Ibrahim Eliawa
Department of Geology, School of Sciences, Azzaytuna University, Trhona, Libya
e-mail: alieliawa@gmail.com

الملخص

يعد ارتفاع مستوى سطح البحر مشكلة حقيقية للحياة على سطح الكرة الأرضية ، حيث يؤدي هذا الارتفاع إلى غمر عدد كبير من المدن البحرية بالمياه. لذلك ، سيتم إجراء الدراسة الحالية في الساحل الشمالي الغربي لليبيا لتحديد تأثير ارتفاع مستوى سطح البحر في المستقبل عن طريق رسم خرائط مناطق الفيضانات باستخدام نظام المعلومات الجغرافية (GIS) من خلال تنفيذ طريقة قاعدة ثمانية جوانب كخوارزميات في سيناريو متر واحد ارتفاع مستوى سطح البحر ، هذه الدراسة تعتد اساسا على البيانات الطبوغرافية التي يتم تمثيلها في نماذج الارتفاع الرقمية، والتي يتم استخدامها كبيانات إدخال للتحليل المكاني والمنتجات المشتقة وتحديد المنطقة المعرضة للفيضانات والمخاطرالتي تنجم عنه. وعليه, تم تحديد مساحة الفيضانات 532.62 كيلومتر مربع بنسبة 16.73٪ من إجمالي المساحة ، ويشمل هذا التأثير المناطق الحضرية والزراعية والطرق ورمال الشاطئ والسبخات والأراضي القاحلة. علاوة على ذلك، تتركز هذه التأثيرات في الجزء الغربي من منطقة الدراسة. علاوة على ذلك ، فإن السكان ليسوا معزولين عن الخطر الذي سيشكل تهديدًا لحياتهم حتى لو حاولوا التكيف ما لم يتم تهجيرهم إلى مناطق أكثر أمانًا تتجلى في الجزء الشرقي من منطقة والتي تعتبر مقيدة ومدعومة بالطوبوغرافيا وهي مثالية لتجاوز مستوى المخاطر ، وكذلك بناء الحواجز الخرسانية ، والحد من الهجرة ، والتحكم في اتجاهات النمو السكاني .

Abstract

Sea level rise (SLR) is a real problem for life on the surface of the globe, as this rise leads to the inundation of a large number of marine cities in water. Therefore, the present study will be conducted in the northwest coast of Libya to determine the impact of future SLR through flood zonation mapping using the Geographical Information System (GIS) by implementing method of an eight-side rule as algorithms at scenario of one meter SLR, depending mainly on topographic data that represented in digital elevation models DEMs (SRTM), which be utilized as an input data for spatial analysis and derivative products and identify the area flooding and determine the vulnerable and risky area. The flooded area is indicated 532.62 km2 with 16.73% of the total area, this effect includes urban, agricultural, roads, beach sand, sabkhas, and barren lands. Moreover, these effects are concentrated in the western part of study area. Furthermore, the residents are not isolated from the danger that will pose a threat to their lives even if they try to adapt unless they are displaced to safer areas that are evident in the eastern part, which is restricted and supported by topography is ideal for exceeding the level of risk, constructing concrete barriers, limiting migration, and controlling population growth trends.

.

Keywords: *sea level rise, flood hazard, digital elevation models, geographical information system*

1. Introduction

The To begin with, climate variation is a widely known happening associated with a lot of environmental and physical consequences. World climate has experienced a lot of changes in diverse ways throughout differing geological aeons. Such reported alterations did not happen abruptly; rather, they took place successively over centuries. However, the current observed changes in climate exhibit a rather different tempo. Departing significantly from the historical patterns, these changes seem to exhibit more brutal and rapid behaviour, suggesting that this CC is not brought about by factors related to the Mother Nature. Rather, this change has a lot to do with what is referred to as the global cycle of carbon. This cycle refers to a natural process where carbon exchanges take place among the atmosphere, the lithosphere, as well as the biosphere. In the course of the past century or so, the whole anthropogony-induced discharge arising from non-

renewable sources and large-scale manufacturing businesses (e.g., manufacturing of concrete or cement), let alone changes brought about by land use, appeared to have played havoc with the nature-bound balance present in distinct composites of the world-wide cycle of carbon in the earth's ecosystems [1]. Apparently, an enormous build-up of gaseous compounds often referred to as greenhouse gases (GHGs) and aerosol substances in the atmosphere have been brought about by human diverse actions throughout the past and present centuries [2], regulating partly the climate on the earth in such a way that the short-wave energy emitted from the sun passes through the molecules and the gases in the atmosphere, and hence entraps the longer wave radiation reflected from Earth [3].This increases the density of aerosol substances as well as that of GHGs to a large extent. Other mishaps that added to the pre-existing problems and have led to big changes in forest lands world-wide and agrarian expansions, never mind urbanization issues. The point is, substantial changes related to energy equilibrium are brought about by considerable disturbance and lessening of natural sequestration activities of carbon dioxide governed by processes of plant photosynthesis. By the same token, the ozone layer exhaustion adds to the severity of the situation owing to the expansion in the radiative flux density of the sun. On this account, the categorical rise in world temperature can be unravelled [4]. Details this earth warming-induced expansion from 1880 to 2015 explained by (Dagbegnon, Djebou, & Singh, 2016; IPCC (2014)) Jepma, Munasinghe, Bolin, Watson, and Bruce (1998) that was because of a rapid accumulation of greenhouse gases in the atmosphere as a result of the use of energy since the beginning of the industrial revolution, which is topped by carbon dioxide(CO2), methane(CH4), and nitrous oxide(N2O), where records of levels higher than the normal or historical. It has been predicted that in the year 2100 the global climate needs the use of wide models. The modelling is assumed three different levels of sensitivity of the global climate (Global temperature) to (high 4.5, medium 2.5 and low 1.5). This increase in the global temperature does not capture considerable regional and local temperature variations in this impact. Moreover, a slight increase in the average is probably to induce large increase in extreme climate events. For instance, the maximum temperature in hot days exceeds 40c. All of these factors are combined to cause heat expansion of the oceans as well as ice sheets and glaciers melting [5]. Additionally, by the second half of the next century 40% of the people around the world will face actual serious shortage in the drinking fresh water due to melting of glacier [6].

Large population live in the coastal areas, in the 1990s 21% and 37% of the world's population were estimated to live within 30 km and 100 km, respectively, of the coastline. As well as, the population density of the coastal zones (CZs) is reached to three times the average of the world's population, and by 2030 it is expected that about 50% of the world population will live within 100 km of the CZs. A large proportion of the world's economic productivity is obtained from coastal areas due to the concentration of human settlements as well as the containment of many large cities near their coastline or directly on their shores. Trends towards urbanization are probably increasing the population densities in Lowlands CZs; it is estimated that the people who live within 30 Km of the coastal zones are increasing at twice the global mean, As a result of global economic well-being that coastal areas are blessed with, it became a major reason for the migration of all this percentage of the population towards these areas and taken as settlements [7]. Thus, they are likely to be exposed to lots of coastal risk, particularly coastal flooding, which mainly depends on the change of flood levels, the standard of flood management infrastructure and human exposure to flooding, Which means that people who will be exposed to flood risks in a typical year because of storms would reach six times and fourteen times given 0.5 and 1 meter in Sea level rise

by the year 2100 [8], together without another changes and the persons who are displayed by inundating will increase consequently; populations CZs growth as well as migration around the world. Moreover, the sea level rise will lead to disruption, economic loss, loss of human activities which provide an important function. For example, flood protection, waste, nursery areas for fisheries, and harbours managements. Furthermore, 1 meter of SLR intimidates about ½ of the coastal wetlands around the world that are modelled as an important internationally more than 168,000 km sq., besides the worst case of the life loss [9-11].

Even though significant efforts by working groups and research organizations to reduce flood hazards through thier programs, only minor reductions in these risks have been accomplished. This is mostly due to the fact that, as the world's population and urbanization accelerates in tandem with climate change, flood threats are getting more severe [12]. Consequently, it is critical to comprehend and access flood threats, as well as establish strategies for dealing with them through adequate planning and mitigation.Thus, The local officials enable to address the negative effects of elevated sea levels by allowing them to identify both built and biotic communities that are at risk, assess the situation, and develop mitigation strategies throughout using Geographical Information System (GIS) that qualified of producing, interpreting, and submitting sea level rise scenarios, which Changing parameter values in the models of sea level rise to allow the user to run a number of impact scenarios for each model and locality [13]. Moreover, in comparison with other modelling approaches, rules have the advantage that key assumptions can easily be made visible and transparent to users [14].

The main target of this research is to determine and assess the effect of future sea level rise in west coastal area of Libya. Thus, Geographical Information System (GIS), geospatial, and hydrological models will be used as tools to obtain primary calculations of CZ exposure of sea level rise without adaptation or defences, which is a major concern. Furthermore, identification coastal receptors; in terms of society, manufacture, human resource and natural environments that might be influenced by the inundation risk through utilizing feature extraction using an object-based approach in order to obtain image classification. Digital Elevation Models will be employed in this research article to display elevation or three-dimensional topography, DEM is a computer performance of the land surface from topographic parameters for instance, slope, upslope area, and the topographic index, which can be digitally produced [15]. Moreover, used as a useful tool for topographic parameterization of hydrological models, which are the basis for any flood modelling procedure [16], these Digital Elevation Models are most commonly produced from topographic maps, which contain of contour lines that show elevation , as well as could be derived from a set of source data such as; ground surveys, aerial photographs and Stereo-pairs such as with ASTER, SPOT, and IRS satellite imagery [17].

2. Materials and Methods

The study area of this project is located in the northwest of Libya as shown in Figure 1, which is approximately 3062.61543 km², it is bounded from north by the Mediterranean Sea, Tunisia's borders from west, Tripoli city from the eastern side and at a depth of 30 km in the direction of the south from coastal line. This area consists of 2893.29213 km² land and 169.3233 km² Sabkha with 125 km coastline. The main cities in this region are; Az Zawiyah, Sabratah and Zuwara with a population of 573,576 people most of them live on the coastal zone, since they use this area as a settlements, oil refinery plant and harbour for instance; Mellitah Oil & Gas B.V

Libyan branch and Az Zawiyah oil refinery. Moreover, the region depends on seasonal agriculture and animal pastures within the grassland areas, as well as considered as location of the commercial service and many tourist villages and resorts. Therefore, this area is considered a great economic importance. The area investigated is located in geomorphological unit that known as the Jeffara plain, this is a nearly flat area is covered by Quaternary deposits with occasional outcrops of limestone hills belonging to the Al Aziziyah formation. This part is the coastal strip, which is ended by the sea cliffs that are made of formation. This strip extends to the South for a distance ranges from 10 to 20 km and its low topographic areas are covered by sebkha. The study area is contains several sediments, including the Tertiary deposits that represented in the Pliocene rocks, and it appears in the deposits of Al Assah formation, which is made mainly of gravels and sands with local occurrence of recrystallized gypsum. Other geologic formations are also spread in this region that contain Quaternary deposits that including Jeffara formation, which consists mainly of fine materials mostly silt and sand occasionally with gravel an caliche bands. As for the Gargaresh Formation, is the coastal slopes consisting of calcarenite and is economically exploited for the extraction of building stones. Finally, sebkha sediments are appear in the coastal area between the cities of Sabratah and Zuwara, consists of brownish silt with saliferous mixture and the lower band is gypsum sand [18].

Figure. 1 Location of the study area

The present study will be conducted in the northwest coast of Libya, with the goal of determining the impact of future sea level rise in coastal zone through flood zonation mapping and determining flooded regions. The following strategies will be used to attain the aforementioned goals:

ASTER-30m Digital Elevation Model (DEM) superimposed on satellite imagery, which will be utilized as an input data for spatial analysis and derivative products, as well as to outline watershed features of the research region and identify the land-area flooding and determine the

vulnerable and risky area using ArcGIS desktop (ArcMap 10.x), this type of data is referred to the Shuttle Radar Topography Mission (SRTM) 1 Arc-Second Global at a resolution of 1 arc-second with 30 meters horizontal resolution with grey colour, in this step an eight-side rule was applied as algorithms at one meter level as a scenario according to [8] and [19], which means starting to delineate the areas that are suitable to be flooded by create binary maps using Raster Calculator in Arc Tool box to builds and performs a single Map Algebra idiom in a calculator-like interface. Each raster cell is assigned an output value of 0 or 1 based on the criteria mentioned. Furthermore, if a criterion is met then assigned with value 1 that means suitable and the altitude below the level of sea and the grid cells seems to be inundated, otherwise 0 that means unsuitable and the altitude higher than previously selected sea levels and the grid cells seems to be not inundated.

After having the results of flood hazard models and knowing the most vulnerable area, this will help to make adapting and new plan or/and enhance of the coastal region. In this stage Landsat Enhanced Thematic Mapper ETM+ data was used to create colour composite with band 5,4,3,which is an appropriate for the identification and area estimation [20], this data was utilized to observe the present coastline and Land use map of the region (Receptors) using ENVI 5.3 software, in addition this assessment will implicate future land cover loss and counting of interaction for receptor systems, therefor, in this case features were extracted using object based approach to improve information extraction, accuracy, automated process, speed with the mind to reduce costs for scaling up. this method definitely much faster and found to be very accurate as compared to the manual methods, although the polygons are might be not as clean but the percentage of area that has been mapped as impervious as compared to the manual method is within 88% accuracy levels [21], Different mathematical algorithms was used in this case to segment the image and extract statistic. First process for classifying the image is an unsupervised classification approach, which is very simply just means that let the computer itself run its own algorithms and identify what considers are the unique spectral classes, since again based purely on the spectra and the statistics within each of bands then the analysts have to figure out what each of those computer identified classes actually are. After gained those object assignments, supervised classification approach was second process that runs within each of previous classes to refine them, meaning that initial information were provided to train the algorithms which are then used to reclassify the rest of the hybrid approach, which means analysts know on the ground where specific interested features and then can actually train at the software to look specifically for a very particular reflectance signatures.

After obtaining the map that shows the flood resulting from the scenario of sea level rise at 1 meter, then interacted with all the maps obtained from the previous classification, which produced the receptors represented in urban areas, agricultural areas and plants, roads, beach sand, sabkha, as well as barren lands in order to calculate the affected area of that scenario.

3. Results and Discussion

This research study sheds light on the important role played by topographic data represented by digital elevation models DEMs and their contribution to the study and evaluation of sea level rise using the available modeling in GIS technology, as well as the use of satellite images represented in the Landsat TM image and remote sensing. The result of this study is divided in two parts: The first part relates to the classification of land in the study area that obtained from the previous supervised classification approach, which created the map of receptors represented in urban areas, agricultural areas and plants, roads, beach sand, sabkha, and barren lands, as shown in Figure 2. As well as, all the areas of the receptors will represented in the Table 1.

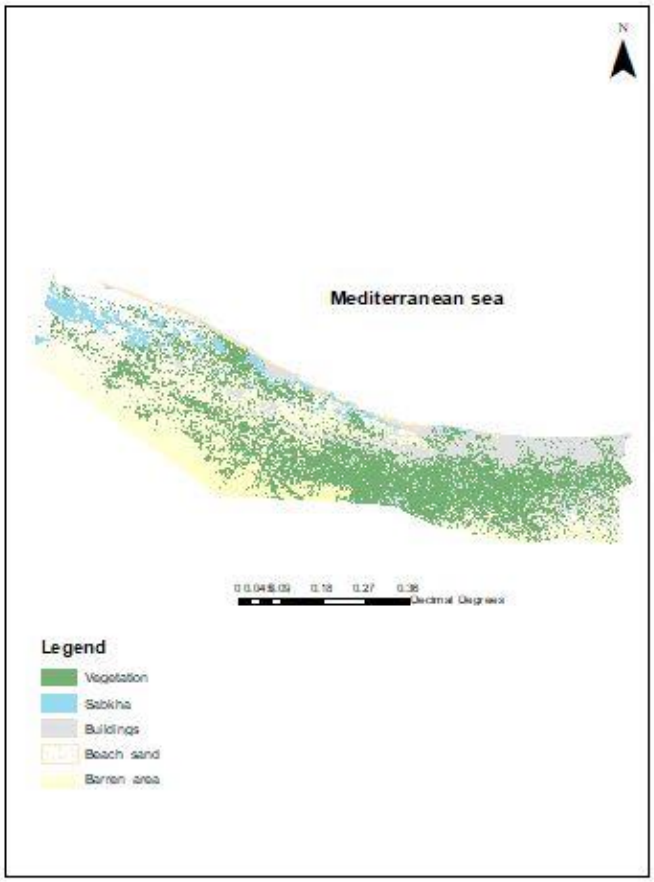

Figure. 2 Receptors of the study area

Table. 1 The areas of the receptors and their percentage related to all area

Receptors	**Areas km^2 / length Km**	**Areas%/ length%**
Urban areas	483.147	15.2
Agricultural and plants areas	1175.4603	36.93
Beach sand	16.9812	0.544
Sabkha	169.3233	5.326
Barren lands	1336.9275	42
Roads	3660.22	-
Total area	3181.8393	-

The second part relates to the results obtained from applying of digital elevation model data using ArcMap software to create slope map in order to describe the topography of the study area and inundation map of sea level rise at one meter. DEM data as shown in Figure 3 showed

that the western part of the study area is characterized by its wideness and low terrain, where its height is less than zero below sea level and then gradually increased toward south. Therefore, it is at risk of flooding at this level that reaches to 16-17 km inland until it touches the residential areas and the road network spread along the coast, as well as its width gradually decreases at the same level whenever towards the east with a distance of approximately 83 km from the western borders of the study area with 8 km depth inland. In contrast, the eastern part of the study area as a whole consists of a rocky coast that narrows toward east as a result of the approach of the feet of the western mountain gradually because of the topography and geomorphology of the land, which reaches to 10 meters above sea level at the coastline and gradually increase until reaches to 115 meters above sea level for a distance about 20 km inland, therefore the areas located in the more spacious lands are more vulnerable to flood risks than the areas located on the eastern side of the study area.

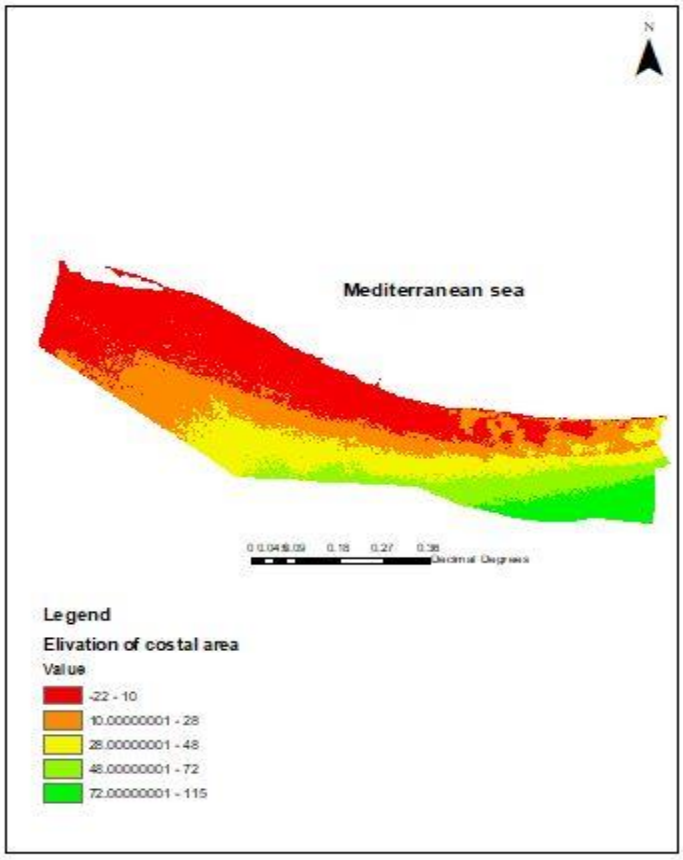

Figure. 3 Slope map of the study area

The scenario, which represented a height of 1 meter from sea level was chosen because it is the highest expected amount in the study [8] by the year 2100 and planning must be carried out within the framework of the worst prediction so as not to encounter unexpected data, especially since climatic variables are now unpredictable. The results are presented in Figure 4, where the percentage of the lands flooded by sea level rise SLR reaches to 16.73% of the total area, which is 532.62 square kilometres.

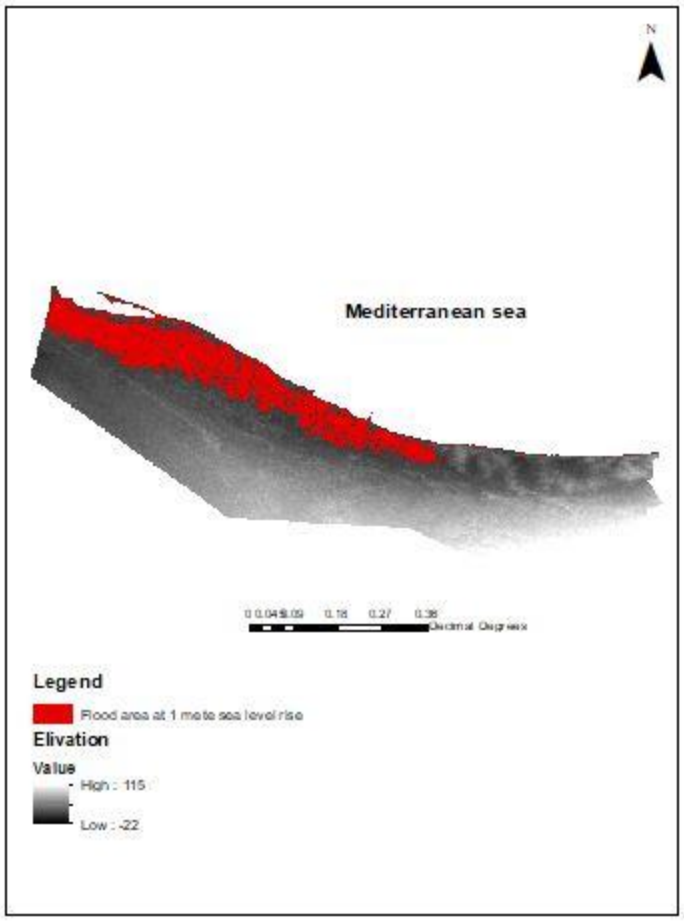

Figure. 4 Flood area at one meter sea level rise

This effect includes all the receptors, which are urban areas, agricultural areas and plants, roads, beach sand, sabkhas, and barren lands, and by using the attribute table from ArcMap table of contents to calculate the intersection of the flooded areas at the level of 1 m with a group of those six previous receptors that produced geographically referenced map of flood risks for each indicator separately as shown in Figures 5, and summarized in Table 2 assuming that no measures or modifications are taken into account to reduce these effects.

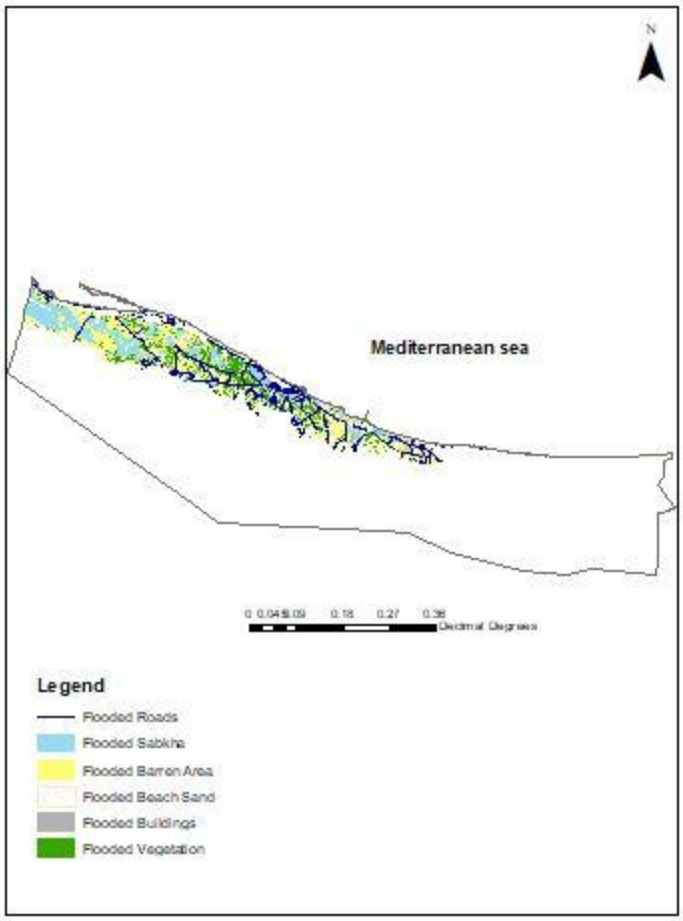

Figure. 5 Map of six flooded receptors at one meter sea level rise

Table. 2 The areas of flooded receptors and their percentage related to the original area of each receptors

Flooded area at 1m SLR	**Areas km^2 / length Km**	**Areas%/ length%**
Urban areas	42.33	8.7
Agricultural and plants areas	114.47	9.7
Beach sand	9.29	54.7
Sabkha	141.28	83.43
Barren lands	198.68	14.86
Roads	373.47	10.2
Total Flooded area	532.62	16.73

Moreover, these effects are concentrated in the western part of the study area much more than the eastern part as shown in Figure 5. Furthermore, these results indicate that the residents of the area are not isolated from the danger posed by the flood at this level and this will pose a threat to their lives even if they try to adapt to this threat unless they are displaced to safer areas that are

evident in the eastern part of the study area, which is restricted and supported by a topography with a height of up to 20 km or towards the south that gradually increase in height to reaches from 10 to 28 meters above sea level in order to avoid this danger, this topography is ideal for exceeding the level of risk. Forthermore, this inundation will negatively affect the ecosystem, economic and environmental aspect of land use in the region, not to mention the intrusion of salt water that directly affects the fresh water and the salinization of the lands and increase the areas of the sabkhas and their level.

4. Conclusion

In this study, the model of sea level rise, which depends mainly on topographic data that represented in digital elevation models DEMs and was applied to assess the vulnerability of the northwestern coast of Libya in order to face the effect of sea level rise, taking into account the scenario of 1 m sea level rise by the year 2100. The results of this study are the absolute importance of the data of digital elevation models, as well as their main role in the success of this study, in addition, its role in directly contributing to identifying the most fragile and weak areas and thus adding a positive value to society to confront and adapt this phenomena and help decision makers to contribute in planning and sustainable development. These results also presented the important role played by GIS and remote sensing technology in obtaining accurate spatial information represented in geographically referenced maps of the risks of global sea level rise that enable decision makers to watch and follow up on these risks and develop plans and strategies to protect those areas from the risk of floods. The results obtained in this study, which were presented in the previous chapter, show the magnitude of the disaster, danger, and the weakness of the region especially in the north western part of the study area. Additionally, there are proposed planning alternatives for the regions of the northwestern coast to face the effects of changes from these expected risks, namely stability and adaptation through emergency flood measures, constructing concrete barriers in the sea, limiting migration to these areas, and controlling population growth trends. It is also necessary to prepare for mitigating the effects of this phenomenon in the long run after 2100 through concentrated spread through the development of some areas and the creation of growth poles in the internal and external areas by providing financial resources and information related to this change and setting a vision about future directions for development and policies for the response of residential communities to this change and its expansion.

5. References

[1] C. Dagbegnon, S. Djebou, and V. P. Singh, "Impact of climate change on the hydrologic cycle and implications for society," *Environment and Social Psychology*, vol. 1, 2016.

[2] C. C. IPCC, *Climate Change 2014–Impacts, Adaptation and Vulnerability: Regional Aspects*: Cambridge University Press, 2014.

[3] R. M. Prabhakar, "Economic impacts and opportunities arising from climate change," *Kaav International Journal of Economics, Commerce & Business Management*, vol. 2, pp. 124-139, 2015.

[4] C. C. IPCC, "The physical science basis. Contribution of working group I to the fifth assessment report of the intergovernmental panel on climate change," ed: USA: Cambridge University Press, 2013.

[5] C. J. Jepma, M. Munasinghe, F. B. B. Bolin, R. Watson, and J. P. Bruce, "Climate change policy," *Climate Change Policy, by Catrinus J. Jepma, Mohan Munasinghe, Foreword by Bert Bolin, Robert Watson and James P. Bruce, pp. 349. Cambridge University Press,*

March 1998. ISBN-10: 052159314. ISBN-13: 9780521593144. LCCN: QC981. 8. C5 J47 1998, vol. 1, 1998.

[6] A. Gore, *An inconvenient truth: The planetary emergency of global warming and what we can do about it*: Rodale, 2006.

[7] N. Brooks, R. Nicholls, and J. Hall, "Sea level rise: coastal impacts and responses," *Norwich WBGU ISBN,* pp. 3-936191, 2006.

[8] N. Harvey and R. Nicholls, "Global sea-level rise and coastal vulnerability," *Sustainability Science,* vol. 3, pp. 5-7, 2008.

[9] R. Nicholls and T. Wilson, "Integrated impacts on coastal areas and river flooding," *Regional Climate Change Impact and Response Studies in East Anglia and North West England (RegIS). Oxford, UK: UK Climate Impacts Programme (UKCIP),* pp. 54-103, 2001.

[10] R. J. Nicholls, "Analysis of global impacts of sea-level rise: a case study of flooding," *Physics and Chemistry of the Earth, Parts A/B/C,* vol. 27, pp. 1455-1466, 2002.

[11] R. J. Nicholls, "Coastal flooding and wetland loss in the 21st century: changes under the SRES climate and socio-economic scenarios," *Global Environmental Change,* vol. 14, pp. 69-86, 2004.

[12] A. Revi, "Climate change risk: an adaptation and mitigation agenda for Indian cities," *Environment and urbanization,* vol. 20, pp. 207-229, 2008.

[13] E.-S. E. Omran and A. M. Negm, "Introduction to "Climate Change Impacts on Agriculture and Food Security in Egypt"," in *Climate Change Impacts on Agriculture and Food Security in Egypt,* ed: Springer, Cham, 2020, pp. 3-19.

[14] A. T. Crooks and C. J. Castle, "The integration of agent-based modelling and geographical information for geospatial simulation," in *Agent-based models of geographical systems,* ed: Springer, 2012, pp. 219-251.

[15] X. Liu, Z. Zhang, and J. Peterson, "Evaluation of the performance of DEM interpolation algorithms for LiDAR data," in *Proceedings of the 2009 Surveying and Spatial Sciences Institute Biennial International Conference (SSC 2009)*, 2009, pp. 771-779.

[16] R. B. Kauffman, "Topographic Maps," in *Map and Compass*, ed Frostburg State University, Frostburg, 2015.

[17] K. S. Subramanian, A. Singh, and M. Sudhakar, "Evaluation of Digital Elevation Models created from different satellite images," *Map India in Technology,* 2003.

[18] I. R. C. S.P.L.A.J, "Explanatory Booklet for the Geological Map of Libya Sheet: TARABULUS NI 33-13," 1975.

[19] A. Nauels, J. Rogelj, C.-F. Schleussner, M. Meinshausen, and M. Mengel, "Linking sea level rise and socioeconomic indicators under the Shared Socioeconomic Pathways," *Environmental Research Letters,* vol. 12, p. 114002, 2017.

[20] S. Tennakoon, V. Murty, and A. Eiumnoh, "Estimation of cropped area and grain yield of rice using remote sensing data," *International Journal of Remote Sensing*, vol. 13, pp. 427-439, 1992.

[21] E. T. Slonecker, D. B. Jennings, and D. Garofalo, "Remote sensing of impervious surfaces: A review," *Remote Sensing Reviews,* vol. 20, pp. 227-255, 2001.

SJST Surman Journal for Science and Technology | ISSN: E 2790-5721 P 2790-5713
Vol3, No.1, Dec_2021 , pp. 115 ~ 132

Competence Amelioration of PMBLDC Motor using LQR- PID, Kalman Filter- PID and LQG Based on Kalman Filter-PID optimal Controllers for disturbance attenuation

Ahmad Mohamad El-fallah Ismail
Department of Electrical and Electronic Engineering, University of Gharian
Gharyan, Jabal Al Gharbi, Libya
dr.ahmad_ismail_alrabty@yahoo.com

الملخص

في هذه الورقة البحثية ، تحليل الأداء ونمذجة ومحاكاة لمحرك التيار المستمر بدون فرش (PMBLDC) باستخدام وحدة التحكم الكلاسيكية (المتحكم التناسبي التفاضلي التكاملي PID) ووحدات التحكم المثلى (المنظم التربيعي الخطي (LQR)والمراقب الخطي الرباعي الخطي (LQG)مستندة على أساس مرشح كالمان) لتوهين وتضعيف الاضطراب وقمع أو تخميد الضوضاء.حيث تتزايد تطبيقات محرك التيار المستمر عديم الفرشاة ذو المغناطيس الدائم (PMBLDC) يومًا بعد يوم. عليه من أجل الحصول على الاستخدام المناسب لهذه المحركات والتحكم فيها بشكل فعال ، من المهم أن يكون لديك نمذجة رياضية مناسبة لهذه المحركات. وبالمثل ، فإن التحكم الفعال في هذه المحركات ضروري أيضًا للتطبيق الناجح للأجهزة عبر مجالات متعددة. تتناول هذه الورقة كلا الجانبين المهمين. تم اشتقاق نموذج رياضي لتمثيل نموذج محرك تيار مستمر بدون فرشاة ذو المغناطيس الدائم (PMBLDC) لدراسة الاستقرار والأداء. من أجل الحفاظ على الاستقرار وتحقيق أفضل أداء عن طريق تقليل توهين الاضطراب وقمع الضوضاء ، تم تطوير أدوات التحكم الثلاثة المثلى في هذا البحث. تم تقديم محاكاة أداء النظام لهذه وحدات التحكم المثلى مع وحدة التحكم الكلاسيكية PID باستخدام برنامج MATLAB للتحكم في محرك التيار المستمر بدون فرش (PMBLDC) ذي المغناطيس الدائم من أجل تخفيف الاضطراب وقمع الضوضاء .. وأظهرت نتائج المحاكاة ذلك و Linear Quadratic Gaussian (LQG) المستند على مرشح كالمان مع وحدة التحكم الكلاسيكية PID ، يوفر أفضل أداء مقارنة بوحدة التحكم PID ، والمنظم الخطي التربيعي (LQR) مع وحدة التحكم PID ومرشح كالمان مع وحدة التحكمPID .

Abstract

In this paper, modeling, simulation and performance analysis of the permanent magnet brushless direct current (PMBLDC) motor using classical controller (PID Controller) and optimal controllers (Linear Quadratic Regulator (LQR) and Linear Quadratic Gaussian (LQG) optimal Controllers Based on Kalman Filter) for disturbance attenuation and noise suppression is presented. The applications of the permanent magnet brushless direct current (PMBLDC) motor are increasing day by day. In order to have proper utilization of these motors and to control them effectively it is important to have proper mathematical modeling of these motors. Similarly effective control these motors are also essential to have successful application of the devices across multiple domains. This paper handles both these important aspects. A mathematical model has been derived to represent permanent magnet brushless direct current (PMBLDC) motor model to study the stability and performance. In order to maintain the stability and to achieve the best performance by reducing disturbance attenuation and noise suppression, the three optimal controllers are developed in this paper. the system performance simulation of these optimal controllers with PID controller is presented using MATLAB program to control the modeled permanent magnet brushless direct current (PMBLDC) motor for disturbance attenuation and noise suppression.. The simulation results show that and Linear Quadratic Gaussian (LQG) Based on Kalman Filter with PID controller provides best as compared to PID controller, Linear Quadratic Regulator (LQR) with PID controller and Kalman Filter with PID controller.

Keyword: *Permanent Magnet Brushless Direct Current (PMBLDC) motor, PID Controller, Linear Quadratic Regulator (LQR), Linear Quadratic Gaussian (LQG), Integral Linear Quadratic Regulator , MATLAB/Simulink etc.*

1. Introduction

Conventional DC motors have many attractive properties such as high efficiency and linear torque-speed characteristics. The control of DC motors is also simple and does not require complex hardware. However, the main drawback of the DC motor is the need of periodic maintenance. The brushes of the mechanical commutator eventually wear out and need to be replaced. The mechanical commutator has other undesirable effect such as sparks, acoustic noise and carbon particles coming from the brushes. Permanent magnet brushless direct current

(PMBLDC) motors can in many cases replace conventional DC motors. Despite the name, PMBLDC motors are actually a type of permanent magnet synchronous motors. They are driven by DC voltage but current commutation is done by solid state switches. The commutation instants are determined by the rotor position and the position of the rotor is detected either by position sensors or by sensorless techniques. PMBLDC motors have many advantages over conventional DC motors. A few of these are [1-2]: Long operating life, high dynamic response, high efficiency, better speed vs. torque characteristics, noiseless operation, higher speed range and higher torque-weight ratio. PMBLDC motors are available in many different power ratings, from very small motors as used in hard disk drives to large motors used in electric vehicles. Three-phase motors are most common but two-phase motors are also found in many application. The purpose of this paper is to build a simple, accurate and fast running Matlab model of a permanent magnet brushless direct current (PMBLDC) motor using Linear Quadratic Regulator (LQR) and Linear Quadratic Gaussian (LQG) optimal Controllers Based on Kalman Filter with PID controller for disturbance attenuation and noise suppression which will lead to an improvement in the transient and steady state response. This paper is organized as follows. Mathematical modeling of the three-phase permanent magnet brushless direct current (PMBLDC) motor is given in Sec. II. Optimal control strategies are given in Sec. III. Classical control strategy is given in Sec. IV. Analysis of Simulation Results is demonstrated in Sec. V. Conclusion is given in Sec. VI.

2. Mathematical Modeling Of The PMBLDC Motor

The mathematical model of the PMBLDC motor is fundamental for the corresponding performance analysis and control system design. The common mathematical models, which mainly include differential equation model, transfer function model, and state-space model, are presented as follow:

A. Differential Equation

The differential equation model is built for a three-phase two-pole PMBLDC motor [3]. Hence, the simplified schematic diagram of the motor can be obtained as shown in Fig. 1.

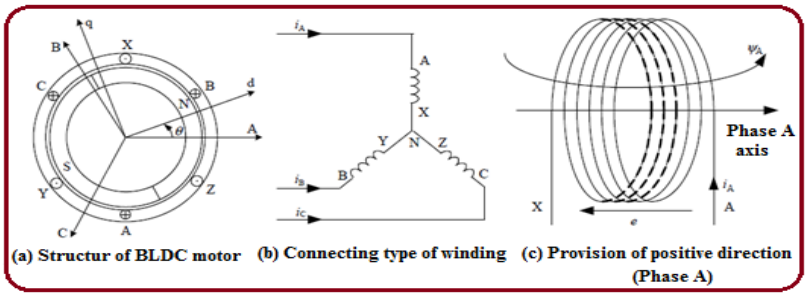

Figure.1 Schematic diagram of the PMBLDC motor.

Under the positive direction shown in Fig. 1, the phase voltage of each winding, which includes the resistance voltage drop and the induced EMF, can be expressed as

$$\boldsymbol{V_x = R_x i_x + e_{\psi x}} \qquad (1)$$

Where

$\boldsymbol{V_x}$: → phase voltage, in which subscript $\boldsymbol{x}$ denotes phase ***A***, ***B*** and ***C***;

$\boldsymbol{i_x}$: → phase current.

$\boldsymbol{e_{\psi x}}$: → phase-induced EMF.

$\boldsymbol{R_x}$: → phase resistance. For three-phase symmetrical winding, there exists $\boldsymbol{R_A = R_B = R_C = R}$).

The three-phase stator windings are symmetrical, the self inductances will be equal, and so as the mutual inductance. As for the three-phase symmetrical windings, there also exist fB(Θ) = fA(Θ -2π /3), and fC(Θ) = fA(Θ +2π /3). Then, the matrix form of phase voltage equation of PMBLDC motor can be expressed as

$$\begin{bmatrix} V_A \\ V_B \\ V_C \end{bmatrix} = \begin{bmatrix} R & 0 & 0 \\ 0 & R & 0 \\ 0 & 0 & R \end{bmatrix} \begin{bmatrix} i_A \\ i_B \\ i_C \end{bmatrix} + \begin{bmatrix} L-M & 0 & 0 \\ 0 & L-M & 0 \\ 0 & 0 & L-M \end{bmatrix} \frac{d}{dt} \begin{bmatrix} i_A \\ i_B \\ i_C \end{bmatrix} + \begin{bmatrix} e_A \\ e_B \\ e_C \end{bmatrix} \quad (2)$$

According to Equation (2), the equivalent circuit of the PMBLDC motor can be shown as in Fig.2.

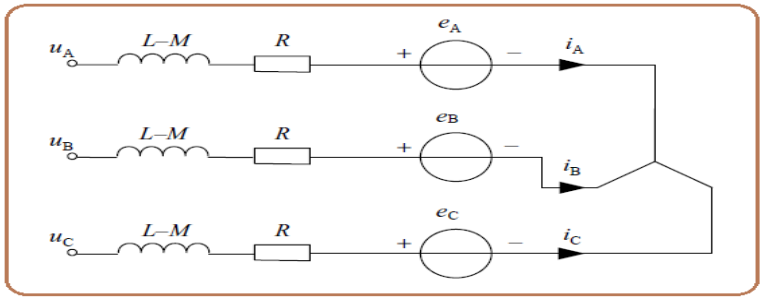

Figure.2 Equivalent circuit of the PMBLDC motor.

The power transferred to the rotor, which is called the electromagnetic power, the electromagnetic power is totally turned into kinetic energy equals the sum of the product of current and back-EMF of the three phases. That is

$$P_e = T_e\omega = e_A i_A + e_B i_B + e_C i_C \Rightarrow$$

$$T_e = \frac{e_A i_A + e_B i_B + e_C i_C}{\omega} \quad (3)$$

Where

T_e : → electromagnetic torque;

ω: → angular velocity of rotation.

Substituting Equations, another form of the torque equation can be

$$T_e = P[\psi_m f_A(\theta)\, i_A + \psi_m f_B(\theta) i_B + \psi_m f_C(\theta) i_C] \quad (4)$$

Where

p : → is the number of pole pairs.

So Equation (4) can be further simplified as represented as

$$T_e = 2P\psi_m\, i_A = K_T i \quad (5)$$

where

K_T: → the torque coefficient;

i : → the steady phase current.

In order to build a complete mathematical model of the electromechanical system, the motion equation has to be included as

$$T_e - T_L = J\frac{d\omega}{dt} + B_V\omega \quad (6)$$

where

T_L : → load torque;

J : → rotor moment of inertia;

B_v : → viscous friction coefficient.

Thus, Equations (2), (3) and (6) constitute the differential equation mathematical model of the PMBLDC motor.

B. Transfer Functions

The three-phase PMBLDC motor is controlled by the full-bridge driving in the two-phase conduction mode, then when the windings of phase A and B are conducted, there exists

$$\begin{cases} i_A = -i_B = i \\ \dfrac{di_A}{dt} = -\dfrac{di_B}{dt} = \dfrac{di}{dt} \end{cases} \quad (7)$$

Thus, the line-voltage V_{AB} can be rewritten as

$$V_{AB} = 2R\,i + 2(L-M)\frac{di}{dt} + (e_A - e_B) \quad (8)$$

Take the transient process out of consideration (i.e. ignore the trapezoid bevel edge), then the steady e_A and e_B are equal in amplitude and opposite in direction when phases A and B are turned on. So, equation (8) can be expressed as

$$V_{AB} = V_d = 2R\,i + 2(L-M)\frac{di}{dt} + 2e_A$$

$$V_{AB} = V_d = r_a i + L_a\frac{di}{dt} + k_e\omega \quad (9)$$

where

V_d : → *DC* bus voltage;

r_a : → line resistance of winding, $r_a = 2R$;

L_a : → equivalent line inductance of winding, $L_a = 2(L - M)$;

k_e : → coefficient of line back-EMF, $k_e = 2p\psi_m = 4pNSB_m$.

The transfer function of a PMBLDC motor with no load can be expressed as

$$G_u(s) = \frac{\omega(s)}{V_d(s)} = \frac{K_T}{L_aJs^2 + (r_aJ + L_aB_V)s + (r_aB_V + K_Tk_e)} \quad (10)$$

In the following, the transfer function of a PMBLDC motor when the load torque is not zero, it is shown in Fig. 3.

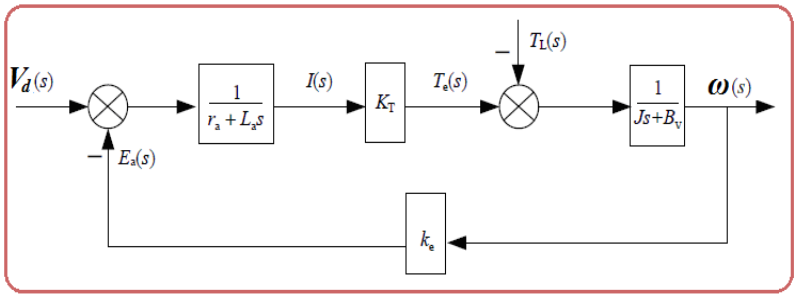

Figure.3 Structure diagram of PMBLDC motor with load torque.

For such a system, the superposition principle holds. Thus, the output of the system equals the sum of outputs when $V_d(s)$ and $T_L(s)$ are applied to the system, respectively. In Fig. 3, when $V_d(s)=0$ holds, then, the transfer function between load torque and speed is

$$G_L(s) = \frac{\omega(s)}{T_L(s)} = -\frac{r_a + L_as}{L_aJs^2 + (r_aJ + L_aB_V)s + (r_aB_V + K_Tk_e)} \quad (11)$$

Therefore, the speed response of a PMBLDC motor affected together by voltage and load torque is given by

$$\boldsymbol{\omega(s) = G_u(s)V_d(s) + G_L(s)T_L(s)}$$

$$\boldsymbol{\omega(s) = \frac{K_T V_d(s) - (r_a + L_a s)T_L(s)}{L_a J s^2 + (r_a J + L_a B_V)s + (r_a B_V + K_T k_e)}} \quad (12)$$

C. State-Space Equations

The state-space equation method is one of the most important analysis methods in modern control theory. From the state equation we can get all the independent variables and then determine all the motion states of the system. A group of first-order differential equations with state variables is used in the state-space method to describe the dynamic characteristics of the system. Since it is helpful to the realization of different digital control algorithms, the state-space method is becoming more and more popular in designing control systems with the fast development of computer techniques. Especially in recent years, computer on-line control systems such as optimal control, Kalman filters, dynamic system identification, self-adaptive filters and self adaptive control have been applied to motor control. All these control techniques are based on the state equation. Currents of three phase windings and the angular speed are selected here as state variables, and the fourth-order state equation is then derived as

$$\boldsymbol{\dot{X} = Ax + Bu} \quad (13)$$

Where

$$\boldsymbol{X = [i_A \quad i_B \quad i_C \quad \omega \ ]^T}$$
$$\boldsymbol{V = [V_A \quad V_B \quad V_C \quad T_L \ ]^T}$$

$$A = \begin{bmatrix} \frac{-R}{L-M} & 0 & 0 & \frac{-P\psi_{pm}(\theta)}{L-M} \\ 0 & \frac{-R}{L-M} & 0 & \frac{-P\psi_{pm}\left(\theta-\frac{2\pi}{3}\right)}{L-M} \\ 0 & 0 & \frac{-R}{L-M} & \frac{-P\psi_{pm}\left(\theta-\frac{4\pi}{3}\right)}{L-M} \\ \frac{P\psi_{pm}(\theta)}{J} & \frac{P\psi_{pm}\left(\theta-\frac{2\pi}{3}\right)}{J} & \frac{P\psi_{pm}\left(\theta-\frac{4\pi}{3}\right)}{J} & \frac{-B_V}{J} \end{bmatrix}$$

$$\boldsymbol{B = \begin{bmatrix} \frac{1}{L-M} & 0 & 0 & 0 \\ 0 & \frac{1}{L-M} & 0 & 0 \\ 0 & 0 & \frac{1}{L-M} & 0 \\ 0 & 0 & 0 & \frac{-1}{J} \end{bmatrix}}$$

The controllability of a linear system is the base of optimal control and optimal estimation, so it should be determined. Assume the controllability matrix is

$$\boldsymbol{M = [M_0 \quad M_1 \quad M_2 \quad M_3 \ ]} \quad (14)$$

Where

$$\boldsymbol{M_0 = B, \qquad M_i(t) = A^i B, \qquad i = 1, 2, 3.}$$

Then, matrix $\boldsymbol{M}$ can be transformed to

$$M = \begin{bmatrix} \lambda & 0 & 0 & 0 \\ 0 & \lambda & 0 & 0 \\ 0 & 0 & \lambda & 0 \\ 0 & 0 & 0 & -\frac{1}{J} \end{bmatrix} \begin{matrix} \\ \\ \\ \\ \end{matrix} M_1 \quad M_2 \quad M_3 \quad (15)$$

Where

$$\boldsymbol{\lambda = 1/(L - M)}$$

The matrix $\boldsymbol{M}$ meets the condition of rank [$\boldsymbol{M}$] = 4. So, the system represented by equation (13) is controllable and all the poles of the system can be arbitrarily placed by state feedback.

3. Optimal Control Strategy

A. Linear Quadratic Regulator (LQR) Control System

The linear quadratic regulator (LQR) is an optimal controller that provides practical state feedback gain matrix. The controller has been used for minimizing the cost function [4]. The LQR is a state feedback control technique that computes optimal feedback gain matrices for given states pace represented systems with respect to a quadratic cost function which is minimized [5]. The feedback gain matrix is associated to a solution of the Riccati equation. The LQR provides an optimal control law with quadratic performance index or quadratic cost function where the system dynamics are described as a set of differential equations [6]. The LQR approach deals with the optimization of a cost function or performance index. Thus, the designer can weigh which states and which inputs are more important in the control action to seek for appropriate transient and steady-state performances [7-8]. The optimal control problem is to find a control u which causes the system

$$\dot{\boldsymbol{X}} = \boldsymbol{g(x(t), u(t), t)} \qquad \textbf{(16)}$$

To follow an optimal trajectory x(t) that minimizes the performance criterion, or cost function

$$\boldsymbol{J = \int_{t_0}^{t_1} h(x(t), u(t), t)dt} \quad \textbf{(17)}$$

The problem is one of contrained functional minimization a quadratic performance index or quadratic cost function is

$$\boldsymbol{J = \int_{0}^{\infty} (x^T Q x + u^T R u)dt} \quad \textbf{(18)}$$

Where

Q: →State weighting matrix (square, symmetric and non-negative definite)

R: →Control weighting matrix (square, symmetric and positive definite)

J: → Is a scalar quantity

The optimal control law or state feedback law is

$$\boldsymbol{U(t) = -Kx(t)} \qquad \textbf{(19)}$$

Where

K: → Is the controller gain or state feedback gain matrix and a value of K that will produce a desired set of

closed-loop poles

The state feedback gain matrix (K) is found by [8]

$$\boldsymbol{K = R^{-1} B^T P} \qquad \textbf{(20)}$$

Where

B: → Is the input matrix of the plant (BLDC motor).

P: →Is the unique positive definite solution to algebraic Riccati equation or matrix Reccati equation.

The feedback gain matrix (K) is associated to a solution of the Riccati equation (P). Therefore, the continuous solution of the matrix Riccati equation or algebraic Riccati equation is

$$\boldsymbol{Q + PA + A^T P - PBR^{-1}B^T P = 0} \qquad (21)$$

Where

A: → Is the system matrix of the plant

By knowing the state matrices A and B and properly selecting Q and R, the value of K can be obtained. The function in MATLAB can be used Lqr(sys,Q,R,N). The discrete quadratic performance index or discrete quadratic cost function is

$$\boldsymbol{J = \sum_{K=0}^{N-1}\left(x^T(k)Qx(k) + u^T(k)Ru(k)\right)T} \quad (22)$$

The discrete solution of the state equation is

$$\boldsymbol{X(k+1) = A(T)x(k) + B(T)u(k)} \qquad (23)$$

Where

T: → Is the sampling time of a discrete-time system

A(T) : → Is the discrete-time state transition matrix $A(T) = e^{A\tau}$

B(T) : →Is the discrete-time control matrix $B(T) = \int_0^T e^{A\tau}Bd\tau$

The discrete solution of the matrix Riccati equation solves recursively for K and P in reverse time, commencing at the terminal time, where [6]

$$\boldsymbol{K(N-(k+1)) = [TR + B^T(T)P(N-k)B(T)]^{-1}B^T(T)P(N-k)A(T)} \quad (24)$$

And

$$\begin{aligned}\boldsymbol{P(N-(k+1))} &= \boldsymbol{\left[TQ + K^T\left(N-(k+1)\right)TRK(N-(k+1))\right]} \\ &+ \boldsymbol{\left[A(T) - B(T)K\left(N-(k+1)\right)\right]^T P(N-k)\left[A(T)\right.} \\ &\boldsymbol{\left. - B(T)K\left(N-(k+)\right)\right]} \quad (25)\end{aligned}$$

As K is increased from 0 to N-1, the algorithm proceeds in reverse time, when run in forward-time, the optimal control law at step k is

$$\boldsymbol{U(k) = -K(k)x(k)} \qquad (26)$$

The LQR design technique has certain advantages over the classical control design methods or Eigen-structure assignment based methods, as it guarantees adequate stability margins [5]. On the other hand, there are some limitations the given system must satisfy e.g. it must be stabilizable and free of non-observable states which means The LQR approach requires the knowledge of all state variables [9]. The performance of LQR may be deviated due to the presence of system noise [4]. The LQR in its basic form forces the controlled states to reach zero, which is a known regulation problem. In order to transform the regulation capability to command tracking, an integral error dynamics must be considered to remove the steady state error. Fig.4 shows Linear quadratic regulator LQR control system

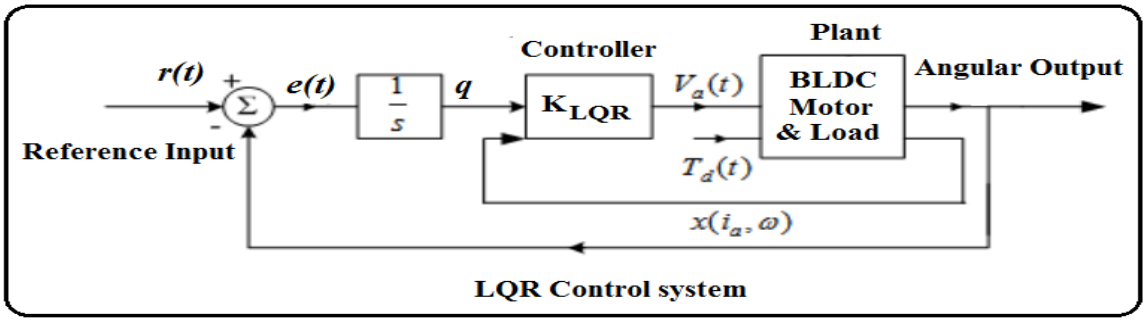

Figure.4 LQR Control System

A. Kalman Filter State Estimator

Kalman Filter is used for both filtering and state estimation purpose. In the design of state observers, it was assumed that the measurements y=Cx were noise free. In practice, this is not usually the case and therefore the observed state vector $\hat{x}$ may also be contaminated with noise. The state estimation is the process of extracting a best estimate of a variable from a number of measurements that contains noise. The classical problem of obtaining a best estimate of a signal by combining two noisy continuous measurements of the same signal was first solved by Weiner (1949), his solution required that both the signal and noise be modeled as random process with known statistical properties. This work was extended process based upon an optimal minimum variance filter, generally referred to as a kalman filter. The kalman filter is a complementary form of the Weiner filter. The plant is subject to a Gaussian sequence of disturbance *w(kT)* with disturbance transition matrix Cd(T). Measurements z(k+1)T contain a Gaussian noise sequence v(k+1)T as shown in fig.5 [6]

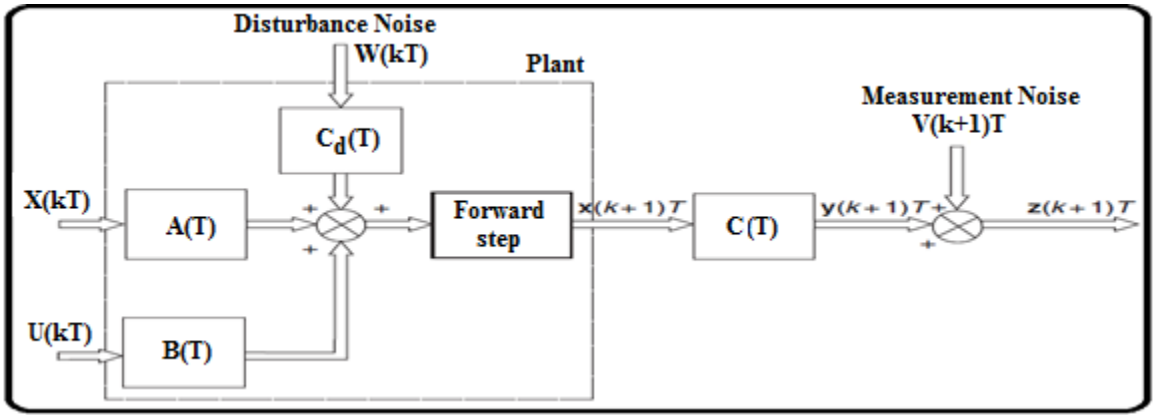

Figure.5 Plant with disturbance and measurements noise

The general form of the Kalman filter usually contains a discrete model of the system together with a set of recursive equations that continuously update the Kalman gain matrix [K] and the system covariance matrix [P]. the optimal value of the Kalman gain matrix [K] is the one that yields the minimtate um variance [P]. The state estimate $\hat{x}(k+1/k+1)$ is obtained calculating the predicted state $\hat{x}(k+1/k)$ from

$$\hat{\boldsymbol{x}}(\boldsymbol{k+1/k})\boldsymbol{T} = \boldsymbol{A}(\boldsymbol{T})\hat{\boldsymbol{x}}(\boldsymbol{k/k})\boldsymbol{T} + \boldsymbol{B}(\boldsymbol{T})\mathbf{U(T)} \qquad \textbf{(27)}$$

And the determine the estimated state at time (k+1)T using

$$\hat{\boldsymbol{x}}(\boldsymbol{k+1/k+1})\boldsymbol{T} = \hat{\boldsymbol{x}}(\boldsymbol{k+1/k})\boldsymbol{T} + \boldsymbol{K}(\boldsymbol{k+1})[\boldsymbol{Z}(\boldsymbol{k+1})\boldsymbol{T} - \boldsymbol{C}(\boldsymbol{T})\hat{\boldsymbol{x}}(\boldsymbol{k+1/k})\boldsymbol{T}]$$

(28)

Where

The term (k/k) : → means data at time k based on information available at time k.
The term (k+1/k) : → means data at time (k+1) based on information available at time k.
The term (k+1/k+1) : → means data at time (k+1) based on information available at time (k+1).

The vector of measurements is given by

$$\boldsymbol{Z}(\boldsymbol{k+1})\boldsymbol{T} = \boldsymbol{C}(\boldsymbol{T})\boldsymbol{xk+1})\boldsymbol{T} + \boldsymbol{V}(\boldsymbol{k+1})\boldsymbol{T} \qquad \textbf{(29)}$$

Where

$Z(k+1)T$: → is the measurement vector
$C(T)$: → is the measurement matrix
$V(k+1)T$: → is a Gaussian noise sequence

The kalman gain matrix [K] is obtained from a set of recursive equations that commence from some initial covariance matrix (P(k/k)).

$$\boldsymbol{P(k+1/k) = A(T)P(k/k)A^T(T) + C_d(T)QC_d^T(T)} \quad \textbf{(30)}$$

$$\boldsymbol{K(k+1) = P(k+1/k)C^T(T)[C(T)P(k+1/K)C^T(T) + R]^{-1}} \quad \textbf{(31)}$$

$$\boldsymbol{P(k+1/k+1) = [I - K(k+1)C(T)]P(k+1/k)} \quad \textbf{(32)}$$

Where

$C_d(T)$: → is the disturbance transition matrix
Q: → is the disturbance noise covariance matrix
R: → is the measurement noise covariance matrix

The recursive process continues by substituting the covariance matrix P(k+1/k+1) computed in equation (32) back into equation (30) as P(k/k) until K(k+1) settles to a steady value. Equations (23) to (32) are illustrated in fig.6 [6] which shows the block diagram of the Kalman filter is

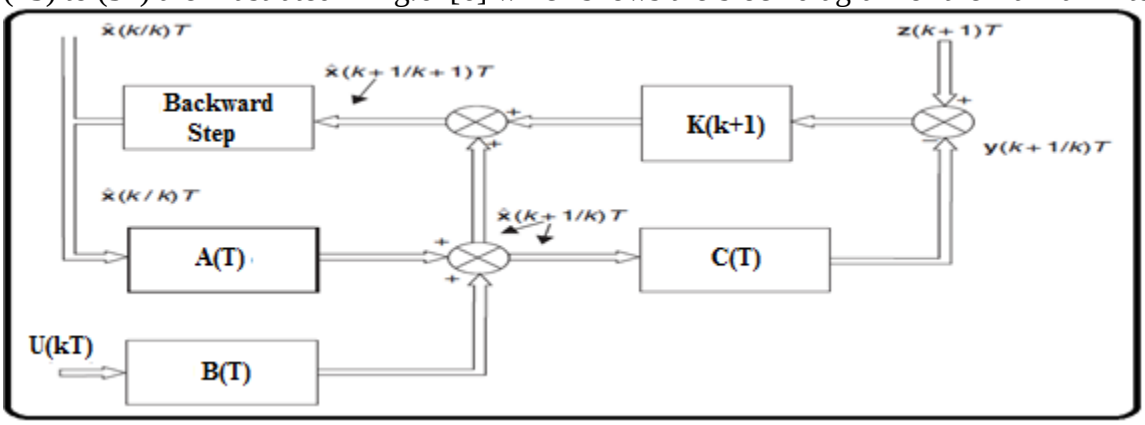

Figure.6 The Kalman Filter

The difference is that the Kalman filter is computed in forward-time, the LQR being computed in reverse-time

C. Linear Quadratic Gaussian (LQG) control system

A control system that contain a LQRegulator/Tracking controller together with a Kalman filter state estimator is called a Linear Quadratic Gaussian (LQG) control system. LQG is shown in fig. 7.

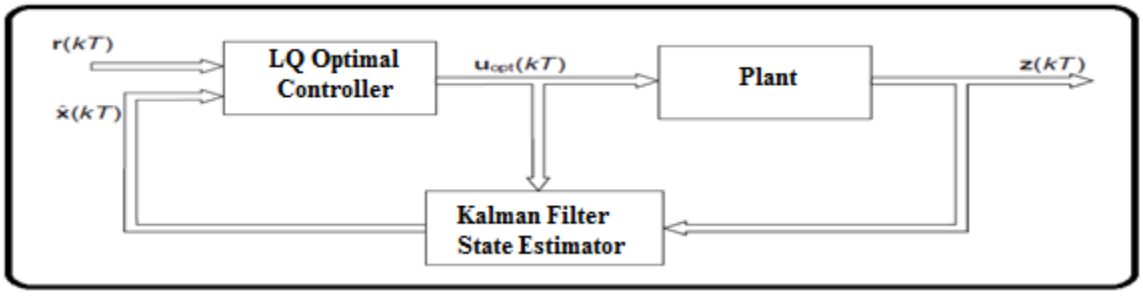

Figure.7 Linear Quadratic Gaussian (LQG) control system

LQG control can be applied to linear time invariant systems as well as linear time variant systems. It deals with uncertain linear systems disturbed by additive white gaussian noise, having incomplete state information. Practically it is used for predicting future courses of dynamic

systems. Designing of optimal LQG controller with the feedback controller designed in such a way that it minimizes cost function [4].

$$\boldsymbol{J = \lim_{n\to\infty} E[\frac{1}{T}\int_0^T (x^T(t)Qx(t) + u^T(t)Ru(t))dt]} \quad \textbf{(33)}$$

Where

$Q \geq 0\ and\ R > 0$: →are symmetric weighting matrices.

$E[\cdot]$: →is the expected value

In the cost function, the term x^TQx corresponds to a requirement to minimize the states of the system. the term u^TRu corresponds to the requirement to minimize the size of control inputs. The selection of matrices Q and R in the cost in the cost function depends on the desired performance objective of the system. Minimizing the tracking error between the command signal and measured output is the main control objective. The continuous time solution to the optimal observer problem is [8]

$$\boldsymbol{L = P_0 C^T R_0^{-1}} \quad \textbf{(34)}$$

Where $P_0$is the solution of the algebraic Riccati equation:

$$\boldsymbol{AP_0 + P_0 A^T - P_0 C^T R_0^{-1} C P_0 + Q_0 = 0} \quad \textbf{(35)}$$

The calculation was executed in Matlab using the kalman(sys,Qn,Rn,Nn) function. The function returns the discrete observer gain vector L if the system sys is in discrete time. The block diagram of the complete LQG controller can be seen on fig. 8 [10].

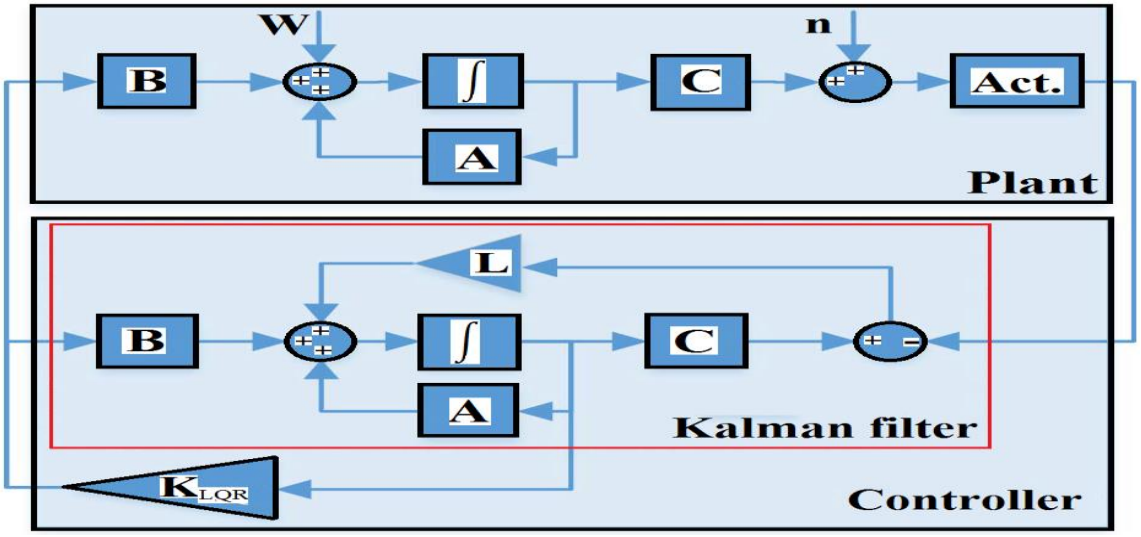

Figure.8 The LQG control system scheme.

Fig.8 shows the combination of the feedback gain matrix K_{LQR} and a Kalman Filter in closed loop with a state-space Plant description. A major advantage of the LQG controller design approach lies in the possibility to estimate the missing states, i.e. so the designer doesn't need to have a complete knowledge of the state vector. The next advantage is in the noise attenuation capabilities. However the cost for these features is in sacrificing the system's closed-loop robustness.

4. CLASSICAL CONTROL STRATEGY

A. PID CONTROLLER

Fundamentally, PID controllers are composed of three basic control actions. They are simple to implement and provide better performance. The tuning process of the gains of PID controllers

can be complex because it is iterative. First, it is necessary to tune the "Proportional" mode, then the "Integral", and then add the "Derivative" mode to stabilize the overshoot, then add more "Proportional", and so on. The PID controller has the following form in the time domain

$$\boldsymbol{U(t) = K_p e(t) + K_i \int_0^t e(t)dt + K_d \frac{de(t)}{dt}} \qquad \textbf{(36)}$$

Where

e(t): → is the system error (difference between the reference input and the system output).
u(t) : → is the control variable.
Kp: → is the proportional gain.
Ki : → is the integral gain.
Kd : → is the derivative gain.

The effects of these parameters on the output response of the system are shown in Table 1 [11]. A PID controller does not "know" the correct output to bring the system to the set point. It moves the output in the direction which should move the process toward the set point and needs to have feedback (measurements) to perform. Using the Laplace Transform for equation (36) and assuming initial conditions equal to zero the transfer function of the PID can be written as

$$\boldsymbol{G(s) = \frac{U(s)}{E(s)} = K_p + \frac{K_i}{s} + K_d s} \qquad \textbf{(37)}$$

Transfer function of a PID controller is rearranged, the three terms can be recognized follows:

$$\boldsymbol{G(s) = K_p \left(1 + \frac{1}{T_i s} + T_d s\right) = K_p \left(\frac{T_i T_d s^2 + T_i s + 1}{T_i s}\right)} \qquad \textbf{(38)}$$

Where:

Ti=Kp/Ki : → is the integral time constant
Td=Kd/Kp : → is the derivative time constant

Table 1: Effect of PID parameter on system response

Parameter	Rise-Time	Overshoot	Settling Time	Sready State Error	Stability
K_p	Decrease	Increase	Small Change	Decrease	Decrease
K_i	Decrease	Increase	Increase	Eliminate	Decrease
K_d	Minor Changes	Decrease	Decrease	No Effect	Improve if Kd is small

The selection of the Proportional Integral and Derivative (PID) controller parameters can be obtained using the Ziegler-Nichols method , trail and error method or other tuning methods. In terms of Ziegler-Nichols method, the PID controller parameters can be found depending on the values of as shown in fig.9 and using the Ziegler-Nichols equations.

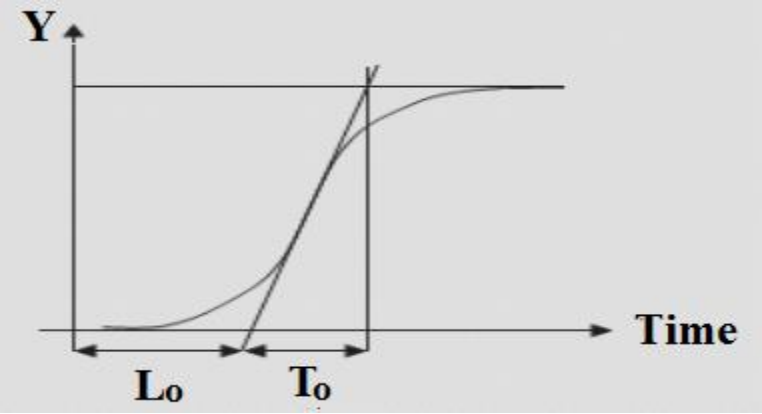

Figure.9 Zegiler-Nichols PID Parameters

Now, using the following equations, the PID parameters can be derived:

$$K_p = 1.2\frac{T_o}{L_o} \quad (39)$$

$$T_i = 2L_O \quad (40)$$

$$T_d = 0.5L_O \quad (41)$$

In this paper, the PID controller parameters can be obtained by the help of optimal control methods

5. Analysis Of Simulation Results Of LQR And LQG Optimal Controllers Based On Kalman Filter

The modeling of three phase permanent magnet brushless direct current (PMBLDC) motor with classical and optimal controllers has been derived. in addition to that, simulation and performance analysis of the PMBLDC motor with and without optimal controllers have been implemented and investigated by using MATLAB/SIMULINK software. The goal of control engineering design is to obtain the configuration, specifications, and identification of the key parameters of a proposed system to meet an actual need [12-13]. Establishment of goals and variables to be controlled, The most basic requirement of PMBLDC motor is that it should rotate at the desired output response (desired value or reference input), as well as, optimals controllers are used for reducing the sensitivity of the actual output response to external load (external disturbances), load variations (changes in the torque opposed by the motor load), noise and parameters changes , where the actual output response variations induced by such disturbances must be minimized .

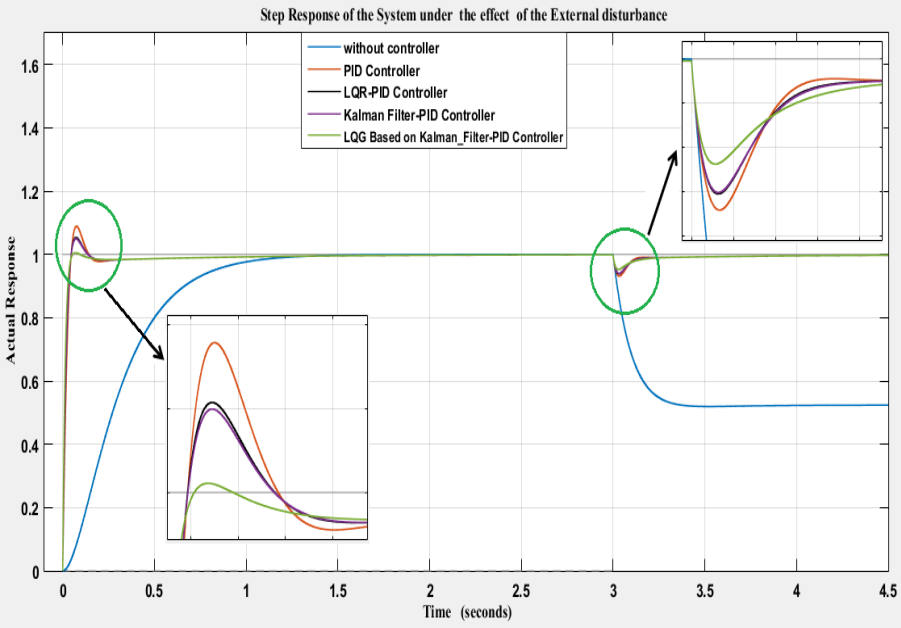

Figure.10 Simulation results of the PMBLDC motor with PID, LQR-PID, Kalman Filter-PID and LQG based on Kalman Filter-PID controllers.

Table 2: A comparison of the simulation results of the PMBLDC motor with classical and optimal control strategy in terms of time response specifications

The PMBLDC Motor with the Effect of External Disturbance				
Time Domain Specifications	Strategy of Control			
	Classical Control Strategy	Optimal Control Strategy		
	PID Controller	LQR-PID Controller	Kalman Filter-PID Controller	LQG Based on Kalman_Filter-PID Controller
Settling Time (t_s)	0.2420 Sec	0.1134sec	0.1117 sec	0.0421 sec
Maximum Overshoot (M_p)	8.9353 %	5.3674%	4.9728 %	0.54333%
Peak Time (t_p)	0.075 Sec	0.072sec	0.072 sec	0.068 sec
Rise Time (t_r)	0.034 Sec	0.031sec	0.0315 sec	0.026 sec
Delay Time (t_d)	0.0133 sec	0.0103 sec	0.01 sec	0.0061 sec
Steady state error (e_{ss})	0.000030477	0.000028722	0.000027152	0.000024772
Damping ratio (ζ)	0.60948	0.68141	0.69076	0.85659

Table 3: A comparison of the simulation results of the PMBLDC motor with classical and optimal control strategy in terms of frequency response specifications

The PMBLDC Motor with the Effect of External Disturbance				
Frequency Domain Specifications	**Strategy of Control**			
	Classical Control Strategy	**Optimal Control Strategy**		
	PID Controller	**LQR-PID Controller**	**Kalman Filter-PID Controller**	**LQG Based on Kalman_Filter-PID Controller**
Phase Margin (P.M)	**84.5691 ^{0}**	**88.115 ^{0}**	**88.4233 ^{0}**	**90.9835 ^{0}**
Gain Margin (G.M)	**Inf dB**	**Inf dB**	**Inf dB**	**Inf dB**
Bandwidth (ω_b)	**121.6004 Hz**	**148.7355 H**	**151.1262 Hz**	**208.8586 Hz**
Resonant Peak (M_r)	**1.0348**	**1.0026**	**1.0010**	**1.1312**
Resonant Frequency (ω_r)	**54.2915 Hz**	**38.3434 Hz**	**31.5745 Hz**	**Damping ratio (ζ) =0.85**

Table 4: Comparison for all performance indices parameters of the PMBLDC motor with classical and optimal control strategy

The Three Phase PMBLDC Motor without the effect of external load [T_L(s)]				
Strategy of Control	**Performance Criteria**			
	IAE $IAE = \int_0^t \lvert e(t)\rvert dt$	**ITAE** $ITAE = \int_0^t t\lvert e(t)\rvert dt$	**ISE** $ISE = \int_0^t (e(t))^2 dt$	**ITSE** $ITSE = \int_0^t t(e(t))^2 dt$
PID Controller	**0.0001523856**	**0.0003809641**	**0.0000000046**	**0.0000000116**
LQR-PID Controller	**0.0001436105**	**0.0003590263**	**0.0000000041**	**0.0000000103**
Kalman Filter-PID Controller	**0.0001357600**	**0.0003394001**	**0.0000000037**	**0.0000000092**
LQG Based on Kalman_Filter-PID Controller	**0.0001238615**	**0.0003096539**	**0.0000000031**	**0.0000000077**

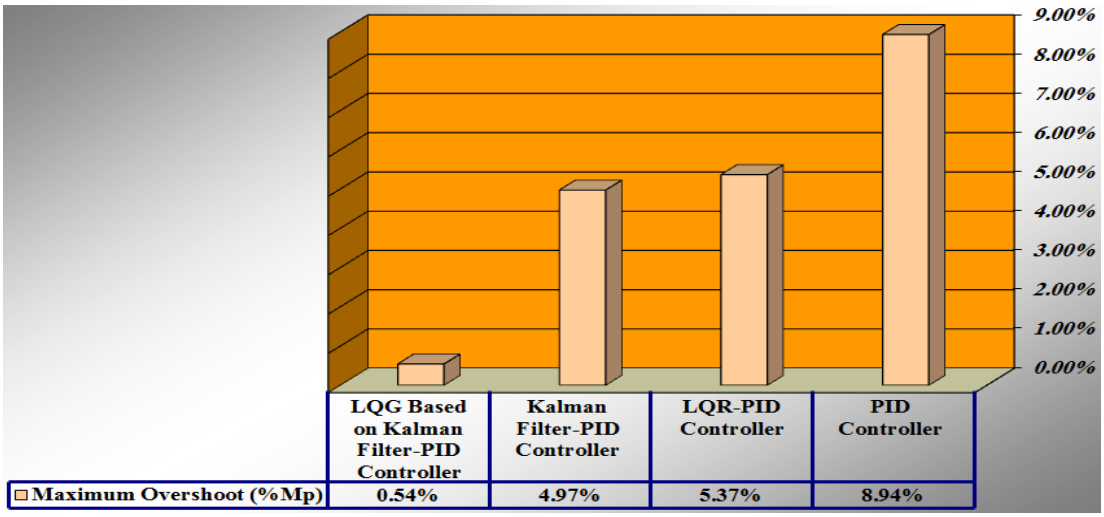

Figure.11 Comparison of maximum overshoot (%Mp) for classical and optimal control strategy

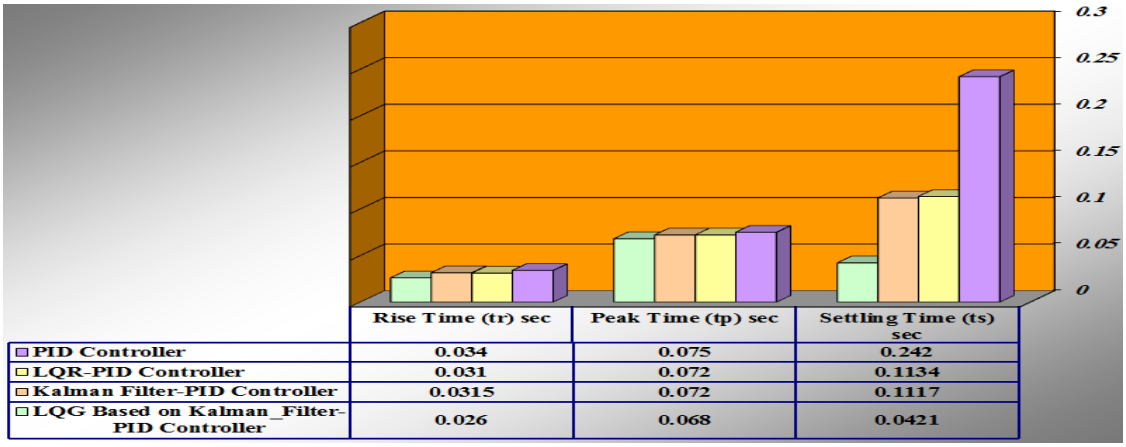

Figure.12 Comparison of Rise Time (t_r), Peak Time (t_p) and Setting Time (t_s) for classical and optimal control strategy

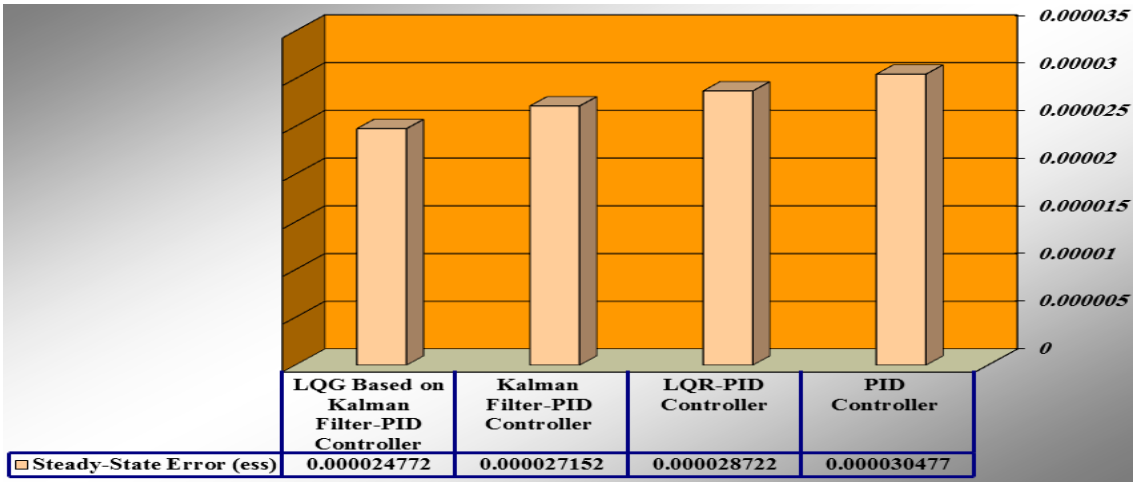

Figure.13 Comparison of Steady State Error (e_{ss}) for classical and optimal control strategy

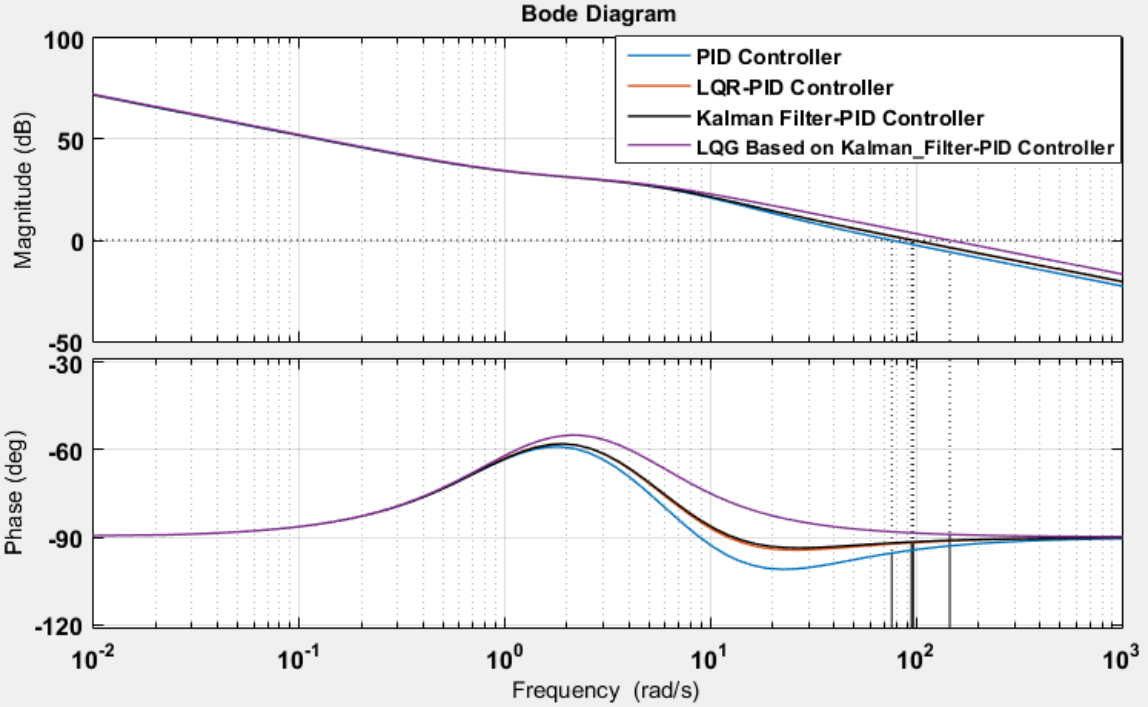

Figure.14 Bode Diagram of the PMBLDC motor with PID, LQR-PID, Kalman Filter-PID and LQR based on Kalman Filter-PID controllers

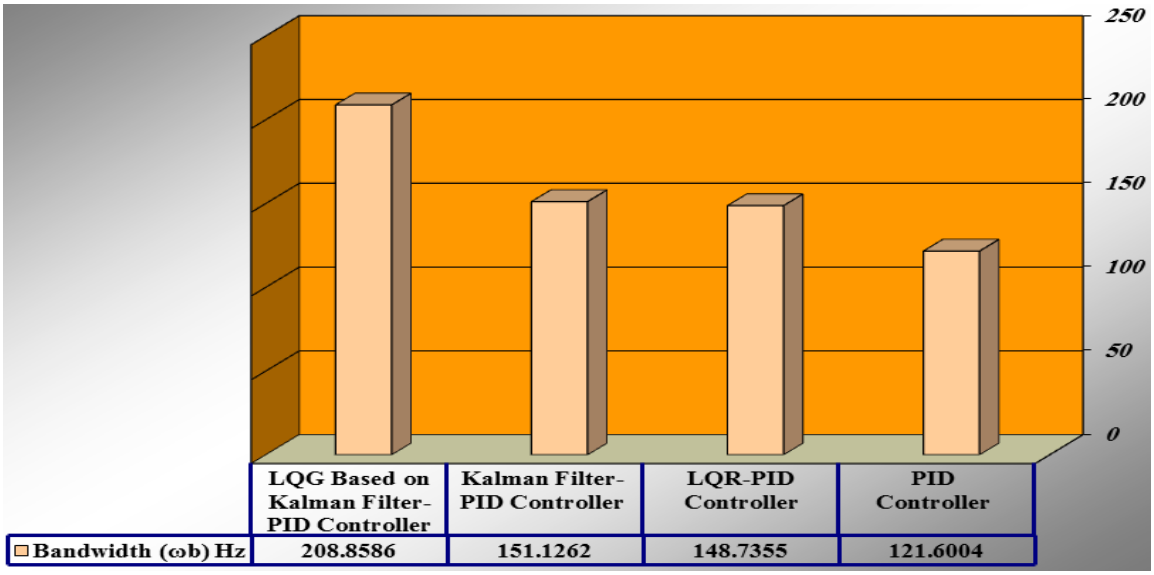

Figure.15 Comparison of Bandwidth (ω_b) for classica l and optimal control strategy

As a result of the simulation, LQG based on Kalman Filter-PID controller is the best controller compared to other controllers, which presented satisfactory performances, process good robustness and also perfect speed tracking. The main objective of controllers is to minimize the error signal or in other words the minimization of performance criteria. Therefore, A set of performance

indicators (Integral Absolute Error (IAE), Integral Time Absolute Error (ITAE), Integral Square Error (ISE), Integral Time-weighted Squared Error (ITSE)) have been used as a design tool aimed to evaluate tuning methods results. Performance criteria shows the superiority of , LQG based on Kalman Filter-PID control method over PID, LQR-PID and Kalman Filter-PID control methods.

6 . Conclusion

This paper has demonstrated that the performance of a BLDC motor can be improved by using LQR and LQG optimal Controllers Based on Kalman Filter with PID controller for disturbance attenuation and noise suppression. The actual output response of the permanent magnet brushless direct current (PMBLDC) Motor is controlled by means of the PID control method, LQR-PID control method, and LQG based on Kalman filter PID control method for enhancement the stability and accuracy under the effect of load variations, external disturbances, noise and parameters changes. In this paper, with reference to the results of the computer simulation by using (MATLAB & SIMULINK) software, the performance characteristics of classical and optimal controllers are compared in terms of the time response and frequency response. The simulation results illustrate that LQG Based on Kalman Filter-PID Control method performs better than PID, LQR-PID and Kalman filter-PID control method, and has verified all design requirements of the system. LQG Based on Kalman Filter-PID Control method is the best Controller which presented satisfactory performances and possesses good robustness This control method seems to have a lot of promise in the real world application.

7. References

[1] Padmaraja Yedamale, "Brushless DC (BLDC) motor Fandamentals" Microchip Technology Inc., 2003.

[2] Krause, P. C. (1986) Analysis of Electric Machinery. Kinsport Press Inc., Kinsport Town.

[3] Pillay, P., Krishnan, R. (1989) Modeling, simulation, and analysis of permanent-magnet motor drives, part II: the brushless DC motor drive. IEEE Transactions on Industry Application, 25(2), 274–279.

[4] Mizanur Rahman∗, Subroto K. Sarkar∗ Sajal K. Das∗ and Yuan Miao “A Comparative Study of LQR, LQG, and Integral LQG Controller for Frequency Control of Interconnected Smart Grid” 2017 3rd International Conference on Electrical Information and Communication Technology (EICT), 7-9 December 2017, Khulna, Bangladesh.

[5] E. Lavretsky and K. A. Wise, Robust and Adaptive Control, London,
England: Springer, 2013.

[6] Roland Burns , Advanced Control Engineering, Copyright © 2001 Elsevier Ltd. All rights reserved, ISBN 978-0-7506-5100-4, Imprint: Butterworth-Heinemann

[7] C. Olalla, R. Leyva, A. El Aroudi, and I. Queinnec, “Robust lqr control
for pwm converters: an lmi approach,” Industrial Electronics, IEEE Transactions on, vol. 56, no. 7, pp. 2548–2558, 2009.

[8] R. Tymerski, A. Chuinard, and F. Rytkonen, “Applied classical and modern control system design,” Lecture Notes, ECE451, Portland State University.

[9] Bence Kurucso , Alfr ed Peschka, P eter Stumpf, Istv an Nagy IEEE Life Fellow,Istv an Vajk "State Space Control of Quadratic Boost Converter using LQR and LQG approaches" 2015 Intl Aegean Conference on Electrical Machines & Power Electronics (ACEMP), 2-4 Sept. 2015 Intl Conference on Optimization of Electrical & Electronic Equipment (OPTIM) & 2015 Intl Symposium on Advanced Electromechanical Motion Systems.

[10] Jan Vlk and Peter Chudy "General Aviation Digital Autopilot Design Based on LQR/LQG Control Strategy" Published in**:** 2017 IEEE/AIAA 36th Digital Avionics Systems Conference (DASC). DOI**:** 10.1109/DASC.2017.8102058.

[11] Ahmad M. EL-Fallah, Surya Prakash, " Enhancement of Stability and Accuracy of the SEDC Motor under the Effect of the External Disturbances and Noise by Using PID Controller" Int. J. on Recent Trends in Engineering and Technology, Vol. 6, No. 1, Nov 2011.

[12]. B. Kuo, Automatic Control Systems, Prentice-Hall, Englewood, Cliffs. NJ, 1995.

[13] N. S. Nise, Control Systems Engineering (3rd Edition), John Wiley and Sons Inc., New York, 2000.

SJST Surman Journal for Science and Technology | ISSN: E 2790-5721 P 2790-5713
Vol.3, No.1, Dec 2021, pp. 135 - 145

تأثير الارتفاع عن سطح البحر على الخصائص الكيميائية للزيت العطري لنبات الزعتر البري النامي في مناطق متفرقة من الجبل الأخضر

حنان علي ادريس[1]، عبدالسلام البخاري[2]، أحمد جبريل محمد ابوبكر[3]، عبدالمنعم فكرون[4] لمياء عبدالجليل[5]، مريم الجنيد[6].

[2،1] . قسم الغابات والمراعي، كلية الموارد الطبيعية وعلوم البيئة، جامعة عمر المختار، البيضاء، ليبيا.
[3] . قسم الكيمياء، كلية العلوم ،القبة، جامعة درنة.
[4]. قسم الاحياء الدقيقة، كلية العلوم، جامعة عمر المختار، البيضاء، ليبيا
[5] . قسم علوم البيئة، كلية الموارد الطبيعية وعلوم البيئة، جامعة عمر المختار، البيضاء، ليبيا.
6 . قسم الغابات والمراعي، كلية الموارد الطبيعية وعلوم البيئة، جامعة عمر المختار، البيضاء، ليبيا.

Corresponding author: abdlmanam.fakron@omu.edu.ly

الملخص

استهدفت هذه الدراسة معرفة تأثير الارتفاعات المتباينة عن سطح البحر على المحتوى الكيميائي لكل من الزيوت العطرية والمستخلصات لنبات الزعتر البري Thymus capitatus حيث تم اختيار موقعي أبو ذراع وسيدي الحمري، جمعت العينات النباتية تم تجفيف أجزاء النبات المستخدمة في الدراسة، تم استخلاص الزيت الطيار لكل عينة باستخدام طريقة التقطير المائي، تم تحضير المستخلصات الخام وذلك بإتباع طريقة الاستخلاص المتعاقب ثم أجريت طريقة الفصل الكروماتوجرافي باستخدام ألواح الطبقة الرقيقة (TLC)، والتعرف على مكونات كل زيت من الزيوت الطيارة المتحصل عليها من النباتات بواسطة GC/MS. أوضحت نتائج الدراسة وجود اختلاف كمي وكيفي في المُحتوى الكيميائي للزيوت العطرية للنبات نتيجة اختلاف مواقع الدراسة، كانت النسبة المئوية للزيت العطري المتحصل عليه من نبات الزعتر البري من موقعي أبو ذراع وسيدي الحمري (1.5%، 1.06%) على التوالي. أظهرت نتائج GC/MS عن التعرف على عدد 12 مركب عطري بنسبة (95.97%) من إجمالي مكونات الزيت العطري لنبات الزعتر البري من موقع أبو ذراع، وعدد 20 مركب عطري بنسبة (87.53%) في زيت الزعتر البري من موقع سيدي الحمري، ولقد كان هناك عدد 7 مركبات عطرية مشتركة في مواقع الدراسة وهي-Aromadendrene, Gamma-terpinene, Alpha-thujene, Thymol, Carvacrol , Delta-cadinene , Alpha-humulene، ولقد كان مركب Carvacrol له أعلى نسبة تواجد في الموقعين أبو ذراع وسيدي الحمري بالنسبة لزيت نبات الزعتر البري (48.56%، 21.28%) على التوالي. وكان محتوى الهيدروكربونات أحادية التربين الغير مؤكسجة والمؤكسجة لها أعلى نسبة تواجد في المحتوى الكلي للزيت العطري تحت الدراسة، كما تم تحضير الخلاصات المختلفة من النباتين تحت الدراسة (خلاصات الهكسان والكلوروفورم والإيثانول بطريقة الاستخلاص المتتابع، كما تم أيضاً تحضير الخلاصة الكحولية الكلية الخام باستخدام طريقة الاستخلاص المباشر). تم فصل محتويات هذه الخلاصات على ألواح من السيلكاجل بواسطة عدة أنظمة للفصل كما تم تحديد عدد الحزم المفصولة في كل خلاصة وحساب قيم RF لكل حزمة.

الكلمات المفتاحية:
الزعتر البري، الزيوت العطرية الطيارة، ألواح الطبقة الرقيقة (TLC)، الجبل الأخضر

Abstract

This study aimed to identify the effect of different altitudes above sea level on the chemical content of each of the essential oils and extracts of wild thyme, Thymus capitatus .Where the locations of Abu Dhra` and Sidi Al Hamri were selected, the plant samples were collected, the plant parts used in the study were dried, the volatile oil was extracted for each sample using the water distillation method, the crude extracts were prepared by following the successive extraction method, then the chromatographic separation method was carried out using thin-layer plates (TLC), and identification of the components of each volatile oil obtained from plants by GC/MS. The results of this study showed a quantitative and qualitative difference in the chemical content of the plant's essential oils as a result of the different study sites, the percentage of essential oil obtained from wild thyme from Abu Dra` and Sidi Al Hamri sites were (1.5%, 1.06%), respectively .The results of GC/MS showed the identification of 12 aromatic compounds with a percentage of (95.97%) of the total components of the essential oil of wild

thyme from Abu Dhra' site, and 20 aromatic compounds with a percentage of (87.53%) in wild thyme oil from Sidi Al-Hamri site, there are 7 common aromatic compounds in the study sites, which are Aromadendrene, Gamma-terpinene, Alpha-thujene, Thymol, Carvacrol, Delta-cadinene and Alpha-humulene. Berry (48.56%, 21.28%), respectively. The content of deoxygenated and oxygenated monoterpene hydrocarbons had the highest presence in the total content of the essential oil under study .The different extracts of the two plants under study were also prepared (extracts of hexane, chloroform and ethanol by successive extraction, and the total crude alcoholic extract was also prepared using the direct extraction method). The contents of these extracts were separated on silica gel plates by several separation systems and the number of separated packets in each feed was determined and RF values were calculated for each bundle.

Keywords: *Thymus capitatus , Essential Oil, Thin-layer plates (TLC), Al Jabal Al Akhdar.*

1. المقدمة

تضم منطقة الجبل الأخضر بليبيا العديد من النباتات العطرية النامية برياً والتي تعتبر ثروة طبيعية هامة يجب الاهتمام بها والاستفادة منها ودراستها. إن العديد من هذه النباتات العطرية ينتمي إلى العائلة الشفوية (Lamiaceae) حيث تنمو برياً في منطقة حوض البحر الأبيض المتوسط[1]. وتعتبر هذه النباتات غنية بمحتواها من الزيوت العطرية الطيارة ذات القيم الاقتصادية العالية حيث يُضاف إلى الصناعات الغذائية كمادة حافظة ومضادة للأكسدة [2] [3] أثناء التخزين وفي تركيب بعض الأدوية والمستحضرات الطبية وفي صناعات الصابون والمنظفات الأخرى[4] ومن بين هذه النباتات نبات الزعتر وهو المعروف باسم الزعتر البري (L.) *Thymus capitatus*، يعتبر هذا النوع من الزعتر من الأنواع المعروفة والمتواجدة بكثرة في منطقة البحر المتوسط وبالأخص في تركيا، اليونان، اسبانيا، وهما من النباتات العشبية المستديمة الخضرة، ينموان في الأرض ذات التربة الصخرية والجيرية، ويعتبر نبات الزعتر من النباتات التي تتحمل درجات الحرارة المنخفضة وكذلك الفترات الطويلة من الصقيع والثلوج [5].

ولقد أجريت العديد من الدراسات على المُحتوى الكيميائي للزيوت الطيارة المستخلصة من نبات الزعتر لمعرفة المكونات الكيميائية وتقدير كمياتها كما ذكر كل من [6] ،[7] ، [8]. قام [9] بدراسة مقارنة للمحتوى الكيميائي للزيت الطيار ونسبة تواجده في نبات *Thymus vulgaris* وذلك أثناء مراحل النمو المختلفة في مناطق منخفضة وأخرى مرتفعة جبلية ووجد أن أعلى نسبة للزيت الطيار قد تم الحصول عليها من المناطق المنخفضة وفي فترة ما بعد الإزهار. كما قام [10] بدراسة وتحليل الزيت العطري لأربعة نباتات عطرية تشتهر بها منطقة ساحل البحر المتوسط وهي: *Coridothymus capitatus, Satureja spinosa, Satureja thymbra, Thymbra calostachya* ووجد أن هذه النباتات غنية بمحتواها من الزيت العطري حيث تصل نسبته 2.6-8.5%، كما وجد أن هناك أربعة مكونات تعتبر المكونات الرئيسية للزيوت العطرية للنباتات الأربعة تحت الدراسة وهى كالآتي:-

P-cymene (13-20%, 10-12%, 22%, 5%) gama-terpinene (7-14%, 25-28%, 6%, 3%) أما مركب Thymol تصل نسبته إلى (0.4-34%, 0.3-36%, 21%, 21%)، مركب Carvacrol تصل نسبته إلى (63%-5 , 3-45%, 41%, 48%) على التوالي للنباتات الأربعة. أجريت دراسة [11] للتعرف على التركيب الكيميائي لمُحتوى الزيت الطيار المُحضر من نبات S.hortensis بواسطة التقطير المائي للنبات تحت الدارسة وذلك بواسطة كروماتوجرافيا الغاز المدمج مع مطياف الكتلة . تم التعرف على 30 مركباً وكان مركب Thymol يمثل 40.54 من محتوى الزيت الطيار، مركب γ-terpinene (18.56%)، Carvacrol (13.98%) ومركب P-cymene (8.97%). في عام [25] تم دراسة المحتوى الكمي للزيت العطري والكيميائي المستخلص من نبات *T. caramanicus* النامي في إيران، أظهرت هذه الدراسة اختلافات كمية وكيفية للزيوت المستخلصة للنبات في مراحله المختلفة (أثناء النمو الخضري، بداية التزهير, التزهير الكامل وخلال مرحلة تكوين الثمار والبذور)، لقد كانت نسب الزيت العطري المستخلص من النبات في مراحله المختلفة كالآتي: 1.9%, 2.1%, 2.5%, 2.0% على التوالي وعند تحليل هذه الزيوت باستخدام GC/MS فقد تم التعرف على 37,37, 29, 35 مركباً عطرياً على التوالي. المحتوى الرئيسي في كل العينات كان مركب carvacrol أما المركبات العطرية الرئيسية الأخرى كالآتي: P-cymene, alpha-terpinene, thymol, borneo. كذلك أجرى [12] دراسة على المحتوى الكيميائي للزيوت العطرية الناتجة من نبات *T. vulgaris , T. tosevii* وتم تحضير هذه الزيوت بواسطة التقطير المائي للأجزاء الجافة للنباتين, كما تم تحليلها بواسطةGC/MS . ولقد وجد أن المركبان thymol (48.9%), P-cymene (19.0%) يعتبران من المكونات الرئيسية للزيت العطري الناتج من نبات *T. vulgaris*, أما مركبات carvacrol (12.8%)، alpha-terpinyl acetate (12.3%), cis-myrtanol (11.2%), thymol (10.4%) تعتبر المكونات الرئيسية للزيت العطري لنبات *T. tosevi*، (*Thymus tosev*، *Thymus longidens* ، *Thymus moesiacus*) وأصنافهم المختلفة، ولقد لوحظ عدم وجود فروق كيفية واضحة في المحتوى الكيميائي للزيوت العطرية المستخدمة كما لوحظ بعض الفروق الكمية

لبعض من المركبات العطرية التي تم التعرف عليها والتي تضم Thymol، Carvacrol، p-cymene، β-pinene, Gamma-terpinene, Linalool ، geranyl acetate ، Terpinyl acetate، كما وجد أن معظم العينات تحت الدراسة يحتوي الزيت العطري لها على مركبات فينولية عطرية بنسب عالية مثل Thymol، carvacrol ، ولوحظ أن هناك بعض الأصناف من النباتات تحت الدراسة تحتوي على زيت عطري قليل في محتواه الفينولي وفي نفس الوقت يحتوي على نسب عالية من Linalool، geraniol، terpinyl acetate ، geranyl acetate مثل Thymus moesiacus.

لقد أشار [13] أن نتائج المسح الكيميائي لنبات *T . capitatus* المزروع في مِصر أسفر عن وجود صابونينات , راتنجات, فلافونيدات, وزيت عطري وزيت ثابت. وفي دراسة قام بها [14] تم تحليل الزيت العطري المستخلص من نبات *T. capitatus* النامي في سردينيا وكذلك عينات تجارية من هذا الزيت بواسطة GC/MS ولقد أسفرت هذه التحاليل عن أن المحتوى العطري الرئيسي يتكون من مركبات أحادية التربين وفينولات, بنسب مختلفة في الزيوت العطرية تحت الاختبار. لقد وجد [4] أن المركبات الرئيسية للزيت الطيار *لنبات Coridothymus capitatus* المستخلص بواسطة التقطير المائي للأجزاء الهوائية للنبات هي من نوع أحادية التربين (98.9%) منها 55.6%هيدروكربونات مؤكسجة, 43.6% هيدروكربونات غير مؤكسجة. حيث أن carvacrol, p-cymene, thymol, gamma-terpinene, alpha-terpinene, B-myrecene , alpha-thujene تعتبر من المركبات الرئيسية لهذا الزيت الطيار على التوالي وذلك من خلال تحليلها بواسطة كروماتوجرافيا الغاز المدمج بمطياف الكتلة. كما أشارت الدراسة التي أجراها [2] أن مركب carvacrol يمثل نسبة 68%, 73% للزيت الطيار المستخلص بواسطة التقطير المائي للأجزاء الهوائية لنبات *T capitatus*. الذي ينمو في تونس في مرحلة الأزهار وما قبل الإزهار وذلك باستخدام كروماتوجرافيا الغاز المتصل بمطياف الكتلة. ومن خلال استعراض نتائج الدراسات السابقة على الأنواع المختلفة لنبات الزعتر يوجد اختلاف في التركيب الكيميائي للزيوت العطرية والمستخلصات بين هذه الأنواع المختلفة وأيضاً اختلاف كيميائي لنفس النوع نظراً لاختلاف البيئات والتوزيع الجغرافي، و حيث تم اختيار موقعين على ارتفاعات مختلفة عن سطح البحر في منطقة الجبل الأخضر، والجدير بالذكر أن ليبيا لم تحظى بدراسات كافية لهذان النوع من حيث إيجاد علاقة بين اختلاف الارتفاع عن مستوى سطح البحر والمحتوى الكيميائي للزيوت الطيارة والمستخلصات وكان هدف هذه الدراسة هو دراسة المحتوى الكيميائي للزيوت العطرية وبعض المستخلصات من الأجزاء الهوائية (الأزهار- الأوراق- السيقان) للعينات المختلفة من النباتين وإجراء مقارنة كروماتوجرافية بينهما.

2. المواد وطرق العمل

2. 1. جمع العينات النباتية وتجهيزها:-

تم الحصول على عينات من الأجزاء الهوائية من الزعتر البري *Thyms capitatus* كما في شكل (1) من موقعين مختلفين (50 نبتة من مواقع عشوائية في كل منطقة)، خلال خريف 2017 وخريف 2018 من نباتات في الجبل الأخضر بليبيا، موقع أبو ذراع وسيدي الحمري حيث يقعان عند إحداثيات شمالاً و شرقاً (1.5% ، 1.06%) وبارتفاع (653 ، 830) متر فوق سطح البحر على التوالي. ولقد تم تعريف النبات طبقاً لما وصف في الفلورا الليبية [15]. تم تجفيف أجزاء النبات المستخدمة في الدراسة وذلك بوضعها في مكان ظليل لمدة 7 – 10 أيام مفردة في طبقة رقيقة وتقلب باستمرار [5] ثم بعد ذلك تم طحنها في الطاحونة للحصول على هذه النباتات تحت الدراسة في شكل مسحوق جاف ثم تحفظ في عبوات داكنة اللون محكمة الإغلاق بعيداً عن الضوء.

2. 2. تقدير الرطوبة:-

تم تقدير المحتوى الرطوبي في العينات التي قد تم جمعها وطحنها وتجفيفها من المواقع المختلفة تحت الدراسة وذلك قبل إجراء عمليات الاستخلاص وحساب العائد المتحصل عليه على أساس الوزن الجاف لكل عينة، ولقد اتبعت طريقة التقطير مع مذيب عضوي (تولوين Toluene) حيث أنه غير قابل للامتزاج مع الماء، وذلك لاحتواء العينات على زيوت طيارة تبعاً لطريقة [16]و [17]

استخلاص الزيوت الطيارة :-

تم استخلاص الزيت الطيار لكل عينة من كل موقع تحت الدراسة باستخدام طريقة التقطير المائي (Hydrodistillation) تبعاً لطريقة [18] و[19].

2. 3 تحضير المستخلصات المختلفة :-

تم تحضير المستخلصات الخام وذلك بإتباع طريقة الاستخلاص المتعاقب (Successive extraction) [20] .

طريقة الفصل الكروماتوجرافي باستخدام ألواح الطبقة الرقيقة (TLC): [21] كما إنه يمكن الاستعانة باستخدام الأشعة الفوق بنفسجية (U.V) عند طول موجة 365 نانوميتر.

طريقة كروماتوجرافيا الغاز المدمج بمطياف الكتلة للزيوت العطرية (GC/MS):-
- تم التعرف على مكونات كل زيت من الزيوت الطيارة المتحصل عليها من النباتات تحت الدراسة بواسطة GC/MS في قسم تصنيف النبات، كلية العلوم، جامعة عمر المختار، البيضاء، ليبيا. طبقاً لطريقة [22].

3. النتائج والمناقشة

3. 1 استخلاص الزيوت الطيارة وتحضير المستخلصات المختلفة :

احتوت الأجزاء الهوائية لنبات الزعتر البري موقع أبو ذراع على 1.5% زيت طيار بينما الزعتر البري موقع سيدي الحمري على 1.06% زيت طيار، جدول (2) يوضح أن هناك فروق معنوية عالية في النسب المئوية للزيوت العطرية المستخلصة من نباتي الزعتر البري بين الموقعين. كانت هذه الزيوت مشابهة في اللون والرائحة والإذابة مع الاختلاف في الكثافة النوعية.

جدول (2) يوضح الخواص الطبيعية والنسبة المئوية للزيت الطيار في الوزن الجاف للعشب

الخواص الطبيعية	Thymus capitatus	
	موقع أبو ذراع	موقع سيدي الحمري
النسبة المئوية	%15b	% 1.06c
الكثافة النوعية	0.7792	0.8373
اللون	أصفر فاتح	
الرائحة	عطرية نفاذة	
الإذابة	لا يذوب في الماء والإيثانول – يذوب في الأيثر والهكسان والكلوروفورم	

الحروف المتشابهة تعني عدم وجود فروق معنوية ، والغير متشابهة تعني وجود فروق معنوية.

كذلك تبين زيادة في عائد الاستخلاص بزيادة قطبية المذيب حيث أن الاستخلاص بالطريقة المباشرة (الخلاصة الكحولية الكلية الخام) يعطي عائداً أعلى مقارنة بالاستخلاص بالمذيبات بالطريقة المتتابعة جدول (3)، وكانت عائد الخلاصة الكحولية الكلية الخام مع كل من الزعتر البري موقع (أبو ذراع ـــــ وسيدي الحمري) بنسبة (7.88% ، 13.22%)، على التوالي، ويتضح من ذلك أن المواقع المرتفعة تعطي أعلى عائد من المواقع المنخفضة، أما نتائج عائد الاستخلاص باستخدام المذيبات بالطريقة المتتابعة (هكسان، الكلوروفورم، إيثانول) لوحظ أن خلاصة الهكسان لنبات الزعتر البري من الموقعين (أبو ذراع ـ سيدي الحمري) نسبتهما (3.8%، 3.82%) تليه خلاصة كلوروفورم بنسبه (3.22%، 3.36%) ثم خلاصة الإيثانول بنسبة (5.73%، 9.32%) على التوالي، حيث لوحظ أن خلاصة الإيثانول تعطي أعلى عائد يليها خلاصة الهكسان ثم الكلوروفروم، يلاحظ أيضاً في الطريقة المتتابعة أن عائد الزعتر البري أعلى بالمواقع الأعلى ارتفاع في حالة خلاصة الإيثانول.

جدول(3) النسب المئوية المختلفة للخلاصات النباتية التي قد تم تحضيرها من النباتين تحت الدراسة.

الموقع	الخلاصات	النسبة المئوية
موقع أبوذراع	A	7.88%
	B	3.8%
	C	3.22 %
	D	5.73 %
موقع سيدي الحمري	A	13.22 %
	B	3.82 %
	C	3.36 %
	D	9.32 %

A ـ خلاصة الكحولية الكلية الخام .
B ـ خلاصة الهكسان الناتجة من الاستخلاص المتتابع بواسطة السوكسلت.
C ـ خلاصة الكلوروفورم الناتجة من الاستخلاص المتتابع بواسطة السوكسلت.
D ـ خلاصة الأيثانول الناتجة من الاستخلاص المتتابع بواسطة السوكسلت.

3. 2. توصيف الزيوت العطرية والمستخلصات المختلفة من نبات الزعتر البري بواسطة (TLC) (كروماتوجرافيا الطبقة الرقيقة) :

تم فصل مكونات الزيوت الطيارة لنبات الزعتر البري التي قد تم تحضيرها بالتقطير المائي وذلك باستخدام كروماتوجرافيا الطبقة الرقيقة (TLC)، تم استخدام نسب مختلفة من بعض المذيبات العضوية كطور متحرك وذلك لتحديد الخليط الأفضل لفصل مكونات الزيت جدول (4). أوضحت النتائج أن أفضل النظم المستخدمة هو خليط الهكسان: خلات الإيثايل (90: 10 v/v) تحت نفس الظروف. أظهرت نتائج الفحص الكروماتوجرافي عدم ظهور حزم ملونة عند الفحص في الضوء المنظور للمواقع تحت الدارسة، أما عند الرش بالجوهر الكاشف فانيلين/حمض الكبريتيك، بينت النتائج جدول (5) ظهور عدد من الحزم الملونة يتراوح عددها من (9، 8) للزعتر البري من موقع أبو ذراع وسيدي الحمري على التوالي، وتتراوح قيم RF (معدل الاحتباس)

بين (0.2 - 0.79) بالنسبة لموقع أبو ذراع، (0.19 – 0.79) موقع سيدي الحمري، ولوحظ وجود 6 مكونات أساسية تتشابه في زيت الزعتر البري T. capitatus من موقعي أبو ذراع وسيدي الحمري ولهم قيم Rf (0.25، 0.36، 0.55، 0.65، 0.75، 0.79) ذات ألوان مختلفة بعضها بنفسجي، وردي، أزرق، بنفسجي غامق.

جدول (4) النتائج المتحصل عليها من الفصل الكروماتوجرافي بواسطة TLC (كروماتوجرافيا الطبقة الرقيقة) للزيوت الطيارة المستخلصة من نباتي الزعتر البري *Thymus capitatus* من مواقع تحت الدراسة باستخدام الطور المتحرك Hexan : ethyl acetate (90 : 10 v/v).

الموقع وعدد الحزم	الضوء المنظور Visible light		استخدام الجوهر الكشاف محلول فنيلين/حمض الكبريتيك	
الموقع (أبوذراع)	لون الحزمة	R F (معدل السريان)	لون الحزمة	R F (معدل السريان)
1	-	-	أزرق فاتح	0.2
2	-	-	بنفسجي	0.25
3	-	-	أزرق غامق	0.36
4	-	-	أزرق	0.41
5	-	-	بنفسجي فاتح	0.48
6	-	-	بنفسجي فاتح	0.55
7	-	-	وردي	0.65
8	-	-	وردي	0.75
9	-	-	بنفسجي فاتح	0.79
الموقع (سيدي الحمري)	لون الحزمة	R F	لون الحزمة	R F
1	-	-	أزرق فاتح	0.19
2	-	-	بنفسجي فاتح	0.25
3	-	-	أزرق فاتح	0.36
4	-	-	أزرق غامق	0.44
5	-	-	بنفسجي فاتح	0.56
6	-	-	وردي	0.64
7	-	-	وردي	0.75
8	-	-	بنفسجي فاتح	0.79

ومما هو جدير بالذكر أن هناك العديد من الدراسات قد أشارت إلى أهمية استخدام كروماتوجرافيا الطبقة الرقيقة في تحديد وفصل محتوى الزيت الطيار والمركبات العطرية الرئيسية[23]، أما بقية النظم التي تم اختبارها بواسطة كروماتوجرافيا الطبقة الرقيقة فقد أظهرت عدد أقل من الحزم بعد الرش بالجوهر الكشاف فانيلين/حمض الكبريتيك كما هو موضح في الجدول (4) ، (5) ، ويتضح من ذلك أن توصيف الزيوت الطيارة بواسطة (TLC) أسهمت في فصل الحزم الرئيسية الموجودة في زيت نبات الزعتر تحت الدراسة وأن عامل الارتفاع عن سطح البحر لم يكن له تأثير معنوي على تركيب الزيوت الطيارة، ولم ينتج عنه اختلاف من حيث عدد الحزم وقيم معدلات السريان RF المختلفة في المواقع تحت الدراسة، لوحظ تشابه واضح بين كل من الموقعين أبو ذراع وسيدي الحمري.

جدول (5) النتائج المتحصل عليها من الفصل الكروماتوجرافي بواسطة TLC (كروماتوجرافيا الطبقة الرقيقة) للزيوت الطيارة المستخلصة مواقع تحت الدراسة ودلك باستخدام الطور المتحرك Hexan : ethyl acetate (95 : 5 v/v).

الموقع وعدد الحزم	الزعتر البري *Thymus capitatus*			
	الضوء المنظور Visible light		استخدام الجوهر الكشاف محلول فنيلين/حمض الكبريتيك	
الموقع (أبوذراع)	لون الحزمة	R F (معدل السريان)	لون الحزمة	R F (معدل السريان)
1	-	-	بنفسجي فاتح	0.4

2	-	-	بنفسجي غامق	0.53
3	-	-	بنفسجي فاتح	0.71
الموقع (سيدي الحمري)	لون الحزمة	R F	لون الحزمة	R F
1	-	-	بنفسجي فاتح	0.4
2	-	-	بنفسجي غامق	0.55
3	-	-	بنفسجي فاتح	0.66

جدول (6) النتائج المتحصـــل عليها من الفصـــل الكروماتوجرافي بواســـطة TLC (كروماتوجرافيا الطبقة الرقيقة) للزيوت الطيارة المستخلصة من مواقع تحت الدراسة باستخدام الطور المتحرك banzen : ethyl acetate (92 : 8 v/v) .

الموقع وعدد الحزم	الضوء المنظور Visible light		استخدام الجوهر الكشاف محلول فنيلين/حمض الكبريتيك	
موقع أبوذراع	لون الحزمة	R F (معدل السريان)	لون الحزمة	R F (معدل السريان)
1	-	-	أصفر	0.2
2	-	-	بنفسجي فاتح	0.23
3	-	-	بنفسجي	0.35
4	-	-	أزرق فاتح	0.47
5	-	-	أحمر فاتح	0.63
6	-	-	بنفسجي فاتح	0.77
7	-	-	بنفسجي	0.84
موقع سيدي الحمري	لون الحزمة	R F	لون الحزمة	R F
1	-	-	أصفر	0.19
2	-	-	بنفسجي غامق	0.36
3	-	-	أزرق فاتح	0.47
4	-	-	أحمر فاتح	0.63
5	-	-	بنفسجي فاتح	0.78
6	-	-	بنفسجي فاتح	0.84

3. 3. توصيف المستخلصات المختلفة لنباتي الزعتر بواسطة TLC :

اســتخدمت كروماتوجرافيا الطبقة الرقيقة TLC لفصــل المســتخلصــات النباتية المختلفة لنبات الزعتر البري وهي الخلاصــة الكحولية الكلية والمســتخلصــات المتحصــل عليها بطريقة الاســتخلاص المتتابع وهي الهكســان والكلوروفورم والإيثانول وللحصــول على فصــل جيد بواســطة TLC اســتخدمت أنظمة مختلفة في هذه الدراســة توضــح المكونات القطبية ، والمكونات الغير قطبية جدول (7) [24] وتم فحص الألواح الكروماتوجرافية في الضوء المنظور وتحت الأشعة فوق بنفسجية (U/V) وبعد الرش بالجوهر الكشــاف حمض كبريتيك/ميثانول وأيضــاً بعد تعرض الألواح لأبخرة الأمونيا. والجدول (8) يبين النتائج المتحصــل عليها من الخلاصــة الكحولية الكلية الخام (A) وخلاصــة الهكســان (B) ، خلاصــة الكلوروفورم (C)، وخلاصــة الإيثانول (D) وفقاً للمركبات الغير قطبية لنباتي الزعتر البري موقع أبو ذراع باســتخدام الطور المتحرك Benzen: ethyle acetate (86 : 14 v/v). أظهرت النتائج عدم وجود حزم في الضوء المنظور بالنسبة لنبات الزعتر البري موقع أبو ذراع.
عند الرش بالجوهر الكشــاف حمض الكبريتيك/ميثانول مع التســخين عند درجة حرارة 110 ْم لمدة 5 دقائق لوحظ ظهور حزم ملونة مختلفة كان عددهم (3، 8، 7) للخلاصات (C, B, A) أما الخلاصة (D) لم تظهر فيها حزم ملونة وتتراوح قيم RF ما بين (0.36-0.92) للخلاصــة A، (0.26-0.91) للخلاصــة B، (0.17-0.91) للخلاصــة C بالنسبة للزعتر البري موقع أبو ذراع.

تبين من الجدول (8،7) بعد الرش بالجوهر الكشــاف الخلاصــة (C, B, A) لنباتي الزعتر البري بعد الرش بالجوهر الكشــاف لوحظ اختلاف في عدد الحزم وألوانها وقيم Rf من الموقعين (أبو ذراع ـــــ سـيدي الحمري) حيث كانت الخلاصــة الكحولية الكلية الخام (A) بها 8 حزم من موقع ســيدي الحمري يقابلها 3 حزم من موقع أبو ذراع، وخلاصــة الهكســان (B) ظهر بها عدد 6 حزم ملونة من موقع ســيدي الحمري، و 8 حزم من موقع أبو ذراع، أما خلاصــة الكلوروفوم (C) تبين وجود 6 حزم من موقع سيدي الحمري يقابلها 7 حزم من موقع أبو ذراع.
ومما هو جدير بالذكر أن هذه الدراســة الكروماتوجرافية للمســتخلصــات المختلفة تحت الدراســة والمواقع المذكورة أوضــحت وجود حزم مشتركة وأخرى مختلفة.

SJST Surman Journal for Science and Technology | ISSN: E 2790-5721 P 2790-5713
Vol.3, No.1, Dec 2021, pp. 135 - 145

جدول (7) نتائج وقيم RF (معدل السريان) المتحصل عليها من الفصل الكروماجرافي TLC للمستخلصات المختلفة من نبات الزعتر البري موقع أبو ذراع وذلك باستخدام الطور المتحرك benzen : ethyl acetate (86:14 v/v)

نوع الخلاصة	الوزن بالجرم	عدد الحزم	معدل RF السريان	الضوء المنظور	محلول H2SO4/ميثانول
الخلاصة A	5.16	3	0.92	-	بني
			0.45	-	أصفر
			0.36	-	زيتوني
الخلاصة B	2.52	8	0.91	-	بني
			0.77	-	بنفسجي فاتح
			0.55	-	بنفسجي فاتح
			0.45	-	أصفر
			0.4	-	بنفسجي
			0.35	-	زيتوني
			0.28	-	زيتي
			0.26	-	زيتوني
الخلاصة C	2.9	7	0.91	-	بني
			0.57	-	بنفسجي فاتح
			0.45	-	أصفر
			0.4	-	أخضر
			0.35	-	زيتي
			0.27	-	أصفر
			0.17	-	أصفر
الخلاصة D	7.1	-	-	-	-

A - خلاصة الكحولية الكلية الخام.
B - خلاصة الهكسان الناتجة من الاستخلاص المتتابع بواسطة السوكسلت.
C - خلاصة الكلوروفورم الناتجة من الاستخلاص المتتابع بواسطة السوكسلت.
D - خلاصة الأيثانول الناتجة من الاستخلاص المتتابع بواسطة السوكسلت.

جدول (8) نتائج وقيم RF (معدل السريان) المتحصل عليها من الفصل الكروماجرافي TLC للمستخلصات المختلفة من موقع سيدي الحمري وذلك باستخدام الطور المتحرك benzene :ethyl acetate (86:14 v/v)

نوع الخلاصة	الوزن بالجرم	عدد الحزم	RF معدل السريان	الضوء المنظور	محلول H2SO4/ميثانول
الخلاصة A	11.9	8	0.92	-	بني
			0.78	-	بنفسجي فاتح
			0.47	-	أصفر
			0.41	-	بنفسجي
			0.37	-	زيتوني
			0.3	-	زيتي
			0.2	-	اصفر

بنفسجي	-	0.11			
بني	-	0.9	6	3.44	**الخلاصة B**
بنفسجي فاتح	-	0.6			
بنفسجي	-	0.37			
أخضر	-	0.3			
زيتوني	-	0.17			
زيتوني	-	0.11			
أصفر	-	0.47	6	3.03	**الخلاصة C**
أخضر	-	0.4			
زيتي	-	0.35			
أصفر	-	0.27			
زيتوني	-	0.16			
-	-	-	-	8.39	**الخلاصة D**

A - الخلاصة الكحولية الكلية الخام.
B - خلاصة الهكسان الناتجة من الاستخلاص المتتابع بواسطة السوكسلت.
C - خلاصة الكلورفورم الناتجة من الاستخلاص المتتابع بواسطة السوكسلت.
D - خلاصة الأيثانول الناتجة من الاستخلاص المتتابع بواسطة السوكسلت.

وبالنسبة لنظام الكلورفورم: ميثانول: حمض الخليك (v/v/v 2 : 20 : 80) لمستخلصات من جميع المواقع جدول (9، 10)، كانت الصورة الكروماتوجرافية لمستخلصات نبات الزعتر البري من موقعي أبوذراع وسيدي الحمري عند تعرضها للأشعة فوق البنفسجية عند طول موجة (365nm) أظهرت عدد (3، 2، 4، 2) حزم ملونة في كلا الموقعين لكل من الخلاصات وكانت الخلاصة الكحولية الكلية (A) من موقعي أبو ذراع وسيدي الحمري مُشابهة من حيث عدد الحزم، قيم RF والألوان عند تعرضها للأشعة فوق البنفسجية وأبخرة الأمونيا ، أما خلاصة الهكسان فظهرت حزمة واحدة متشابهة في قيمة RF (0.89) واللون، بينما خلاصة الكلورفورم كان لها حزمتان متشابهتان في قيم RF وهما (0.38، 0.84) على التوالي، وبينت النتائج بالنسبة لخلاصة الإيثانول ظهور حزمة مشابهة في قيمة RF وهي (0.48) للموقعين.

مما سبق يتضح أن TLC لها أهمية في تحديد عدد المكونات الرئيسية لنبات الزعتر وهذا يتفق مع ما نشره [24] عن أهمية استخدام الكروماتوجرافيا الطبقة الرقيقة TLC في التعرف على بعض المركبات الموجودة في النبات.

جدول (9) نتائج وقيم RF (معدل السريان) المتحصل عليها من الفصل الكروماتوجرافي TLC للمستخلصات المختلفة من موقع أبو ذراع وذلك باستخدام الطور المتحرك Chloroform: methanol: acetic acid (v/v/v 2: 20: 80)

نوع الخلاصة	الوزن بالجرام	الضوء المنظور			التعرض للأشعة الفوق بنفسجية (nm365)			التعرض لأبخرة الأمونيا		
		عدد الحزم	RF	الألوان	عدد الحزم	RF	الألوان	عدد الحزم	RF	الألوان
الخلاصة A	5.16	-	-	-	3	0.86	أخضر	4	0.86	أصفر
						0.40	أصفر فاتح		0.52	أصفر

			أصفر فاتح	0.17					0.39	أصفر
									0.18	أصفر فاتح
الخلاصة B	2.52	-	-	-	2	0.89	أحمر	2	0.51	أصفر فاتح
						0.75	أحمر		0.39	أصفر فاتح
الخلاصة C	2.9	-	-	-	4	0.91	أحمر	5	0.82	أصفر
						0.82	أخضر		0.8	أصفر فاتح
						0.38	اصفر فاتح		0.51	أصفر
						0.15	أصفر فاتح		0.37	أصفر
									0.14	أصفر فاتح
الخلاصة D	7.1	-	-	-	2	0.48	أزرق	3	0.84	أصفر فاتح
						0.55	أصفر فاتح		0.57	أصفر
									0.18	أصفر فاتح

A ـ الخلاصة الكحولية الكلية الخام .
B ـ خلاصة الهكسان الناتجة من الاستخلاص المتتابع بواسطة السوكسلت.
C ـ خلاصة الكلوروفورم الناتجة من الاستخلاص المتتابع بواسطة السوكسلت.
D ـ خلاصة الإيثانول الناتجة من الاستخلاص المتتابع بواسطة السوكسلت.

جدول (10) نتائج وقيم RF (معدل السريان) المتحصل عليها من الفصل الكروماتوجرافي TLC للمستخلصات المختلفة من موقع سيدي الحمري باستخدام الطور المتحرك Chloroform: methanol: acetic acid (v/v/v 2: 20: 80).

نوع الخلاصة	الوزن بالجرام	الضوء المنظور	التعرض للأشعة الفوق بنفسجية (365nm)	التعرض لأبخرمونيا

		عدد الحزم	الألوان	RF	عدد الحزم	الألوان	RF	عدد الحزم		الألوان
الخلاصة A	11.9	-	-	-	-	-	0.86	4	أخضر	0.86
							0.36		أصفر فاتح	0.54
							0.17		أصفر فاتح	0.37
										0.18
الخلاصة B	3.44	-	-	-	2	أحمر	0.89	2	أحمر	0.86
							0.83		أصفر فاتح	0.81
الخلاصة C	3.03	-	-	-	4	أخضر	0.84	5	أخضر	0.84
							0.55		أصفر فاتح	0.82
							0.38		أصفر فاتح	0.52
							0.20		أصفر فاتح	0.39
										0.19
الخلاصة D	8.39	-	-	-	2	أزرق	0.48	3	أصفر فاتح	0.84
							0.23		أصفر فاتح	0.59
										0.21

A ـ الخلاصة الكحولية الكلية الخام.

B ـ خلاصة الهكسان الناتجة من الاستخلاص المتتابع بواسطة السوكسلت.

C ـ خلاصة الكلوروفورم الناتجة من الاستخلاص المتتابع بواسطة السوكسلت.

D ـ خلاصة الإيثانول الناتجة من الاستخلاص المتتابع بواسطة السوكسلت.

3. 4. التعرف على مكونات الزيوت الطيارة لبناتي الزعتر البري بواسطة GC/MS:

أمكن التعرف على مكونات الزيوت الطيارة لنبات الزعتر المستخلصة بالتقطير المائي للأجزاء الهوائية بواسطة GC/MS وأظهرت نتائج تحليل مكونات الزيت الطيار المستخلص من نبات الزعتر البري تفاوتاً في عدد ونسب المركبات جدول (11) ونظراً لوجود عدد كبير من المركبات المختلفة ولسهولة التعامل معها تم تقسيم هذه المركبات إلى ستة مجموعات كيميائية مختلفة وهي (هيدروكربونات أحادية التربين، هيدروكربونات أحادية التربين المؤكسجة، هيدروكربونات السيسكوتربين، هيدروكربونات ثنائية التربين، هيدروكربونات ثنائية التربين المؤكسجة)، وقد تتواجد هيدروكربونات أخرى غير تربينية. وتم فصل عدد 12 مركب من زيت الزعتر البري موقع أبو ذراع تمثل 95.97% من إجمالي المركبات وعدد 20 مركب من زيت الزعتر البري موقع سيدي الحمري تمثل 87.53% من إجمالي المركبات، فيما يتعلق بالهيدروكربونات أحادية التربين تم التعرف على مركبين مشتركين في زيت الزعتر البري موقع أبو ذراع وسيدي الحمري alpha thujene بنسبة (1.64%، 7.93%) على التوالي، gamma-terpinene بنسبة (0.76%، 16.18%) على التوالي، وتبين من الجدول أن نسبة المركبات الهيدروكربونية أحادية التربين في زيت الزعتر البري موقع سيدي الحمري كانت أعلى من نسبة المركبات في موقع أبو ذراع (24.11%، 2.4%) على التوالي، أما هيدروكربونات أحادية التربين المؤكسجة فقد تم التعرف على مركبان من زيت الزعتر البري موقع أبو ذراع وسيدي الحمري وهما Carvacrol ، Thymol بنسبة (48.56%، 21.28%)، (1.77%، 0.07%) على التوالي.

جدول (11) نتائج تحليل كروماتوجرافيا الغاز المدمج مع مطياف الكتلة GC/MS للزيوت المستخلصة من نبات الزعتر البري من المواقع تحت الدراسة

الرقم			الاسم	النسبة المئوية

SJST Surman Journal for Science and Technology | ISSN: E 2790-5721 P 2790-5713
Vol.3, No.1, Dec 2021, pp. 135 - 145

موقع سيدي الحمري	موقع أبوذراع	الكيميائي	الرمز الكيميائي	وقت الاحتجاز (دقيقة)	
7.93	1.64	Alpha-thujene	C10H16	6.8	1
16.18	0.76	Gamma-terpinene	C10H16	8.74	2
21.28	48.56	Carvcrol	C10H14O	12.37	3
0.07	1.77	Thymol	C10H14O	14.93	4
8.59	7.41	Trans-caryophllene	C15H24	17.77	5
0.78	-	Aromadendrene	C15H24	18.12	6
1.82	5.20	Alpha-humulene	C15H24	18.20	7
1.63	6.57	Ledene	C15H24	18.32	8
0.69	1.93	Gamma cadinene	C15H24	18.41	9
0.79	-	Delta- cadinene	C15H24	18.45	10
1.03	-	(-) – spathulenol	C15H24O	18.90	11
10.43	6.26	Caryophullene oxide	C15H24O	19.00	12
0.25	-	Alpha cadinol	C15H26O	19.54	13
0.62	2.27	Iso aromadrene epoxide	C15H24O	19.60	14
1.08	0.71	Cis- alpha bisabolene	C15H24	19.70	15
1.11	-	Vulgarol B	C15H24O	19.81	16
2.63	-	2-ethyl- 4-methyl anisole	C10H14O	21.8	17
0.84	-	Hexanoic acid, oct – 3 –en – zyl ester	C14H26O2	22.78	18
8.54	12.18	Phenol,2,3,5,6 tertramethyl	C10H14O	23.96	19
1.24	-	Anisole	C7H8O	25.35	20
20	12	عدد المركبات التي تم التعرف عليها			
%24.11	%2.4	* هيدروكربونات أحادية التربين			
%21.35	%50.33	* هيدروكربونات أحادية التربين المؤكسجة			
%15.38	%21.82	* هيدروكربونات السيسكوتربين			
%13.44	%9.24	* هيدروكربونات السيسكوتربين المؤكسجة			
-	-	* هيدروكربونات ثنائية التربين			
-	-	* هيدروكربونات ثنائية التربين المؤكسجة			
%13.25	%12.18	* هيدروكربونات غير تربينية			
%87.53	%95.97	* النسبة المئوية الكلية للمواد العطري التي قد تم التعرف عليها			

ولم يتم التعرف على مركبات هيدروكربونية ثنائية التربين، هيدروكربونات ثنائية التربين المؤكسجة، وتم التعرف على عدد 4 مركبات هيدركربونية غير تربينية في الزيت من موقع سيدي الحمري ومركب واحد من موقع أبو ذراع وكان هناك مركب مشترك من موقع أبو ذراع وسيدي الحمري هو مركب phenol,2,3,5,6 tetramethyl كما هو موضح في الجدول (11)، وتتفق هده النتائج مع ما ذكره [10] الذي قام بدراسة المحتوى الكيميائي للزيت الطيار المستخلص من أربعة أنواع من الزعتر ومن بينهم الزعتر البري ولقد وجد أن الزيت العطري لنبات الزعتر البري يحتوي على 4 مركبات وهم:

p-cymene (13-20%)، gamma-terpinene (7-14%)، Thymol (0.4-34%)، Carvacrol (5-63%)، وتتوافق مع ما نشره [25] عند تحليل الزيت الطيار الذي تم تحضيره من نبات الزعتر T. capitatus الذي ينمو في جنوب إيطاليا باستخدام GC/MS يحتوي على 75 مركب ويمثل Thymol , Carvacrol أكثر من 50% من محتوى الزيت الطيار، ووجد أن p- borneol , cymene , alpha-terpinene يشغلون الغالبية من محتوى الزيت وكذلك وجود علاقة بين هذه المركبات حيث قلة المحتوى من Thymol يكون مصحوب بزيادة تركيزات gamma-terpinene , alpha-terpinene , myrecene والعكس صحيح ومع ما ذكره [26]عند تحليل الزيت العطري المستخلص من نبات *T. capitatus* باستخدام GC/MS وجد أنه يحتوي على المركبات العطرية الأتية: Carvacrol (62-83%) ، p-cymene (5-17%) ، gamma-terpinene (2-14%)، B-caryophyllene (1-4%) وأشارو[27] بعد دراسة وتحليل الزيوت العطرية المستخلصة من نبات *T. caramanicus* النامي في إيران بواسطة GC/MS عن وجود اختلافات كمية وكيفية للزيوت المستخلصة من النبات في مراحله المختلفة (أثناء النمو الخضري، بداية التزهير، التزهير الكامل، وخلال مرحلة تكوين الثمار والبدور) وكانت نسب الزيت في مراحله المختلفة هي (1.9%، 2.1%، 2.5%، 2.0%) على التوالي وعند تحليلها بواسطة GC/MS وجد (37، 37، 29، 35) مركبات عطرية على التوالي وكان المحتوى الرئيسي في كل العينات مركب Carvacrol أما المركبات العطرية الرئيسية الأخرى هي borneol, p-cymene, alpha-terpinene , Thymol، وقد أتضح في

هذه الدراسة أن مركب Carvacrol يوجد بنسب عالية في كلا الموقعين تحت الدراسة أما مركب Thymol يوجد بنسب منخفضة على خلاف ما ذكره [6] عند تحليل الزيوت العطرية باستخدام GC/MS من نباتي الزعتر البري والجبلي تم جمعهما من مناطق جزيرة كريت تبين وجود مركب Carvacrol بنسبة مرتفعة في الزيت العطري من المناطق المنخفضة للنباتين ومركب Thymol يمثل المكون الرئيسي للنباتين من المناطق المرتفعة.

4. الخلاصة

أوضحت النتائج وجود اختلاف كمي وكيفي في المحتوى الكيميائي للزيوت العطرية لنبات الزعتر البري نتيجة اختلاف مواقع الدراسة، فقد أجريت دراسات كروماتوجرافية باستخدام كروماتوجرافيا الطبقة الرقيقة TLC لكل من الزيوت العطرية والخلاصات المختلفة، وكروماتوجرافيا الغاز المدمج مع مطياف الكتلة GC/MS لكل زيت من الزيوت العطرية . كانت النسبة المئوية للزيت العطري المتحصل عليه من نبات الزعتر البري من موقعي أبو ذراع وسيدي الحمري (1.5% ، 1.06%) على التوالي. أسفرت نتائج GC/MS عن التعرف على عدد 12 مركب عطري بنسبة (95.97%) من إجمالي مكونات الزيت العطري لنبات الزعتر البري من موقع أبو ذراع ، وعدد 20 مركب عطري بنسبة (87.53%) في زيت الزعتر البري من موقع سيدي الحمري علاوة على ذلك استخلاص عدد 7 مركبات عطرية للنبات في مواقع الدراسة وهي Aromadendrene, Gamma-terpinene, Alpha-thujene, Thymol, Carvacrol, Delta-cadinene, Alpha-humulene، ولقد كان مركب Carvacrol له نسبة تواجد مرتفعة في الموقعين أبو ذراع وسيدي الحمري لزيت نبات الزعتر البري (48.56%، 21.28%) كذلك تم فصل محتويات الخلاصات النباتية على ألواح من السيلكاجل بواسطة عدة أنظمة للفصل كما تم تحديد عدد الحزم المفصولة في كل خلاصة وحساب قيم RF لكل حزمة.

5. تضارب المصالح:

يعلن المؤلفون أنه لا يوجد تضارب في المصالح.

6. المراجع العربية:-

[1] **جامعة عمر المختار.** 2005. دراسة وتقييم الغطاء النباتي الطبيعي في منطقة الجبل الأخضر التقرير النهائي. البيضاء.

[5] **أبو زيد، الشحات نصر. 1992**. النباتات العطرية ومنتجاتها الزراعية والدوائية، الدار العربية للنشر والتوزيع، الطبعة الثالثة، القاهرة.

[20] **فيفي، فتحي عبد العزيز، خالد عبد العزيز محمد . 2000** . التحليل الدقيق لمتبقيات السموم والملوثات البيئية في مكونات النظام البيئي، دار الفجر للنشر والتوزيع ـ القاهرة.

[23] **العجيلي ، وصال حسن . 2007 .** تأثير النشاط المضاد للأكسدة لمستخلصات بعض النباتات العطرية المستوطنة على ثباتية زيت عباد الشمس . دراسة ماجستير من جامعة عمر المختار، كلية الموارد الطبيعية وعلوم البيئة.

المراجع الأجنبية

[2] Bounatirou, S., S. Smiti, M. G. Miguel, M. N. Rejeb, M. Neffati, M. M. Costa, L. Faieiro, A. C. Figueireao, J. G. Barroso and L. G. Pedro. 2008. *Thymus capitatus* grown in Tunisia: antioxidant ability of the essential oils on linolic acid evaluated by different methods. Acta Horticulture.765:315-323.

[3] Kulisic, T., V. Dragouic – uzelac and M. Milos. 2006a. Antioxidant Activity of aqueous Tea infusions prepared from Oregano Thyme and wild Thyme. Food Technology Biotechnology 44(4): 485 – 492 .

[4] Goren, A.C., G. Bilsel, M. Bilsel, H. Demir and E. E. kocabas. 2003. Analysis of essential oil of *Coridothymus capitatus* (L.) and its antibacterial and antifungal activity. Zeithchrift for naturforschung. 58: 687 – 690 .

[6] Karousou, R., D. N. Koureas and S. Kokkini. 2005 . Essential oil composition is related to the natural habitats *: Coridothymus_Capitatus* and *Satureja thymbra* in NATURA 2000 Site of Crete. Phytochemistry. 66 (22) : 2668-2673 .

[7] Kaileh, M., W. V. Berghe , E. Boone, T. Essawi and G. Heageman . 2007. Screening of indigenous Palestinian medicinal plants for potential anti-inflammatory and cytotoxic activity. Journal of Ethnopharmacology. 113 (3) : 510-516.

[8] Mathew, N., S. Misra-Bhattacharya, V. Perumal and K. Muthuswamy. 2008. Anti-filarial lead molecules isolated from *Trachyspermum ammi*. Molecules. 13 : 2156-2168.

[9] Ozguven, N. and S. Tansl. 1998. Drug yield and essential oil of *Thymus vulgaris* L. as influenced by ecological and ontogenetical variations. Journal of Agriculture and forestry. 22: 537- 542.

[10] Skoula, M., R. J. Grayer and G. C. Kite. 2005 . Surface flavonoids in *Satureja thymbra* and *Satureja Spinosa* (Lamiaceae) . Biochemical Systematic and Ecology. 33 : 541-544.

[11]Adiguzel, A., H. Ozer, H. Kili and B. Cetin. 2007. Screening of antimicrobial activity of essential oil and methanol extract of *Satureja hortensis* on food borne bacteria and fungi. Czech, Journal Food Science. 25 (2) : 81-89 .

[12] Sokovic, M. D., J. Vukojevic, P. D. Marin, D. D. Brkic, and V. Vajs 2009. Chemical Composition of essential oils of *Thymus* and *Mentha* species and their antifungal activities. Molecules. 14(1):238-249.

[13] Kandil, O., N. M. Redwan, A. B. Hassan, A. M. M. Amer, H. A. El-Bama and W. M. M. Amer. 1994. Extracts and fraction of *Thymus capitatus* exhibit antimicrobial activities. Journal of Ethnopharmacology. 44(1): 19 – 24.

[14] Cosentino, S., C.I. Tuberoso, B. Pisano, M. Satta, V. Mascia, E. Arzedi and F. Palmas .1999. *In vitro* antimicrobial activity and chemical composition of Sardinian *Thymus* essential oils. Letters of Applid Microbiology . 29 (2) : 130-135.

[15] Sherif, A. S. and A. El-Taife. 1986. Flora of Libya : Gymnosperms Al Fateh University .

[16] AOAC. 1990. Official methods of analysis 13th ed .Association of Official Analytical Chemists. Washington. DC.

[17] David, P. 1976. The chemical analysis of foods. 7th ed . Churchill livingston Edinburgh, London . and New York .

[18] Balbaa, S. I. H., S. Hilal and A. Y. Zaki. 1981. Medicinal plant constituents . 3th ed General Organization for University and School Books.

[19] Dob, T., D. Dahamane and C. Chelghom. 2008. Chemical composition of the essential oil of *Juniperus phoenicea* L. from Algeria. Journal of Essential oil Research. 20 (1) : 15-20 .

[21] Vekiari, S., A., V. Orcopulo, C. Tzia and C.D. Thompoulos . 1993 . Oregano flavonoids as lipid antioxidants. Journal of American Oil Chemists Society. 70 (5) : 384-487.

[22] Adams, R. P. 2001. Identification of essential oil components by GC/MS. Allured Publ. Crop. Carol stream. Illinois.

[24] Shabana, M. M., E. Abdelsattar, M.H. Gonaid, M.M. Salama and A.A. Sleem. 2006. Phytochemical and biological investigation of *Leptadenia heteropyhlla* Decne. fruit and it latex. Bull . Faculty Pharmacy Cairo University . 44 (1) : 59-74.

[25] Miceli, A., C. Negro and L. Tommasi. 2006. Essential oil variability in Thymbra capitata (L.) Cav. growing wild in Southern Apulia (Italy). Biochemical Systematics and Ecology. 34 (6) : 528 – 535

[26] Bounatirou, S., S. Smiti, M. G. Miguel, L. Faleiro, M. N. Rejeb, M. Neffati, M. M. Costa, A. C. Figueiredo, J. G. Barroso and L. G. Pedro. 2007. Chemical composition, antioxidant and antibacterial activities of the essential oils isolated from Tunisian *Thymus capitatus* Hoff. et link. Food Chemistry. 105: 146 – 155.

[27] Ebrahimi S.N., J.Hadian , M.H. Mirijalili , A.Sonboli and M.Yousefzadi. 2008. Essential oil composition and antibacterial activity of *Thymus caramanicus* at different phenological stages.Food chemistry.110(4):927-931..

SJST
https://sjst.scst.edu.ly
Surman Journal for Science and Technology
ISSN: Online 2790-5721 Print 2790-5713
مجلة صرمان للعلوم والتقنية
Vol. 3, No.1, Dec.2021
Pages: 146 ~ 155

دراسة التسربات النفطية وتأثيرها من الناحيتين البيئية والاقتصادية وتطبيق الدراسة على حقل الراقوبة بشركة سرت للعمليات النفطية

خالد حسن كوكو[1] , علي الهادي الأسود[1] , الصالحين مصباح الصالحين[2]
[1] كلية النفط والغاز, جامعة الزاوية
[2] قسم التقنية الميكانيكية, كلية صرمان للعلوم والتقنية
*Corresponding author: k.kaukau@zu.edu.ly[1]
a.elaswed@zu.edu.ly[1]
elselhan@scst.edu.ly[2]

الملخص

تعرف البيئة على أنها الوسط المحيط بالإنسان بجميع عناصره من ماء وهواء وكائنات حية، والذي يتيح له ممارسة نشاطاته المختلفة ضمن نظام دقيق ومتوازن، لكن هناك بعض المشاكل التي تؤثر على سير هذا النظام، ومن أكثر المشاكل المؤثرة على البيئة هي مشكلة التلوث. إن التلوث بشكل عام هو عبارة عن تغير سلبي في شكل وطبيعة مادة معينة نتيجة تأثرها بعوامل دخيلة، قد تكون طبيعيةً أو كيميائية، الأمر الذي من شأنه أن يحدث اختلالاً في توازن هذا النظام، والذي بدوره سيؤثر على جميع العناصر والموجودات فيه.
إن التلوث البيئي هو ليس نتاج العصر الحديث فقط، بل إنه بدأ من وجود الإنسان، و ذلك لأن الإنسان منذ تعرفه على الطبيعة وتعامله معها و محاولة استكشافها وتلبية متطلباته وهو يسهم في تلويثها، وأكبر مثال على ذلك كان الإنسان الأول الذي اكتشف النار وقام بعمليات الحرق، و لكن النسب و التأثير يختلف مع تطور العصر فالتلوث الذي حدث نتيجة إضرام النار في العصر الحجري للتدفئة والآكل ليس هو نفسه الناتج من مخلفات المصانع الحارقة للمواد الكيماوية والمنتشرة حول العالم وهو نفسه الذي يحدث نتيجة تسرب للنفط او الغاز سوي في مناطق الإنتاج او مناطق الشحن والتصدير حيث تعتبر عملية نقل النفط والغاز من العمليات المهمة في الصناعات النفطية لأنها مكمل لعملية استخراج النفط وفرزه في الحقول وبعدها ارساله الى المصافي ليتم تكريره وتحويله الى مشتقات نفطية .
وتركز هذه الدراسة على عملية التسربات التي تحدث في أنابيب نقل النفط من حيث حصر الكميات المتسربة والمسببة للتلوث وتكلفة الكميات المفقودة وكذلك تكلفة صيانة الانابيب ومعالجة التسربات ومن ثم حساب الوقت اللازم لعملية الصيانة وقد تم تطبيق هذه الدراسة على حقل الراقوبة التابع لشركة سرت خلال الفترة من 2002 الى 2003 واتضح ان الفاقد بسبب التسربات حوالي 210 برميل وبتكلفة حوالي 10500 دولار أمريكي.

1. مقدمة

النفط أو ما يُسمّى بالبترول هو عبارة عن وقود أحفوري يتم إيجاده في باطن الأرض بشكلهِ الطبيعيّ الخام وهوَ إمّا أن يكون خفيفاً مثلَ البنزين أو كثيفاً مثل القطران ويكون أسود اللون، حيث يعتمد اللون على المكوّنات الداخلية للسائل بشكل عام ، يتواجد بشكل طبيعيّ في طبقات الأرض، أو قد يكون مختلطاً بالرمال، وهو مزيج معقّد من الهيدروكربونات، والغاز الطبيعيّ، وشمع البارا فين، ويحتوي على عناصر غير معدنيّة، مثل: الكبريت، والأكسجين، والنيتروجين(خليل ,2014).

يوجد النفط في جميع أنحاء العالم تقريباً ولكنّهُ يتمركز بكميّاتٍ كبيرة في بُلدانٍ مُعينة. يتم استخراج النفط الخام من الخزانات البترولية الموجودة تحت الأرض باستخدام آلات حفر عملاقة، ويتم مُعالجته وتكريره لصُنع مواد رئيسيّة ومُهمّة في حياة الإنسان كالبنزين والإطارات ومواد التخدير، ويُعد النفط من المواد غير متجددة للطاقة (النفط والغاز ,2005). عندما يتم انتاج النفط من البئر يكون مصاحبا ببعض الشوائب غير المرغوب فيها والتي تؤثر في خواصه مثل الأملاح والمياه والرمل وبعض الشوائب الغازية مثل كبريتيد الهيدروجين. لذلك يتم انشاء محطات معالجة في الحقول النفطية للتخلص من كل هذه الشوائب ويفترض أن يكون هناك مراعاة للتلوث الذي قد تسببه هذه الشوائب على المحيط البيئي في هذه الحقول (النفط والغاز ,2005).

2. طرق نقل النفط الخام من الحقول الى أماكن التكرير

الحقول المنتجة للنفط والغاز عادة توجد في مناطق بعيدة عن موانى التصدير وعن الأماكن المكتظة بالسكان , لذلك يستوجب ايجاد وسائل لنقل النفط أو الغاز من الحقول الى الأماكن التي سيتم الاستفادة منها سواء بتصديرها أو معالجتها للاستخدام المحلي . هذه الوسائل يجب أولا أن تكون آمنة لأن المواد المنقولة خطرة وقابلة للاشتعال وكذلك وجود أي تسربات في وسيلة النقل قد يؤدي الى كوارث بيئية يمتد أثرها لسنوات طويلة وقد شهد العالم العديد من هذه الحوادث وخاصة في البحار والمحيطات. ومن أهم طرق نقل النفط الخام والغاز الطبيعي هي الطرق التالية:

SJST
https://sjst.scst.edu.ly
Surman Journal for Science and Technology
ISSN: Online 2790-5721 Print 2790-5713
مجلة صرمان للعلوم والتقنية
Vol. 3, No.1, Dec.2021
Pages: 146 ~ 155

2.1. النقل بخطوط الأنابيب:

تعتبر من أكثر وسائل نقل النفط انتشارا في العالم وذلك نظرا لكفاءتها العالية اقتصاديا وكذلك تعتبر الأفضل من ناحية الأمان والسلامة. هذه الانابيب تمتد لمسافات طويلة ويتم ضخ الخام النفطي خلالها من الحقول الى الموانئ المصدرة أو الى مصافي التكرير .

قد يصل طول هذه الانابيب الاف الاميال فوق الأرض أو حتى تحت البحر لذلك يستوجب انشاء محطات ضخ على مناطق متفرقة في طريق الانبوب حتى يصل الخام الى منطقة الوصول (حمادي و عبدالباقي, 2018) وكذلك يجب وضع علامات مميزة تشير الى وجود الانبوب تفاديا لأي نوع من الحوادث .وبالرغم من ان التكلفة الاجمالية لإنشاء أنابيب النقل مرتفعة مقارنة بالوسائل الاخرى الا ان فعاليتها وتكلفة التشغيل والصيانة تجعلها الافضل اقتصاديا (حمادي و عبدالباقي, 2018) .

وبالطبع فإن الاحتكاك بين المادة النفطية مع جدران الأنابيب يقلل من سرعتها، وبالتالي تحتاج إلى مرحلة جديدة من الضغط، لذا يوجد كل حوالي 50 إلى 250 كيلومترا نقاط تقوية . لهذه الأنابيب أنواع مختلفة تبعاً لنوع المادة المستخدمة في صنعها. ويتحكم الوسط المنقول ومواصفاته الكيميائية (درجة القلوية أو الحموضة، قوة الأكسدة) والوسط المحيط (الرمال المخرشة في الصحراء) وكذلك شروط التشغيل من سرعة التدفق وضغط التشغيل في تحديد مادة الأنبوب المختارة (خليل ,2014). ومن أهم هذه الأنواع ما يأتي:

أ- الأنابيب المعدنية : Metallic pipes التي تصنع من معادن مختلفة كالرصاص والألمنيوم وغيرها. بينما الأنابيب النحاسية والمصنعة بطريقة السحب هي الأكثر رواجاً في المجالات الصناعية المحدودة من حيث الأطوال والضغوط والتدفقات. وتصنع الأنابيب الفولاذية من صفائح فولاذية مقاومة للصدأ تلف بشكل حلزوني، وتلحم من الجوانب لتشكل أنابيب ذات أقطار متعددة. وتستخدم هذه الأنابيب في نقل المياه والنفط والغاز تحت شروط صعبة من ضغط وتبدلات حرارية ومناخية(حمادي و عبدالباقي, 2018).

ب- أنابيب الحديد المطاوع : Ductile iron تُصنّع بالسباكة بوساطة آلات الطرد المركزي. ويشيع استخدامها في نقل المياه والتطبيقات التي تستلزم طمر الأنابيب في الأرض مما يزيد صعوبة ظروف العمل. وتتميز هذه الأنابيب من الأنابيب الفولاذية آنفة الذكر بسماكة كبرى للجدران ومقاومة كبرى لظروف التربة والطقس.

ج- الأنابيب اللدائنية (البلاستيكية) : Plastic pipes تستخدم هذه الأنابيب في التطبيقات الصناعية التي تحتاج إلى المقاومة الكيمياوية العالية التي تبديها المواد اللدائنية. وحديثاً دخلت الأنابيب اللدائنية المصنعة من البوليإيتيلين عالي الكثافة high density polyethylene (HDPE)وكلوريد البوليفينيل polyvinyl chloride (PVC) في مشروعات نقل المياه التي تتميز بعدم تآكلها أو التعرض للصدأ وما يترافق معها من مشكلات اهتراء.

الأنابيب الخرسانية Concrete pipes: تُصنّع من الخرسانة، ويغلب استعمالها في شبكات الصرف الصحي والنقل بالراحة حيث يتم التدفق تحت تأثير الجاذبية.إن جميع الأنابيب السابقة تتمّ معالجتها وتبطينها لتحقيق أفضل المواصفات وشروط التشغيل المناسبة لكل نوع من المواد المنقولة. ومن المهم الإشارة إلى إمكانية استخدام النقل بالأنابيب للمواد الصلبة كالقمح والحبوب، فهذه التقنية في النقل ليست حكراً على المواد السائلة والغازية فقط. ومثالاً على ذلك، فإن تفريغ السفن الناقلة لشحنات الحبوب والراسية في الموانئ يتم عبر أنابيب خاصة تقوم بنقل الحبوب إلى صوامع التخزين المجاورة (Oil and Natural Gas Transportation 2019).

2.2. النقل البحري أو باستخدام الناقلات:

ناقلة النفط هي سفينة مصممة لنقل النفط، وهي عادة مصممة لعبور المحيطات بين القارات. وهنالك نوعان أساسيان من ناقلات النفط : ناقلة النفط الخام وناقلة مشتقات النفط. ناقلات الخام، تكون عادة في غاية الضخامة وتقوم بنقل النفط الخام إلى مصانع التكرير. ناقلة مشتقات النفط، وعادة تكون أصغر من ناقلة النفط الخام بكثير، وتهدف إلى نقل البتروكيماويات من مصانع التكرير إلى الأسواق المستهلكة. وغالباً ما تصنف ناقلات النفط حسب الحجم وكذلك الوظيفة.يبدأ النصنيف من ناقلات مشتقات النفط الساحلية أو الداخلية والتي تبلغ حمولتها الوزنية بضعة آلاف من الأطنان وصولا إلى ناقلات النفط الخام الهائلة الضخامة والتي تصل حمولتها إلى 550,000 طن ،تعد تلك الوسيلة مكملة لعملية النقل بالأنابيب في بعض المناطق، حيث بوصول النفط الخام

من مناطق إنتاجه إلى مرافئ التصدير، أو الحاجة لنقل المشتقات بعد التكرير يأتي دور ناقلات النفط التي تستخدم أيضا في عملية التخزين من قبل الشركات والدول في حال انخفاض الأسعار للاستفادة بتحقيق الربح لاحقا عند ارتفاعها.

وربما تكون عملية النقل البحري هي الخيار الوحيد المتاح في بعض الحالات لطول المسافة وصعوبة مد خطوط الأنابيب وعدم جدواها عملياً.
فعلى سبيل المثال فإنه بتواجد حقول إنتاج كبرى في الشرق الأوسط ومع بعدها الكبير عن مراكز الاستهلاك في أوروبا وأمريكا لا يكون هناك خيار سوى استخدام الناقلات البحرية خصوصا العملاقة منها. لأن المحيطات والبحار والبحيرات والأنهار (الصالحة للملاحة) تشغل مساحات واسعة من الكرة الأرضية فقد أنشأت دول عدة أساطيل بحرية ونهرية لنقل النفط ومنتجاته المكررة، وتتألف هذه الأساطيل من ناقلات النفط . إن أكثر ناقلات النفط البحرية انتشاراً هي التي تراوح حمولاتها مابين 5000 - 50000 طن، وهنالك في الوقت الحاضر ناقلات نفط تزيد حمولاتها على 80000 طن، ومنها ما تصل حمولته إلى 500000 طن. وكلما زادت حمولة الناقلة ازدادت اقتصادية النقل بهذه الطريقة. وأكثر مرافئ العالم البترولية مصممة لاستقبال الناقلات ذات الحمولات غير الكبيرة (Oil and Natural Gas Transportation 2019).

2.3. النقل عن طريق الصهاريج:

ويتم ذلك بنقل الخام أو مشتقاته عن طريق خطوط السكك الحديدية أو الشاحنات الكبرى، حيث تعد الأخيرة ضرورية لنقل المشتقات لنقاط الاستهلاك النهائية حيث من الصعب تواجد وسيلة أخرى. وتعد عملية نقل النفط الخام بواسطة صهاريج السكك الحديدية في بعض الولايات الأمريكية أساسية، ووفقا لبيانات إدارة معلومات الطاقة فإن النقل بتلك الوسيلة ارتفع 9% خلال الأشهر السبعة الأولى عام 2014 بالمقارنة مع نفس الفترة عام 2013.

وبالطبع فإنه توجد مواصفات خاصة للصهاريج المستخدمة في عملية النقل سواء بالشاحنات أو السكك الحديدية لضمان أعلى معايير للسلامة خصوصا لتهدئة حركة السوائل أثناء عملية السير. تستخدم الصهاريج لنقل النفط ومشتقاته المكررة، وتبنى مراكز لاستقبال النفط الخام أو منتجاته وتوزيعها، بالقرب من خطوط السكك الحديدية عادة (Oil and Natural Gas Transportation 2019).

3. تجهيزات السلامة الفنية

وهي مجموعة المعدات والتجهيزات المستخدمة لضمان سلاسة عمليات التشغيل المختلفة لأنظمة النقل بالأنابيب وسلامتها. وتشمل تجهيزات خاصة للقياس، وتجهيزات حماية ضد المطرقة المائية التي تعدّ ظاهرة سلبية مخربة لاتقتصر على أنابيب المياه كما يوحي الاسم، وتجهيزات لطرد الهواء المتسرب إلى خطوط النقل.

3.1. تجهيزات السلامة البيئية

وهي مجموعة التجهيزات المستخدمة لضمان سلامة تشغيل الأنظمة ومنع الحوادث البيئية، ولاسيما أن أهم الحوادث التي يمكن أن تصيب البيئة بأضرار جسيمة هي حوادث التسربات النفطية أو الكيمياوية. إحدى التجهيزات التي يمكن استخدامها للكشف مباشرةً عن تسرب النفط وبعض المواد الكيمياوية هي استخدام كبل كهربائي موصول من أحد طرفيه بمصدر منخفض الجهد مشكلاً دارة كهربائية مفتوحة. يعزل السلكان المكوّنان للكبل عن بعضهما بمادة شديدة الحساسية للسائل المنقول، وعند حصول أي تسرب وانسكاب السائل على الكبل يذوب العازل ويحصل تماس مباشر، وتغلق الدارة الكهربائية، وبقياس تيار القصر ومعرفة المقاومة الكهربائية الطولية للكبل يتم تحديد موقع التسرب بدقة كبيرة جداً.

3.2. الحوادث التي قد تقع نتيجة استخدام الانابيب :

عانت بعض دول العالم تجارب سيئة مع خطوط النقل بالأنابيب خاصةً أنابيب نقل النفط والمشتقات الكيمياوية، وذلك يعود إلى حوادث تسربات عدة تجاوزت في بعض الأحيان الأثر البيئي إلى تهديد الحياة البشرية والموارد الطبيعية(الركابي, 2009). وقد يجهل بعض الناس خطورة المواد النفطية كونها من أكثر المواد سميةً وتأثيراً سرطانياً على البشر. كما أن أثرها يمتد فترات طويلة، ويتسرب ليصل إلى المياه الجوفية. لذلك فقد سُنَّت قوانين كثيرة لتنظيم إنشاء خطوط الأنابيب، ليس فقط وفق ما تقتضيه المصلحة الوطنية والاقتصادية، بل ربطت الموافقة بدراسة الأثر البيئي للمشروعات.

SJST
https://sjst.scst.edu.ly
Surman Journal for Science and Technology
ISSN: Online 2790-5721 Print 2790-5713
مجلة صرمان للعلوم والتقنية
Vol. 3, No.1, Dec.2021
Pages: 146 ~ 155

3.3. التلوث المائي الناتج من النفط :

يتعرض النفط عند تسربه إلى مياه البحر للعديد من العوامل البيئية التي تؤثر عليه مسببة حدوث بعض التغييرات الطبيعية والكيميائية ويمكن إيجاز ذلك فيما يلي:

عند تسرب النفط إلى مياه البحر يبدأ في الانتشار الفوري والامتداد في صورة طبقة رقيقة في سمكها طبقاً لنوعية الزيت ودرجة لزوجته وفي نفس الوقت تتحرك البقع الزيتية المتكونة من الموقع الذي تسربت فيه بطريقة تعتمد على عوامل كثيرة منها:

أ- طبيعة الزيت ونوعيته(خام- بقع رقيقة أو اشد رقة) (الركابي, 2009).

ب- الأحوال الجوية مثل، سرعة الرياح، درجة الحرارة ، اتجاه الموج، سرعة واتجاه التيارات البحرية. فأثناء تحركه وتعرضه للعوامل الجوية والبيئية لفترات طويلة يتم الكثير من المتغيرات الطبيعية والكيميائية. يعتبر التبخر بمرور الزمن أول هذه المتغيرات حيث تتبخر المكونات البترولية ذات درجة غليان منخفضة تاركة المكونات التي تغلي عند درجة حرارة 300م-370م ومن اخطر المركبات البترولية التي قد تتكون نتيجة التبخر هي مركب البنزوبيرين وهو من الهيدروكربونات المسببة للسرطان(سليم ,1990).

3.3.1. الترسيب على الشواطئ:

عندما تصل البقع الزيتية العائمة إلى الشاطئ يختلف سلوكها طبقاً لطبيعة الزيت ونوعية الشاطئ فعندما يكون التلوث خفيفاً يحمل غالبية الزيت بفعل الموجات المتتالية إلى أقصى موقع تصل إليه الموجه على الشاطئ وفي درجات الحرارة المرتفعة أو عندما يكون التلوث ناتجاً من زيت ذو كثافة منخفضة أو زيت حديث الانسكاب يتخلل الزيت الشقوق بين الصخور أو طبقات الرمال الجافة وقد يصل تخلله إلى أعماق تصل من نصف متر إلى متر ولا يتخلل الرمال الرطبة بسهولة ولكن يقذف الموج طبقات من الرمال فوق طبقات الزيت على الشاطئ فتدفنه مكوناً بذلك طبقات متتالية من الزيت والرمل (سليم,1990)

3.3.2. تحلل الزيت:

وتؤدي عملية تحلل الزيت إلى إزالة المواد الهيدروكربونية من البحر ويتم ذلك أساسا في فترات طويلة جداً عن طريق:

أ- الأكسدة التلقائية: وتساعد عليها الظروف الجوية خاصة درجة الحرارة.

ب- التحلل الميكروبي: ويتم بفعل نوعيات مختلفة من البكتريا التي تتغذى على المواد الهيدروكربونية ويساعد على ذلك تفتت الزيت إلى قطرات صغيرة بفعل المواد المتشتتة الموجودة أصلا في الزيت (عياش و بن فرحان ,2005). وتؤدي حوادث التلوث بالنفط في المياه إلى نقص كبير في نوعية الكائنات الحية التي ينتجها البحر او المحيط والتي تساهم بدرجة كبيرة في تغذية الإنسان (عياش و بن فرحان ,2005).

3.4. اساليب مكافحة التلوث النفطي:

ان الاسلوب الامثل لمعالجة التلوث النفطي للبيئة الساحلية والبحرية الملوثة بالنفط في مياه الخليج يمكن الاستعانة في بعض الحالات بأكثر من طريقة أو اسلوب لمكافحة التلوث النفطي في النطاق الساحلي والبحري. واهم الطرق المستخدمة هي كالتالي:

1. إقامة الحواجز العائمة لمحاصرة البقعة النفطية ومنع انتشارها بفعل الامواج والرياح والتيارات البحرية (عياش و بن فرحان 2005).
2. شفط النفط المتسرب لمياه البحر بواسطة مضخات الى خزانات على الشاطئ أو على ظهر السفن ثم إعادة فصل النفط عن الماء.
3. رش مواد ماصة على البقع النفطية حتى تتشبع بالنفط ثم استعادته منها.
4. حرق البقع النفطية الملوثة باللهب حيث يعمد الإنسان الى حصر هذه البقع وإضرام النيران فيها بالرغم من أن طريقة الإحراق ليست المرجوة تماماً في كل الاحوال لتسببها في تلوث البيئة الهوائية(حسين واليمني،2009).
5. تنظيف الشواطئ بجرف كميات كبيرة من الرمال والتخلص منها بعيداً عن شاطئ البحر.
6. التلوث البحري تتم محاصرته بإستخدام اجهزة ومعدات خاصة مع الاستعانة بالجرافات والكانسات، وهذه التقنية تستغرق وقتاً طويلاً تتعرض هذه البقع النفطية لعوامل المناخ والتيارات البحرية حيث تتشتت وتتحطم بفعل الضوء مما يزيد صعوبة عملية المكافحة (سليم ،1990) .
7. الطريقة الكيميائية لعلاج تلك المشكلة فتتم برش انواع من المذيبات والمنظفات الصناعية أو المساحيق عالية الكثافة على سطح البقع النفطية في البحار الملوثة للالتصاق بها لتحويلها بعد تفتيتها الى ما يشبه المستحلب فينتشر في الماء ويذوب فيه اويرسب على القاع، حيث يعتبر تسربه الى القاع زيادة للمشكلة لأن وصول تلك المواد الى قاع البحر يسبب إبادة للأسماك

والقواقع واليرقانات وديدان الرمل التي تعيش فيها، وتعتبر هذه الطريقة زيادة في تعقيد مشكلة التلوث وليست حلاً أخير لها(الصطوف ، 1995).

8. المكافحة الطبيعية أو البيولوجية احدى وسائل مقاومة التلوث البحري ببقع النفط حيث يتم استخدام انواع من البكتريا التي تقوم بتحليل هذه المكونات الهيدروكربونية من مخلفات الزيوت النفطية الى جزئيات اقل منها وزناً وتركيباً وادنى خطراً بسهولة ذوبانها في الماء مما يحولها من مواد خطره الى مواد ذائبة ادنى خطرا وأقل تلوثاً (الصطوف ، 1995).
9. احدث ما توصل اليه علماء الهندسة الوراثية للقضاء على هذه المشكلة فهو تخليق انواع من البكتريا لها القدرة على تحمل سمية هذه المواد النفطية وتحويلها الى مادة غذائية لها ويتم ذلك بتهجين اكثر من نوع من انواع البكتريا الموجودة في الطبيعة وإحداث عدد كبير من التبادل بين جيناتها المختلفة للوصول الى الصفات المطلوبة وإنتاج نوع جديد من البكتريا التي لا وجود لها في الطبيعة لها القدرة على استعمال النفط كغذاء لها ، وقد استخدمت هذه الطريقة الخيرة على نطاق واسع لمعالجة مشكلة بحيرات النفط التي خلفتها حرب الخليج الثانية وحققت نتائج مدهشة.

4. دراسة للتسربات التي حدثت بالخزانات والأنابيب بحقل الراقوبة

4.1. نبذة مختصرة عن حقل الراقوبة

يقع حقل الراقوبة في حوض سرت جنوب مرسى البريقة، تم اكتشاف الحقل عام 1961 , تحت امتياز 20.دخل الحقل للإنتاج الفعلي عام 1963 إفرنجي، تم حفر عدد 98 بئر نفطي وصل الإنتاج في أوائل عمر الحقل مائة وخمسون ألف برميل من الزيت الخام و100 مليون قدم مكعب من الغاز الطبيعي المصاحب للنفط. ونظراً لإتباع الشريك الأجنبي الطرق الإستنزافية التي أدت إلى انخفاض الإنتاج بشكل حاد وبعد تأميم الشركة بالكامل والتي أصبحت شركة سرت لإنتاج وتصنيع النفط والغاز التابعة للمؤسسة الوطنية للنفط بدلا"من شركة آسو الأمريكية ، تم الترشيد وأتباع الطرق والوسائل الحديثة التي من شأنها التقليل من الانهيار الحاد في ضغوط المكامن النفطية والمحافظة على المخزون الجوفي المتبقي ، حيث يبلغ الإنتاج الحالي للحقل (22,500) اثنان وعشرون ألف وخمسمائة برميل يومياً من الزيت الخام و 30 مليون قدم مكعب من الغاز المصاحب يومياً وعدد الآبار المنتجة حالياً 35 بئرا وهي 25 بئر تنتج بالتدفق الطبيعي وعدد 10 بئر تنتج بطريقة الرفع بالغاز.

4.2. المعلومات المتحصل عليها من التقارير الفنية لبعض التسربات في انابيب انتاج والفواصل والمعدات الخاصة بالآبار المنتجة بحقل الراقوبة وتقديرات الخسائر والتوقفات عن الإنتاج .

4.2.1. التسربات التي حدثت بخطوط انتاج الابار

تتعرض أنابيب نقل النفط من الآبار لمحطات المعالجة والعزل الى حوادث تسريب وذلك نتيجة لعدة عوامل منها التآكل والذي تسببه الموائع المتدفقة من الابار وكذلك العوامل البيئية الخارجية (حسين واليمني،2009) . فيما يلي حصر لكل حوادث التسريبات التي حدثت خلال الفترة من سنة 2002 الى سنة 2003(1 جدول) وتتضمن هذه الاحصائية خطوط الابار التي حدث بها تسرب وقطر انابيب النقل وكمية انتاج كل بئر بالإضافة الى فترة المعالجة والكميات المفقودة وتكلفة الصيانة .

التاريخ	البئر	قطر خط التسرب	إنتاجية البئر	عدد التسريبات	كمية التسرب	المدة اللازمة لإصلاح التسرب	تكلفة الصيانة
من 2002-09-09 الى 2002-12-18	E – 22	4 inch	OIL – 462 bpd	4	32 BBL	14 HOURS	433.68 L.D
من 2002-09-19 الى 2002-12-22	E – 27	4 inch	OIL – 462 bpd	3	9 BBL	12 HOURS	318.84 LD
من 2002-11-15 الى 2003-03-12	E – 24	4 inch	OIL – 1020 bpd Water- 167 bpd	3	5 BBL	20 HOURS	304.00 LD
من 2002-01-08 الى 2003-09-05	E – 26	6 inch	OIL – 284 bpd	6	24 BBL	12 HOURS	229.32 LD
2003-09-01	E – 05	4 inch	OIL – 59 bpd Water- 288 bpd	1	-	8 HOURS	108.42 LD
من 2002-04-26 الى 2002-06-01	E – 77	6 inch	OIL – 231 bpd Water- 25 bpd	6	6 BBL	6 HOURS	298LD

https://sjst.scst.edu.ly
Surman Journal for Science and Technology
ISSN: Online 2790-5721 Print 2790-5713
مجلة صرمان للعلوم والتقنية
Vol. 3, No.1, Dec.2021
Pages: 146 ~ 155

146LD	24 HOURS	12 BBL	6	OIL – 40 bpd Water- 94 bpd	4 inch	E – 79	من 2002-06-02 الى 2003-04-23
146LD	24 HOURS	12 BBL	6	OIL – 40 bpd Water- 94 bpd	4 inch	E – 70	من 2003-4-24 الى 2003-07-31
99.32 LD	3 HOURS	5 BBL	6	OIL – 325 bpd Water- 862 bpd	6 inch	E – 39	2003-09-01
108.42. LD	2 HOURS	3 BBL	2	OIL – 1201 bpd Water- 44 bpd	4 inch	E – 87	من 2002-10-12 الى 2003-07-01
108.42. LD	2 HOURS	1 BBL	2	OIL – 67 bpd Water- 212 bpd	4 inch	E – 59	من 2002-10-12 الى 2003-07-01
300 LD	-	2 BBL	1	OIL – 339 bpd Water- 756 bpd	4 inch 6 inch	E – 78	2003-05-14
99.32 LD	2 HOURS	2 BBL	2	OIL – 426 bpd Water- 97 bpd	6 inch	E – 85	2003-09-18
108.42 LD	2 HOURS	1 BBL	1	OIL – 203 bpd Water- 493 bpd	4 inch	E – 81	2003-03-05
108.42 LD	2 HOURS	3 BBL	3	OIL – 147 bpd	4 inch	E – 76	2003-12-05
108.42 LD	4 HOURS	2 BBL	1	OIL – 469 bpd Water- 1046 bpd	4 inch	E – 64	2003-03-23
100 LD	2 HOURS	2 BBL	1	OIL – 150 bpd Water- 1046 bpd	4 inch	E – 69	2002-04-11
108.42 LD	2 HOURS	1 BBL	1	OIL – 0 bpd Water- 89 bpd	4 inch	E – 74	2003-03-5
108.42 LD	2 HOURS	1 BBL	1	OIL – 1 bpd Water- 37 bpd	4 inch	E – 35	2003-07-1

الجدول رقم (1): حصر بحوادث التسريب النفطي في آبار حقل الراقوبة خلال سنة 2002 و 2003

4.2.2. التسربات التي حدثت بمعدات الإنتاج الرئيسية وبخط انتاج النفط الرئيسي

كما تتعرض أنابيب نقل النفط من الآبار الى حوادث تسريب فإن المعدات المستخدمة في عمليات المعالجة والتخزين تتعرض هي أيضا لحوادث تسرب. وهذه المعدات تشمل الخزانات والفواصل وكذلك المضخات وكذلك انبوب النقل الرئيسي المسئول عن نقل النفط المعالج من الحقل الى الميناء للتصدير نتيجة لعدة عوامل منها التآكل والذي تسببه الموائع المتدفقة من الابار وكذلك العوامل البيئية الخارجية (حسين واليمني،2009) . فيما يلي حصر لكل حوادث التسريبات التي حدثت خلال الفترة من سنة 2002 الى سنة 2003(1 جدول) وتتضمن هذه الاحصائية خطوط الابار التي حدث بها تسرب وقطر انابيب النقل وكمية انتاج كل بئر بالإضافة الى فترة المعالجة والكميات المفقودة وتكلفة الصيانة . وفيمل الجدول رقم 2 الذي يقدم حصر لهذه التسريبات والتي تم الحصول عليها من التقارير الفنية.

التاريخ	موقع التسرب	قطر خط التسرب	إنتاجية الحقل	عدد التسريبات	كمية التسرب	المدة اللازمة لإصلاح التسرب	تكلفة الصيانة
2002-5-20	خط الزيت الرئيسي عند الكيلومتر 43	inch20	,000 BBL21	6	10 BBL	10 HOURS	123.50 LD
2002-09-09	خط الزيت الرئيسي عند الكيلومتر 43	inch20	,000 BBL21	6	10 BBL	8 HOURS	123.50 LD
2002-09-15	خط الزيت الرئيسي عند الكيلومتر 43	inch20	,000 BBL21	6	15 BBL	12 HOURS	123.50 LD
2002-09-16	خط الزيت الرئيسي عند الكيلومتر 43	inch20	,000 BBL21	6	05 BBL	10 HOURS	123.50 LD

https://sjst.scst.edu.ly
Surman Journal for Science and Technology
ISSN: Online 2790-5721 Print 2790-5713
مجلة صرمان للعلوم والتقنية
Vol. 3, No.1, Dec.2021
Pages: 146 ~ 155

123.50 LD	8 HOURS	10 BBL	6	,300 BBL21	inch20	خط الزيت الرئيسي عند الكيلومتر 43	2002-10-01
123.50 LD	10 HOURS	12 BBL	6	,000 BBL21	inch20	خط الزيت الرئيسي عند الكيلومتر 43.7	2002-05-18
100.00 LD	28 HOURS	تم تغيير خط الدخول بالكامل	-	-	-	معمل الفرز	2002-04-12
102.00 LD	24 HOURS	تم تغيير جزء من خط التصريف	2	-	-	مجمع التصريف معمل الفرز	2002-12-01
100. LD	12 HOURS	تم تغيير الجزء المتآكل	4	-	-	منظومة الإطفاء	2003-12
100. LD	6 HOURS	تغيير الخط المغذي للخزان	1	-	-	تسرب خط الهواء في خزان الزيت رقم 2	2003-11
108.00 LD	-	-	-	Water line	6 inch	A2 sep. drain line	2003-04-20

الجدول رقم (2): حصر بحوادث التسريب النفطي في الخط الرئيسي والمعدات السطحية بحقل الراقوبة خلال سنة 2002 و سنة 2003

5. النتائج والخلاصة

من خلال المعلومات المتحصل عليها من شركة سرت للنفط والغاز والخاصة بالتسربات التي حدثت بحقل الراقوبة والقراءات المسجلة خلال السنوات 2002 و 2003 وفق التقارير الفنية وتأثير هذه التسربات والحوادث الصناعية بصفة عامة علي المناطق الصناعية ومستخدميها .الشكل رقم 1 يوضح معدل الإنتاج الشهري لكل الابار بالحقل ويمكن ملاحظة عدم الانتظام والتذبذب في الانتاج ويرجع ذلك لعدم ثبات الانتاج من الابار وذلك نتيجة التوقف المستمر للآبار لأغراض مختلفة من بينها التسربات النفطية الموضحة في الجدول رقم 1.

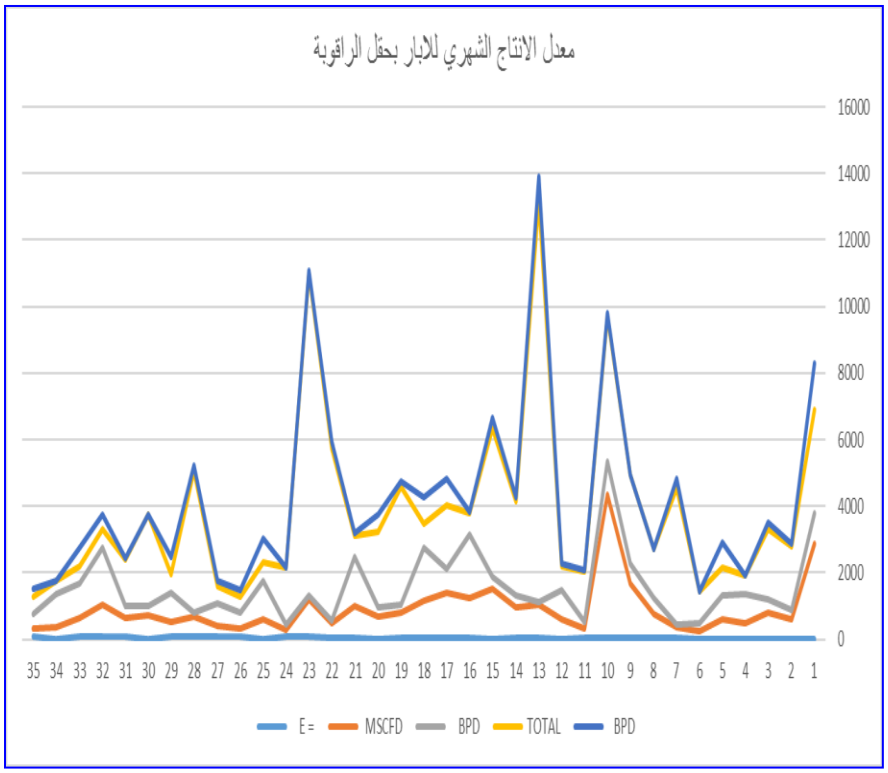

https://sjst.scst.edu.ly
Surman Journal for Science and Technology
ISSN: Online 2790-5721 Print 2790-5713
مجلة صرمان للعلوم والتقنية
Vol. 3, No.1, Dec.2021
Pages: 146 ~ 155

شكل(1) معدل الإنتاج الشهري للحقل

الشكل رقم (2) يوضح معدل التوقف للآبار المنتجة خلال الصيانة وتكلفة الصيانة والوقت التي حدثت بها . ويتم ملاحظة أن وقت الصيانة كان متقارب لكل التسريبات وهذا يدل على سرعة استجابة فريق الصيانة بحقل الراقوبة لمعالجة التسرب وبالتالي تقليل الكميات المفقودة من النفط وبهذا يتم الحد من التلوث الذي قد ينتج من هذه التسربات . ويلاحظ ايضا كثرة عدد حوادث التسريبات في بعض الابار والسبب قد يكون في الانابيب الناقلة من حيث ملائمتها لخواص الموائع المنقولة خلالها .

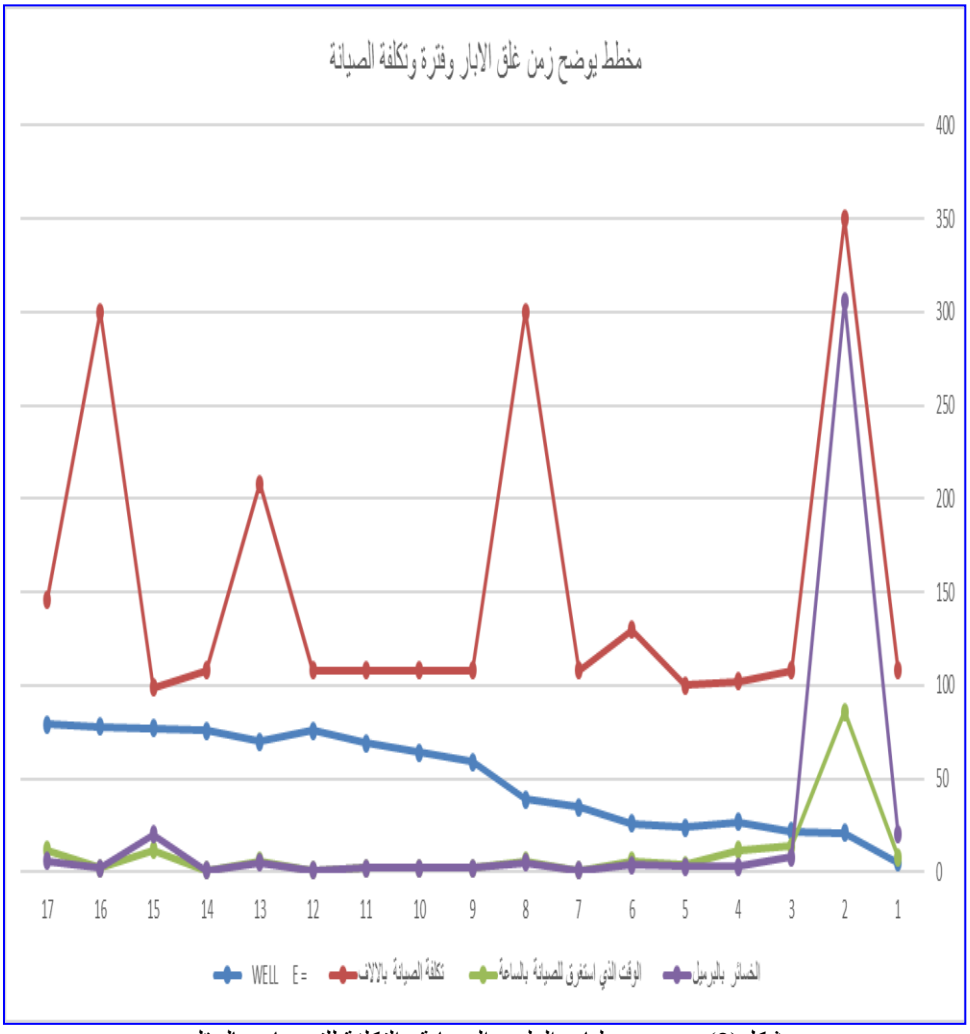

شكل(2) يوضح عمليات الغلق والصيانة والتكلفة للتسربات بالحقل

أخطر التسريبات التي من الممكن أن تحدث في أي حقل هي تلك التسريبات التي تحدث بالمعدات وخط الإنتاج الرئيسي وذلك لأن كميات النفط ستكون أكبر وكذلك نسبة الماء تكون قليلة جدا مقارنة بأنابيب نقل النفط من الابار حيث ان النفط المنقول خلال الانابيب الرئيسية يكون معالج وجاهز للتصدير. والشكل رقم 3 والشكل رقم 4 يوضحان أن التكلفة ووقت اصلاح الخط الرئيسي او المعدات السطحية يكون أكبر مقارنة بتسرب يحدث في خط نقل النفط من البئر لمحطة المعالجة.

https://sjst.scst.edu.ly
Surman Journal for Science and Technology
ISSN: Online 2790-5721 Print 2790-5713
مجلة صرمان للعلوم والتقنية
Vol. 3, No.1, Dec.2021
Pages: 146 ~ 155

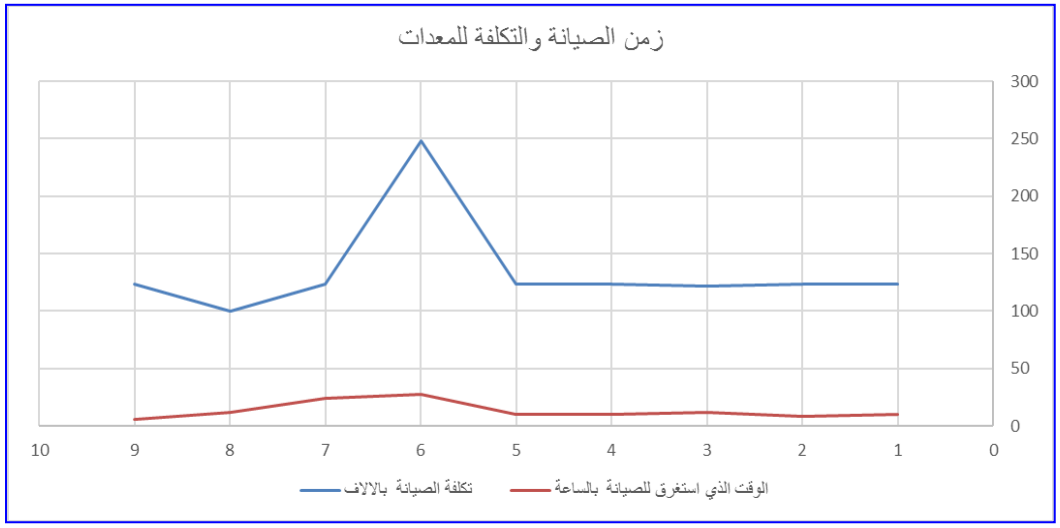

شكل (3) وقت الصيانة وتكلفتها للمعدات

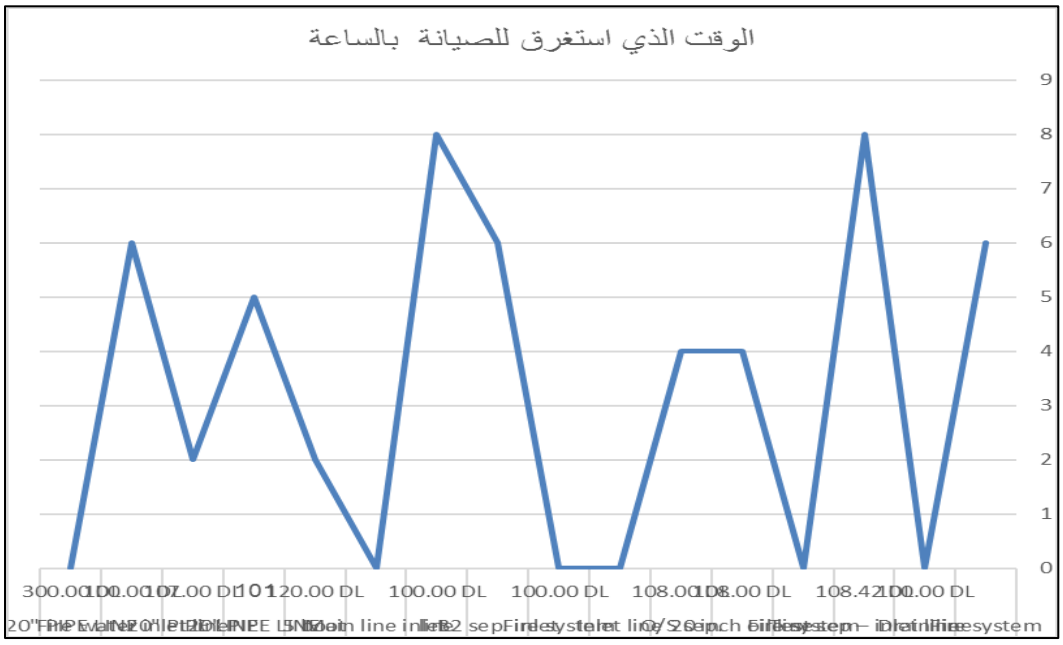

شكل (4) وقت الصيانة وتكلفتها للمعدات

من خلال النتائج المذكورة سابقا تم اجراء الحسابات التالية:

أ- حساب عدد البراميل التي تسربت من الانابيب والمعدات تقديرا وفق القارير خلال ثلاث سنوات ميلادية فقط 2002 من 2003 بلغ 210 برميل من النفط الخام . 210* 50 دولار متوسط سعر البرميل = 10500 دولار

ب- بلغ عدد الساعات التي توقف فيها عملية الضخ 450 ساعة خلال الفترة السابقة لغرض الصيانة وفق التقارير الفنية .
45 ساعة /24 = 19 يوم صيانة تسربات للمعدات والانابيب خلال ثلاث سنوات

ج- صاحب هذم العمليات تلوث للتربة والمناطق المحيطة لهذه التسربات التي بلغ عددها اكثر من 65 تسرب للنفط الخام في طبقات التربة .

SJST
https://sjst.scst.edu.ly
Surman Journal for Science and Technology
ISSN: Online 2790-5721 Print 2790-5713
مجلة صرمان للعلوم والتقنية
Vol. 3, No.1, Dec.2021
Pages: 146 ~ 155

6. -التوصيـــــــــــــات

1- استخدام المواد الكيماوية التي تساعد علي منع التأكل بأنواعه .
2- في حالة التلوث وحدوث إصابات يجب إبعاد المصابين عن منطقة التلوث .
3- ربط كل الحقول بمنظومة الحماية المهبطية للمحافظة علي المعدات .
4- اختيار الانابيب والمعدات والطلاء المناسب والتغليف الجيد للمحافظة علي المعدات .
5- استخدام التقنيات الحديثة للكشف علي المعدات .
6- نوصي بضرورة ضخ مادة كيميائية مانعة لتكون وتجلط النفط بالخزانات والأنابيب
7- نوصي بتعلم برامج المحاكاة (Softwares) الحديثة التي تعمل على أجراء عمليات المحاكاة لخطوط الأنابيب من أجل تنظيف الخطوط والتنبؤ بالمشاكل وأيضا لمعرفة أماكن ونقاط الضعف على طول الخط للحصول على نتائج أكثر دقة.

7. المراجـــــــع

1. أكرم عبدالمنعم حسين ومحمد بن ناصر اليميني (2009) ، قياس ملوثات البيئة، جامعة الملك سعود .
2. سمير رجب سليم (1990)،دليل المواد الكيميائية الخطرة ، دار نشر القاهرة الحديثة للطباعة.
3. عبدالإله الحسين الصطوف (1995)، التلوث البيئي مصادره - آثاره – طرق ا لحماية، سبها: جامعة سبها.
4. علاء حسين الركابي (2009), دراسة تأثير التسرب النفطي على الخواص الهندسية للتربة في مدينة النصر/محافظة ذي قار, جامعة ذي قار، العراق.
5. أسعد عياش ، عبد الله بن فرحان (2005), أساليب الحماية من تسربات النفط في المنشآت النفحية للحد من التلوث البيئي, جامعة نايف العربية للعلوم الأمنية
6. مجموعة مؤلفين (2005) ,النفط والغاز , مكتبة لبنان ناشرون السلسلة: موسوعة الطاقة المبسطة , الترقيم الدولي 9953336407
7. د .منهل عبدالله حمادي، نور فنر عبدالباقي(2018)، طرق النقل بواسطة الأنابيب للنفط الخام الحالية والمقترحة في العراق,JOURNAL OF HISTORICAL & CULTURAL STUDIES
8. محمد أحمد السيد خليل (2014) , الحماية من التآكل: لمعدات انتاج ونقل وتصنيع البترول والغاز , دار الكتب العلمية – بيروت.
9. Oil and Natural Gas Transportation (2019) CAPP. Retrieved from: https://www.capp.ca/energy/transportation/

SJST Surman Journal for Science and Technology | ISSN: E 2790-5721 P 2790-5713
Vol3, No.1, Dec_2021 , pp. 156 - 168

An Approach to Integrate IoT and Mobile Technology for Remote Camera Management

Noureddin Mohammed Elazumi[1], Abubaker Kashada[2], Mohamed Alforgani[3]
[1, 2]Surman College of Science and Technology
[3]Sok Jomma Institute for Technical Science, Tripoli
n_elazumi@scst.edu.ly, kashada@scst.edu.ly, mabdunnabi1970@gmail.com

Abstract
The goal of most control systems is to create external tools that can manage larger, more complex machines. Recently, however, control devices have become more compact, with smaller smart devices being utilized to control larger machines. This shift offers significant advantages in industries, particularly in terms of mobility and simplicity. This study proposes a camera control system designed to use mobile devices through wireless technology, offering enhanced mobility at a lower cost. The system enables a mobile phone to control an intelligent IP camera via Bluetooth and was developed using the Java Application Development Kit (JDK). The design and implementation of this system were informed by research into existing technologies and tools, as well as methods used to bring the research to fruition. several potential areas for future research and development were identified to further improve the system's capabilities.

Keywords: *IoT, internet of things, Mobile device, wireless technology, Bluetooth, I.P. camera,*

Introduction

Control systems in engineering comprise a vast and essential field of study. In recent years, these systems have become integral to daily life, permeating nearly every interaction and activity. Numerous devices and gadgets are designed with foundational principles of control engineering, playing crucial roles in various aspects of our lives. Examples such as home appliances like televisions and advanced systems like space shuttles at the International Space Station illustrate the pervasive influence of control engineering concepts. The evolution of wireless communications and mobile technologies has further expanded the application areas for these concepts. Cameras, traditionally used for monitoring and recording events, have significantly advanced with autonomous capabilities and remote accessibility. Combining these technologies represents a substantial enhancement in modern technology.

Early remote camera systems required direct attachment to a computer or dedicated device to function effectively. Control was typically managed through keyboards or specialized head gestures, such as "head motion" and "head flicking," as described by Dingyun et al. [1]. Scott, Bradley, et al. [2] noted that remote camera systems not only enable user control over camera movements but also over the supporting camera mechanisms. There is a growing demand for multifunctional controls beyond basic camera manipulation, such as Pan/Tilt/Zoom functionalities integrated into contemporary cameras.

A typical remote camera control system includes an IP camera, a stand, a web server application for data transmission, network infrastructure, a storage device or data receiver, and an external control device. This proposed system incorporates additional components like mobile devices (phones) and Bluetooth technology, enhancing flexibility and accessibility.

The entire system was developed using Java, highlighting its robustness and adaptability in integrating IoT and mobile technologies for effective remote camera management.
With the rise of smart devices and advancements in Information Technology (IT), these objectives can now be achieved using compact and efficient mobile technologies [3]. The central aim of this study is to develop a system for remotely controlling and monitoring a camera via a mobile phone using Bluetooth technology, leveraging the Internet of Things (IoT) framework.

A mobile phone was selected as the control device due to its portability and widespread availability, making it ideal for user interaction with the remote camera system. Bluetooth technology was chosen for its low energy consumption, adequate range, and compatibility with mobile devices. Java was selected as the programming language due to its platform independence and strong capabilities in mobile and IoT integration [4].

This study focuses on the ability to control a remote camera via a mobile phone, specifically utilizing Bluetooth and IoT technologies. While the possibility of incorporating multi-device access for dynamic, concurrent control is acknowledged, this falls outside the scope of the current research and is reserved for future work.

Recent advancements in mobile and IoT technologies have opened new avenues for remote system management, particularly in multimedia and real-time applications. This study explores how integrating mobile devices and IoT frameworks can simplify and enhance the control of remote systems, such as cameras, providing users with greater mobility and flexibility.
The ability to remotely manage systems has broad applications across several industries, including healthcare, security, aerospace, robotics, and more, where IoT-driven remote-control systems offer efficiency, safety, and operational scalability.

Literature Review

Mobile phone technologies have become an essential part of daily life for most people, and the industry has increasingly integrated camera functionalities into mobile devices. Information technology industries have leveraged this trend, enabling cameras to be embedded in various gadgets, from laptops to smartphones. It is now "normal to access information, take photographs, record our thoughts, and share these with others through a single device [5]. Although a wide variety of cameras exist, many are still limited by technological constraints such as image resolution, real-time event capture, and autonomous functionality. However, focusing on cameras with autonomous capabilities is essential for achieving the objectives of this research, which aims to integrate IoT and mobile technology for remote camera control.

Cameras with autonomous systems are often referred to as remote cameras or IP cameras. IP cameras, also known as network cameras, utilize Internet Protocol to transmit image data and control signals over an Ethernet link. This aligns with the definition provided by Network Camera Review [6], which confirms that IP cameras function similarly to analog closed-circuit television (CCTV) systems but with enhanced connectivity and network functionality. Many modern IP cameras are equipped with embedded internet video servers or web server systems making them powerful tools for surveillance and remote monitoring.

A typical remote camera management system comprises several components: a remotely controllable camera, a mounting stand, an application to facilitate data transfer, a storage device or data receiver, and a control device. These components work together within an IoT framework, where mobile technology plays a pivotal role in remote access and control. The following section will explore various applications of such systems, emphasizing their role in integrating IoT and mobile technologies for enhanced camera management. In the medical field, the integration of remote camera control systems has significantly enhanced the ability of healthcare professionals to perform procedures more efficiently. As confirmed by [7], cameras are crucial tools for both external and internal imaging in medicine. For instance, dentists use digital imaging technology to enhance diagnostics and treatment by deploying cameras on probes that can be maneuvered inside the mouth, transmitting real-time images to screens for better visibility and patient communication.

In robotics, remote camera systems are integral to navigating dynamic environments and capturing visual data. The field of artificial evolution in robotics, as explored by Morales, et al [8], focuses on developing adaptive behaviors for robots in real-time, allowing them to autonomously adjust to environmental changes. This research has led to advancements in autonomous robot control systems, capable of responding to varying conditions effectively. One key application of remote cameras in robotics involves their attachment to mobile robots, allowing the capture of real-time images from previously inaccessible areas. While these systems face challenges such as bandwidth limitations and connection speed, their use in space exploration missions like the Apollo program demonstrates their potential. Remote cameras attached to robots continue to play a critical role in collecting and transmitting visual data in space and other challenging environments.

Security is one of the most widespread applications of remote camera systems, particularly in the form of Closed-Circuit Television (CCTV). These systems are commonly deployed in parking lots, streets, offices, and various other public and private spaces. Remote cameras used in security require a monitoring system, often referred to as a surveillance system, which retrieves and stores the captured footage for future reference. These systems are frequently utilized by law enforcement and security services. In financial institutions, where fraud and other financial crimes may occur, remote camera systems are essential for monitoring activities and maintaining security. As Turanjanin [9] points out, footage from security cameras is often used as evidence in court to confirm the presence or actions of individuals in specific locations. However, despite their utility, these systems can also be subject to misuse, as noted by Nissenbaum [10], raising concerns over privacy and the potential for criminal exploitation.

The application of remote camera control systems in education is a highly effective and increasingly relevant area. Education, being the foundation of knowledge, faces challenges such as exam malpractice, where students resort to unethical means like cheating to pass exams. Remote camera systems offer a solution to this issue by enabling enhanced surveillance in examination halls. By installing cameras that are controlled remotely by designated personnel, the behavior and conduct of students during exams can be closely monitored. Recordings from these cameras can be reviewed afterward, allowing authorities to make informed decisions based on the footage [11]. This system not only ensures the integrity of the examination process but also deters students from engaging in dishonest practices [13][14][15][16][17].

There are numerous wireless technologies with varying ranges, including radio frequency (RF), infrared light, laser light, visible light, acoustic energy, Bluetooth, and Wi-Fi [11]. The emergence of wireless technologies is seen as a move towards replacing wired connections. Some of these technologies, like 802.11a and Bluetooth, operate without the need for licensing.

In this research, Bluetooth technology is the primary focus. Bluetooth enables communication between diverse devices that implement the technology according to global standards. It is a low-power, short-range wireless technology, ideal for mobile devices, and is integral to the research's objective of controlling remote cameras through mobile phones. Bluetooth follows a specific protocol stack, which ensures compatibility and communication between devices worldwide, making it a suitable choice for IoT and mobile device integration in remote camera management systems.

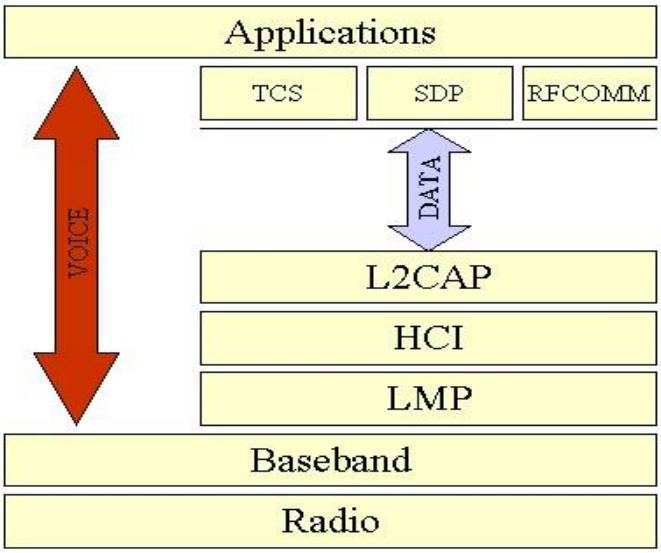

Fig 1 Bluetooth protocol stack

The radio layer is regarded as the physical wireless connection. To avoid interference with other devices that communicate in the industrial, scientific and medical (ISM) band, the modulation is based on fast frequency hopping. Bluetooth divides the 2.4 GHz frequency band into 79 channels 1 MHz apart (from 2.402 to 2.480 GHz), and uses this spread spectrum to hop from one channel to another, up to 1600 times a second. The standard wavelength range is 10 cm to 10 m, and can be extended to 100 m by increasing transmission power. [12]. The baseband layer is said to be in charge of "controlling and sending data packets over the radio link. It provides transmission channels for both data and voice. The baseband layer maintains Synchronous Connection-Oriented (SCO) links for voice and Asynchronous Connectionless (ACL) links for data. SCO packets are never retransmitted but ACL packets are, to ensure data integrity [12]. The Link Manager Protocol (LMP) used to use the links set up by the baseband to establish connections and manage piconets. Responsibilities of the LMP also include authentication and security services, and monitoring of service quality [12].

The Host Controller Interface (HCI) is an interface that "is the dividing line between software and hardware. The L2CAP and layers above it are currently implemented in software, and the LMP and lower layers are in hardware. The HCI is the driver interface for the physical bus that connects these two components. The HCI may not be required. The L2CAP may be accessed directly by the

application, or through certain support protocols provided to ease the burden on application programmers [12]. The Logical Link Control and Adaptation Protocol (L2CAP) is used to receive application data and adapts it to the Bluetooth format. Quality of Service (QoS) parameters are exchanged at this layer [12].

The approach to developing this framework builds on the foundational research of existing remote camera control systems. To meet the research's objectives, the ideas from similar systems were adapted to form a comprehensive method. Researching existing similar systems, was crucial as it provided insights into how remote camera management systems are designed and operated. This research enabled the identification of key features that could be beneficial to the new system, allowing for a more informed and efficient development process. Various systems were analyzed, and the most relevant ideas were integrated into the proposed design.

One of the systems that strongly influenced the approach was the Interactive PTZ Camera System. This system was chosen because its architecture closely aligns with the requirements of the proposed IoT and mobile-integrated camera system. The interactive PTZ camera uses wireless control via a Nintendo remote, while the proposed system uses a mobile phone for wireless control. Both systems also feature a server-based intermediate system that facilitates communication between the camera and the control device, making it an ideal model for this research. This systematic approach and integration of existing technologies and new knowledge have resulted in a robust IoT-based remote camera management system, effectively achieving the research's aims.

Research Analysis

After critically analyzing existing systems and available technologies, a structured plan was developed for the implementation of the proposed IoT-based remote camera management system. The insights gained from various researched systems were instrumental in shaping the research's design and functionality.

System Design

The system design was decided and planned out considering a means of communication with a remote camera through a medium (Bluetooth) from the mobile device, the system is designed and illustrated by the fig 2 below.

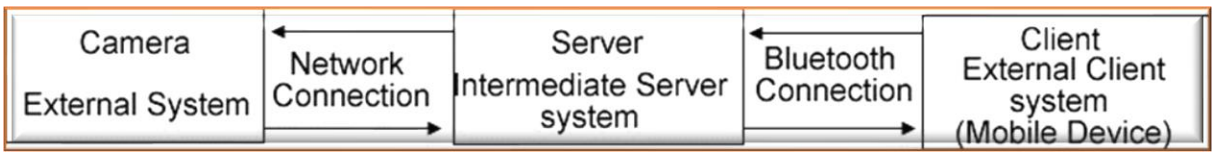

Fig 2 System Design.

Proper investigation was done with the aid of the internet to research existing hardwares needed for the proposed system. Hardwares, such as camera, network devices, and mobile devices. To make the proposed system as standard as possible the research requires industrial standard devices. Below is list of the selected devices used in the development of the research. Axis M1054 Network Camera: this equipment is an industrial standard I.P. camera that supports voice, PTZ and other functionalities.

Linksys EtherFast Cable/DSL Router model no. BEFSRA1: this equipment is another industrial standard network device that supports TCP/IP, DHCP DSL and other network functionalities.
A computer machine with minimum of 1 gigabyte RAM, 10 gigabyte hard drive, Bluetooth device, and windows XP operating system or any of the like and later. Sony Ericson k800i: this equipment is a mobile phone with the support for java platform, Bluetooth and midp 2.0 and other functionalities. The next section explains the software application used in the implementation of the proposed system. This was a top challenge to decide at the beginning of the implementation of the proposed system due to the following reasons. Application software development kit from camera manufacturer only supports Microsoft development environment and system is required to run on any platform; which means JAVA is at the point in time the best option. The system will have to be able to manage its data autonomously.

Selecting the software development environment was a tough decision as one of the system requirements is to be able to run on a multiple platform. This was a risk and that I had to take.
Adobe Fireworks was used for the interface design and Java was used to implement the actual application design for both the server side (Computer machine) and the client side (Mobile Phone). The server application development side utilize the java2 enterprise edition (J2EE) was used because of its robustness and easy implementation using Netbeans 6.8 version. Also, the client +side application development makes use of the java2 micro edition (J2ME) and it was also done using Netbeans 6.8 version. Netbeans is a java package just like visual studio, it is very robust, very easy and user-friendly application development environment. Netbeans is not restricted to Java only; it can also be used to write scripts in C#, C++, Javascript and so on. Since the proposed system will be making use of some data there must be another application that should handle the data management. Therefore, there is a need for database management software and Microsoft access database application was selected because of its simplicity.
Below are some the interfaces designed prior to the actual implementation of the interfaces in Netbeans. The interfaces were designed as part of the plan as well as to imagine how the interfaces of the application would look like in order to achieve the aim of the research. Below are explained the software interfaces. The server login is designed in a way to get the user's name and password supplied from the operator and then perform login into the main application environment, fig 3

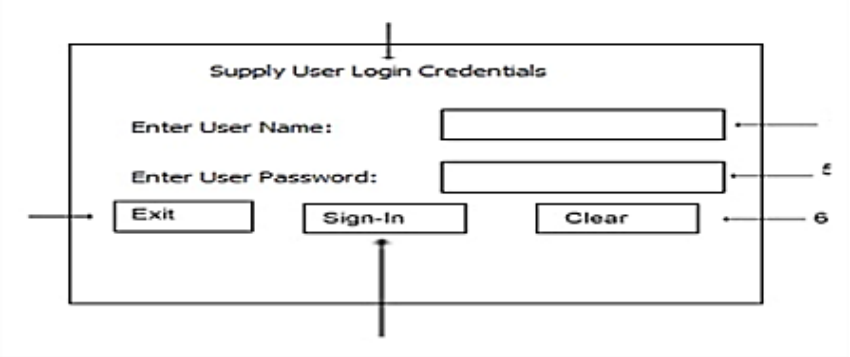

Fig 3 Server Login

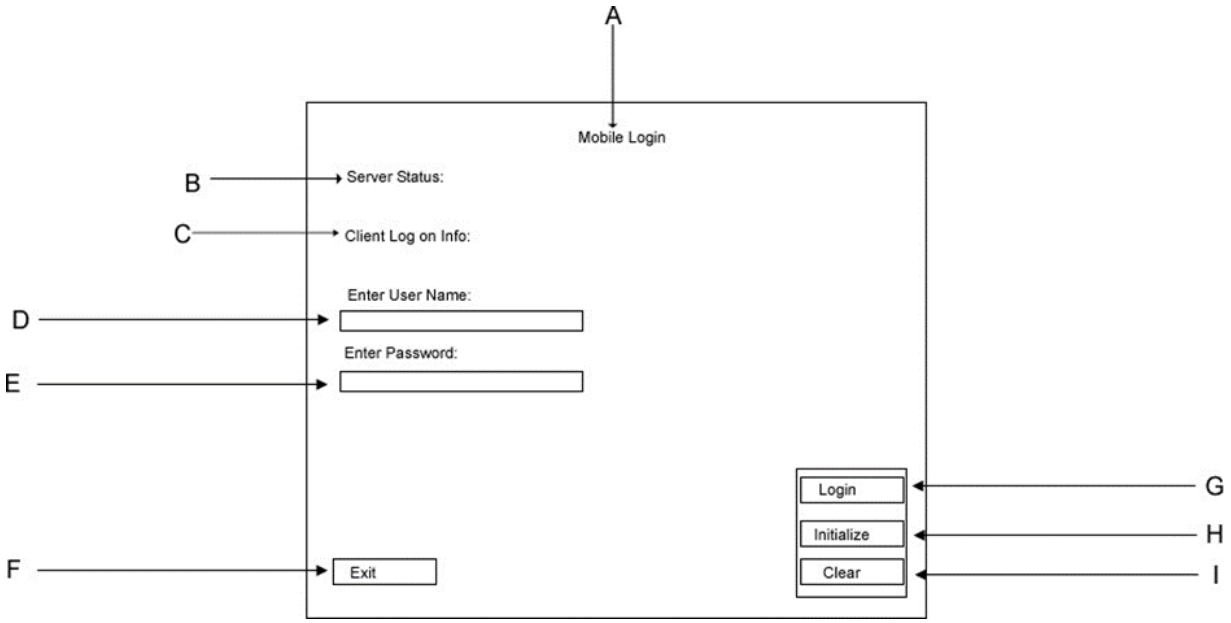

Fig 4: Client Login Design

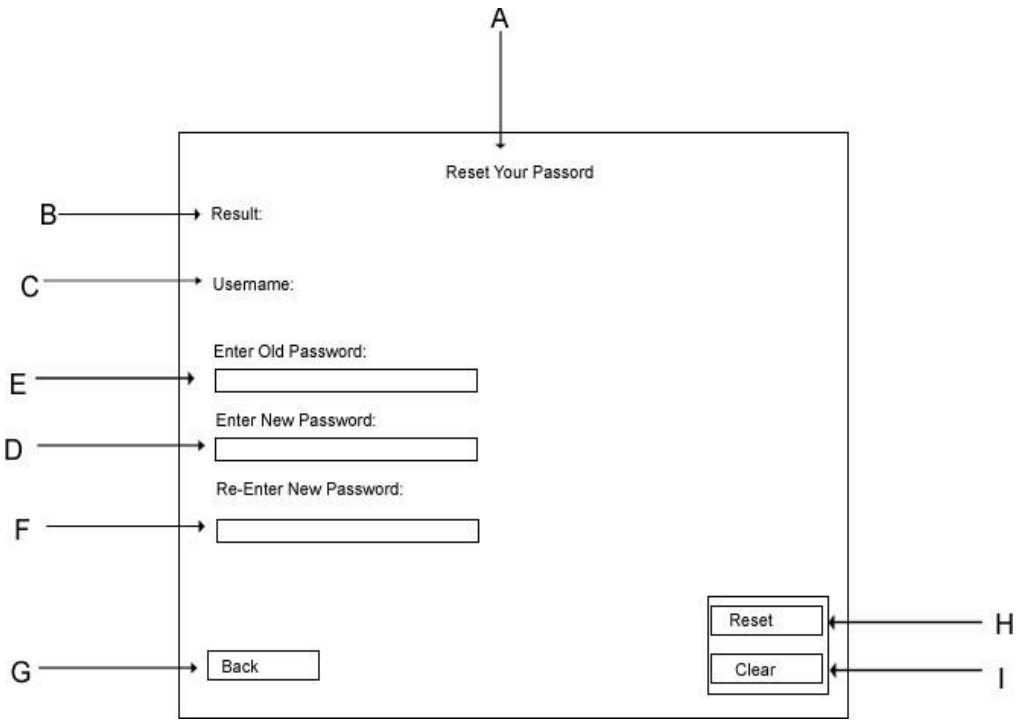

Fig 5: Client Password Reset Form Design

Database Design

When the interface was designed then the next task was to find a means of accommodating the data that will be used for the software. The database design was kept simple so as to avoid complicated data management and to be able to achieve the main aim of the proposed system. Since the database tool selected is relational in nature then simple design was made. See table 1 for the description of the database structure.

Column Name	Data Type	Description
tblUser		For storing user details
Sno	Numeric (integer)	For auto numbering
UID	Text	For storing user names (primary key column)
Pass	Text	For storing associated passwords
Stat	Text	For storing the status of the user
Tblcam		For storing camera credentials
Sno	Numeric (Integer)	For auto numbering
LOC	Text	For storing the camera I.P. address or location (combined primary key column with UID)
UID	Text	For storing the camera user id (combined primary key column with LOC)
Pass	Text	For storing camera password
Stat	Text	For storing the current status of active camera credential that is active
Tbldir		For storing the picture directory string
Sno	Numeric (Integer)	For auto numbering
Dir	Text	For storing the string directory full path string (primary key column)
Tblbt		For storing the Bluetooth number of established connections
Sno	Numeric (Integer)	For auto numbering (primary key column)
Maxno	Number	For storing the current number of Bluetooth connection

Table 1: Database Structure

Software Algorithm

The algorithm is designed to make the application flexible and easily operated, the following points will clarify the software algorithm. When the system (Server) is started it will first check the database and to make sure the database is intact and then performs a user availability check especially the admin account. If the admin account is not found then it will create the admin account and notify the operator as the time of the changes made to the database and then proceeds by displaying the application login form. This form will prompt for the user's name and password to be entered as without this information supplied the operator will not be allowed to proceed from the form. This

login form will validate the user details supplied and then when appropriate data required for the login is tested valid then the program will display the main application main form.
The main application form environment will provide main functions such as the camera pan/tilt/zoom (PTZ) control, camera light control, camera connection, picture capture, mobile devices connection settings, real-time image streaming, mobile device communication, Bluetooth settings, and administration.

Dataflow Diagram

The dataflow diagram illustrates the way the data flows through the system entire proposed system. Fig9 below describes the dataflow of the system.

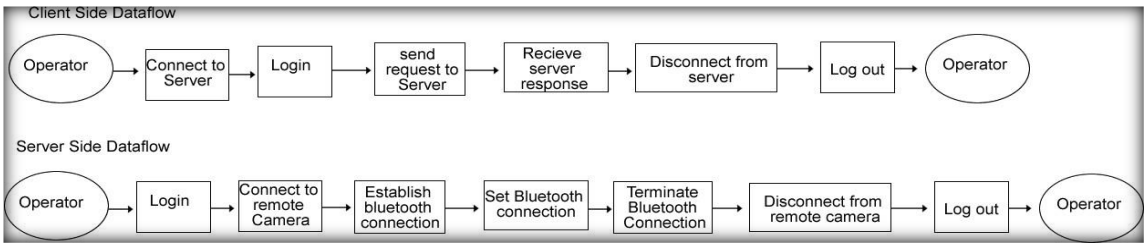

Fig6: dataflow diagram

Flow Chart

The flow chart of the system shows algorithm of the entire operation performed within the proposed system. The following figures illustrate at a glance how the program runs. This flow chart explains the program from when the operator logins into the server side of the application how the application will handle the data from provided in order to display the main application environment with other processes such as setting Bluetooth connection and saving the captured image currently displayed.

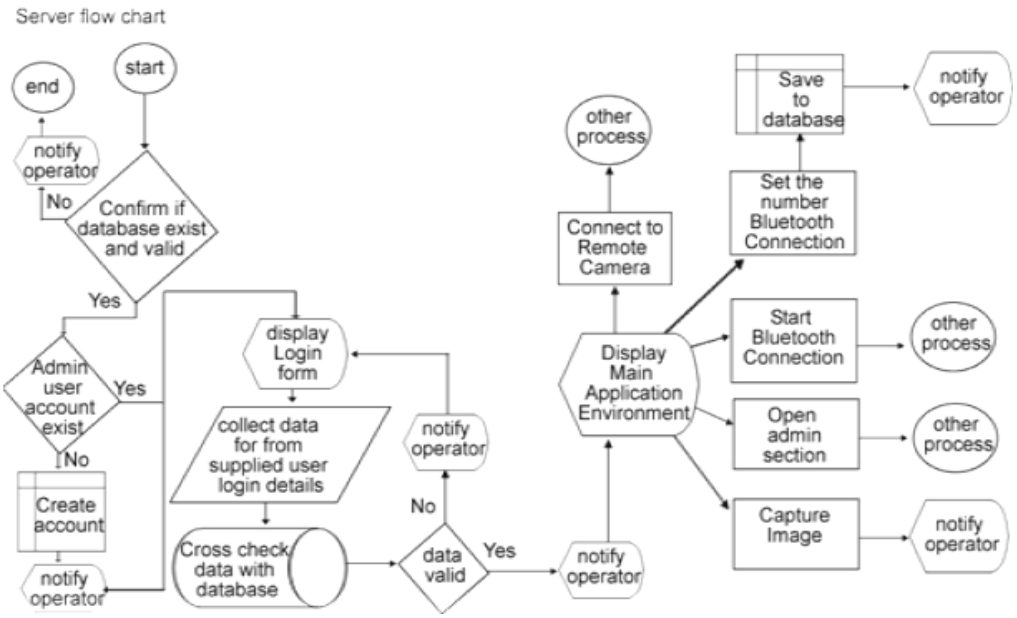

Fig 7: server flow chart A

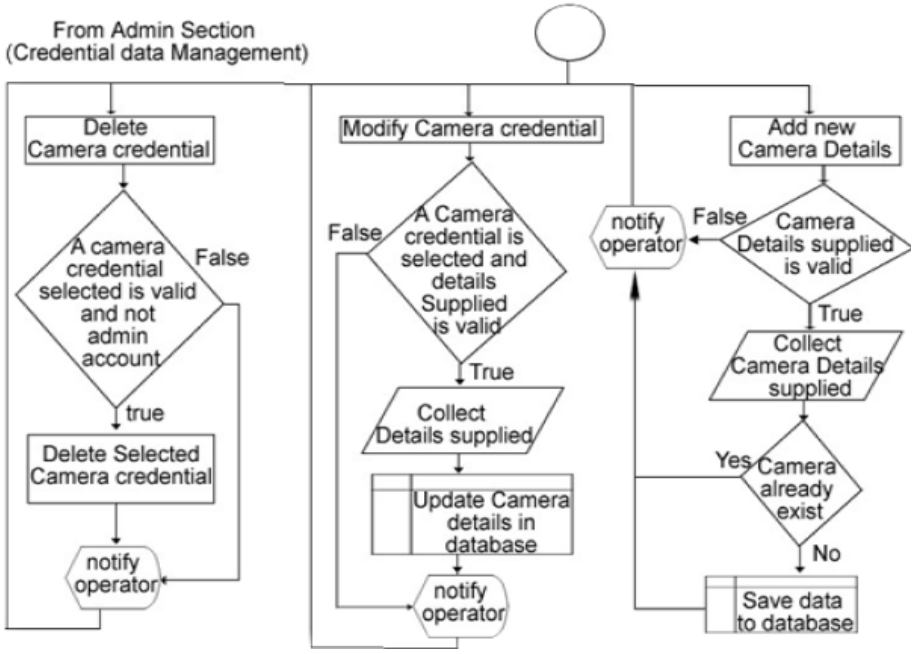

Fig 8: server application

This flow chart gives details at a glance the procedure that occurs when the credential data management section of the admin section is invoked from the server application. The research was executed in stages, the first stage was to research the type of system, then next was to get the requirement of the system, after that a form of survey was conducted to know how and what users of this system would require. Then the development of the system was carried out. After that the system was tested and results were provided. The following statements will explain path of the significant tasks undertaken in the operation of implementing the research.

Survey: this method involved the collecting of information from the users in order to know their view of how this kind of system is to be implemented and what they will prefer in the system.
thereby bringing about how the research can be accomplished to meet the system requirement as well as users, requirement. Analysis of data: the data gathered was analysed and quick and adequate resolution was made, and preparation for the development of the research was immediately underway. Testing: the software involved in the research underwent a lot of tests within stages of development and always ensuring it is free of errors; such as syntactic and semantic before it is finally packaged for implementation.

Challenges: there where series of challenges during the development stages of this paper which brought a necessity to do more research as to find more information about the current challenge. For instance, challenges involved are most technical in nature like the creation of single to multi-point Bluetooth connection was very easier said than done in the execution of the research, other ones which involved transferring images from server-side application to client-side application proved to be another challenging task to do. Another challenge of being able to communicate to and from the server to the client and vice versa.

Conclusion

Extensive research was conducted on existing systems and technologies to understand the requirements and potential challenges. This included studying similar systems, evaluating the technologies to be used, and preparing for any professional or technical issues. A risk management strategy was also developed to handle potential problems during the research. Valuable insights were gained from various Java forums, websites, and professional resources, such as the Sun website. These resources provided essential information on Java technologies, Bluetooth, mobile phone integration, client-server systems, and security. The knowledge acquired was crucial in guiding the research and overcoming technical challenges.

During the development, a significant challenge was the incompatibility of the camera's video codec with the Java Media Framework. The camera's RTSP server provided a video format that could not be handled by the framework. This issue highlighted the need for further research into video streaming protocols and codecs. An alternative approach involving real-time image streaming was adopted, where snapshots were captured at high frequency and combined into a video stream. This solution effectively addressed the video format compatibility issue and enabled real-time display. There are opportunities for further research in areas such as video codec compatibility with Java Media Framework, advanced streaming protocols, and additional features like enhanced video analytics or improved wireless communication. Exploring these areas could provide more robust solutions and enhance the system's capabilities.

In conclusion, the research provided valuable insights and challenges, making the experience both interesting and rewarding. The knowledge gained was significant, and further exploration of identified challenges and new technological advancements could lead to even more innovative solutions in the future.

References

[1] Zhu, Dingyun, Tom Gedeon, and Ken Taylor. "Keyboard before head tracking depresses user success in remote camera control." *Human-Computer Interaction–INTERACT 2009: 12th IFIP TC 13 International Conference, Uppsala, Sweden, August 24-28, 2009, Proceedings, Part II 12*. Springer Berlin Heidelberg, 2009.

[2] Scott, Bradley, et al. "Healthcare applications of single camera markerless motion capture: a scoping review." *PeerJ* 10 (2022): e13517.

[3] Abubaker Kashada, Mohamed Alforgani, Awatif Isnoun, Lamia Gweder, Salha Alhadad. Barriers to sustainable telemedicine implementation in Libya. International Journal of Science & Healthcare Research. 2023; 8(3): 103-110.

[4] Kashada, Abubaker, and Wesam Mohamed AllaEddinGhaydi. "The impact of perceived usefulness & perceived ease of use on the successful adoption of information systems in developing countries." *IOSR Journal of Computer Engineering (IOSR-JCE)* 22.1 (2020): 45-48.

[5] Larsen, Lars, and Jonghwa Kim. "Path planning of cooperating industrial robots using evolutionary algorithms." *Robotics and Computer-Integrated Manufacturing* 67 (2021): 102053.

[6] Paneru, Suman, and Idris Jeelani. "Computer vision applications in construction: Current state, opportunities & challenges." *Automation in Construction* 132 (2021): 103940.

[7] Eslamian, Shahab, Luke A. Reisner, and Abhilash K. Pandya. "Development and evaluation of an autonomous camera control algorithm on the da Vinci Surgical System." *The International Journal of Medical Robotics and Computer Assisted Surgery* 16.2 (2020): e2036.

[8] Morales, Alejandro, et al. "A multispectral camera development: From the prototype assembly until its use in a UAV system." *Sensors* 20.21 (2020): 6129.

[9] Turanjanin, Veljko. "Video surveillance of the employees between the right to privacy and right to property after Lopez Ribalda and others v. Spain." *U. Bologna L. Rev.* 5 (2020): 268.

[10] Nissenbaum, Helen. "Protecting privacy in an information age: The problem of privacy in public." *The ethics of information technologies*. Routledge, 2020. 141-178.

[11] Wells, Gary L., et al. "Policy and procedure recommendations for the collection and preservation of eyewitness identification evidence." *Law and human behavior* 44.1 (2020): 3.

[12] Kambourakis, Georgios, et al. "A state-of-the-art review on the security of mainstream IoT wireless PAN protocol stacks." *Symmetry* 12.4 (2020): 579.

[13] Kashada, Abubaker, Hongguang Li, and Osama Koshadah. "Analysis Approach to Identify Factors Influence Digital Learning Technology Adoption and Utilization in Developing Countries." *International Journal of Emerging Technologies in Learning* 13.2 (2018).

[14] Kashada, Abubaker, Hongguang Li, and Chong Su. "Adoption of flipped classrooms in K-12 education in developing countries: Challenges and obstacles." *International Journal of Emerging Technologies in Learning (Online)* 12.10 (2017): 147.

[15] Kashada, Abubaker, Hongguang Li, and Osama Kashadah. "The impact of user awareness on successful adoption of decision support System DSS in Developing Countries: THE Context of Libyan Higher Education Ministry." *American Scientific Research Journal for Engineering, Technology, and Sciences (ASRJETS)* 16.1 (2016): 334-345.

[16] Kashada, Abubaker, Awatif Isnoun, and Nureddin Aldali. "Effect of information overload on decision's quality, efficiency and time." *International Journal of Latest Engineering Research and Applications* 5.1 (2020): 53-58.

[17] Kashada, Abubaker, Eiman Ehtiwsh, and Haythem Nakkas. "The role of technology acceptance model (TAM) towards information systems implementation success: A Meta-Analysis." *The International Journal of Engineering and Science (IJES)* 9.1 (2020): 3036.